IMPACTS OF TOPOLOGICAL AND MOLECULAR MASS POLYDISPERSITY ON SELF-ASSEMBLED POLYMERIC MICELLES

JOHANNES GUTENBERG
UNIVERSITÄT MAINZ

Marios Giannakou
Born: 19/12/1996 in Limassol, Cyprus

Dissertation for the award of the title
Doctor of Natural Science
submitted to the Institute of Physics in the
Faculty of Physics, Mathematics and Computer Sciences (FB 08)
of the Johannes Gutenberg-Universität Mainz
on 23/06/2025

DECLARATION

I hereby declare that I have written this thesis independently and without the use of sources other than those indicated. All passages and ideas taken from other sources, either literally or in substance, are appropriately cited. Additionally, I declare that I have used generative AI tools as an aid in the preparation of this thesis. These tools were employed to support tasks such as language refinement, text clarity, grammar suggestions, and formatting advice. All scientific content, interpretations, and conclusions are my own, and I take full responsibility for the originality and accuracy of the work presented.

Mainz, 04/11/2025
Marios Giannakou

Marios Giannakou
Impacts of Topological and Molecular Mass Polydispersity on Self-Assembled Polymeric Micelles
Oral examination: 30/10/2025
First advisor: Prof. Friederike Schmid
Condensed Matter Physics (KOMET)
Institut für Physik
Staudingerweg 7-9
Johannes Gutenberg Universität
55128 Mainz

ABSTRACT

This thesis investigates how architectural complexity and mass polydispersity influence the self-assembly, structure, and mechanics of polymer systems, using a combination of analytical theory and self-consistent field theory (SCFT) calculations. Across four studies, we extend theoretical frameworks, develop computational tools, and apply them to underexplored polymer architectures with relevance to soft materials design.

The first study extends strong stretching theory to polydisperse linear brushes on curved surfaces in good solvent and melt conditions. Using realistic Schulz-Zimm chain length distributions, we quantify how curvature and polydispersity affect chain end distributions, brush shape, and bending moduli. We identify conditions under which end exclusion zones (EEZs)—regions devoid of chain ends—appear in convex geometries, and show that their location can be tuned via the polymer length distribution, offering a novel route to control brush structure and mechanical response.

In the second study, we develop a SCFT algorithm using real-space methods with adaptive spatial and contour discretization. By refining resolution near surfaces and grafting points, the method captures sharp gradients and reduces numerical instability with minimal cost. Validated on block copolymer films and brushes, it enables accurate and efficient simulations in three dimensions, expanding the tractable range of SCFT applications.

The third study examines micelles formed from polydisperse linear-hyperbranched block copolymers (LHBCs), comparing them to linear-dendritic (LDBC) and linear diblock polymers. Using molecular dynamics to generate realistic LHBC structures, we show via SCFT that LHBC micelles have lower critical micelle concentrations, greater stability, and higher drug loading capacity than LDBC micelles—benefits that increase with polydispersity. LHBCs also exhibit a high number of terminal groups for functionalization, independent of branching heterogeneity.

Lastly, we explore the self-assembly of amphiphilic gradient copolymers with a $1:1$ styrene-isoprene composition in a selective solvent. SCFT calculations reveal a transition from spherical to cylindrical to lamellar micelles as the gradient flattens, with near-degenerate free energies. A phase diagram for idealized gradient copolymers shows that solvophobic block size dominates morphology selection, while gradient shape further modulates micelle structure and stability.

ZUSAMMENFASSUNG

Diese Dissertation untersucht, wie architektonische Vielfalt und Massenpolydispersität die Selbstorganisation, Struktur und mechanische Eigenschaften von Polymersystemen beeinflussen. Dazu verwenden wir eine Kombination aus analytischer Theorie und self-consistent field theory (SCFT)-Berechnungen. In vier Studien erweitern wir theoretische Modelle, entwickeln numerische Werkzeuge und wenden diese auf bislang wenig erforschte Polymerarchitekturen an, welche für die Entwicklung weicher Materialien relevant sind.

Die erste Studie erweitert die sogenannte "strong stretching theory" auf polydisperse Polymerbürsten auf gekrümmten Oberflächen, sowohl unter guten Lösungsmittelbedingungen als auch im Schmelzzustand. Mithilfe realistischer Schulz-Zimm-Verteilungen für die Kettenlänge quantifizieren wir, wie Krümmung und Polydispersität die Endverteilungen der Ketten, die Bürstenform und die Biegemodule beeinflussen. Wir identifizieren Bedingungen, unter denen sogenannte "end exclusion zones" (EEZs) – Bereiche ohne Kettenenden – in konvexen Geometrien auftreten, und zeigen, dass deren Position über die Polymerlängenverteilung steuerbar ist. Dies eröffnet einen neuartigen Ansatz zur Kontrolle der Bürstenstruktur und ihrer mechanischen Eigenschaften.

In der zweiten Studie entwickeln wir einen SCFT-Algorithmus basierend auf Realraummethoden mit adaptiver räumlicher und konturlängenspezifischer Diskretisierung. Durch eine verfeinerte Auflösung in der Nähe von Oberflächen und Bindestellen erfasst die Methode scharfe Gradienten und reduziert numerische Instabilitäten bei minimalem Rechenaufwand. Anhand von Blockcopolymerfilmen und -bürsten getestet, ermöglicht sie präzise und effiziente Simulationen in drei Dimensionen und erweitert so den anwendbaren Bereich der SCFT.

Die dritte Studie untersucht Mizellen, die sich aus polydispersen linear-hyperverzweigten Blockcopolymeren (LHBCs) zusammensetzen, im Vergleich zu linear-dendritischen Blockcopolymeren (LDBCs) und linearen Diblockcopolymeren. Mittels molekulardynamischer Simulationen zur Erzeugung realistischer LHBC-Strukturen zeigen wir anhand von SCFT-Berechnungen, dass LHBC-Mizellen niedrigere kritische Mizellenkonzentrationen, höhere Stabilität und eine größere Wirkstoffbeladung als LDBC-Mizellen aufweisen. Diese Vorteile für LHBC-Mizellen nehmen mit zunehmender Polydispersität zu. Zudem besitzen LHBCs eine hohe Anzahl funktionalisierbarer Endgruppen, unabhängig von der Verzweigungsheterogenität.

Abschließend untersuchen wir die Selbstorganisation amphiphiler Gradientencopolymere mit einem 1 : 1-Verhältnis aus Styrol und Isopren in einem selektiven Lösungsmittel. SCFT-Berechnungen zeigen einen Übergang von kugelförmigen über zylindrische, bis hin zu lamellaren Mizellen mit zunehmender Abflachung des Gradienten. Ein

Phasendiagramm für idealisierte Gradientencopolymere zeigt, dass die Größe des solvophoben Blocks die Morphologie dominiert, während die Gradientenform zusätzlich die Struktur und Stabilität der Mizellen moduliert.

PREFACE

The main purpose of this thesis is to explore the effects of topological and molecular mass polydispersity on micelle-forming linear-dendritic block copolymers. Monodisperse linear-dendritic micelles have been studied extensively in the past as promising candidates for targeted drug delivery. Their less well-defined and often more economical—counterparts, linear-hyperbranched block copolymers, have received comparatively little attention due to the perception that their structural randomness is a disadvantage. In this thesis, I demonstrate that this need not be the case; in fact, these systems can outperform their more precise analogues in certain aspects.

In addition to this central topic, several related projects that emerged indirectly from the original research question are also explored. These include the study of polydisperse curved polymer brushes, the development of adaptive discretization schemes for numerical calculations, and investigations into micelle-forming gradient copolymers.

The main theoretical tool employed throughout this work is self-consistent field theory (SCFT). Although many detailed sources on SCFT exist, I found it challenging to understand where specific assumptions and terms in the theory originate. This thesis attempts to clarify these aspects.

While I do not aim to offer a comprehensive treatment of SCFT and related methods, I hope to provide a clear and accessible account that will benefit future students. My goal is for readers with only a basic background in statistical mechanics to be able to follow the theory and gain the confidence to perform their own SCFT calculations.

To that end, I briefly review essential topics in polymer physics, including the Gaussian chain model and Flory-Huggins theory, before introducing SCFT in a more systematic manner.

Following this, both published and unpublished projects are presented.

Finally, a summary of the main results is provided, along with a brief discussion of future perspectives.

PUBLICATIONS

The following publications appear in the thesis:

- Giannakou Marios, Oleg V. Borisov, and Friederike Schmid. Strong stretching theory of polydisperse curved polymer brushes. *The Journal of Chemical Physics* **161** (2024), 014903-15.
- Qiao Le, Giannakou Marios and Friederike Schmid. An Efficient and Accurate SCF Algorithm for Block Copolymer Films and Brushes Using Adaptive Discretizations. *Polymers* **16** (2024), 1228.
- Giannakou Marios, Oleg V. Borisov, and Friederike Schmid. Micelle Forming Linear–Dendritic Block Copolymers: A Theoretical Comparison between Random Hyperbranched and Precise Dendrimer Polymer Architectures. *Macromolecules* **58** (2025), 5872–5882.

The following unpublished work is part of the thesis:

- Thi T. D. Dinh, Giannakou Marios, Mikhail Laktionov, Kinza Y. Ghulam, Sebastian Pusse, Ioannis Tzourtzouklis, Nora Fribiczer, Sebastian Seiffert, George Floudas, Markus Gallei, Oleg V. Borisov, Friederike Schmid and Axel Müller. Influence of gradient on gradient copolymer micelle morphologies in solution (**In preparation**)

ACKNOWLEDGMENTS

The past years in Mainz have been filled with invaluable experiences that have shaped me both personally and professionally, and that will undoubtedly continue to guide me in the future. These moments would not have been possible without the people I had the privilege to meet along the way. Therefore, I would like to express my deepest gratitude to the following individuals:

My supervisor, Prof. Friederike Schmid, for her guidance, critical feedback, and support. Her mentorship not only helped shape this work but also me grow as a researcher.

Dr. Le Qiao for his recommendations on scientific illustration and presentation aesthetics.

Daniela Reibel and Dr. Markus Haack for their support in administrative and other miscellaneous tasks.

My friends and colleagues: Gaurav, Rodrigue, Emanuele, Yash, Kay, Maurice, Yannick, Niklas and Jafar for the stimulating discussions in the coffee room, during lunch, and beyond the university walls.

My flatmates, Yuliya and Fadi, for creating a space where I could feel at ease and recharge after a long day of work.

To my parents, whose guidance and example have instilled in me the value of patience and perseverance.

Finally, I would like to thank the German Research Foundation (DFG) for funding my doctoral studies under Grant No.446008821 and Grant No.429613790, Agence Nationale de la Recherche (ANR), France and TRR 146, Grant No.23363005 for funding my research secondment at Princeton University.

CONTENTS

Part I

INTRODUCTION & THEORY

1

INTRODUCTION

1.1 A Brief History of Polymers

Polymers have been a ubiquitous part of civilization for many centuries, which might sound surprising to many, as the first synthetic polymer was created only a little over a century ago. Cotton, hemp, jute, and many other plants have long been used across different civilizations to produce essential products such as ropes, paper, textiles, sails, etc., with the common denominator among these materials being cellulose—a type of polymer (polysaccharide). Cellulose provides many of the advantages characteristic of polymers, such as lightness, durability, and plasticity, a combination rarely found in other classes of materials. In most of these products, naturally occurring cellulose was used with minimal chemical modification, and as a result, the properties of such materials were limited. However, the 19th century saw several developments in which natural polymers were chemically modified to create enhanced products. One notable example was the toughening of rubber, a type of polyisoprene extracted from *Hevea brasiliensis*[1]. The process, known as vulcanization, was developed by Charles Goodyear in the 1830s when he accidentally discovered that heating rubber with sulfur produced a harder material. Unbeknownst to him and contemporary scientists, vulcanization caused the polymer molecules to form crosslinks, creating a network spanning the material and giving rise to the hardened properties of rubber that are widely known today[1].

Up until then, polymers were not recognized as macromolecular substances, and their properties were instead attributed to association theory, originally proposed by Thomas Graham in 1861[1,2]. This theory suggested that polymers were aggregates of smaller molecules held together by weak forces. Although the macromolecular hypothesis was occasionally considered, it found little support at the time. For instance, in 1910, Pickles, based on his experiments with isoprene, concluded that the molecules formed covalent bonds but argued they were cyclic and of low molecular weight[3]. Interestingly, researchers were already calculating molecular weights far exceeding those of small molecules, but such findings were often dismissed[1]. Additionally, skepticism about high molecular weights stemmed from the belief that the crystallographic unit cell obtained via X-ray diffraction could not be smaller than the molecule it represented—implying a maximum possible molecular weight[1,4].

The macromolecular nature of polymers was only firmly established in the 1930s, primarily through the work of Staudinger and others. Staudinger, a well-established and highly respected chemist before entering the field of polymer chemistry, ventured

into a topic then derided as *Schmierenchemie* (grease chemistry) due to its ill-defined subject matter. He was even discouraged by the 1927 Chemistry Nobel Prize winner, Heinrich Wieland, from further pursuing the macromolecular hypothesis of polymers[4]. Nevertheless, Staudinger persisted, and in his seminal paper "*Über Polymerisation*", he laid the foundation for modern polymer chemistry by demonstrating how polymerization of monomers could give rise to macromolecules with high molecular weights[5]. In a later work, "*Der polymere Formaldehyd, ein Modell der Cellulose*"[6], he provided further evidence for the macromolecular nature of polymers by resolving the issue of the small unit cell, showing that only a monomer unit, rather than an entire molecule, occupied the crystallographic cell. From that point on, macromolecular theory overtook association theory as the prevailing explanation, and in 1953, Staudinger was awarded the Nobel Prize for his contributions.

On the theoretical front, the understanding of polymers evolved significantly. One of the earliest theoretical contributions was made by Werner Kuhn, who introduced the simple freely-jointed chain model to describe polymer conformations[7]. Paul J. Flory made major contributions in the 1940s and 1950s, particularly in elucidating the miscibility of polymers in melts and solutions, as well as in formulating key scaling laws[8]. In 1965, Samuel Edwards introduced one of the most powerful theoretical tools in polymer physics—the self-consistent field theory (SCFT)[9]—bringing field-theoretic methods into the study of polymers. Later, Alexander Semenov introduced the Strong Stretching Limit/Theory[10] (SSL/SST), which became essential for understanding polymer brushes, block copolymers, and their self-assembly behavior. Finally, Mark Matsen made significant contributions to the numerical implementation of SCFT, enabling detailed analyses of complex polymer systems[11]. While many other scientists have contributed to this field over the years, the work of those mentioned here will be explored in greater depth in Chapter 2.

1.2 Polymer morphologies and their applications

As new polymer synthesis protocols were developed[12], an ever-growing array of polymer architectures and chemical compositions became accessible. In addition to traditional linear homopolymers—composed of a single type of repeating monomer in a linear arrangement—chemists have been able to synthesize copolymers containing more than one type of monomer. One of the most prominent subclasses of such copolymers is block copolymers, which consist of distinct segments (blocks) of chemically different monomers. The simplest example of this class is the diblock copolymer, composed of two such blocks, as shown in Fig. 1.1a.

One of the most intriguing properties of such copolymers in solution is their ability to microphase separate into a variety of nanostructures. This behavior stems from the chemical dissimilarity between blocks, which is typically chosen such that each block exhibits different affinities for the solvent—and is also mutually incompatible with

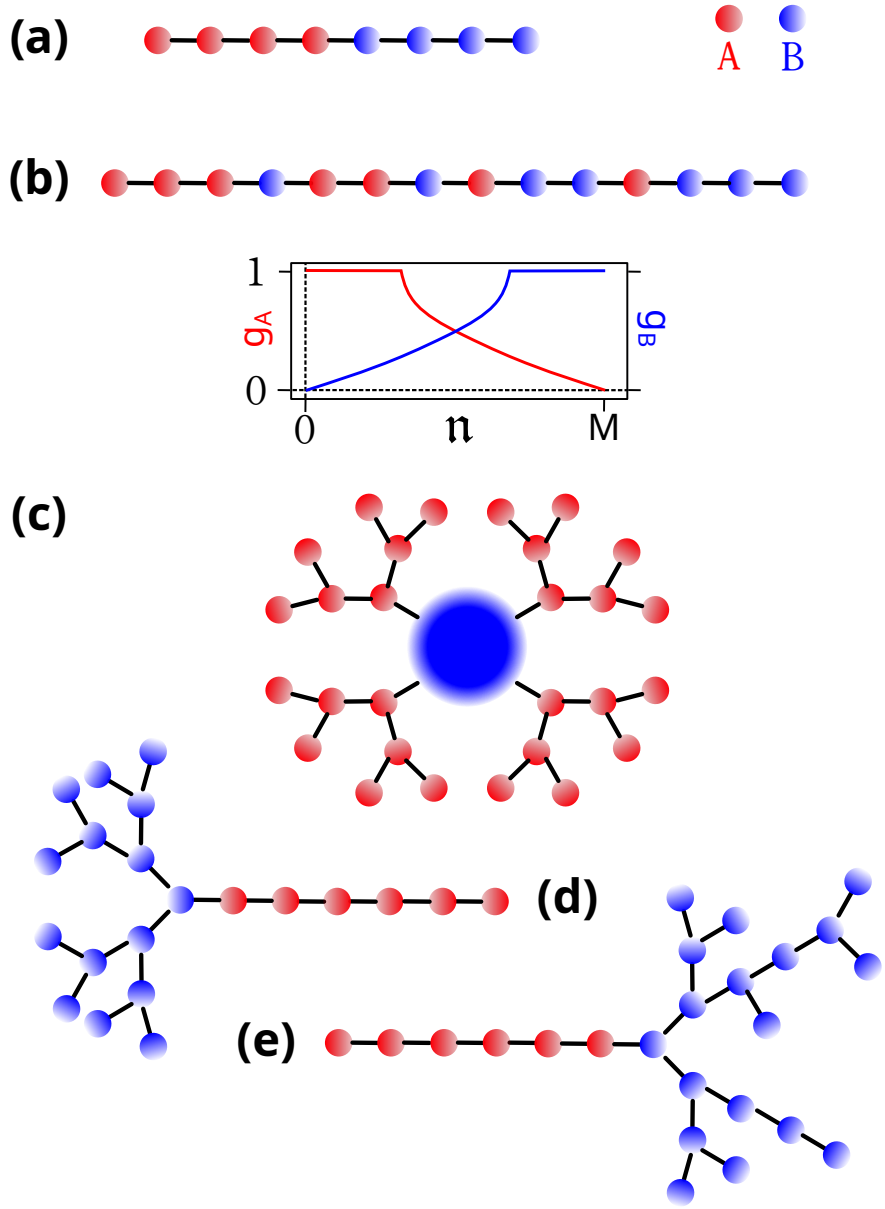

Figure 1.1: Cartoon representation of copolymer types with A monomer represented in red and B monomers represented in blue. (a) Diblock copolymer. (b) Gradient copolymer. g_A and g_B in the graph below represent the proportion of monomer A and B respectively along the backbone of the polymer with the monomer count n ranging from 0 to the total number of monomers M. (c) Dendritic copolymer with the center representing the core. (d) Linear-dendritic block copolymer (LDBC). (e) Linear-hyperbranched block copolymer (LHBC).

the other block. For instance, diblock copolymers can be engineered so that one block is solvophobic (disfavoring contact with the solvent), while the other is solvophilic (favoring interaction with the solvent). Under these conditions, and when the polymer concentration exceeds a threshold known as the Critical Micelle Concentration (CMC)[13], the copolymers spontaneously self-assemble into various morphologies in order to minimize their free energy. The specific structures that form can depend on several factors, including the solvophobic block fraction, the interactions scale and the overall polymer concentration[13,14].

A widely used guideline for predicting the resulting morphology of block copolymer assemblies is the packing parameter concept developed by Israelachvili *et al.*[15], originally in the context of surfactants. The dimensionless packing parameter, defined as $p = v/(a_o l_c)$, provides insight into the preferred morphology. Here, v is the volume of the solvophobic block, a_o is the optimal area occupied by the solvophilic block at the interface, and l_c is the length of the solvophobic block normal to the interface[16]. According to this framework, spherical micelles are expected for $p \leq 1/3$, cylindrical micelles for $1/3 \leq p \leq 1/2$, and bilayers or vesicles for $1/2 \leq p \leq 1$. In these morphologies, the solvophobic blocks typically form the core, while the solvophilic blocks extend into the solvent, forming the corona. Vesicles, on the other hand, are capable of encapsulating solvent within a membrane-like shell. The concept of the packing parameter and corresponding morphologies are illustrated in Fig. 1.2.

While similar morphologies can be achieved through other approaches, polymeric micelles have garnered special interest—especially in the field of drug delivery—due to the distinct advantages they offer over traditional carriers such as lipids or surfactants. The overarching aim in this context is to develop effective drug delivery vehicles capable of navigating the complex *in vivo* environment, such as the bloodstream, and delivering therapeutic payloads in a controlled and targeted fashion.

In the absence of such vehicles, drugs face numerous challenges: many are poorly soluble in aqueous environments[18], and most lack any inherent mechanism for targeting diseased tissues, often leading to off-target effects and systemic toxicity. Spherical polymeric micelles have demonstrated the capacity to encapsulate hydrophobic drugs within their cores, thereby solubilizing compounds that would otherwise be insoluble[19]. Additionally, they shield encapsulated drugs from clearance mechanisms and enzymatic degradation[20].

Polymeric micelles can also be engineered to respond to external stimuli such as temperature, pH, or light[21], enabling controlled or localized release of their payload. Furthermore, the chain ends of the solvophilic blocks provide accessible sites for functionalization. Molecular moieties can be attached to these chain ends to deter protein adsorption[22], prolonging circulation time, or to selectively bind to overexpressed receptors on unhealthy cells[23], as illustrated in Fig. 1.3.

As a result, polymer architectures that feature numerous chain ends or internal cavities naturally offer better opportunities for drug encapsulation and surface modification[24].

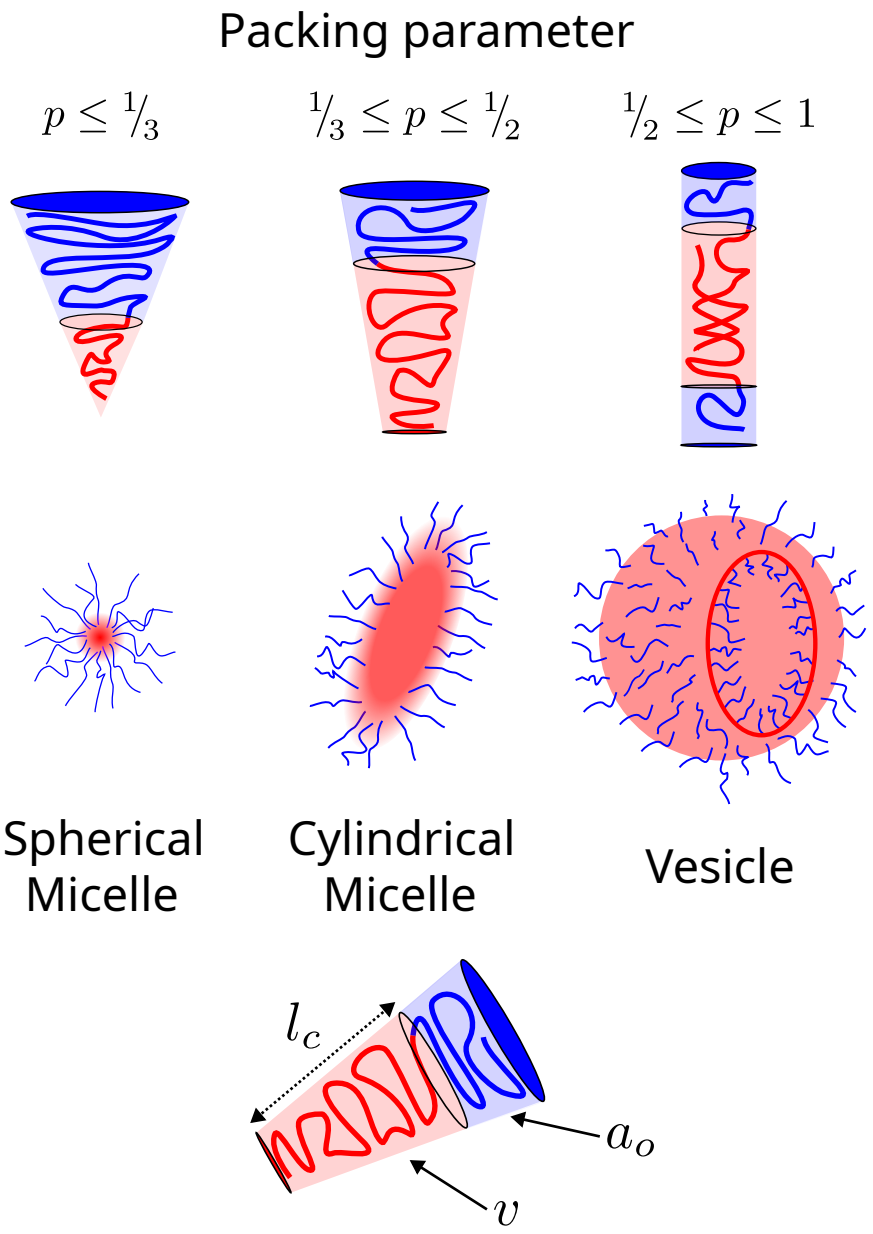

Figure 1.2: Schematic representation of the packing parameter concept, inspired by Blananz *et al.* [17]. Different ranges of the packing parameter p correspond to distinct polymer arrangements and morphologies, such as spherical and cylindrical/worm-like micelles and vesicles. Cylindrical/worm-like micelles and vesicles, in particular, often form at length scales an order of magnitude larger than the polymers that constitute them. The optimal interfacial area of the solvophilic (blue) block is denoted by a_o, while v is the volume of the solvophobic (red) block and l_c is its length normal to the interface. The illustrated morphologies are not to scale.

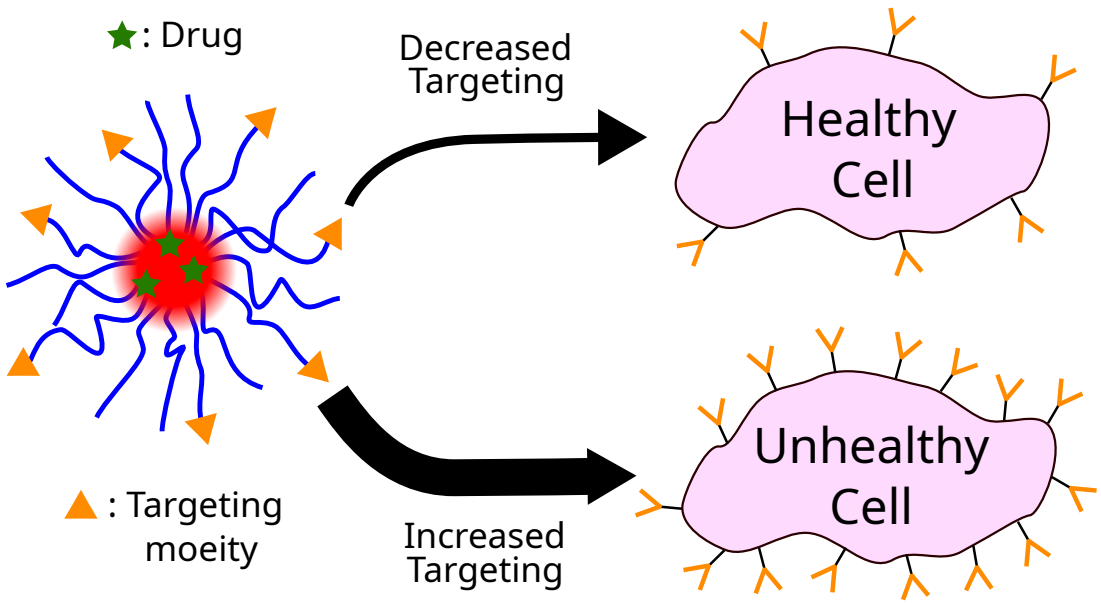

Figure 1.3: Schematic illustration of micelle-based drug delivery: solvophobic drugs are encapsulated within the micelle core, while targeting moieties are attached to the solvophilic, end-functionalized corona to enable site-specific delivery. These moieties enable selective binding to overexpressed receptors on diseased cells, improving specificity and therapeutic efficacy[23].

Among the architectures of particular interest are dendrimers[25], shown in Fig. 1.1c, and linear-dendritic block copolymers (LDBCs)[26], shown in Fig. 1.1d. LDBCs, in particular, exhibit an almost exponential number of available chain ends[27], which can be functionalized to impart highly tailored properties to the resulting micelles[24,26].

Returning to the subject of morphology control, there is increasing interest in going beyond traditional parameters such as monomer chemistry, block ratios, and polymer architecture. One alternative strategy involves the use of gradient copolymers[28], in which the chemical composition varies gradually along the chain. This results in a spatially varying likelihood of encountering a particular monomer type, as shown in Fig. 1.1b. By tuning the gradient profile, researchers can effectively alter monomer-monomer and monomer-solvent interactions without changing the overall chemical composition, thereby enabling access to a broader range of self-assembled structures[29].

Finally, another important class of polymer-based structures arises when polymers are densely grafted onto surfaces or nanoparticles, forming what are known as polymer brushes[30], depicted in Fig. 1.4. These structures have been widely studied for their ability to impart desirable surface properties. For instance, they can inhibit bacterial adhesion or even exhibit bactericidal effects[31,32]. Moreover, polymer brushes can enhance surface

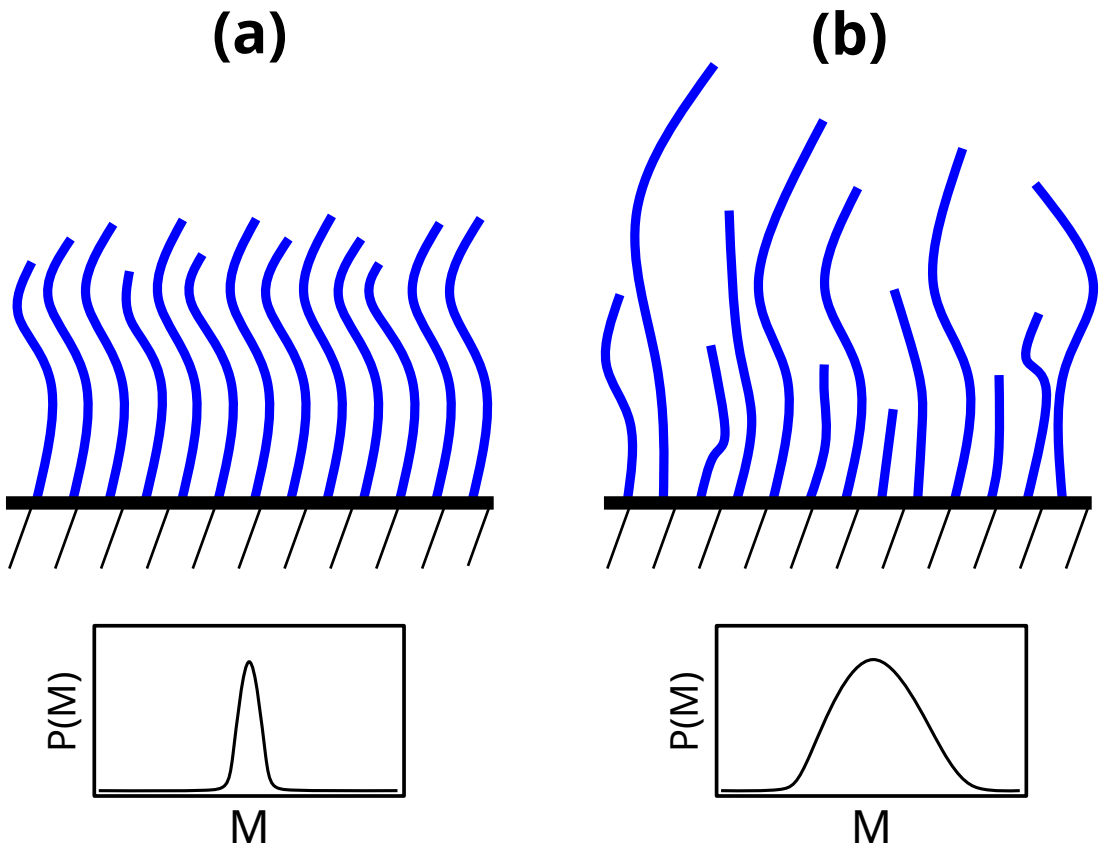

Figure 1.4: Illustration of polymer brushes: (a) nearly monodisperse and (b) polydisperse. M denotes the number of monomers in a polymer chain, while $P(M)$ represents the distribution of polymers with M monomers.

hydrophobicity[32] and stabilize colloidal suspensions[30], making them highly versatile across materials science and biomedical applications.

1.3 Polymer randomness: Origin, Impact and Prospects

In the previous section, we discussed the ability of polymers to assemble into intricate morphologies, but we have not yet addressed how these polymers are synthesized. Although synthetic protocols exist that can yield polymers with highly controlled and nearly monodisperse features in terms of architecture, size, and composition, these methods often require expensive and time-consuming multi-step procedures[33] or, in the case of polymer brushes, result in low grafting densities[34]. Other synthesis strategies can avoid some of these limitations but typically introduce imprecision in the final

product, leading to broad distributions in macromolecular weight and/or topological heterogeneity[12]. This is exemplified in densely grafted polymer brushes produced via the grafting-from method[34] or in linear-hyperbranched block copolymers (LHBCs), Fig. 1.1e, synthesized through slow monomer addition[35]. Put more intuitively, the resulting polymers exhibit distributions in both macromolecular weight, as illustrated in Fig. 1.4, and architecture.

This inherent randomness is generally seen as undesirable in most applications, based on the belief that variability in polymer size and architecture leads to inconsistency and reduced reliability. In drug delivery, for example, achieving stable and monodisperse delivery vehicles is often considered essential, as deviations in size or structure can impair drug performance and reproducibility. While this concern seems justified at first glance, it is not universally valid. On the contrary, Mantha *et al.*[36] demonstrated that micelles composed of polydisperse diblock copolymers can be more stable and better size-defined than those composed of monodisperse diblocks. This finding is illustrated in Fig. 1.5a, where the free energy penalty of spherical micelles is plotted as a function of micelle radius for different polydispersity indices. The local minimum corresponds to the equilibrium micelle, while the maximum indicates the unstable configuration. The energy difference between these two states represents the dissolution energy—that is, the energy required to destabilize the equilibrium micelle. A larger difference implies greater stability against thermal fluctuations.

Moreover, the probability distribution of micelle sizes scales as "$\exp(-\beta F_M(R))$", where $\beta = 1/k_B T$ and $F_M(R)$ is the free energy penalty for a spherical micelle with radius R. Paradoxically, higher diblock polydispersity can result in a narrower micelle size distribution, as shown in Fig. 1.5b. Finally, since drug delivery vehicles encounter a highly dilute environment after administration, it is advantageous for them to have a low CMC. As shown in Fig. 1.5c, increasing polydispersity lowers the CMC, further supporting the idea that controlled polydispersity can enhance drug delivery performance.

In the context of polymer brushes, high grafting density is often essential for their intended function. This density is typically achieved using the grafting-from method, which inherently produces polydisperse chains. Additionally, polymers are frequently grafted onto curved surfaces, such as cylindrical pores or spherical nanoparticles, which has also been shown to induce polydispersity in brush structures[37]. Despite the prevalence of these conditions, the combined effects of curvature and polydispersity in polymer brushes have not been thoroughly studied.

Finally, randomness can also be intentionally introduced into polymer design. This is the case for gradient copolymers, where the chemical composition varies along the chain in a prescribed manner. Although the placement of monomers is random, the overall distribution follows a controlled gradient, as shown in Fig. 1.1b. Gradient copolymer micelles have garnered considerable attention for biomedical applications, particularly

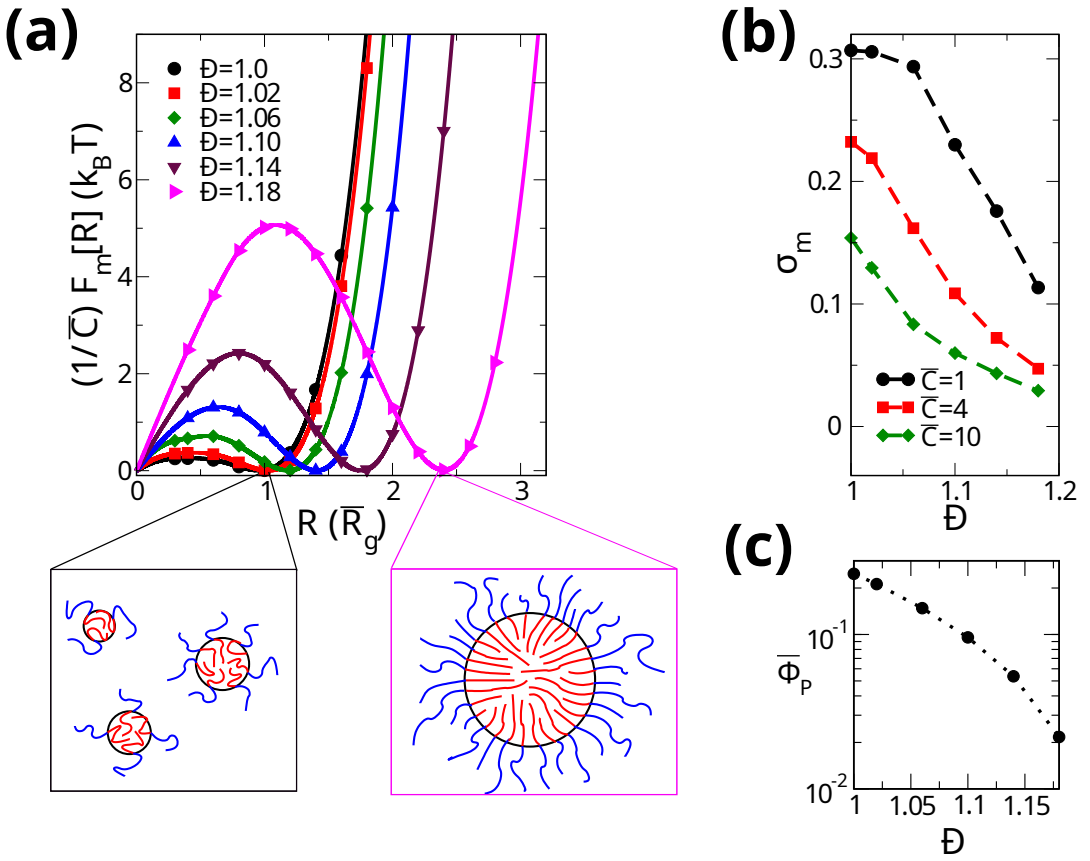

Figure 1.5: (a) Free energy penalty $F_M(R)$ for spherical micelles as a function of micelle radius R, shown for several polydispersity indices Đ= M_w/M_n, where M_w and M_n are the weight average and number average macromolecular weight of polymers respectively. Radii are normalized by the average ideal radius of gyration $\bar{R}_g$ and energies are scaled by the Ginzburg parameter $\bar{C} = \bar{R}_g^3/V_{ch.}$, where $V_{ch.}$ is the total volume of the chain. (b) Standard deviation of micelle size distribution σ_m plotted against Đ for different values of $\bar{C}$. (c) Average polymer volume fraction $\bar{\Phi}_p$ at the CMC, shown as a function of Đ. Figures adapted with permission from Ref.[36].

in drug delivery, due to their tunable internal environments[38–40] and advantageous release profiles[41,42].

1.4 Project Goal

In this thesis, we aim to address key gaps in our understanding of the inherent randomness present in many polymer systems—whether introduced intentionally or resulting from the synthetic methods employed. To this end, we use self-consistent field theory (SCFT) and related approximations, such as the strong stretching limit (SSL), which enables analytical treatment in certain cases. These methods are preferred over more conventional approaches like molecular dynamics (MD) or Monte Carlo simulations due to their efficiency in computing equilibrium properties of complex systems. For instance, simulating polydisperse diblock micelles necessitates the use of the grand canonical ensemble, as micelles constantly exchange chains with their surroundings[43]. This ensemble is readily implemented within SCF, as discussed in Section 2.2, and lends itself well to parallel computation.

Accordingly, Chapter 2 introduces the SCF formalism and the SSL approximation, along with essential background material on Gaussian chains and Flory–Huggins theory—foundational concepts often assumed in SCF discussions.

In Chapter 3, we investigate the combined effects of polydispersity and curvature on linear polymer brushes in both good solvent and melt conditions using the SSL.

Chapter 4 then presents an adaptive grid scheme to improve the accuracy of polymer brush profiles and free energy calculations of polymer film morphologies within SCF.

Chapter 5 focuses on linear-hyperbranched block copolymers with topological and size polydispersity in their hyperbranched blocks and monodisperse solvophobic blocks. We examine their micellization and encapsulation behavior, comparing them to more architecturally defined systems such as linear diblocks and linear–dendritic block copolymers.

In Chapter 6, we study gradient copolymers in solution, highlighting how variations in the gradient profile influence the resulting self-assembled morphologies and their stability.

Finally, in Part III, we summarize the key findings of this work and outline potential directions for future research in this area.

Ultimately, more than a century after Staudinger's time, we still find ourselves confronting the same fundamental issue—the pervasive randomness in polymer systems—and continue to wrestle with the legacy of what was once called *Schmierenchemie*.

2

THEORY

In this section, we aim to equip the reader with the background necessary to understand the theoretical tools found in Part II, as well as some fundamental polymer physics concepts that accompany them. However, we do not aim to provide a comprehensive discussion of these tools, as they have already been discussed in numerous sources[44,45], but rather outline and justify the various terms and relations used. Particular emphasis is placed on self-consistent mean field theory (SCFT), one of the principal theoretical tools applied in this thesis.

Therefore, we begin with a brief overview of the fundamentals concepts in polymer theory, examining the origins of the statistical behavior and conformations of polymer chains, introducing key concepts such as Gaussian chains and statistical segments. We then introduce the main assumptions and results of Flory-Huggins theory. This sets the stage for the introduction of SCFT, where we explain the main concepts such as: the fields, the propagators, the mean-field approximation, the self-consistent loop of equations, and some of the numerical methods employed in solving them. We then delve into a further approximation that can be made in SCFT, known as the Strong Stretching Limit (SSL) or Strong Stretching Theory (SST), and briefly introduce one of its classical applications: the planar polymer brush.

2.1 Polymer Theory Fundamentals

2.1.1 Gaussian chains

Polymers, as mentioned in the introduction, are composed of many monomers, whose chemistry can vary significantly, leading to flexible polymers such as polystyrene or stiff polymers such as double-helical DNA[45]. However, a full chemical description is often unnecessary to capture most physical behaviors. Instead, a coarse-grained description is often sufficient. At this point, we introduce one of the simplest and most fundamental models of polymer chains: the freely jointed chain. This model describes a polymer as a sequence of rigid segments connected by flexible joints, with no constraints on the angles between adjacent segments. It is assumed that the polymer exists in a homogeneous and ideal environment, which means that there are no effective interactions between the segments. Such an environment is nearly realized in the case of polymer chains in a θ-solvent (polymers behave ideally at certain scales[45]), which is defined such that the net excluded volume $v_{ex.}$ between monomers is zero (Eq. 3.95 in Ref.[45]). Another case is in the melt, where a polymer is surrounded by many other

polymers and therefore has no incentive to avoid the monomers belonging to itself or monomers belonging to neighboring polymers[45]. We define the size of the monomer bonds in such a model as a, and each monomer is joined in a linear fashion such that each monomer's position is uncorrelated with the previous one. The normalized probability distribution of the distance vector $\boldsymbol{r}$ of adjacent monomers is thus given by:

$$p_1(\boldsymbol{r}) = \frac{\delta(r-a)}{4\pi a^2}. \tag{2.1}$$

Hence, the variance of the end-to-end vector $\mathbf{R}$ for a polymer with a total of M monomers is given by:

$$\langle \mathbf{R}^2 \rangle = \sum_{i=1}^{M}\sum_{j=1}^{M}\langle \boldsymbol{r}_i \cdot \boldsymbol{r}_j \rangle = \sum_{i=1}^{M}\langle |\boldsymbol{r}_i|^2 \rangle + \sum_{i=1}^{M}\sum_{j\neq i}^{M}\langle \boldsymbol{r}_i \cdot \boldsymbol{r}_j \rangle = Ma^2, \tag{2.2}$$

where we used the fact that monomers are uncorrelated and thus for $i \neq j$, $\langle \boldsymbol{r}_i \cdot \boldsymbol{r}_j \rangle = 0$. In order to coarse-grain such a chain, we need to consider what happens as we 'zoom out,' i.e. look at larger scales. Therefore, we define the function $p_m(\boldsymbol{r})$ as the probability of finding the m'th monomer at a position $\boldsymbol{r}$ given that the 0th monomer is set at the origin. Such a probability distribution, for any nth monomer, where $n < m$, necessarily follows the recursion relation:

$$p_m(\boldsymbol{r}) = \int d\boldsymbol{r}_1\, d\boldsymbol{r}_2\, p_{m-n}(\boldsymbol{r}_1)\, p_n(\boldsymbol{r}_2)\, \delta(\boldsymbol{r}_1 + \boldsymbol{r}_2 - \boldsymbol{r}). \tag{2.3}$$

One can use this recursion relation to progressively construct the functional forms for $p_2(\boldsymbol{r})$ using $m = 2$, $n = 1$ and Eq. (2.1), then $p_4(\boldsymbol{r})$ and so on. What we are essentially trying to do is to consolidate monomers into $N = M/m$ so called "statistical segments", whose size b is such that the coarse-grained chain reproduces the end-to-end vector $R_o = \langle |\boldsymbol{R}| \rangle = N^{1/2}b = M^{1/2}a$. As one continues accumulating more monomers into such statistical segments, the probability distribution of a single statistical segment, given by $p_m(\boldsymbol{r})$, converges to a certain function, as seen in Fig. 2.1. Indeed, for $m \to \infty$ the convergence of the recurrence relation Eq. (2.3) leads to a normal distribution:

$$p_m(\boldsymbol{r}) \to \left(\frac{3}{2\pi b^2}\right)^{3/2} \exp\left(-\frac{3r^2}{2b^2}\right). \tag{2.4}$$

This convergence is due to the fact that if each of the distributions in the integral in Eq. (2.3) were each a Gaussian, then $p_m(\boldsymbol{r})$ would also be another Gaussian. Thus, the Gaussian represents a so called fixed point in this recurrent relation. In fact, what is even more interesting is that, even if there was some finite sized correlation between multiple monomers, the limit would still apply, albeit with a slower convergence to the Gaussian[46]. This convergence is a consequence of a fundamental result in probability theory: the Central Limit Theorem (CLT). The CLT states that if the random variables $(X_1, X_2, ...)$ are independent and identically distributed with a finite mean value of

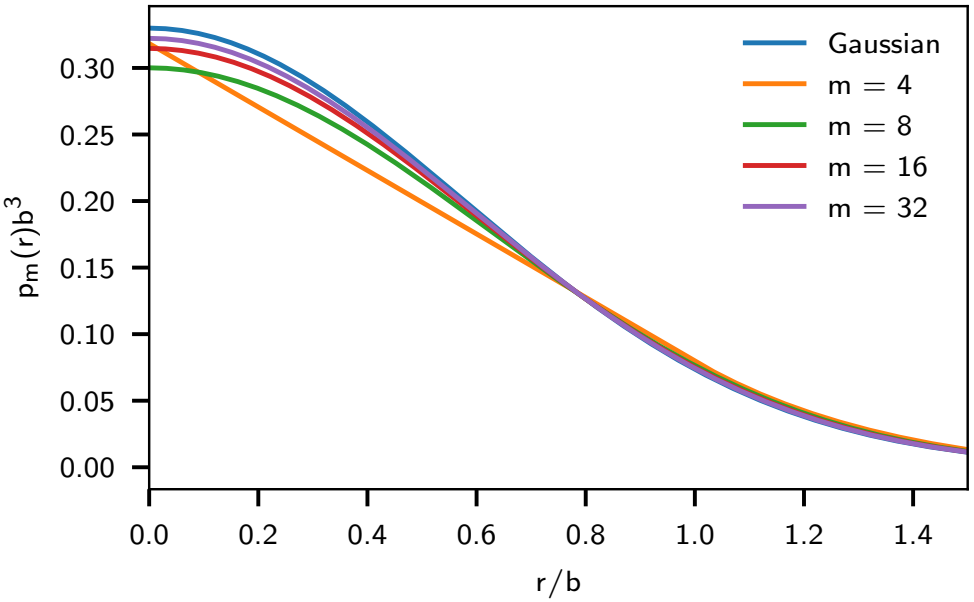

Figure 2.1: Plots of the probability distributions $p_m(r)$ for various values of m as well as the limit case of $m \to \infty$ from Eq. (2.4) labeled as "Gaussian".

$E[X_i] = \mu$ and a finite variance of $\mathrm{Var}[X_i] = \sigma^2$, then the normalized sum of these random variables:

$$Z_n = \frac{\sqrt{n}(\overline{X}_n - \mu)}{\sigma} \quad \text{with} \quad \overline{X}_n \equiv \frac{1}{n}\sum_{i=1}^{n} X_i,$$

converges to a standard normal distribution $\mathcal{N}(0,1)$ as $n \to \infty$. The coarse-graining procedure is also illustrated in Fig. 2.2a,b.

One of the most important takeaways from this analysis is that one can come up with a statistical segment length such that the configurations of the polymer can be described as those of a freely jointed chain. The volume occupied by the polymer molecule also needs to be preserved by the coarse-graining procedure, therefore if the volume of a monomer is v_m then the statistical segment must have a volume $v_o = Mv_m/N$.

If one then considers a Gaussian chain with N statistical segments, the end-to-end vector $\boldsymbol{R}$ is distributed according to a Gaussian with variance $2Nb^2/3$:

$$\mathcal{P}(\boldsymbol{R}) = \left(\frac{3}{2\pi N b^2}\right)^{3/2} \exp\left(-\frac{3\boldsymbol{R}^2}{2Nb^2}\right). \tag{2.5}$$

One can further consider such a chain as a continuous curve described by the space curve $r(n)$, shown in Fig. 2.2c, where n is the monomer count along the polymer

backbone and since one can also write $\boldsymbol{R} = \sum_{i=1}^{N-1}(\boldsymbol{r}_{i+1} - \boldsymbol{r}_i)$, the distribution of the space curve can be written as:

$$\mathcal{P}\left(r(\mathfrak{n})\right) = \left(\frac{3}{2\pi N b^2}\right)^{3/2} \exp\left(-\frac{3}{2b^2}\left(\int_0^N \left|\frac{d\boldsymbol{r}(\mathfrak{n})}{d\mathfrak{n}}\right|^2 d\mathfrak{n}\right)\right), \tag{2.6}$$

where we have made the replacements $\sum \to \int d\mathfrak{n}$ and $1/N \to d\mathfrak{n}$, which are justified in the limit $N \to \infty$. The last thing to note is that the effective Hamiltonian of such a chain is given by:

$$\mathcal{H}_e = \frac{3k_B T}{2b^2}\int_0^N \left|\frac{dr(\mathfrak{n})}{d\mathfrak{n}}\right|^2 d\mathfrak{n}, \tag{2.7}$$

which can be thought of as a Hookean spring with a spring constant defined by the temperature T.

Such a result has wide implications for the statistics of long polymer molecules, as it implies that the scaling exponent ν of the end-to-end distance $R_o \propto N^\nu$ is $\nu = 1/2$, when no long-distance correlations are present and the environment is ideal. If one were to however account for a non-ideal environment such as in the case of a polymer in good or bad solvent, then the scaling exponent is $\nu = 0.6$ (mean-field approximation; 0.588 via renormalization[45]) or $\nu = 1/3$, respectively, and Gaussian statistics do not apply.

2.1.2 Flory-Huggins theory

So far, we have discussed entropic contributions to the free energy of isolated chains, however, we have not accounted for energy contributions originating from monomer-monomer or monomer-solvent interactions, which play a crucial role in understanding micro and macro phase separation as well as the scaling of the end-to-end distance in solvents of varying quality. To do so, we now turn to the simple yet quite successful Flory-Huggins (FH) theory, which incorporates these short-range interactions via a lattice mean field model and helps explain non-ideal chain behavior.

The main concern of FH theory is to construct an expression for the free energy of mixing of polymers with solvent. To do so, a lattice with W available sites of equal volume v_L is assumed, whereupon each lattice site is either filled with a statistical segment belonging to a polymer chain or a solvent particle. The volume fraction occupied by either the solvent ϕ_s or the polymer ϕ_A is then given by:

$$\phi_\alpha = \frac{V_\alpha}{\sum_\alpha^{A,S} V_\alpha} \quad \text{for} \quad \alpha = \text{A or S}, \tag{2.8}$$

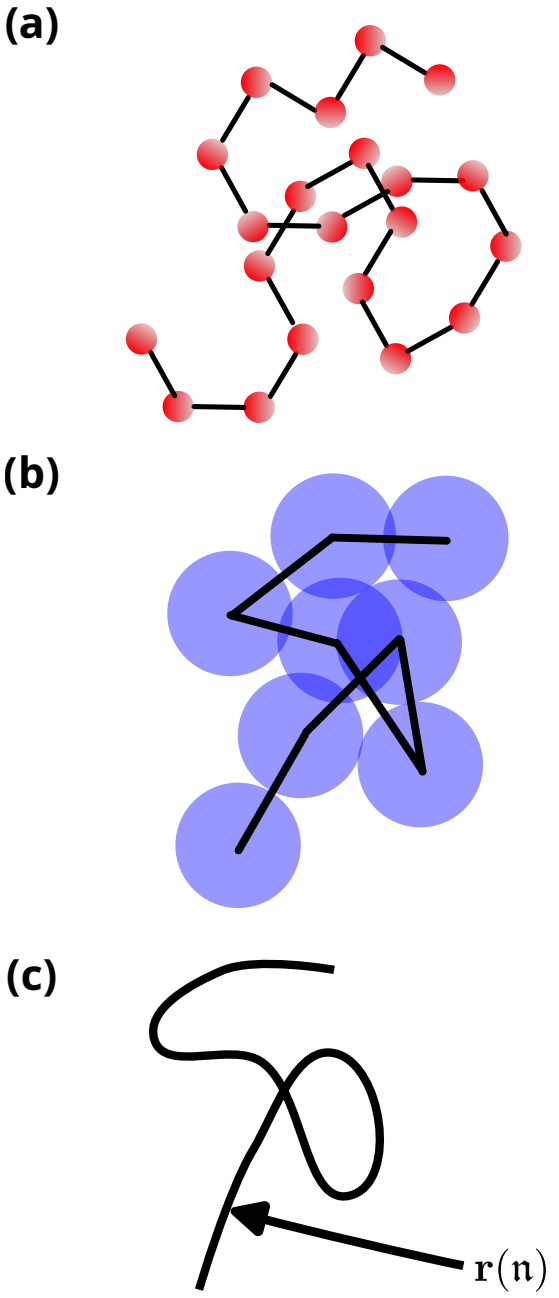

Figure 2.2: Coarse-graining procedure illustration. (a) Cartoon representation of a "real polymer", showing monomers (red) connected via bonds (black), whose directions are correlated with their neighbors. (b) Accumulating the monomers in (a) into statistical segments (blue), shown here as spheres, "buries" the correlations between neighbors. Continuing this coarse-graining procedure results in a random walk between statistical segments. (c) Continuous curve representation of the chain in (b) given by the space curve $\boldsymbol{r}(n)$.

where V_α is the total volume taken by either the solvent or the polymer. In the mean field approximation the entropy of mixing (difference between mixed and unmixed) per lattice site can then be approximated to be[45]:

$$\overline{\Delta S}_{mix} = -k_B(\frac{\phi_A}{N}\ln(\phi_A) + \phi_S\ln(\phi_S)). \tag{2.9}$$

The internal energy is assumed to be short ranged and only between nearest neighbors, whose probability of occupying a lattice site is assumed to be given by their corresponding volume fractions. Additionally, the number of neighbors is determined by the lattice coordination number $z = 2d$, where d is the number of dimensions, while the pairwise interaction energies between each species are given by u_{AA}, u_{SS} and u_{AS}. The energy of mixing per lattice site can thus be expressed as[45]:

$$\frac{\overline{\Delta U}_{mix}}{k_B T} = \chi_{AS}\phi_A\phi_S, \tag{2.10}$$

where we have defined the Flory-Huggins parameter as:

$$\chi_{AS} = \frac{z}{2}\frac{(2u_{AS} - u_{AA} - u_{SS})}{k_B T}. \tag{2.11}$$

The Helmholtz energy of mixing per lattice site is therefore given by:

$$\frac{\overline{\Delta F}_{mix}}{k_B T} = \frac{\overline{\Delta U}_{mix} - T\overline{\Delta S}_{mix}}{k_B T} = \frac{\phi_A}{N}\ln(\phi_A) + \phi_S\ln(\phi_S) + \chi_{AS}\phi_A\phi_S. \tag{2.12}$$

One of the main drawbacks of this theory is that it does not account for the change in volume upon mixing and other packing effects[45], and therefore Eq. (2.12) does not capture all the physics. In practice, all the effects that are not accounted for by the theory are clumped into an empiric expression of the FH parameter, given by:

$$\chi = A + \frac{B}{T}, \tag{2.13}$$

where A and B are fit parameters. The A term is often called the entropic part of the FH parameter, while the B/T term is called the enthalpic part[45]. In reality, A and B also weakly depend on other quantities such as the macromolecular weight, the composition and more[45] and the parameters A and B are not purely entropic or enthalpic, despite what their description suggests. Given such an expression for the FH parameter, macrophase separation of a polymer solution can occur, with either an upper critical solution temperature (UCST) (if $B > 0$) or a lower critical solution temperature (LCST) (if $B < 0$).

As a last point in this discussion, we wish to draw a link between the excluded volume $v_{ex.}$ that quantifies whether the polymer segment volume is inaccessible to other segments or not and connect it to the Flory-Huggins parameter. To do this, we

need to find the osmotic pressure Π exerted on a semi-permeable membrane which allows the solvent in a solution of polymers to go through unimpeded, while preventing any of the polymer from crossing. Such a pressure in the limit of $\phi_A \ll 1$ and $N_a \gg 1$ can be calculated as:

$$\begin{aligned}\Pi(\rho) \equiv -\left.\frac{\partial \Delta F_{\text{mix}}}{\partial V}\right|_{n_A} &= kT\left(\frac{\rho}{N_A} + (1-2\chi_{AS})b^3\frac{\rho^2}{2} + \frac{b^6}{3}\rho^3 + \cdots\right) \\ &= kT\left(\frac{\rho}{N_A} + \frac{v_{\text{ex}}}{2}\rho^2 + w\rho^3 + \cdots\right), \end{aligned} \tag{2.14}$$

where n_A is the number of polymer molecules, ρ is the statistical segment number density and w is the three-body interaction coefficient[45]. The last line of Eq. (2.14) is simply the virial expansion of the osmotic pressure into n-body terms and the excluded volume is simply the 2-body term. Therefore, by comparison of the two lines in Eq. (2.14) the excluded volume can be expressed as:

$$v_{ex.} = b^3(1-2\chi_{AS}). \tag{2.15}$$

For a θ-solvent, there are no excluded volume effects ($v_{ex.} = 0$) and therefore values of $\chi_{AS} < 1/2$ ($v_{ex.} > 0$) indicate the good solvent regime, whereas $\chi_{AS} > 1/2$ ($v_{ex.} < 0$) indicate the poor solvent regime. The discussion above mirrors the analysis found in [45]. Having explored simple polymer models, we are now ready to introduce self-consistent field theory, which allows one to explore a wealth of problems unreachable by analytical means.

2.2 Self-Consistent Field Theory

2.2.1 Background

Polymer systems such as polymer melts consist of many tightly packed polymers, each composed of many monomers. Often, systems like this exhibit relaxation times that scale with the macromolecular size of the polymers[45], resulting in slow relaxation dynamics. Therefore, dynamic methodologies such as molecular dynamics can be prohibitively expensive for the investigation of their equilibrium properties. Self-consistent field theory, on the other hand, is a mesoscale method that instead of being limited by the large number of particles, in fact benefits from it. One of the main simplifications of SCFT is the reduction of the problem of many polymers interacting with each other, to a problem of a single polymer interacting with a field $w(\boldsymbol{r})$ that is itself determined by the statistical segments number density $\rho(\boldsymbol{r})$ (Fig. 2.3). Also, the fact that it is not a dynamic method like MD simulations allows it to bypass the issue of slow relaxation times.

In this section, we aim to introduce SCFT and the necessary theoretical tools that go along with it, through an example of a linear monodisperse diblock melt, which helps

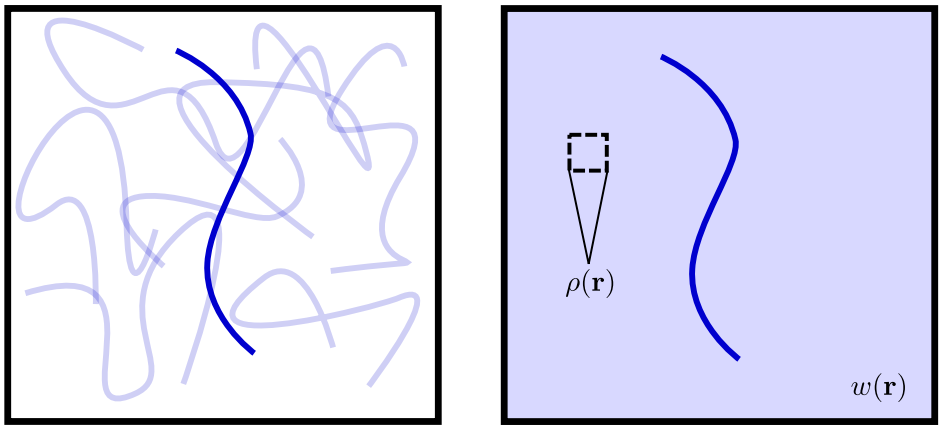

Figure 2.3: Cartoon representation of polymer interacting with many polymers (left) vs. a polymer interacting with a field $w(\boldsymbol{r})$ determined by the segment number density $\rho(\boldsymbol{r})$, illustrating the main idea of SCFT.

---

familiarize the reader with the notation and methodologies used in Part II. Throughout the thesis we use Greek characters to refer to different monomer types/chemistry while for sums over chains, we use Latin characters.

We begin by considering an ensemble of identical linear diblock chains composed of a block of monomers A and a block of monomers B. For simplicity, the statistical segment length b is assumed to be the same for both blocks, while the volume of each statistical segment is given by v_α and the total number of segments is N. We model these chains as continuous Gaussian chains, described by the space curve $\boldsymbol{r}(\mathfrak{n})$, with monomer count $\mathfrak{n}$, such that the entropic penalty to the polymer configurations is given by Eq. (2.6). Alternatively, one can employ a lattice-based method such as in Scheutjens–Fleer lattice theory[47] to describe the conformations of the polymers more accurately.

To describe the type of the statistical segments found along this space curve, we introduce the function $g_\alpha(\mathfrak{n})$ which is equal to 1 if the type found at $\mathfrak{n}$ is the same as α and 0 otherwise. Consequently:

$$\int_0^N g_\alpha(\mathfrak{n})\, d\mathfrak{n} = N f_\alpha, \tag{2.16}$$

where f_α is the fraction of the polymer that is of type α and $\sum_\alpha f_\alpha = 1$, but since we are only dealing with a diblock here we set $f_A = f$ and $f_B = 1 - f$.

The weight of a particular chain configuration $\boldsymbol{r}(\mathfrak{n})$ is thus given by:

$$\mathcal{P}\left(\boldsymbol{r}(\mathfrak{n})\right) \propto \exp\left[-\sum_{a} \frac{3}{2b^2} \int_0^N \left|\frac{d(\boldsymbol{r}(\mathfrak{n}))}{d\mathfrak{n}}\right|^2 g_\alpha(\mathfrak{n})\, d\mathfrak{n}\right]. \tag{2.17}$$

Now let us consider a canonical ensemble of n such identical polymers in a volume V, in contact with a thermal reservoir of temperature T or inverse temperature $\beta = 1/(k_B T)$. The local statistical segment number density operator is given by:

$$\hat{\rho}_\alpha(r) = \sum_{i=1}^{n} \int_0^N \delta(\boldsymbol{r} - \boldsymbol{r}_i(\mathfrak{n}))\, g_\alpha(\mathfrak{n})\, d\mathfrak{n}. \tag{2.18}$$

Moreover, we define the path integral over all possible polymer configurations as:

$$\int \mathcal{D}\left(\boldsymbol{r}(\mathfrak{n})\right) \mathcal{P}\left(\boldsymbol{r}(\mathfrak{n})\right) = \int \widehat{\mathcal{D}}\left(\boldsymbol{r}(\mathfrak{n})\right) = V, \tag{2.19}$$

where the last step is simply our choice of normalization. Therefore, the partition function in the canonical ensemble is given by:

$$\mathcal{Z}_C = \frac{1}{n!} \prod_{i=1}^{n} \left[\frac{1}{v^*} \int \widehat{\mathcal{D}}_i(\boldsymbol{r}(\mathfrak{n}))\right] \exp\left(-\beta \mathcal{V}\{\hat{\rho}_\alpha\}\right), \tag{2.20}$$

where $\mathcal{V}\{\hat{\rho}_\alpha\}$ is the coarse-grained interaction functional which we will define later on. Note that we have also divided by a reference volume v^* to make the partition function unitless, since, after all, it is a sum of probabilities, and we are allowed to do so since the partition function can be defined up to a multiplicative constant. Using Eq. (2.18), the identity can be shown to be:

$$\begin{aligned} \mathbf{1} &= \int \mathcal{D}\{\rho_\alpha\}\, \delta\left(\rho_\alpha - \hat{\rho}_\alpha\right) \\ &= \int \mathcal{D}\{\rho_\alpha\} \int_{i\infty} \mathcal{D}\{w_\alpha\} \exp\left[\int d\boldsymbol{r}\, w_\alpha(\boldsymbol{r})\left(\rho_\alpha(\boldsymbol{r}) - \hat{\rho}_\alpha(\boldsymbol{r})\right)\right], \end{aligned} \tag{2.21}$$

where the path integral over the fields w_α is performed from $-i\infty$ to $i\infty$. One can then show that the partition function can be morphed into:

$$\mathcal{Z}_C = \left\{\prod_\alpha \int \mathcal{D}\{\rho_\alpha\} \int_{i\infty} \mathcal{D}\{w_\alpha\}\right\} \exp\left[-\beta \mathcal{F}_C\{\rho_\alpha, w_\alpha\}\right], \tag{2.22}$$

where we have defined the energy functional as:

$$\beta \mathcal{F}_C\{\rho_\alpha, w_\alpha\} = \beta \mathcal{V}\{\rho_\alpha\} - \sum_\alpha \int w_\alpha(\boldsymbol{r}) \rho_\alpha(\boldsymbol{r})\, d\boldsymbol{r} - n \ln\left(\frac{\mathcal{Q}\{w_\alpha\}}{n}\right), \tag{2.23}$$

and the single chain partition function, defined here as unitless, as:

$$\mathcal{Q}\{w_\alpha\} = \frac{1}{v^*}\int \widehat{\mathcal{D}}(\boldsymbol{r}(\mathfrak{n}))\,\exp\left[-\sum_\alpha \int_0^N w_\alpha(\boldsymbol{r}(\mathfrak{n}))\,g_\alpha(\mathfrak{n})d\mathfrak{n}\right]. \tag{2.24}$$

We are now ready to introduce the two approximations made in SCFT, which are to approximate the two path integrals in Eq. (2.22) over the fields w_α and densities ρ_α with their saddle points. These two approximations are equivalent to finding the extrema of the free energy functional with respect to the fields and densities, which lead to:

$$\rho_\alpha(\boldsymbol{r}) = -n\frac{\delta(\ln(\mathcal{Q}\{w_\alpha\}))}{\delta(w_\alpha(\boldsymbol{r}))}, \tag{2.25}$$

$$w_\alpha(\boldsymbol{r}) = \frac{\delta(\beta\mathcal{V}\{\rho_\alpha\})}{\delta(\rho_\alpha(\boldsymbol{r}))}. \tag{2.26}$$

These approximations render the fields and densities interdependent and additionally, the densities are now equivalent to their mean-field solution[46,48] i.e. $\rho_a(\boldsymbol{r}) = \langle\hat{\rho}_\alpha(\boldsymbol{r})\rangle_C$, where $\langle\cdots\rangle_C$ represents the ensemble average over all possible fields.

Alternatively, the same system can also be considered in the grand canonical ensemble with the chains chemical potential set to μ, which is a more appropriate ensemble when the system in question can exchange chains with its environment. The partition function in the grand canonical ensemble is given:

$$\mathcal{Z}_{GC} = \sum_{n=0}^{\infty}\left\{\frac{e^{\beta\mu n}}{n!}\prod_{i=1}^{n}\int\frac{1}{v^*}\widehat{\mathcal{D}}\{\boldsymbol{r}_i(\mathfrak{n})\}\right\}\exp\left[-\beta\mathcal{V}\{\hat{\rho}_\alpha\}\right]. \tag{2.27}$$

Following the same steps as before, this can be rewritten as:

$$\mathcal{Z}_{GC} = \left\{\prod_\alpha\int\mathcal{D}\{\rho_\alpha\}\int_{i\infty}\mathcal{D}\{w_\alpha\}\right\}\exp\left[-\beta\mathcal{F}_{GC}\{\rho_\alpha, w_\alpha\}\right], \tag{2.28}$$

with the free energy now being:

$$\beta\mathcal{F}_{GC}\{\rho_\alpha, w_\alpha\} = \beta\mathcal{V}\{\rho_\alpha\} - \sum_\alpha\int w_\alpha(\boldsymbol{r})\rho_\alpha(\boldsymbol{r})d\boldsymbol{r} - e^{\beta\mu}\mathcal{Q}\{w_\alpha\}, \tag{2.29}$$

where we used the fact that:

$$\sum_{n=0}^{\infty}\frac{1}{n!}x^n = e^x \quad \text{with} \quad x = e^{\beta\mu}\mathcal{Q}.$$

Upon the SCFT approximations the fields are still given by Eq. (2.26), whereas the densities are given by:

$$\rho_\alpha(\boldsymbol{r}) = -e^{\beta\mu}\frac{\delta(\mathcal{Q}\{w_\alpha\})}{\delta(w_\alpha(\mathbf{r}))}. \tag{2.30}$$

Although in principle one could calculate the densities using Eqs. (2.25) and (2.30), the calculation is intractable since the single chain partition function involves a path integral calculation. Thankfully, there is a way to overcome this via another pathway. We first rewrite $\mathcal{Q}\{w_\alpha\}$:

$$\begin{aligned}\mathcal{Q}\{w_\alpha\} &= \frac{1}{v^*}\int \widehat{\mathcal{D}}\{\boldsymbol{r}(\mathfrak{n})\}\exp\left[-\int_0^N \sum_\alpha w_\alpha(\boldsymbol{r}(\mathfrak{n}))g_\alpha(\mathfrak{n})d\mathfrak{n}\right] \\ &= \frac{1}{v^*}\int \mathcal{D}\{\boldsymbol{r}(\mathfrak{n})\}\exp\left[-\left\{\int_0^N\left(\frac{3}{2b^2}\left|\frac{d(\boldsymbol{r}(\mathfrak{n}))}{d\mathfrak{n}}\right|^2+\sum_\alpha w_\alpha(\boldsymbol{r}(\mathfrak{n}))g_\alpha(\mathfrak{n})\right)d\mathfrak{n}\right\}\right] \\ &= \frac{1}{v^*}\int \mathcal{D}\{\boldsymbol{r}(\mathfrak{n})\}\exp[-\beta E\left[\boldsymbol{r}(\mathfrak{n});0,N\right]], \end{aligned} \tag{2.31}$$

where we have defined:

$$\beta E[\boldsymbol{r}(\mathfrak{n});\mathfrak{n}_1,\mathfrak{n}_2] = \sum_\alpha \int_{\mathfrak{n}_1}^{\mathfrak{n}_2}\left(\frac{3}{2b^2}\left|\frac{d(\boldsymbol{r}(\mathfrak{n}))}{d\mathfrak{n}}\right|^2 + w_\alpha(\boldsymbol{r}(\mathfrak{n}))g_\alpha(\mathfrak{n})\right)d\mathfrak{n}. \tag{2.32}$$

Now the partial partition function of a chain fixed with the constrained points $\boldsymbol{r}(0)=\boldsymbol{r}_0$ and $\boldsymbol{r}(\mathfrak{n}')=\boldsymbol{r}$ is given by:

$$G(\boldsymbol{r},\boldsymbol{r}_0,\mathfrak{n}') = \int \mathcal{D}\{\boldsymbol{r}(\mathfrak{n})\}\exp\left[-\beta E[\boldsymbol{r}(\mathfrak{n})];0,\mathfrak{n}'\right]\delta(\boldsymbol{r}(0)-\boldsymbol{r}_0)\delta(\boldsymbol{r}(\mathfrak{n}')-\boldsymbol{r}), \tag{2.33}$$

and due to the additive nature of $E[\boldsymbol{r}(\mathfrak{n});\mathfrak{n}_1,\mathfrak{n}_2]$, namely:

$$E[\boldsymbol{r}(\mathfrak{n});0,\mathfrak{n}'] = E[\boldsymbol{r}(\mathfrak{n});0,t] + E[\boldsymbol{r}(\mathfrak{n});t,\mathfrak{n}'] \quad \text{for} \quad 0\le t\le \mathfrak{n}, \tag{2.34}$$

a type of Chapman-Kolmogorov integral equation holds:

$$G(\boldsymbol{r},\boldsymbol{r}_0,\mathfrak{n}) = \int d\boldsymbol{r}_1\, G(\boldsymbol{r}_1,\boldsymbol{r}_0,t)\, G(\boldsymbol{r},\boldsymbol{r}_1,\mathfrak{n}-t). \tag{2.35}$$

In general, these types of equations can be reduced to partial differential equations known as Fokker-Planck equations (also by other names depending on the discipline one encounters them in). This can be done by Taylor-expanding Eq. (2.35), which leads to the following modified diffusion equation (MDE)[46]:

$$\frac{\partial G(\boldsymbol{r},\boldsymbol{r}_0,\mathfrak{n})}{\partial \mathfrak{n}} = \left(\frac{b^2}{6}\nabla^2 - \sum_\alpha w_\alpha(\boldsymbol{r})g_\alpha(\mathfrak{n})\right)G(\boldsymbol{r},\boldsymbol{r}_0,\mathfrak{n}),$$

with the initial condition given by:

$$G(\boldsymbol{r},\boldsymbol{r}_0,0) = \delta(\boldsymbol{r}-\boldsymbol{r}_0). \tag{2.36}$$

One can further define for a free chain end at $\mathfrak{n}=0$, the forward propagator:

$$q(\boldsymbol{r},\mathfrak{n}) = \int d\boldsymbol{r}_0\, G(\boldsymbol{r},\boldsymbol{r}_0,\mathfrak{n}), \tag{2.37}$$

and thus reduce the MDE to an even simpler expression:

$$\frac{\partial q(\boldsymbol{r},\mathfrak{n})}{\partial \mathfrak{n}} = \left(\frac{b^2}{6}\nabla^2 - \sum_\alpha w_\alpha(\boldsymbol{r}) g_\alpha(\mathfrak{n})\right) q(\boldsymbol{r},\mathfrak{n}), \tag{2.38}$$

with the initial condition $q(\boldsymbol{r},0) = 1$. Analogously one can define a complementary partial partition function $G^\dagger(\boldsymbol{r},\boldsymbol{r}_N,\mathfrak{n}')$ with a fixed end $\boldsymbol{r}(N) = \boldsymbol{r}_N$:

$$G^\dagger(\boldsymbol{r},\boldsymbol{r}_N,\mathfrak{n}') = \int \mathcal{D}\{\boldsymbol{r}(\mathfrak{n})\}\, \exp\left[-\beta E[\boldsymbol{r}(\mathfrak{n}),\mathfrak{n}';N]\right) \delta(\boldsymbol{r}(\mathfrak{n}') - \boldsymbol{r})\, \delta(\boldsymbol{r}(N) - \boldsymbol{r}_N), \tag{2.39}$$

and following similarly to the forward propagator case, we can derive a similar MDE for the backward propagator $q^\dagger$:

$$\frac{\partial q^\dagger(\boldsymbol{r},\mathfrak{n})}{\partial \mathfrak{n}} = -\left(\frac{b^2}{6}\nabla^2 - \sum_\alpha w_\alpha(\boldsymbol{r}) g_\alpha(\mathfrak{n})\right) q^\dagger(\boldsymbol{r},\mathfrak{n}), \tag{2.40}$$

with the initial condition $q^\dagger(\boldsymbol{r},N) = 1$. Lastly, it can be shown that the full single chain partition can be expressed as a simple integral over these propagators:

$$\mathcal{Q}\{w_\alpha\} = \frac{1}{v^*}\int d\boldsymbol{r}\, q(\boldsymbol{r},\mathfrak{n}) q^\dagger(\boldsymbol{r},\mathfrak{n}) = \frac{1}{v^*}\int \mathcal{D}\{\boldsymbol{r}(\mathfrak{n})\} \exp\left[-\beta E[\boldsymbol{r}(\mathfrak{n});0,N]\right]. \tag{2.41}$$

We note that, in our definitions, the partition functions $\mathcal{Q}$, $\mathcal{Z}_C$, $\mathcal{Z}_{GC}$, and the propagators $q(\boldsymbol{r},\mathfrak{n})$, $q^\dagger(\boldsymbol{r},\mathfrak{n})$ are defined to be unitless. This choice is made explicit because the definitions and units of these quantities often vary across the literature.

The density can be calculated via these propagators by noticing that:

$$\begin{aligned}\frac{\delta Q}{\delta(w_\alpha(\boldsymbol{r}))} &= \frac{-1}{v^*}\int \mathcal{D}(\boldsymbol{r}(\mathfrak{n})) \int_0^N g_\alpha(\mathfrak{n})\delta(\boldsymbol{r}-\boldsymbol{r}(\mathfrak{n})) \exp\left[-\beta E\left[\boldsymbol{r}(\mathfrak{n});0,N\right]\right] d\mathfrak{n} \\ &= -\frac{1}{v^*}\int_0^N q(\boldsymbol{r},\mathfrak{n}) q^\dagger(\boldsymbol{r},\mathfrak{n}) g_\alpha(\mathfrak{n})\, d\mathfrak{n}\,,\end{aligned} \tag{2.42}$$

and using Eq. (2.25). The density in the canonical ensemble is thus given by:

$$\rho_\alpha(\boldsymbol{r}) = \frac{n}{\mathcal{Q} v^*}\int_0^N q(\boldsymbol{r},\mathfrak{n}) q^\dagger(\boldsymbol{r},\mathfrak{n}) g_\alpha(\mathfrak{n})\, d\mathfrak{n}, \tag{2.43}$$

while for the grand canonical ensemble, using Eq. (2.30) instead, the density is given by:

$$\rho_\alpha(\boldsymbol{r}) = \frac{e^{\beta\mu}}{v^*}\int_0^N q(\boldsymbol{r},\mathfrak{n}) q^\dagger(\boldsymbol{r},\mathfrak{n}) g_\alpha(\mathfrak{n})\, d\mathfrak{n}. \tag{2.44}$$

We next consider the calculation of the fields which are solely determined by the functional $\beta\mathcal{V}\{\rho_\alpha\}$ which we have so far ignored. This functional consists of terms

describing the monomer-monomer interactions $\mathcal{V}_{inter}$ and depending on the model used, the density fluctuation and compressibility constraints $\mathcal{V}_o$:

$$\beta\mathcal{V}\{\rho_\alpha\} = \beta\mathcal{V}_{inter}\{\rho_\alpha\} + \beta\mathcal{V}_o\{\rho_\alpha\}. \tag{2.45}$$

We first start with the monomer-monomer interactions which are typically short-range interactions and can be reasonably described using Flory-Huggins interactions. For a more thorough derivation see Schmid [48]. For further convenience we introduce the dimensionless volume fractions $\phi_\alpha = \rho_\alpha v_\alpha$. The interactions functional can therefore be written as:

$$\beta\mathcal{V}_{inter}\{\rho_\alpha\} = \frac{1}{2v^*}\sum_\alpha\sum_{\alpha\neq\beta}\int \chi_{\alpha\beta}\phi_\alpha\phi_\beta \, d\boldsymbol{r}, \tag{2.46}$$

and is essentially the interaction term from Eq. (2.10).

Now liquids such as melts and polymer solutions have a compressibility that is usually large enough that one can model them as incompressible. This constraint can be added to our theory by introducing a delta function:

$$\delta\left[\sum_\alpha \phi_\alpha - 1\right], \tag{2.47}$$

to Eqs. (2.20) and (2.27), which can then be converted into a new field $\xi(\boldsymbol{r})$, in a similar manner to how the other fields were introduced. The result is an additional term in the free energies $\mathcal{F}_C$ and $\mathcal{F}_{GC}$:

$$\beta\mathcal{V}_o\{\rho_\alpha\} = \int \xi(\boldsymbol{r})\left(1 - \sum_\alpha \phi_\alpha\right) d\boldsymbol{r}, \tag{2.48}$$

and an additional term to the fields (2.26):

$$\frac{\delta\left(\beta\mathcal{V}_o\{\rho_\alpha\}\right)}{\delta\left(\rho_\alpha(\boldsymbol{r})\right)} = -\xi(\boldsymbol{r})v_\alpha. \tag{2.49}$$

However, it is often preferred, to relax such a constraint and allow the total volume fractions to deviate from one, and instead of adding an explicit constraint, one adds a harmonic term that penalizes any deviation away from one. Such a term was introduced by Helfand[49,50] and is written as:

$$\beta\mathcal{V}_o\{\rho_\alpha\} = \frac{\kappa}{2v^*}\int\left(\sum_\alpha \phi_\alpha(\boldsymbol{r}) - 1\right)^2 d\boldsymbol{r}, \tag{2.50}$$

where κ is the isothermal compressibility.

The numerical solution of these equations (see Section 2.2.2), enables the calculation of a phase diagram for the diblock melt, shown in Fig. 2.4c as a function of χN

and the block fraction f. Despite the seemingly bold assumptions presented earlier, SCFT remarkably manages to capture the phase diagram of diblock copolymer melts quite well, as demonstrated by comparison with experimental data for a polyisoprene (PI)–polystyrene (PS) melt in Fig. 2.4b. One notable difference between experiments and SCFT is that for a symmetric diblock, the disorder-lamella (Fig. 2.4a-L) transition, is predicted in SCFT to occur at the multicritical order disorder transition (ODT) point, shown in Fig. 2.4c. In experiments however, the melt is still disordered[51] at this SCFT predicted point, and the transition that happens at larger values of χN, is in fact first order. This discrepancy, is due to SCFT effectively ignoring fluctuations, which are present for finite values of N. The omission of fluctuations overestimates the stability of ordered phases, but more sophisticated theories[44,52–54] can incorporate these fluctuations and predict more accurate values of the ODT for finite values of N. In addition, SCFT has managed to show that if one assumes a certain conformational asymmetry between the blocks, i.e., different statistical segment sizes and volumes between the monomers A and B, that Frank-Kasper phases, such as the A15 and σ phases are possible[55].

As a last point in this section, we turn our focus to polymers in a solution (S). Assuming a canonical ensemble with n_S solvent particles or a grand canonical ensemble with a solution chemical potential μ_S, the partition functions for polymers in an explicit solvent are given by:

$$\mathcal{Z}_C = \frac{1}{n!}\prod_{i=1}^{n}\left[\frac{1}{v^*}\int \widehat{\mathcal{D}}_i(\boldsymbol{r}(\mathfrak{n}))\right]\frac{1}{n_S!}\prod_{k=1}^{n_S}\left[\frac{1}{v^*}\int d\boldsymbol{r}_k\right]\exp\left(-\beta\mathcal{V}\{\hat{\rho}_\alpha,\hat{\rho}_S\}\right), \tag{2.51}$$

$$\mathcal{Z}_{GC} = \sum_{n=0}^{\infty}\left\{\frac{e^{\beta\mu n}}{n!}\prod_{i=0}^{n}\frac{1}{v^*}\int \widehat{\mathcal{D}}\{\boldsymbol{r}_i(\mathfrak{n})\}\right\}\sum_{n_S=0}^{\infty}\left\{\frac{e^{\beta\mu_S n_S}}{n_S!}\prod_{k=1}^{n_S}\frac{1}{v^*}\int d\boldsymbol{r}_k\right\} \times \exp\left[-\beta\mathcal{V}\{\hat{\rho}_\alpha,\hat{\rho}_S\}\right], \tag{2.52}$$

and the local concentration of the solvent is given by:

$$\hat{\rho}_S(\boldsymbol{r}) = \sum_{k=1}^{n_S}\delta(\boldsymbol{r}-\boldsymbol{r}_k). \tag{2.53}$$

Following the same steps as before, the free energies can be expressed as:

$$\beta\mathcal{F}_C\{\rho_\alpha,w_\alpha,\rho_S,w_S\} = \beta\mathcal{V}\{\rho_\alpha,\rho_S\} - \sum_\alpha\int w_\alpha(\boldsymbol{r})\rho_\alpha(\boldsymbol{r})\,d\boldsymbol{r} - \int w_S(\boldsymbol{r})\rho_S(\boldsymbol{r})\,d\boldsymbol{r} - n\ln\left(\frac{\mathcal{Q}\{w_\alpha\}}{n}\right) - n_S\ln\left(\frac{\mathcal{Q}_S\{w_S\}}{n_S}\right), \tag{2.54}$$

$$\beta\mathcal{F}_{GC}\{\rho_\alpha,w_\alpha,\rho_S,w_S\} = \beta\mathcal{V}\{\rho_\alpha,\rho_S\} - \sum_\alpha\int w_\alpha(\boldsymbol{r})\rho_\alpha(\boldsymbol{r})\,d\boldsymbol{r} - \int w_S(\boldsymbol{r})\rho_S(\boldsymbol{r})\,d\boldsymbol{r} - e^{\beta\mu}\mathcal{Q}\{w_\alpha\} - e^{\beta\mu_S}\mathcal{Q}_S\{w_S\}, \tag{2.55}$$

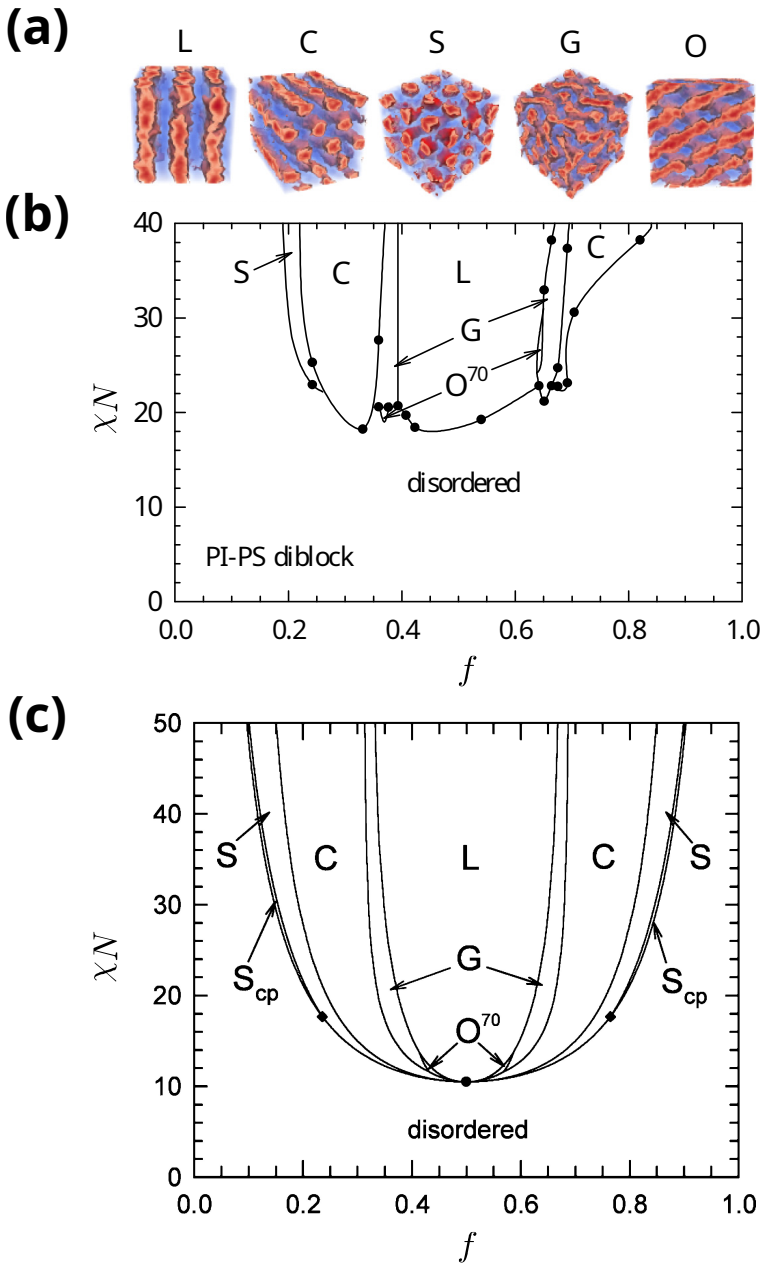

Figure 2.4: (a) Representation of the diblock melt morphologies: Lamellar (L), cylindrical (C), bcc spherical (S), gyroid (G) and *Fddd* (O_{70}). (b) Phase diagram obtained from experiments of Polyisoprene-Polystyrene diblock with a Polyisoprene block fraction f against the Flory-Huggins parameter χN. (a,b) Figures adapted from Ref.[56]. (c) SCFT calculation of diblock copolymer with conformational symmetry between blocks. Note that an additional spherical hcp phase (S_{cp}) is predicted. The order-disorder transition (ODT) point is marked by a dot in the center. Figure adapted from Ref.[57] with permission from the American Chemical Society.

where the solvent particle partition function is given similarly:

$$Q_S\{\rho_S\} = \frac{1}{v^*}\int \exp\left[-w_S(\boldsymbol{r})\right]\, d\boldsymbol{r}. \tag{2.56}$$

The solvent concentrations are then given by:

$$\rho_S(\boldsymbol{r}) = \frac{n_S}{v^* Q_S}\exp\left[-w_S(\boldsymbol{r})\right], \tag{2.57}$$

in the canonical ensemble and in the grand canonical ensemble by:

$$\rho_S(\boldsymbol{r}) = \frac{\exp(\beta\mu_S)}{v^*}\exp\left[-w_S(\boldsymbol{r})\right]. \tag{2.58}$$

The calculation of the monomer densities and the fields follow the same equations as before, although now $\mathcal{V}$ includes interactions with the solvent and therefore is written as:

$$\beta\mathcal{V}_{inter}\{\rho_\alpha,\rho_S\} = \frac{1}{2v^*}\sum_\alpha\sum_{\alpha\neq\beta}\int \chi_{\alpha\beta}\phi_\alpha\phi_\beta\, d\boldsymbol{r} + \frac{1}{2v^*}\sum_\alpha\int \chi_{\alpha S}\phi_\alpha\phi_S\, d\boldsymbol{r}, \tag{2.59}$$

and

$$\beta\mathcal{V}_o\{\rho_\alpha,\rho_S\} = \frac{\kappa}{2v^*}\int\left(\phi_S(\boldsymbol{r}) + \sum_\alpha\phi_\alpha(\boldsymbol{r}) - 1\right)^2 d\boldsymbol{r}. \tag{2.60}$$

Lastly, one can instead model the solvent implicitly. First, one considers a polymer solution with no polymer-solution interactions and the equivalent incompressibility constraint from (2.47), i.e.,:

$$\delta\left[\phi_S + \sum_\alpha\phi_\alpha - 1\right], \tag{2.61}$$

into the partition function. One can then convert the delta function again into a field $\xi(\boldsymbol{r})$, set $\phi_S = 1 - \sum_\alpha\phi_\alpha$ and since $w_S(\boldsymbol{r}) = \xi(\boldsymbol{r})v_S$ (where v_S is the solvent particle volume), one can determine $\xi(\boldsymbol{r})$ fully by $\rho_\alpha(\boldsymbol{r})$ using equations (2.57) and (2.58). This results in the following expression for the fields:

$$w_\alpha(\boldsymbol{r}) = \frac{\delta(\beta\mathcal{V}_{inter}\{\rho_\alpha\})}{\delta(\rho_\alpha(\boldsymbol{r}))} - \frac{v_\alpha}{v_S}\ln\left(1 - \sum_\alpha\phi_\alpha(\boldsymbol{r})\right). \tag{2.62}$$

These fields can be alternatively computed by adding a potential $\mathcal{V}_o$:

$$\beta\mathcal{V}_0\{\rho_\alpha\} = \frac{1}{v_S}\int d\boldsymbol{r}\left(1 - \sum_\alpha\phi_\alpha(\boldsymbol{r})\right)\ln\left(1 - \sum_\alpha\phi_\alpha(\boldsymbol{r})\right) + \frac{1}{v_S}\int d\boldsymbol{r}\sum_\alpha\phi_\alpha(\boldsymbol{r}), \tag{2.63}$$

which is equivalent to the potential term derived from the Sanchez-Lacombe equation of state[48,58]. This way, we effectively perform the integral over the positions of the solvent in the partition function and no longer have to account for the partition function Q_S, the fields w_S, and the chemical potential μ_S, which is why this is considered an implicit solvent. For completeness, the free energies of a polymer solution in an implicit solvent are given by:

$$\beta\mathcal{F}_C\{\rho_\alpha, w_\alpha\} = \beta\mathcal{V}\{\rho_\alpha\} - \sum_\alpha \int w_\alpha(\boldsymbol{r})\rho_\alpha(\boldsymbol{r})\, d\boldsymbol{r} - n\ln\left(\frac{\mathcal{Q}\{w_\alpha\}}{n}\right), \tag{2.64}$$

$$\beta\mathcal{F}_{GC}\{\rho_\alpha, w_\alpha\} = \beta\mathcal{V}\{\rho_\alpha\} - \sum_\alpha \int w_\alpha(\boldsymbol{r})\rho_\alpha(\boldsymbol{r})\, d\boldsymbol{r} - e^{\beta\mu}\mathcal{Q}\{w_\alpha\}, \tag{2.65}$$

where the functional $\beta\mathcal{V}\{\rho_\alpha\}$ is given by:

$$\beta\mathcal{V}\{\rho_\alpha\} = \beta\mathcal{V}_{inter}\{\rho_\alpha\} + \beta\mathcal{V}_o\{\rho_\alpha\}, \tag{2.66}$$

and the two terms above are given by (2.59) and (2.63).

Although in some special cases the above self-consistent equations may be exactly solvable, it is often the case that they need to be solved numerically. In the next subsection, we introduce the numerical scheme involved in solving such equations, and also explain some variations of the steps involved in such endeavor.

2.2.2 Numerical Scheme

Numerically solving the self-consistent equations involves the iterative procedure shown in Fig. 2.5, whereupon one begins with an initial guess for the fields $w_\alpha(\boldsymbol{r})$ or the densities $\rho_\alpha(\boldsymbol{r})$ (where one can calculate the fields via Eq. (2.26)) and then proceeds by calculating the forward $q(\boldsymbol{r}, \mathfrak{n})$ and backward $q^\dagger(\boldsymbol{r}, \mathfrak{n})$ propagators by solving the pair of MDEs in (2.38) and (2.40). We refer to the fields used in the latter step as the old fields $w_\alpha^{old}(\boldsymbol{r})$. Once the propagators have been calculated, one can calculate a set of new densities $\rho_\alpha^{new}(\boldsymbol{r})$ via Eqs. (2.43) or (2.44) depending on the ensemble used, and the corresponding new fields $w_\alpha^{new}(\boldsymbol{r})$ via Eq. (2.26). Then, the new and old fields (or densities) are compared, to access whether convergence has been achieved. This is usually done by testing whether the l^2-norm between new and old, is below a user-defined value. If the convergence criterion has not been reached, then the new fields are mixed with the old via a mixing scheme and are then used to calculate a new set of propagators as in the second step. This procedure does not guarantee that the converged solution is the global minimum, since the saddle-point approximation employed in SCFT allows for convergence to metastable states as well.

The state to which the scheme will converge is dependent on many variables, including the initial guess, the numerical method involved in solving the MDEs, and

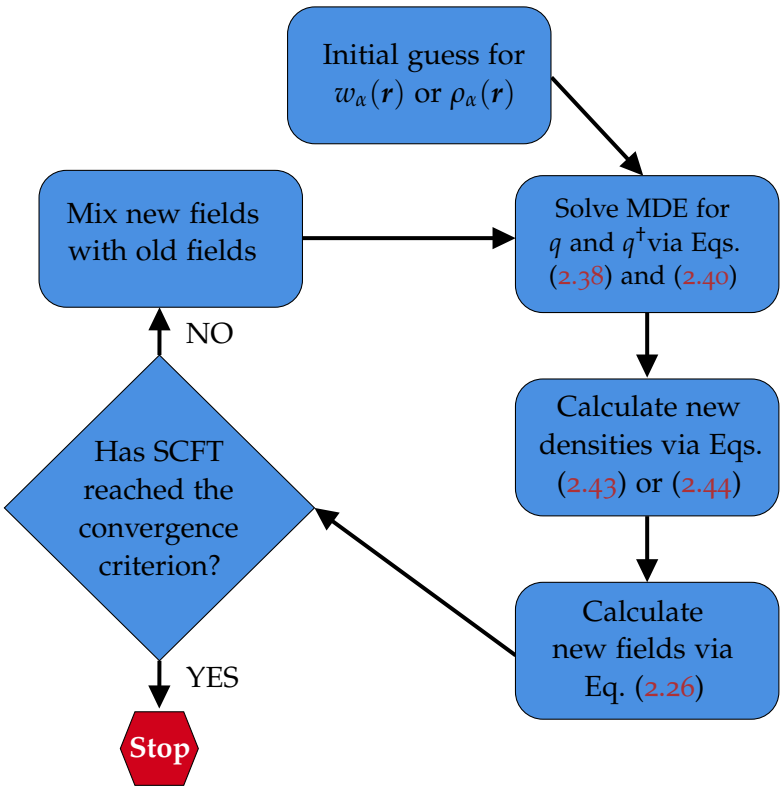

Figure 2.5: Flowchart representation of the numerical scheme involved in solving the self-consistent equations.

the mixing scheme. For example, when applying this numerical scheme in the grand canonical ensemble for micelles, consisting of solvophobic and solvophilic monomers, we found that the initial guess was of great importance in converging to meaningful inhomogeneous states and not the uninteresting homogeneous state. Therefore, to start with a good initial guess, we often first solved a constrained version of these equations, whereupon we would force the solvophobic density in a region of the simulation box to be above a user-defined value (acting effectively as a nucleus). Then we used the converged solution as an initial guess for the unconstrained self-consistent equations.

The most computer-intensive part of this numerical scheme is in finding the solution to the MDEs. Depending on the problem and its associated boundary conditions, different methods may be preferred. For highly symmetric and periodic structures, such as those found in diblock melts, where one is usually already aware of the possible morphologies, the spectral method may be applied[11]. Such a method, solves the MDEs by using a basis, oftentimes a Fourier series basis, for the spatial component of the propagators. This method reduces the problem into a problem of coupled first-order ODEs with respect to the monomer count $\mathfrak{n}$, which can be solved much faster than the original MDEs[11,44,46]. One of the main issues of this method however, is that if the fields $w_\alpha(\boldsymbol{r})$ are sharp or insufficiently smooth—such as near boundaries—more basis functions are required for an accurate representation. This increases the number of coupled ODEs that must be solved, thereby raising the computational cost.

Alternatively one could employ a real-space method to solve the MDEs, which is more appropriate when dealing with complex boundary conditions and low-dimensional problems, which are not that computationally expensive. To do this, one can use a finite difference scheme to discretize the MDEs in both the contour and the spatial dimensions. For example, in the scenario where only one dimension is relevant to the problem e.g. lamella, the spatial dimension, say X, would be discretized into N_x points, while the polymer contour would be discretized into N_s points. Solving the MDEs would then be transformed into a linear algebra problem, which depending on the finite difference scheme used, can be solved with a computational cost scaling with $\mathcal{O}(N_x)$ and $\mathcal{O}(N_s)$. The Crank-Nicolson scheme is a common finite difference scheme that can be shown to be unconditionally stable i.e. the fineness of the polymer contour, does not impact the propagation of errors when solving for successive steps along the polymer contour, and only impacts the accuracy of the solution, not its stability[44]. An adaptive version of this method is described more explicitly in Chapter 4.

Another very efficient method that we also employed and is commonly used with periodic-boundary conditions, is the pseudo-spectral method. This method takes advantage of the fact that the Laplacian operator found in the MDEs is local in reciprocal space and performing its computation there instead of real space is a far more efficient pathway.

The first step in this method is to integrate Eq. (2.38) from $\mathfrak{n}$ to $\mathfrak{n} + \Delta\mathfrak{n}$ for some small $\Delta\mathfrak{n}$ which results in the following expression:

$$q(\boldsymbol{r}, \mathfrak{n} + \Delta\mathfrak{n}) = \exp\left(\mathcal{L}\Delta\mathfrak{n}\right) q(\boldsymbol{r}, \mathfrak{n}), \tag{2.67}$$

which we can do because $\mathcal{L} = \mathcal{L}^D + \mathcal{L}^W$ is a linear operator and is composed from the operators $\mathcal{L}^D = b^2/6\,\nabla^2$ and $\mathcal{L}^W = -\sum_\alpha w_\alpha(\boldsymbol{r}) g_\alpha(\mathfrak{n})$. Eq. (2.67) can be then approximated as:

$$q(\boldsymbol{r}, \mathfrak{n} + \Delta\mathfrak{n}) = \exp\left(\mathcal{L}^W \Delta\mathfrak{n}/2\right) \exp\left(\mathcal{L}^D \Delta\mathfrak{n}\right) \exp\left(\mathcal{L}^W \Delta\mathfrak{n}/2\right) q(\boldsymbol{r}, \mathfrak{n}) + \mathcal{O}(\Delta\mathfrak{n}^3). \tag{2.68}$$

One can then insert the identity operator, $1 = \mathfrak{F}^{-1}\mathfrak{F}$, where $\mathfrak{F}$ is the Fourier transform operator and commutes with the $\mathcal{L}^D$ operator. This leads to:

$$\begin{aligned} q(\boldsymbol{r}, \mathfrak{n} + \Delta\mathfrak{n}) = \exp&\left(\mathcal{L}^W \frac{\Delta\mathfrak{n}}{2}\right) \\ &\mathfrak{F}^{-1}\left\{\exp\left(\mathcal{L}^D \Delta\mathfrak{n}\right)\, \mathfrak{F}\left[\exp\left(\mathcal{L}^W \frac{\Delta\mathfrak{n}}{2}\right)\, q(\boldsymbol{r}, \mathfrak{n})\right]\right\}. \end{aligned} \tag{2.69}$$

The gradient operator ∇, acting on the Fourier transform, is equivalent to multiplying with $i\mathbf{k}$, where $\mathbf{k}$ is the reciprocal vector and therefore the action of $\mathcal{L}_D$ leads to the final expression:

$$\begin{aligned} q(\boldsymbol{r}, \mathfrak{n} + \Delta\mathfrak{n}) = \exp&\left(\mathcal{L}^W \frac{\Delta\mathfrak{n}}{2}\right) \\ &\mathfrak{F}^{-1}\left\{\exp\left(-(\frac{b^2}{6}\mathbf{k}^2)\Delta\mathfrak{n}\right)\, \mathfrak{F}\left[\exp\left(\mathcal{L}^W \frac{\Delta\mathfrak{n}}{2}\right)\, q(\boldsymbol{r}, \mathfrak{n})\right]\right\}. \end{aligned} \tag{2.70}$$

Although transforming between real and reciprocal space may seem cumbersome at first, the fact that the Fast Fourier Transform (FFT) algorithm can be leveraged, means that the computational time scales like $\mathcal{N}_o \log(\mathcal{N}_o)$ for an $\mathcal{N}_o$ amount of spatial points.

As a last point in this iteration scheme, one has to mix the new values of the fields with old values of the fields for stability reasons instead of just using the new values. The iteration scheme can be viewed as a mapping, where the fields at the k^{th} iteration are mapped to updated fields i.e.:

$$w_\alpha^{new}(\boldsymbol{r}) = \Delta(w_\alpha^k(\boldsymbol{r})). \tag{2.71}$$

The new fields, are then taken and mixed according to a mixing scheme, the simplest of which is called simple mixing, whereupon a small percentage λ (typically less than 10 %) of the new fields is mixed with the old fields i.e.:

$$w_\alpha^{k+1}(\boldsymbol{r}) = w_\alpha^k(\boldsymbol{r}) + \lambda(\Delta(w_\alpha^k(\boldsymbol{r})) - w_\alpha^k(\boldsymbol{r})). \tag{2.72}$$

Another method, that we found to be quite successful in our work is lambda mixing[59], which uses an adaptive mixing percentage to accelerate the convergence, but is also

more stable than just simple mixing. In this scheme λ changes at every iteration and is defined as:

$$\lambda_k = \sqrt{\frac{\sum_\alpha |w_\alpha^k - w_\alpha^{k-1}|^2}{\sum_\alpha |\Delta(w_\alpha^k) - w_\alpha^k - (\Delta(w_\alpha^{k-1}) - w_\alpha^{k-1})|^2}}, \tag{2.73}$$

where the vertical lines are considered as a sum over all discretized spatial points. More advanced methods, like Anderson mixing[60], instead use the fields from multiple past iterations to enhance the stability and make no use of empirically user-defined values like mixing percentages as in simple mixing. Oftentimes, with such a mixing method we had found that the initial state played a large role in the converged state, as stated earlier, so we opted to only use lambda mixing in our work.

2.2.3 Strong Stretching Theory

In this last subsection we aim to introduce the reader to the Strong Stretching Theory/Limit, introduced first by Semenov[10], but written in its modern path integral formulation later by Milner *et al.* [61]. This theory goes a step further than SCFT and assumes not only that the polymers are highly packed and that their fluctuations are insignificant, but also that the polymers are highly stretched. This assumption is justified for systems where repulsion between monomers are strong, as in diblock melts where $\chi N \gg 1$, or in polymer brushes that are densely packed. Under this assumption, the conformations of polymers are heavily restricted, and are mostly found around their 'classical path'. This means that the single chain partition function (2.31) can be approximated by a third saddle point approximation.

To demonstrate how this theory/approximation can be used to extract information about a system, we demonstrate its application in monodisperse, planar, densely packed, linear homopolymer brushes under good solvent conditions. In this scenario the canonical free energy is given by:

$$\beta\mathcal{F}_C\{\rho\} = \beta\mathcal{V}\{\rho\} - \int w(\boldsymbol{r})\rho(\boldsymbol{r})\, d\boldsymbol{r} - n \ln\left(\frac{Q}{n}\right). \tag{2.74}$$

The interaction functional in this scenario can be approximated using the equation of state in Eq. (2.14) by taking the limit $N_A \to \infty$ and according to Schmid [62] then the functional $\beta\mathcal{V}$ can be expressed as:

$$\beta\mathcal{V}\{\rho\} = \beta\mathcal{V}_o\{\rho\} = \int d\boldsymbol{r}\, \rho(\boldsymbol{r}) \int_0^{\rho(\boldsymbol{r})} d\rho' \frac{\Pi(\rho')}{(\rho')^2} \approx \frac{v_{ex.}}{2} \int \rho(\boldsymbol{r})^2\, d\boldsymbol{r} \tag{2.75}$$

Under the SCFT approximation the field can of course be written as:

$$w(\boldsymbol{r}) = \rho(\boldsymbol{r}) v_{ex.}. \tag{2.76}$$

Setting z as the direction perpendicular to the surface, simplifies the problem to a one-dimensional problem, since there is no variation of the density profiles in the x and y directions. Under SST the single chain partition function as mentioned, can be approximated by its saddle point, i.e.,:

$$\begin{aligned} Q &= \frac{1}{v^*} \exp\left[-\left\{ \int_0^N \left(\frac{3}{2b^2} \left| \frac{d(z(\mathfrak{n}))}{d\mathfrak{n}} \right|^2 + w(z(\mathfrak{n})) \right) d\mathfrak{n} \right\} \right] \\ &= \frac{1}{v^*} \exp\left[-\left\{ \int_0^N \mathcal{L}\left\{ z(\mathfrak{n}), \frac{dz}{dn} \right\} d\mathfrak{n} \right\} \right], \end{aligned} \tag{2.77}$$

where $z(\mathfrak{n})$ is "classical path" of the chain, so-called because the saddle-point approximation of Q results in extremizing the exponent, and thus the classical "equation of motion", given by the Euler-Lagrange equation:

$$\frac{\partial \mathcal{L}}{\partial z} - \frac{d}{d\mathfrak{n}} \left(\frac{\partial L}{\partial (\frac{dz}{d\mathfrak{n}})} \right) = 0. \tag{2.78}$$

One of the chain ends is of course grafted to the surface and therefore $z(\mathfrak{n} = 0) = 0$, while the other end needs to be tensionless due to the extremization, i.e.,:

$$\left. \frac{dz}{d\mathfrak{n}} \right|_{\mathfrak{n}=N} = 0. \tag{2.79}$$

In this context, the free polymers ends have no benefit from not being distributed throughout all of the polymer brush and thus there are no spaces in the polymer brush devoid of chain ends, i.e., there are no end-exclusion zones (EEZs). As we will see in Chapter 3, this is not always the case.

Nonetheless one can proceed and solve Eq. (2.78), for a chain of N statistical segments and its chain end at $z(N)$, and get the following expression:

$$\frac{dz}{d\mathfrak{n}}(\mathfrak{n}) = \sqrt{\frac{2b^2}{3}} \sqrt{w(z(\mathfrak{n})) - w(z(N))}. \tag{2.80}$$

Furthermore, one can define the chain size associated with a chain end at z with the inverse function $N(z)$, which is of course constant in our case since we are considering a monodisperse polymer brush. Thus:

$$\begin{aligned} N = N(z) &= \int_0^N d\mathfrak{n} = \int_0^z \frac{1}{\frac{dz'}{d\mathfrak{n}}} dz' \\ &= \sqrt{\frac{3}{2b^2}} \int_{w(0)}^{w(z)} \frac{\frac{dz'}{dw(z')}}{\sqrt{w(z') - w(z)}} dw(z') \\ &= \sqrt{\frac{3}{2b^2}} \int_0^U \frac{\frac{dz(U')}{dU'}}{\sqrt{U - U'}} dU' = N(U), \end{aligned} \tag{2.81}$$

where we introduced the transformation $w(z) = w(0) - U(z)$. One can then use an Abel transform to reverse this integral equation, resulting in:

$$\frac{dz}{dU} = \frac{N}{\pi}\sqrt{\frac{2b^2}{3}}\frac{1}{\sqrt{U}}, \tag{2.82}$$

and integrating the above leads to:

$$z(U) = \frac{2N}{\pi}\sqrt{\frac{2b^2}{3}}\sqrt{U}, \tag{2.83}$$

which is the famous quadratic dependence of U that is often used in many other contexts regarding polymers in the SSL[27]. Lastly, using Eq. (2.76) the density profile of a brush with thickness h can be shown to be:

$$\rho(z) = (h^2 - z^2)\left(\frac{\pi}{2Nb}\right)^2 \frac{3}{2v_{ex.}}, \tag{2.84}$$

which is a well-known result for planar brushes in a good solvent.

Part II

PUBLICATIONS

3

STRONG STRETCHING THEORY OF POLYDISPERSE CURVED POLYMER BRUSHES

Note: This chapter is a reproduction of the publication:

Giannakou Marios, Oleg V. Borisov, and Friederike Schmid. Strong stretching theory of polydisperse curved polymer brushes. *The Journal of Chemical Physics* **161** (2024), 014903-15.

Any additions are marked in violet.

Contributions to the publication:

- **Numerical scheme and analytics:** The set of self-consistent equations were first derived by F. Schmid and the numerical scheme for solving them was made by M. Giannakou. F. Schmid also implemented the numerical scheme for reassurance.
- **Analysis and figures:** The analysis and figure production was made by M. Giannakou with input from F. Schmid.
- **Writing:** M. Giannakou and F. Schmid wrote together the publication, while O. V. Borisov suggested minor modifications to the final draft.

3.1 Introduction

Tethering polymers onto a substrate is an efficient and versatile strategy to engineer surfaces with adjustable and potentially responsive characteristics. The resultant structures, known as polymer brushes, have been the subject of intensive exploration for several decades. These brushes find applications in diverse fields, including protein immobilization and isolation[63–65], water filtration enhancement, anti-fouling[65,66], bacterial adhesion, surface wettability tuning[67–69], colloid stabilization[70], as well as in designing responsive colloids[71] and soft surfaces[67,72–74].

Theoretical frameworks for understanding polymer brushes have evolved since the 1970s, starting with the seminal work by de Gennes[75] and Alexander[76]. Sophisticated mean-field approaches such as the self-consistent field (SCF) theory[77] and the analytical strong-stretching theory (SST)[61,70] have facilitated comprehensive investigations into brush properties[78–83], including monomer density and chain end distribution. Furthermore, such theories are also used to describe the molecular structure of copolymer-based micelles, membranes, and bulk mesophases[83–93]. In theory, it is common to adopt simplifying assumptions, with one prevalent choice being the assumption that brushes consist of polymer chains of uniform length, also known as the monodisperse limit. However, in reality, most polymer brushes exhibit polydispersity, characterized by broad chain length distributions. Despite this, only a handful of papers have delved into the implications of polydispersity. An influential semi-analytical extension of SST was devised by Milner, Witten, and Cates in 1989 [94]. Subsequent theoretical and simulation studies focusing on polydisperse brushes have highlighted significant variations in their properties compared to their monodisperse counterparts[95,96].

A key reason for the prevalence of polydisperse brushes is the limited precision in controlling chain lengths and grafting density afforded by current brush synthesis methods[97]. The most precise approach in this regard is the ”grafting to” method[98,99], where polymers are synthesized prior to attachment to a surface. This permits a narrow chain length distribution, but comes with the limitation of achieving only relatively low grafting densities. The challenge arises from the difficulty of introducing new chains near the substrate once other polymers have been already introduced. In the ”grafting from” method[99,100], chains grow monomer by monomer from the solution, originating from initiators attached to the substrate. While this method enables the creation of denser brushes[99], it comes with the trade-off of less control over the chain length distribution. Finally, the recently introduced ”grafting through”[101] adopts a strategy akin to the ”grafting from method” but employs a porous membrane as a substrate. Monomers are supplied from a solution on the membrane side opposite to the brush. As the monomers approach the initiators from below, shorter chains can grow more readily than longer chains, leading to a more uniform chain length distribution. However, this method has limitations in substrate choice and is less universally applicable compared to other methods.

Here, our focus lies on dense brushes with chain length distributions typical of those resulting from the ”grafting from” method. In such instances, the chain length distributions exhibit a similar overall form, resembling those of polymers grown in solution. These distributions are often well-described by the Schulz-Zimm distribution[102,103].

Recent developments have enabled the design of structures where polymers are attached to spherical nanoparticles[104–107], commonly referred to as "hairy" particles, or onto cylindrical nanopores[107–111]. In the former case, polymer brushes have been employed to regulate the distribution of nanoparticles in a solution or to alter the rheological properties of the nanoparticle dispersion. In the latter case, cylindrical nanopores were coated with responsive polymers capable of either closing or opening the nanopore depending on the solvate. It is crucial to note that the polymers attached to these nanopores and particles often possess a radius of gyration that can be of the same order, or even many orders of magnitude larger than the size of the pore or particle. Therefore, it is natural to anticipate significant effects from geometric curvature constraints in this scenario.

The impact of curvature on the structure of polymer brushes has been subjected to theoretical examination for many years by various researchers[112–118]. A notable prediction posits the existence of a ”dead zone” or ”End Exclusion Zone” (EEZ), marked by the lack of free end monomers[91,112,113,116,118]. However, these investigations have predominantly focused on monodisperse brushes, or, at most, bidisperse[119] brushes. In the latter case, it was found that adding a small amount of longer chains can significantly diminish the bending modulus of molten brushes[119].

The present authors are only aware of two theoretical studies addressing the conjoined influence of polydispersity and curvature, a Monte Carlo simulation by Dodd and Jayaraman [120]. They observed that polydispersity exerts a pronounced effect on the distribution of chain ends, shifting them closer to the surface eliminating the dead zone in the process. Analytical or semi-analytical mean-field theories can help to rationalize and predict such phenomena at low computational cost. In particular, given the historical success of SST and the increasing technological relevance of strongly curved polydisperse brushes, an expansion of the SST to accommodate curved brushes appears highly desirable.

In the present study, we extend the semi-analytical SST framework developed by Milner *et al.* [94] for polydisperse brushes, adapting it to dense brushes on curved surfaces with arbitrary curvature. Our investigation primarily centers on spherical geometries under good solvent conditions, delving into the brush structure across a range of experimentally relevant or theoretically promising chain length distributions. The SST framework yields results consistent with Dodd and Jayaraman’s findings. However, depending on the chain length distribution, we find that dead zones are still possible in polydisperse brushes. Moreover, we show that it is even possible to engineer a dead zone such that it appears at some distance from the substrate. Lastly, we show that it is possible to engineer a desired chain end distribution.

The rest of the paper is organized as follows. In section 3.2 we introduce the model and briefly go over the foundations, while also providing the analytical extension of polydisperse brushes on curved geometries. In section 3.3 we present results obtained from the analysis of our model for the Schulz-Zimm distribution 3.3.1 and explore the effect of polydispersity on the chain end profiles, bending moduli and more. Moreover, in section 3.3.2 we explore the emergence of an EEZ in polydisperse brushes and show that it is possible within the framework of SST, for an EEZ to also exist within the brush. Furthermore, in section 3.3.3 we show that the self-consistent equations in 3.2 can be also used to design chain end profiles.

3.2 Theoretical Model

We consider a polymer brush that is grafted upon a curved surface. The grafting density is given by σ and each chain i may have a different chain length N_i, characterizing the number of segments. The chain lengths are distributed according to a prescribed probability distribution $P(N)$. The local geometry of the substrate at a given surface point is characterized by the mean curvature $H = \frac{1}{2}(\frac{1}{R_1} + \frac{1}{R_2})$ and the Gaussian curvature $K = 1/(R_1 R_2)$, where R_1 and R_2 are the radii of curvature (see Fig. 3.1a). A useful formula regarding the geometry is the Steiner formula, which describes the fraction of areas between an area element on the substrate and one which is parallel at a perpendicular distance z (see Fig. 3.1b). It is given by

$$g(z) = 1 + 2Hz + Kz^2. \tag{3.1}$$

We assume that the chains are sufficiently long that they can be described as Gaussian chains with statistical segment length a. Chains i are thus modelled by continuous curves $\boldsymbol{r}_i(n)$ with $n \in [0 : N_i]$. Non-bonded interactions are described by an energy functional $\mathcal{V}[\hat{\phi}]$, where $\hat{\phi}(\boldsymbol{r})$ is the number density of monomers given by

$$\hat{\phi}(\boldsymbol{r}) = \sum_i \int_0^{N_i} \mathrm{d}n\, \delta(\boldsymbol{r} - \boldsymbol{r}_i(n)). \tag{3.2}$$

Consequently, the Hamiltonian of a patch of unit area on the substrate is given by

$$\frac{\mathcal{H}[\{\boldsymbol{r}_i\}]}{k_B T} = \sum_i \int_0^{N_i} \mathrm{d}n\, \frac{3}{2a^2} \left| \frac{\mathrm{d}\boldsymbol{r}_i(n)}{\mathrm{d}n} \right|^2 + \mathcal{V}[\hat{\phi}]. \tag{3.3}$$

Here the sum on the r.h.s runs over all chains in the patch, the first term describes the conformational energy of Gaussian chains, and the term $\mathcal{V}[\hat{\phi}]$ accounts for nonbonded interactions between monomers. In the following, we primarily focus on the good solvent case, whereupon the excluded volume interaction is given to first approximation by

$$\mathcal{V}[\hat{\phi}] = \frac{w}{2} \int \mathrm{d}^3 r\, \hat{\phi}(\boldsymbol{r})^2, \tag{3.4}$$

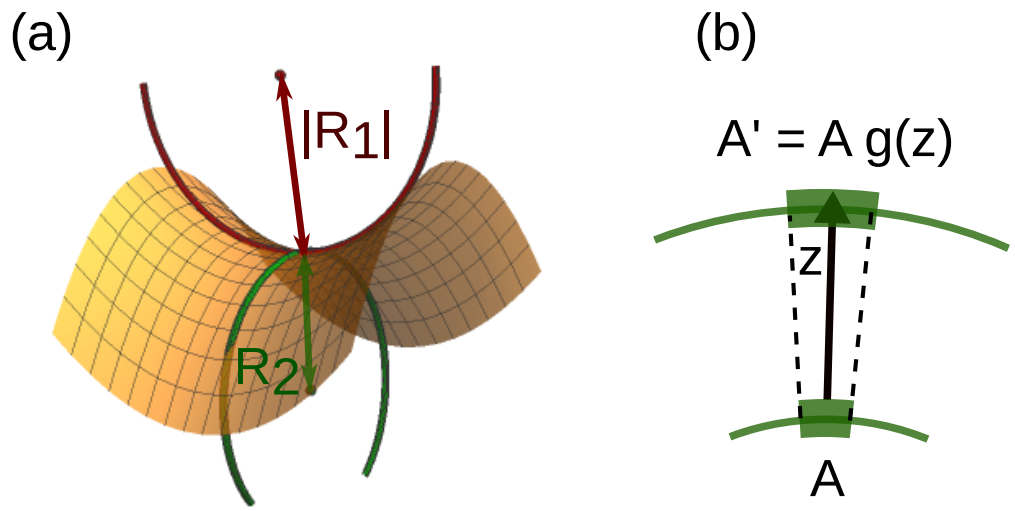

Figure 3.1: (a) Principle radii of curvature at a point on a curved surface: The largest and smallest radii of tangent circles, where by convention, a radius is negative if the curvature turns upwards (as for R_1). (b) Illustration of the Steiner formula.

---

where w is the excluded volume, but the theory can also be applied to other types of potentials, and to incompressible melts (see Appendix 3.7.1).

3.2.1 Background: SCF and SST approximations

In the regime of high grafting density, the chains are closely packed together, and a chain has many more interactions with its neighbouring chains than it has with itself. In such an instance, density fluctuations are suppressed and one can justifiably employ a mean-field approximation, where chains are taken to move independently in the average field of the surrounding chains. This leads to the popular self-consistent field (SCF) theory [50]. The conformations of chains i of length N_i are independently distributed according to the distribution functions $\mathcal{P}_i[\boldsymbol{r}_i] \sim \exp\big(-\mathcal{S}_i[\boldsymbol{r}_i; W]\big)$ with the "action"

$$\mathcal{S}_i[\boldsymbol{r}_i; W] = \int_0^{N_i} \mathrm{d}n \left(\frac{3}{2a^2} \left| \frac{\mathrm{d}\boldsymbol{r}_i(n)}{\mathrm{d}n} \right|^2 + W\big(\boldsymbol{r}_i(n)\big) \right), \tag{3.5}$$

where $W(\boldsymbol{r}) = \delta\mathcal{V}/\delta\phi(\boldsymbol{r})$, i.e., $W(\boldsymbol{r}) = w\,\phi$ in the good solvent case. In the incompressible melt case, $W(\boldsymbol{r})$ acts like a constraint field that adjusts itself such that $\phi(\boldsymbol{r})$ is constant ($\phi(\boldsymbol{r}) \equiv \bar{\phi}$) everywhere. The distributions $\mathcal{P}_i[\boldsymbol{r}_i]$ can be used to calculate the average segment density ϕ, but they also depends on ϕ via $W(\boldsymbol{r})$, which creates a self-consistent loop. The SCF Ansatz reduces the complexity of the problem con-

siderably, but the numerical solution of the SCF equations remains time consuming for polydisperse brushes especially in the limit of very long chains and high grafting densities.

In this limit, however, a further simplification is provided by the Strong-Stretching approximation or Strong-Stretching theory (SST)[70,94]. It assumes that fluctuations of chain conformations are small, because the natural scale of such fluctuations is the radius of gyration, while the end-to-end distance of stretched chains may be much larger in dense brushes. Thus the ensemble averages over conformations of chains with a given length N_i are approximated by the most probable ones, i.e., the ones that minimize the actions $\mathcal{S}_i[\boldsymbol{r}_i(n)]$ (Eq. 3.5). Due to symmetry, the problem is now reduced to a one dimensional problem for the paths $z_i(n)$ in the direction z perpendicular to the substrate.

Following Milner *et al.* [94], we further define a "potential" U as

$$U(z) = W(0) - W(z) =: U_{\max} - W(z). \tag{3.6}$$

Minimizing Eq. (3.5) with respect to $z_i(n)$ with the constraint $z_i(0) = 0$ then gives the Euler-Lagrange equation

$$\frac{3}{a^2}\frac{\mathrm{d}^2 z_i}{\mathrm{d}n^2} = -\frac{\mathrm{d}U}{\mathrm{d}z}\Big|_{z=z_i}, \tag{3.7}$$

and the boundary condition $(\mathrm{d}z_i/\mathrm{d}n)\big|_{N_i} = 0$. The latter results from the minimization with respect to $z_i(N_i)$ and corresponds to the physically reasonable requirement that chain ends are tensionless[61]. Furthermore, we can identify integration constants

$$E(N_i) = \frac{3}{2a^2}\left(\frac{\mathrm{d}z_i}{\mathrm{d}n}\right)^2 + U(z_i) \equiv \text{const.}, \tag{3.8}$$

which depend on the chain length N_i, and can be calculated as $E(N_i) = U\big(z_i(N_i)\big)$ (using $(\mathrm{d}z_i/\mathrm{d}n)\big|_{N_i} = 0$). This allows us to derive an expression for the tension $\mathrm{d}z_i/\mathrm{d}n$ of a chain i of length N_i at the segment n as a function of the potential $U\big(z_i(n)\big)$ and the integration constant $E(N_i)$:

$$\frac{\mathrm{d}z_i}{\mathrm{d}n} = \sqrt{\frac{2}{3}}\, a \sqrt{E(N_i) - U\big(z_i(n)\big)}. \tag{3.9}$$

Next, we make two further physically reasonable assumptions. First, the tension $|\mathrm{d}z_i(n)/\mathrm{d}n|$ drops monotonically from the grafting point to the chain end. This implies, by virtue of Eq. (3.7), that $U(z)$ is a strictly monotonous function. Second, we assume that chains with a larger length have their ends placed further away from the substrate than their shorter counterparts. As a consequence, a monotonically increasing relationship can be established between the potential U, $z(U)$, and the length $N(U)$ of a chain which has its end at distance $z(U)$ from the substrate.

3.2.2 SST approach for curved brushes

Based on the above model and approximations, we can derive a set of self-consistent equations for polydisperse curved brushes. In the following, we will summarize these equations. A detailed derivation and an algorithm to solve them are presented in the Appendix, 3.7.2 and 3.7.6.

Before listing the self-consistent equations, we note that by inserting $z(U)$, we can express the local monomer density $\phi(z)$ as a function of the potential U. Specifically, for brushes in good solvent, we have (using Eqs. (3.4,3.6))

$$\phi(U) = (U_{\max} - U)/w. \tag{3.10}$$

For melts, the relation is even simpler:

$$\phi(U) \equiv \bar{\phi}_{\text{melt}}. \tag{3.11}$$

Furthermore, we define a "projected monomer density", $\lambda(U)$, such that $\lambda\big(U(z)\big)\,\mathrm{d}z$ is the amount of monomers between z and $z + dz$ per *substrate* unit area. Another useful quantity is the "cumulative end density" $\sigma_c(U)$, which is defined such that $\sigma_c(U)/\sigma$ is the fraction of chains with ends located at distances less than $z(U)$ from the substrate.

In the absence of an EEZ, our self-consistent set then consists of four equations: The first allows one to determine $z(U)$ from a given function $N(U)$,

$$z(U) = \sqrt{\frac{2}{3}}\,\frac{a}{\pi}\int_0^U \mathrm{d}U'\,N(U')\,\frac{1}{\sqrt{U-U'}}. \tag{3.12}$$

The second subsequently gives the projected monomer density $\lambda(U)$ as a function of $z(U)$,

$$\lambda(U) = \phi(U)\,g\big(z(U)\big) \tag{3.13}$$

($g(z)$ was introduced in Eq. (3.1)). The third expresses the cumulative end density $\sigma_c(U)$ in terms of $\lambda(U)$,

$$\sigma_c(U) = \sigma - \sqrt{\frac{2}{3}}\,\frac{a}{\pi}\int_U^{U_{\max}} \mathrm{d}U'\,\lambda(U')\,\frac{1}{\sqrt{U'-U}}. \tag{3.14}$$

Since $\sigma_c(0) = 0$, this equation also encompasses an expression for σ. Finally, the fourth equation connects $\sigma_c(U)$ with the chain length distribution $P(N)$ and can be used to determine $N(U)$ from $\sigma_c(U)$,

$$\frac{\sigma_c(U)}{\sigma} = \int_0^{N(U)} \mathrm{d}N'\,P(N') \tag{3.15}$$

which closes the self-consistent loop. Eq. (3.13) follows directly from the definition of the projected monomer density $\lambda(U)$, and Eq. (3.15) from the definition of the

cumulative end density $\sigma_c(U)$, taking into account that $N(U)$ increases monotonically. The derivations of Eqs. (3.12) and (3.14) are detailed in Appendix 3.7.2.

In the presence of an EEZ, Eq. (3.15) does not fully determine the function $N(U)$, because $\sigma_c(U)$ is constant inside the EEZ region. This introduces an apparent ambiguity. The reason is that $N(U)$ has no physical meaning inside the EEZ, since the EEZ does not contain any chain ends by definition. However, the ambiguity can be removed if one adds, as a fifth equation in the self-consistent set, the explicit requirement:

$$\frac{\mathrm{d}\sigma_c(U)}{\mathrm{d}U} \begin{cases} > 0 & \text{outside EEZs} \\ = 0 & \text{inside EEZs} \end{cases} \tag{3.16}$$

This requirement, together with Eqs. (3.12)–(3.15), then uniquely determines $N(U)$ in the whole range of U. We can rationalize the physical meaning of $N(U)$ inside the EEZ by imagining a modified chain length distribution that would be identical to the one considered, but has a vanishingly small population of chains with the appropriate chain lengths that would fill in the EEZ. Such a brush would have almost identical properties than the original brush, but $N(U)$ would be perfectly defined everywhere.

When can we expect an EEZ? To answer this question, we inspect the following explicit expression for $\mathrm{d}\sigma_c(U)/\mathrm{d}U$,

$$\frac{\mathrm{d}\sigma_c}{\mathrm{d}U} = \sqrt{\frac{2}{3}}\frac{a}{\pi}\Big(\frac{\lambda(U_{\max})}{\sqrt{U_{\max}-U}} - \int_U^{U_{\max}} \mathrm{d}U' \, \frac{\mathrm{d}\lambda}{\mathrm{d}U'}\frac{1}{\sqrt{U'-U}}\Big) \tag{3.17}$$

which is derived in Appendix 3.7.2. The equation shows that $\mathrm{d}\sigma_c(U)/\mathrm{d}U$ can only vanish if there are regions inside the brush where the projected monomer density, λ, increases as a function of U and hence z. In general, the monomer density ϕ decreases monotonically with increasing z (see, e.g., Eqs. (3.10) and (3.11)). Hence, considering Eq. (3.13), we see that EEZs can only occur in convex brushes where $g(z)$ increases with z. A second obvious requirement is the existence of a gap in the chain length distribution, i.e., $P(N)$ is zero for a range of chain lengths below the maximum chain length.

In addition to the equations listed above, we also use reorganized versions of Eqs. (3.12)-(3.14) in our actual algorithm to enforce the requirement (3.16). They are listed in Appendix 3.7.2.

Having solved the self-consistent equations, one can use the solution to calculate the free energy per substrate area A of the brush via

$$\frac{F}{A\, k_B T} = \mathcal{V}[\phi] + \frac{1}{2}\int_0^{U_{\max}} \mathrm{d}U' \, \lambda(U')\, z(U'). \tag{3.18}$$

The theoretical background and the derivation of Eq. (3.18) are detailed in Appendix 3.7.1. Specifically, the term $\mathcal{V}[\phi]$ can be expressed as

$$\mathcal{V}[\phi] = \frac{1}{2}\int_0^{U_{\max}} \mathrm{d}U' \, \frac{\mathrm{d}z}{\mathrm{d}U'}\, \lambda(U')\, (U_{\max}-U') \tag{3.19}$$

in the good solvent case, and as $\mathcal{V}[\phi] = 0$ in the melt case.

For completeness we also define one further quantity that we will use below. One is the projected chain end density $\varepsilon(z)$ which is defined as the amount of chain ends between z and $z + dz$ per *substrate* unit area. It can be related to quantities introduced above in a straightforward manner:

$$\varepsilon(z)\,\mathrm{d}z = \frac{\mathrm{d}\sigma_c(U)}{\mathrm{d}U}\,\mathrm{d}U = \sigma\, P(N)\,\mathrm{d}N. \tag{3.20}$$

In the remainder of this paper, we will mostly discuss brushes in good solvent. We will assume that the chain length distribution $P(N)$ has an upper bound, and hence the brush has a well-defined height h, above which the monomer density vanishes. In that case, we can identify $U_{\max} = U(h)$. We should note, however, that this assumption is not strictly necessary.

3.3 Results and Discussion

We will now present and discuss some results obtained with the SST framework introduced in the previous section. With few exceptions, we mostly show results for spherical geometries; the results for cylindrical geometries were qualitatively similar.

We will first consider brushes with chain lengths distributed according to the experimentally relevant Schulz-Zimm distribution, which we will characterize with respect to brush height, chain end density profiles, and curvature elastic moduli. Then we will consider other chain length distributions and discuss, among other, the emergence of end exclusion zones. Note that we limit our results to values of $\sigma w/a \leq 1$, since w has the physical interpretation of an excluded volume, and $\sigma w/a \approx 1$ thus marks the limit where grafted monomers on the surface are densely packed.

3.3.1 Polydisperse brushes with Schulz-Zimm distribution

The Schulz-Zimm distribution is essentially a Gamma distribution with mean N_a and variance N_a^2/k. Experimentally, the variance is often characterized in terms of the polydispersity index, which is defined as the ratio of weight averaged and number averaged chain length, $N_w/N_a = \langle N^2\rangle/\langle N\rangle^2 = 1 + 1/k$.

For numerical convenience, we use a truncated version of the Schulz-Zimm distribution:

$$P(N) = \mathcal{N}\begin{cases} N^{k-1}\exp(-k\,N/N_a), & \text{if } P(N) > p_{\text{cut}} \\ 0 & \text{otherwise} \end{cases} \tag{3.21}$$

where the normalization factor $\mathcal{N}$ is chosen as to ensure $\int \mathrm{d}N P(N) = 1$. The maximum cutoff value employed was set to $p_{\text{cut}} = 0.005$. The truncation effectively establishes

both a minimum and maximum chain length. It aids in bypassing numerical issues associated with small numbers of $P(N)$ and also facilitates a straightforward definition of the brush thickness h as the distance from the substrate at which the monomer density vanishes.

In the following, we present and analyze results derived from the solution of the self-consistent equations relevant to curved polydisperse brushes in spherical and cylindrical geometries. We employ Schulz-Zimm distributions corresponding to polydispersity indices of 1.02, 1.2, and 2. The first index of 1.02 is considered primarily for prospective interests, as achieving such narrow polydispersities is challenging in practical applications. Such precise control of the polymer size is restricted to special cases such as for example biopolymers or precision polyamides[121]. The latter two indices are of greater experimental significance, as they are more easily accessible.

Before we proceed to the results, it is important to highlight some limitations of the Ansatz: First, in highly polydisperse brushes, the outermost parts of the longest chains are expected to be in the 'mushroom' regime and not in the conditions assumed by the SST. However, because of the relative small portion of such chains, the expected impact on our results would be minimal. Second, in strongly curved concave geometries, the SST becomes questionable if the width of the brush layer becomes comparable to the curvature radius. If the free ends of polymers that have grafted ends in different substrate regions intermingle, one expects a cross-over from the strong-stretching regime to a concentrated bulk melt, and the theory should be modified accordingly. If the brush width exceeds one of the curvature radii, our SST Ansatz cannot be used at all because the Steiner formula (3.1) is no longer valid.

We first inspect the thickness h of the brushes as a function of grafting density σ. It is shown for different polydispersity indices in Fig. 3.2a (convex brushes) and Fig. 3.2b (concave brushes). On curved substrates, the relation between h and σ clearly deviates from the straightforward universal dependence in planar brushes, characterized by a scaling exponent of $1/3$.

On curved surfaces, such a strict scaling behavior is no longer observed. As the curvature increases, the thickness grows more slowly with σ for convex geometries, and more rapidly with σ for concave geometries. The shape of the curves is independent of the polydispersity; however, the polydispersity index has an influence on the prefactor. Additionally, according to Eq. (3.1), area elements at a distance z away from the substrate increase or decrease in convex or concave geometries, respectively.

Consequently, chains encounter more space available at shorter distances in convex curved geometries, leading to a decrease in brush thickness. Conversely, the brush thickness increases with increasing curvature in concave geometries.

We know from the structure of the SST equations (see Appendix 3.7.5) that some scaling is still expected. Indeed, according to the SST theory, the combination $(h/aN_a)\,(\sigma w/a)^{-1/3}$ should be a universal function of h/R for given $P(N)$. This function is shown in Fig. 3.2c (solid lines) which summarizes the results in Fig. 3.2a and

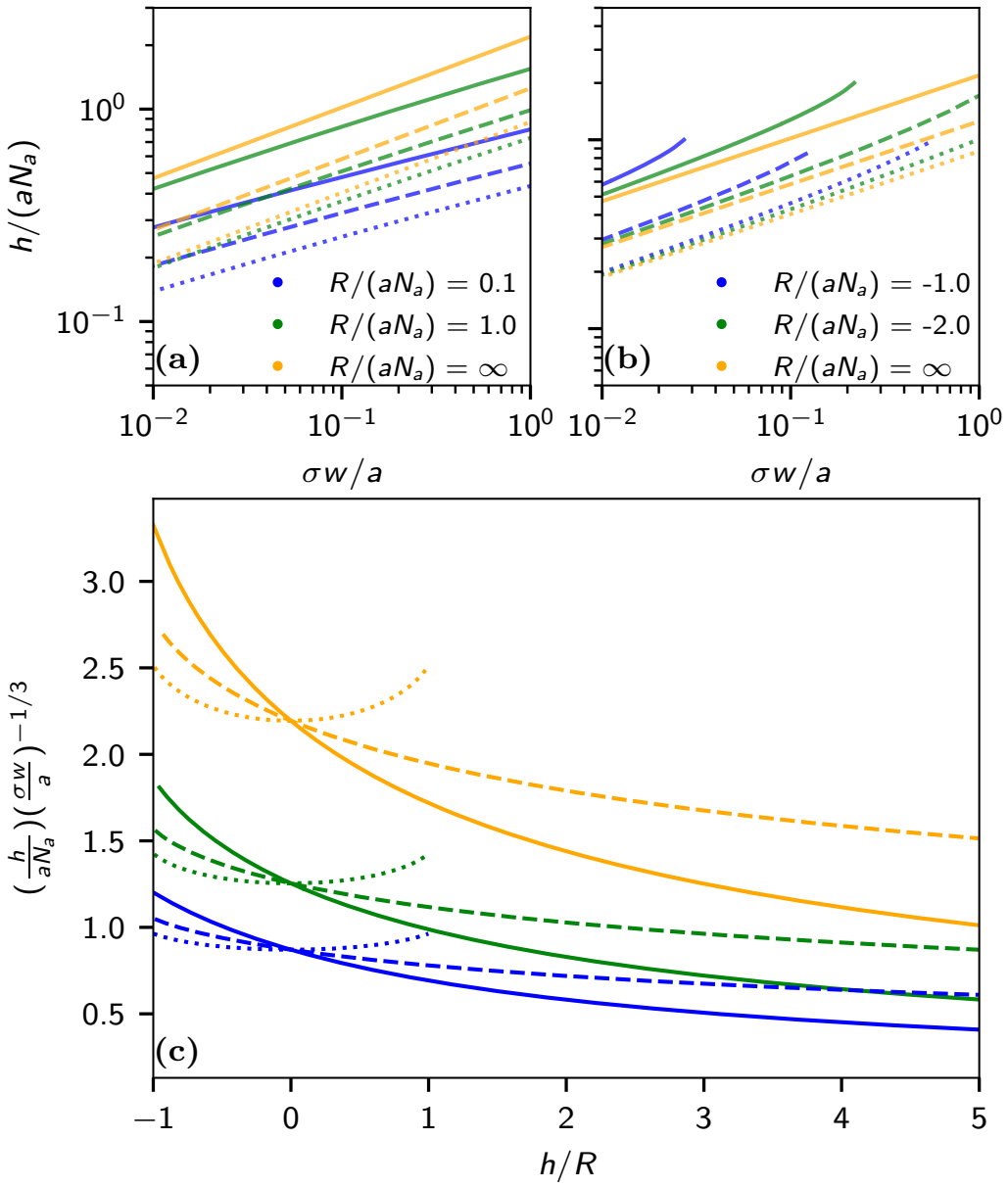

Figure 3.2: Scaled brush height $h/(aN_a)$ vs. scaled grafting density $\sigma w/a$ for spherically convex (a) and concave (b) geometries and scaled curvature radii R as indicated, $R = \infty$ represents the planar case. The 'dotted', 'dashed' and 'solid' lines, represent polydispersity indices of $N_w/N_a = 1.02, 1.2$ and 2.0 respectively. Panel (c) shows a universal scaling plot of the same quantities (see text). Here the 'solid', 'dashed' and dotted lines represent spherical, cylindrical and saddle geometries respectively, while 'blue', 'green' and 'orange' colours represent polydispersity indices of $N_w/N_a = 1.02$, 1.2 and 2.0 respectively.

3.2b. In addition we have also plotted the corresponding curves for cylinder geometries (with $H = 1/2R$, $K = 0$) and for saddle like geometries where $H = 0$ and $K = -1/R^2$. Comparing these curves further confirms the claim that the geometry essentially governs the functional dependence of the thickness h on the grafting density σ, while the polydispersity mainly affects the prefactor. While the curves decrease monotonically as a function of $1/R$ in spherical and cylindrical geometries, the curves for saddle points show qualitatively different behaviour, they resemble parabolae centered at zero. This is due to symmetry, as grafting polymers on either side of such a geometry is equivalent.

Continuing our examination, we explore the behavior of the projected chain end distribution, $\varepsilon(z)$, for different curvatures, with $\sigma w/a$ held constant (see Fig. 3.3). The impact of polydispersity on the chain end density profile becomes particularly noticeable in convex geometries. Notably, the projected chain end distribution in highly polydisperse brushes with $N_w/N_a = 2.0$ differs qualitatively from those at lower polydispersities: It no longer features a peak at some distance from the substrate, but decays monotonically. Interestingly, the most probable distance between chain ends and substrate depends on the curvature in a nonmonotonous way for polydispersities of 1.2 and 1.02: It first increases, and then decreases again. This behavior stems from the concurrent reduction in brush thickness with increasing curvature, and the displacement of chain ends closer to the substrate in convex configurations.

Compared to convex geometries, the curvature has a much smaller influence on the projected chain end distribution in concave geometries, even if the curvature radii are comparable (i.e., $R/aN_a = \pm 1$). Furthermore, as discussed earlier, the SST breaks down for concave geometries if the curvature radius becomes very small. In the range of physically reasonable curvature radii and grafting densities, the projected chain end distributions were not significantly affected by curvature.

In both Fig. 3.3 and Fig. 3.4, we see that the narrow distribution $N_w/N_a = 1.02$ leads to an apparent EEZ for high convex curvatures and high $\sigma w/a$. This outcome is a consequence of our truncation of the Schulz-Zimm distribution, which introduces a non-zero minimum chain length in the distribution. Without this truncation, the omitted chains would have populated this region, resulting in a region of highly reduced chain end density rather than a true EEZ. Further insights into EEZs and their characteristics are further explored in the following section.

In Fig. 3.4 the chain end distribution is plotted for a fixed geometry and varying $\sigma w/a$. Here, the effect of competing space can be seen more clearly. As the excluded volume or the grafting density increases, the chains find it preferable to extend their ends further away from the substrate independent of geometry or polydispersity.

In order to further quantify the difference between a given projected chain end density profile $\epsilon(z)$ and the corresponding profile $\epsilon_{\mathrm{pl}}(z)$ for planar brushes with the

same chain length distribution $P(N)$ and the same grafting density σ, we define a profile overlap parameter as follows:

$$\text{Overlap} = \int_0^1 \mathrm{d}x \, \min\left(\epsilon(x \cdot h)\,\frac{h}{\sigma}, \epsilon_{\text{pl}}\,(x \cdot h_{\text{pl}})\,\frac{h_{\text{pl}}}{\sigma}\right). \tag{3.22}$$

This parameter turns out to be a good measure for quantifying at which curvatures, grafting densities or excluded volume values we expect a significant departure from the planar chain end distribution. As shown in Fig. 3.5, the overlap is a decreasing function of the scaled curvature, $H(aN_a)(\sigma w/a)^{1/3}$. It reaches a limiting value for high curvature values. Moreover, the overlap increases with increasing polydispersity. This correlation is expected because the necessity for different chains to adjust their position in a progressively crowded environment diminishes if all chains have different length. Most importantly, the most significant changes to the projected chain end distribution occur in the range of $H(aN_a)(\sigma w/a)^{1/3} = 0 - 5$. We know from Fig. 3.2c that the ratio $h/(aN_a)(\sigma w/a)^{-1/3}$ is of order $1 - 2$ for all convex brushes investigated in this work. Hence we conclude that significant polydispersity effects occur in curvature ranges $H\,h \sim 0 - 10$, ranges which are experimentally relevant.

Lastly, we investigate the curvature elastic moduli of polymer brushes as a function of polydispersity. We should note that, generally, polymer brushes experience a force towards outwards bending, since the stretching energy of the brush polymers can be reduced if the brush surface is curved. This can be seen in Fig. 3.6a which shows the free energy as a function of curvature for different grafting densities and polydispersity index $N_w/N_a = 2$. The free energy decreases monotonically with increasing curvature.

The elastic moduli of the surface are defined in the planar limit $1/R \sim 0$. In this regime of slightly curved surfaces, the expression for the free energy per area is approximated by the so-called Helfrich Hamiltonian[122]:

$$\frac{F}{A} = \frac{\kappa}{2}\,(2H - c_0)^2 + \bar{\kappa}\,K + \frac{F_0}{A}. \tag{3.23}$$

Here κ is the bending modulus, $\bar{\kappa}$ is the Gaussian modulus, c_0 is the so-called spontaneous curvature and F_0 is an surface energy offset. To extract the bending and Gaussian moduli, we have determined the free energy as a function of H and K for a range of values of H and K in the vicinity of the planar limit, $1/R = 0$. Specifically, we used a 7×7 square grid of evenly space points in the (K, H) plane, in the range $H(aN_a)U_{\text{max}}^{1/2} \in [-0.06 : 0.06]$ and $K(aN_a)^2 U_{\text{max}} \in [-0.06 : 0.06]$. To assess the monodisperse limit we used a uniform step-like distribution (see next section) with vanishing width. The results were then fitted to Eq. (3.23). An example of a corresponding fitted free energy landscape is shown in Fig. 3.6b.

The Helfrich Hamiltonian was originally proposed for lipid bilayers. It is important to note that in the brush case, c_0 is just a fit parameter and does *not* correspond to a preferred curvature, since the true free energy decreases monotonically as a function of

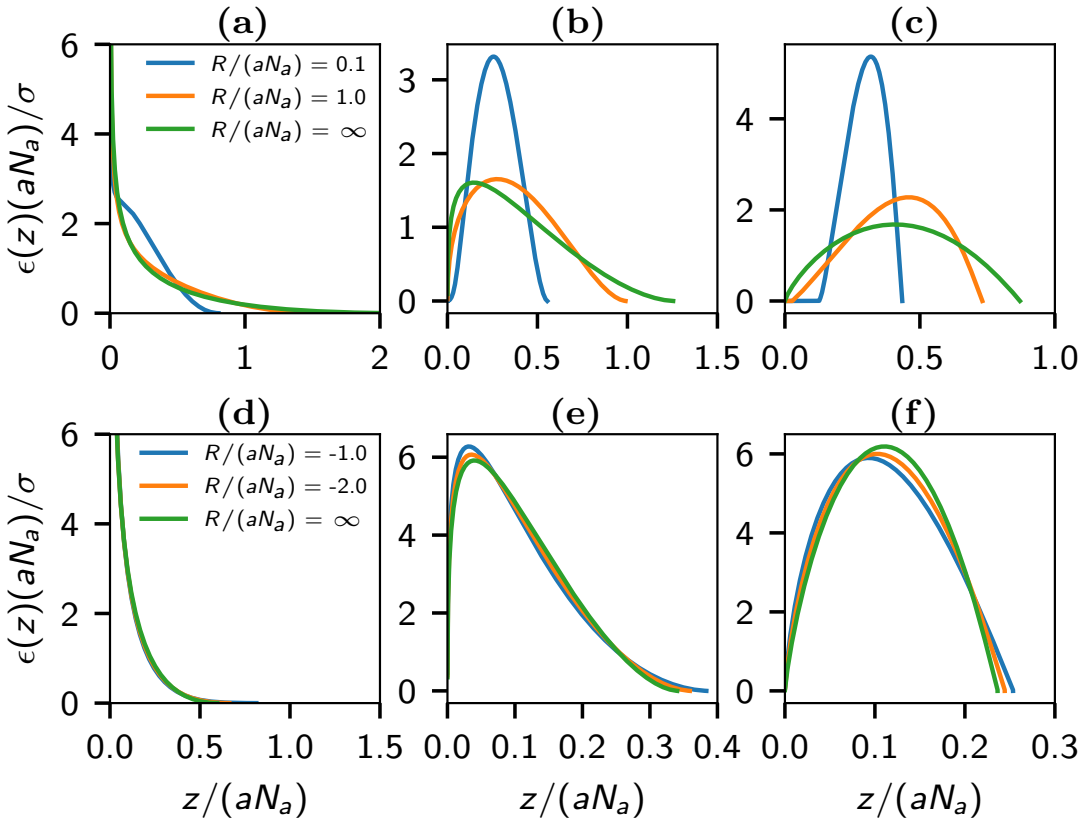

Figure 3.3: Chain end density profiles for brushes in convex (first row (a)(b)(c)) and concave (second row (d)(e)(f)) spherical geometry. For the convex case, $\sigma w/a = 1$, and for the concave case, $\sigma w/a = 0.02$. The first ((a)(d)), second((b)(e)) and third ((c)(f)) columns correspond to $N_w/N_a = 2$, 1.2, 1.02 respectively. The colour in each graph represents the radius $R/(aN_a)$ of the sphere whose value is displayed in the legend of the first column plot of each row.

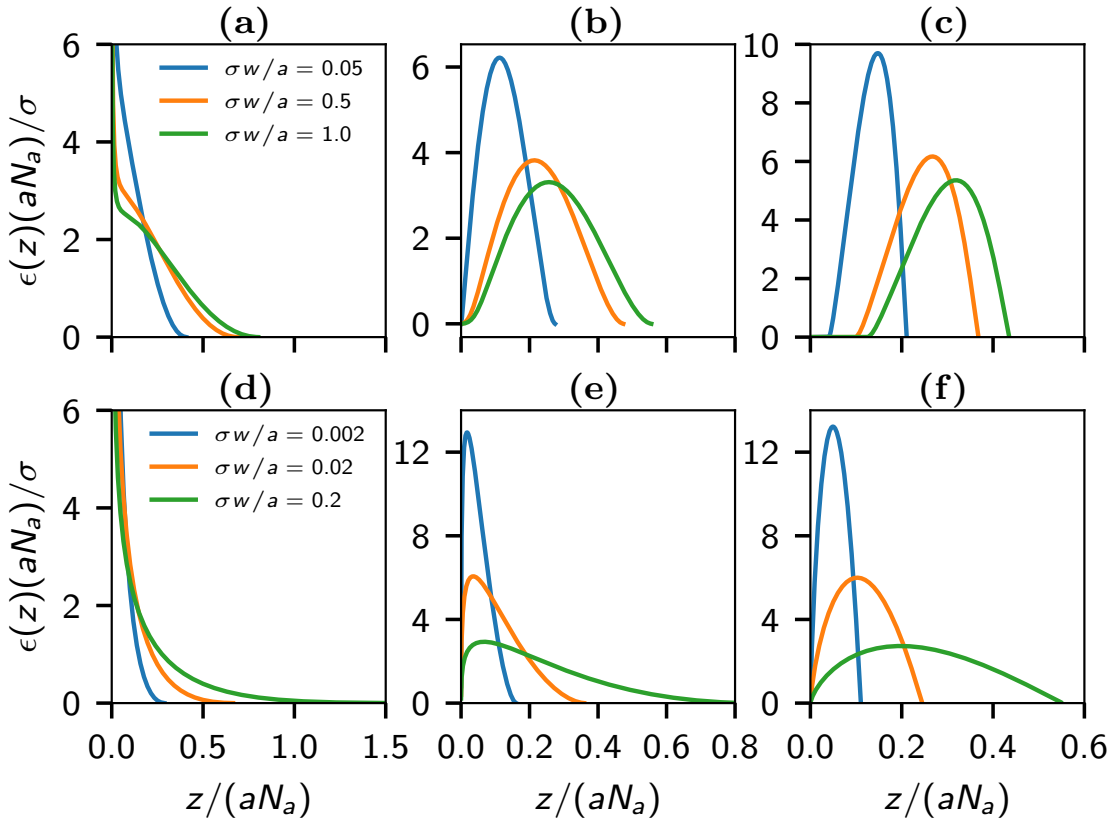

Figure 3.4: Chain end density profiles for brushes in convex (first row (a)(b)(c)) and concave (second row (d)(e)(f)) spherical geometry. For the convex case is $R/(aN_a) = 0.1$ and for the concave case $R/(aN_a) = -2$. The first ((a)(d)), second((b)(e)) and third ((c)(f)) columns correspond to $N_w/N_a = 2$, 1.2, 1.02 respectively. The colour in each graph represents the value of $\sigma w/a$ whose value is displayed in the legend of the first column plot of each row.

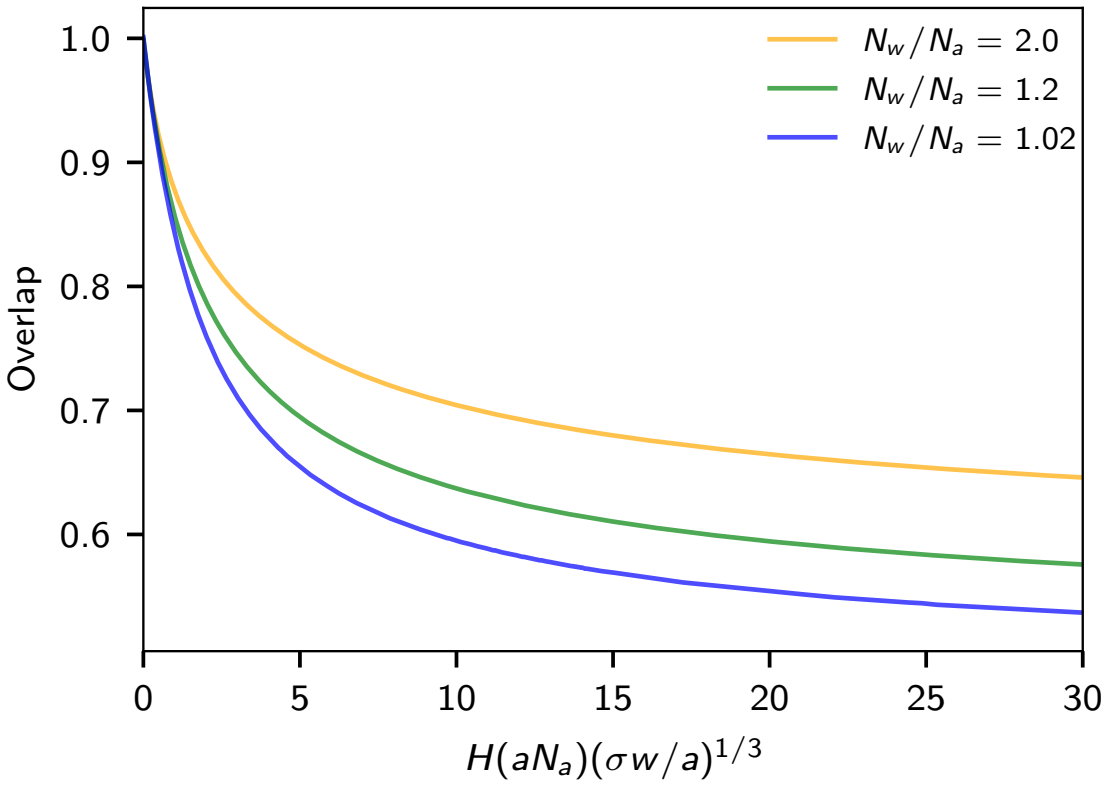

Figure 3.5: Overlap as defined in Eq. (3.22) for different polydispersity indices in spherical geometries.

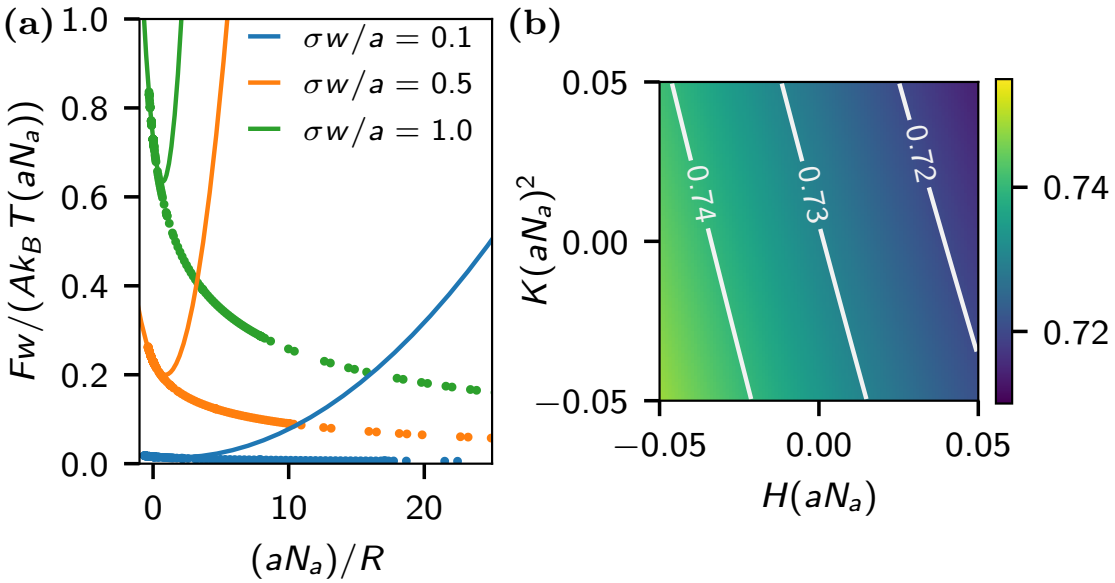

Figure 3.6: (a) Scaled free energy $Fw/(Ak_BT(aN_a)$ plotted against $(aN_a)/R$ for a spherical geometry and a polydispersity index of $N_w/N_a = 2.0$ for different values of $\sigma w/a$. The solid lines correspond to Eq. (3.23) with elastic parameters determined as described in the main text. (b) 2D plot of the free energy landscape $Fw/(Ak_BT(aN_a)$ for a Schulz-Zimm brush with a polydispersity index $N_w/N_a = 2.0$ and $\sigma w/a = 1.0$. The free energy data were calculated on a square grid (see text) and interpolated by the fit to Eq. (3.23).

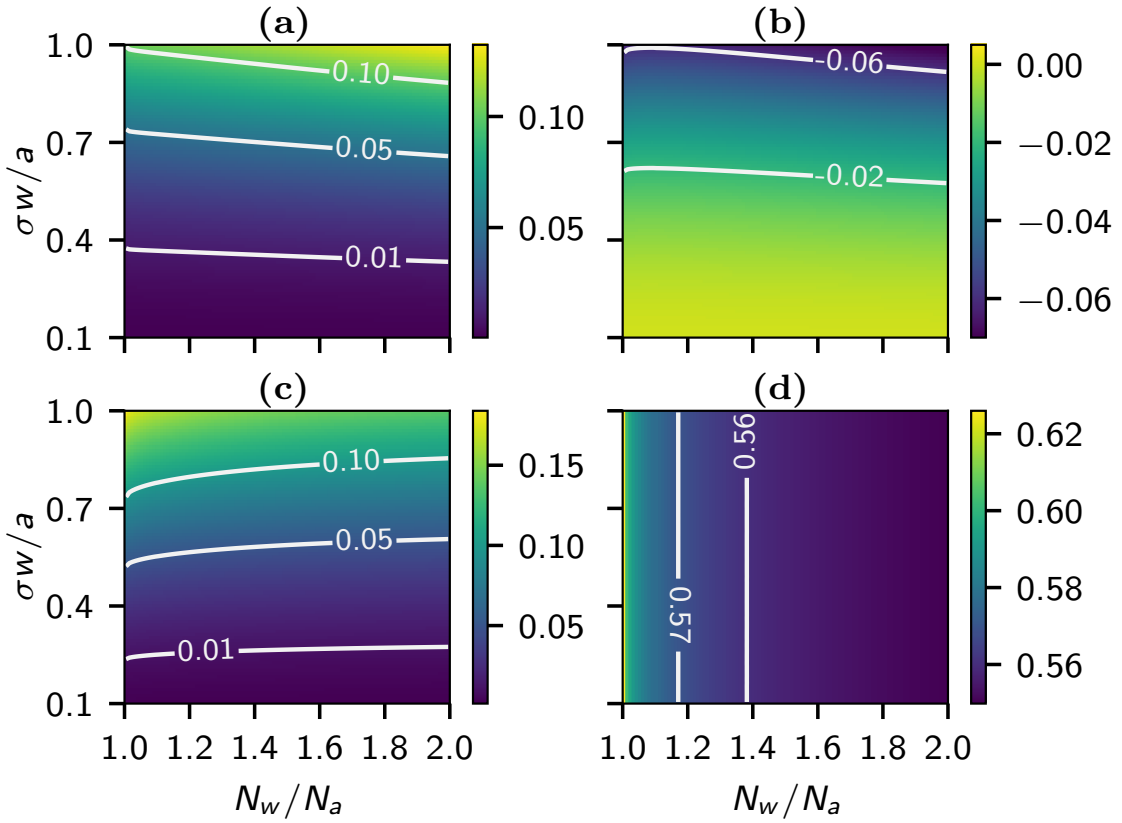

Figure 3.7: Elastic curvature moduli (a) $\kappa w/(k_B T(aN_a)^3)$ (b) $\bar{\kappa} w/(k_B T(aN_a)^3)$ (c) $\kappa c_0 w/(k_B T(aN_a)^2)$ (d) $-\bar{\kappa}/\kappa$ as a function of scaled grafting density $\sigma w/a$ and polydispersity index N_w/N_a for Schulz-Zimm brushes in good solvent.

curvature as discussed above. However, the parameter κc_0 still quantifies the tendency of a planar brush to bend.

In Fig. 3.7 , the scaled quantities $\kappa w/(k_B T(aN_a)^3)$, $\bar{\kappa} w/(k_B T(aN_a)^3)$, $\kappa c_0 w/(k_B T(aN_a)^2)$ and $-\bar{\kappa}/\kappa$ are plotted as a function of N_w/N_a and $\sigma w/a$. As expected, the absolute values of $\kappa w/(k_B T(aN_a)^3)$ and $\bar{\kappa} w/(k_B T(aN_a)^3)$ increase with increasing scaled grafting density $\sigma w/a$. It is surprising that these two quantities are largely insensitive to the polydispersity, although a small increase in both moduli is observed with increasing polydispersity. The latter can be explained by the fact that the more polydisperse brushes have a greater portion of small chain population which compete for space near the surface.

For comparison, we also show corresponding results for melt brushes in Fig. 3.8. They were determined in a manner identical to the good solvent case. In molten brushes, polydispersity has the opposite effect on the elastic moduli than in the good solvent case: Polydisperse brushes have lower stiffness than monodisperse brushes, because chains can rearrange more flexibly upon bending of the substrate if they have different length.

Both in the good solvent and the melt case, the ratio $-\bar{\kappa}/\kappa$ is independent of the grafting density (see Figs. 3.7d and 3.8d). This was analytically predicted for monodisperse brushes by Milner and Witten[119], and it still holds true in the polydisperse case, albeit with a change in the prefactor: The ratio decreases with increasing polydispersity. In the monodisperse limits, our values agree with analytical predictions by Milner and Witten[119], $-\bar{\kappa}/\kappa \approx 0.61$ for brushes in good solvent, and $-\bar{\kappa}/\kappa \approx 0.267$ for molten brushes. Furthermore, we also inspect the quantity κc_0 (Figs. 3.7c and 3.8c). It increases with increasing grafting density and decreases with increasing polydispersity, both for brushes in good solvent and for molten brushes. Thus the variety of chain lengths in polydisperse brushes generally reduces the driving force towards bending in the brushes.

3.3.2 Polydisperse Brushes with End Exclusion Zones

After addressing brushes characterized by chain lengths distributed according to the experimentally relevant Schulz-Zimm distribution, our attention now shifts to distributions with a truly non-zero minimum chain length, in order to investigate the emergence of an EEZ within polydisperse chain length distributions. For simplicity, we focus on uniform distributions and convex spherical geometries, noting that the findings can be generally extended to other convex geometries as well.

First we explore the emergence of an EEZ with thickness h_{eez} for a single uniform step-like chain length distribution defined by:

$$P(N) = \begin{cases} \dfrac{1}{N_{\max} - N_{\min}} & , N \in [N_{\min}, N_{\max}] \\ 0 & , N \notin [N_{\min}, N_{\max}] \end{cases}$$

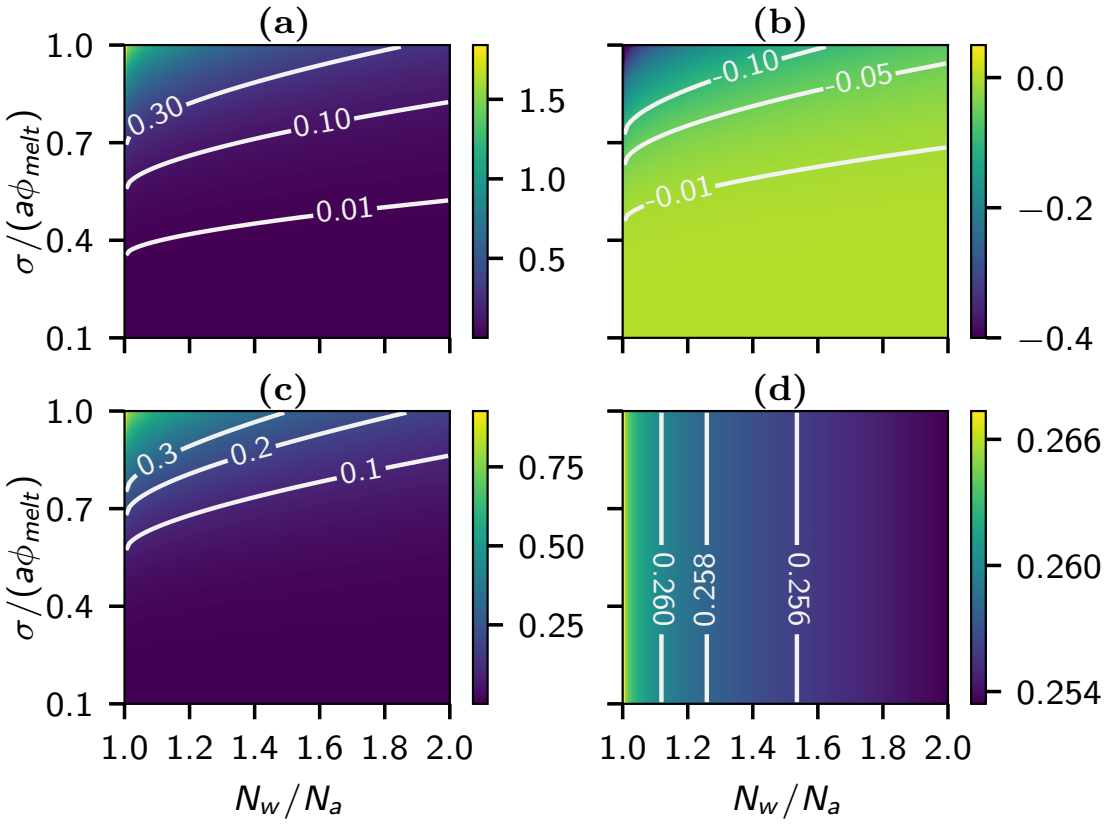

Figure 3.8: Similar to Fig. 3.7 for melt brushes (a) $\kappa/(\bar{\phi}_{\text{melt}}k_BT(aN_a)^3)$, (b) $\bar{\kappa}/(\bar{\phi}_{\text{melt}}k_BT(aN_a)^3)$, (c) $\kappa c_0/(\bar{\phi}_{\text{melt}}k_BT(aN_a)^2)$, (d)$-\bar{\kappa}/\kappa$. Plotted as a function of $\sigma/a\bar{\phi}_{\text{melt}}$ and the polydispersity index N_w/N_a for Schulz-Zimm brushes in good solvent.

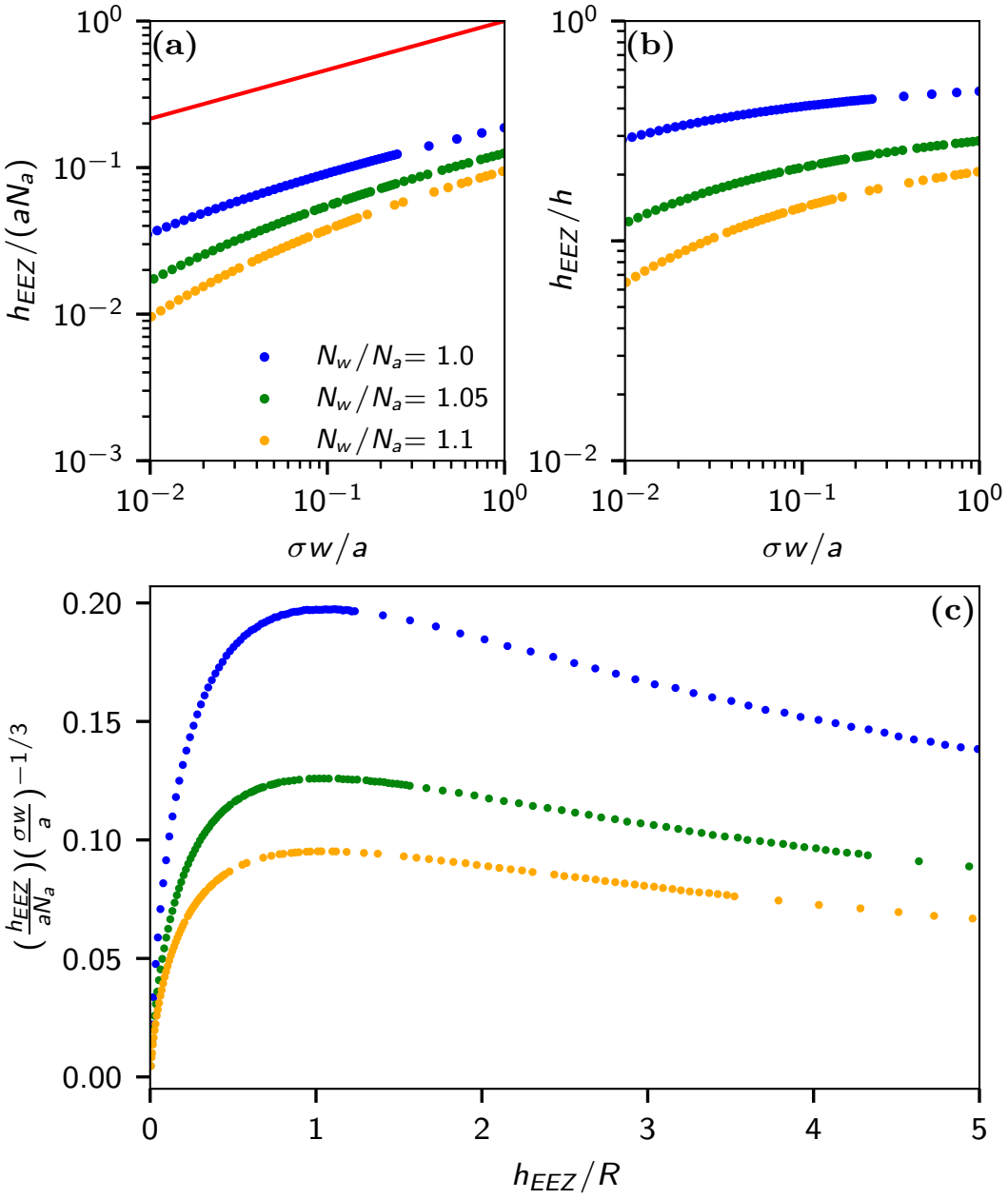

Figure 3.9: Thickness of exclusion zone $h_{EEZ}/(aN_a)$ (a) and the ratio h_{EEZ}/h (b) against $\sigma w/a$ for a spherically convex geometry with a radius of $R/(aN_a) = 0.1$ and polydispersity indices N_w/N_a as indicated. The red line in (a) is there for reference and represent a power law with an exponent of $1/3$. Panel (c) shows a scaling plot of the same quantities for spherically convex geometries for polydispersity indices $N_w/N_a = 1$ (blue), $N_w/N_a = 1.05$ (green), and $N_w/N_a = 1.1$ (orange).

with non-zero minimum chain length N_{min}, a maximum chain length N_{max}, an average chain length $N_a = \frac{1}{2}(N_{\text{min}} + N_{\text{max}})$ and a weight averaged chain length $N_w = \frac{1}{3}(N_{\text{min}}^2 + N_{\text{max}}^2 + N_{\text{min}}N_{\text{max}})$.

We examine three polydispersity indices, with one of them representing the monodisperse limit. Specifically, our focus lies in studying the EEZ thickness as a function of $\sigma w/a$ at a constant curvature. As anticipated, Fig. 3.9 shows an increase in the EEZ thickness with rising values of $\sigma w/a$. Common intuition suggests that a larger value of N_{min}, corresponding to a smaller polydispersity in our setup, results in a lower threshold of $\sigma w/a$ for the emergence of an EEZ. Furthermore, this implies that, for equivalent values of $\sigma w/a$, the thickness of such a region would be larger for larger N_{min}. This is indeed observed in Fig. 3.9a. Another noteworthy observation is that the EEZ thickness initially grows rapidly, but for later values of $\sigma w/a$, it appears to increase at the same rate as the thickness of the entire brush, which is demonstrated in Fig. 3.9b.

Just like in the Schulz-Zimm distribution. we know from the scaling properties of the SST equations (Appendix 3.7.5) that it is possible to identify hidden scaling laws, i.e., the quantity $(h_{EEZ}/aN_a)\,(\sigma w/a)^{-1/3}$ can be written as a unique function of h_{EEZ}/R. This function is shown in Fig. 3.9c. As it can be deduced the scaling behaviour is different than the scaling behaviour observed in Fig. 3.2c, albeit for higher values of h_{EEZ}/R or h/R their scaling behaviour appears similar.

Inspired by these results, it appears that one can also attempt to unconventionally place the EEZ by choosing an appropriate chain length distribution. One possibility for example would be to place the EEZ away from the substrate, perhaps somewhere in the middle of the polymer brush. To test this idea, we employ the following chain length distribution:

$$P(N) = h_0\,\theta(N_0 - N) + h_1\,\theta(N - N_1)\theta(N_2 - N), \tag{3.24}$$

with $N_0 = 0.29$, $N_1 = 0.91$, $N_2 = 1.28$ and the average chain length $N_a = 1$. h_0 and h_1 are chosen so that 10 % of the chains have chain lengths below N_0 and the rest of the chain lengths are between N_1 and N_2. The rationale behind this choice of chain length distribution is that the ends of chains of size N_0 would mark the beginning of the EEZ, while the ends of chains of size N_1 would determine the end of it. We would thus expect an EEZ to occur in some interval $z \in [z_1, z_2]$, which is apriori unknown. Fig. 3.10 shows that this is indeed the case. We can identify a region where chain ends of shorter chains are located (orange), an EEZ which is devoid of chain ends, and a region containing chain ends of larger chains (blue).

3.3.3 Designing chain end density profiles

In practice, another useful quantity one would like to specify instead of the chain length distribution, would be the chain end density. This could be interesting in the case of end-functionalized brush polymers, where the chain end distribution would

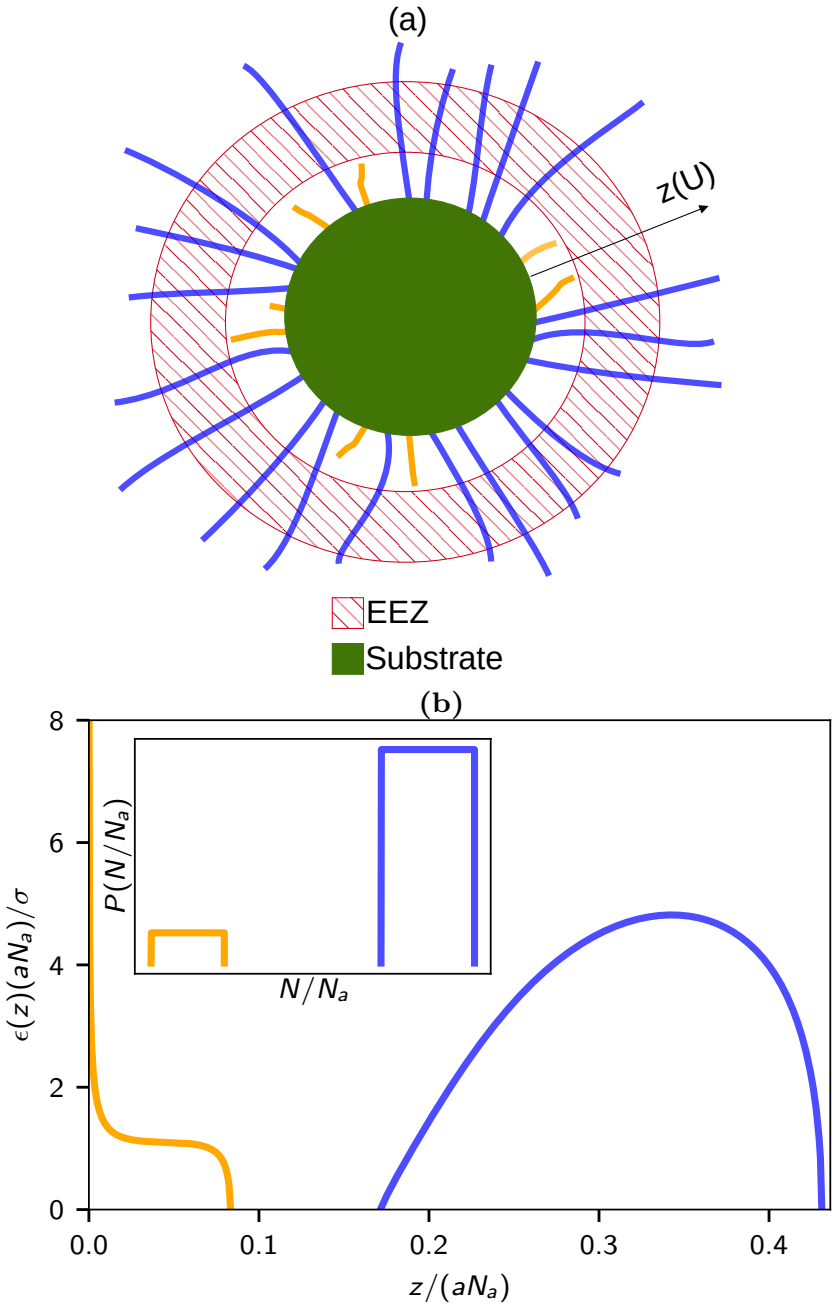

Figure 3.10: Projected chain end density against the distance from the substrate (b) for a spherically convex geometry with $\sigma w/a = 1$ and $R/(aN_a) = 0.1$. The inset represents the corresponding chain length distribution of the polymer brush. The orange color represent chains with a size below N_0 while blue represents chains with size above N_1. A cartoon representation (a) of the polymer brush in question is also shown where the color coding is the same as the plots below it.

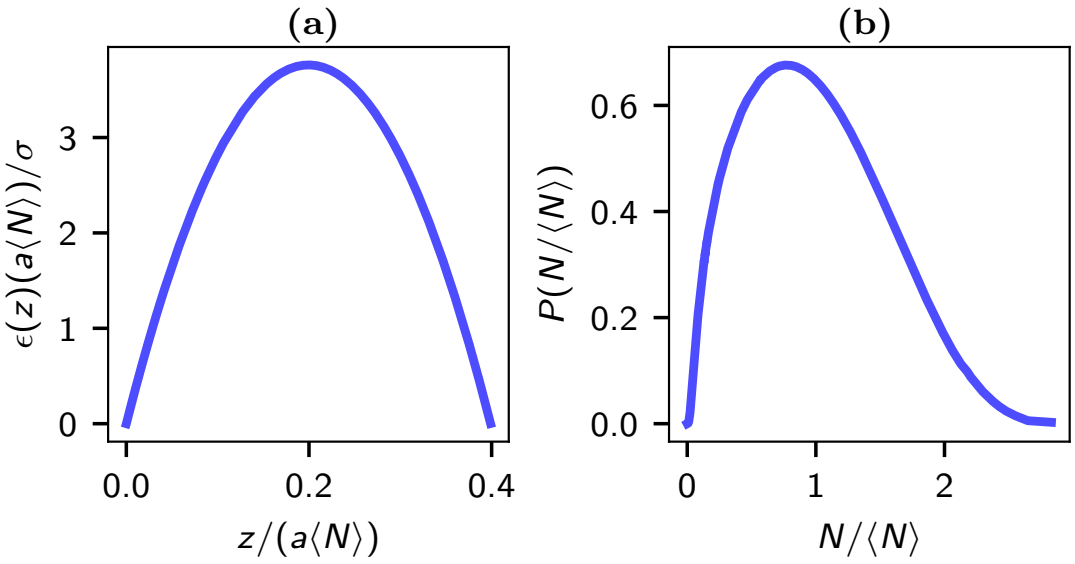

Figure 3.11: (a) Projected chain end density versus $z/(a\langle N\rangle)$ on a convex spherical geometry with $R/(aN_a) = 0.1$ and $\sigma w/a = 1$. The resulting chain length distribution is shown in (b).

correspond to the density distribution of functional entities. By specifying the chain end density and the geometry, it is possible to in return calculate self-consistently, the chain length distribution. The corresponding numerical scheme is given in the Appendix 3.7.7.

We demonstrate this procedure with the following example projected chain end density:

$$\epsilon\left((z/aN_o)(\frac{\sigma w}{a})^{-1/3}\right) = \left((z/aN_o)(\frac{\sigma w}{a})^{-1/3}\right)\left(1-\left((z/aN_o)(\frac{\sigma w}{a})^{-1/3}\right)\right), \tag{3.25}$$

where N_o is a reference chain length and not necessarily the average chain length $\langle N\rangle$. This projected chain end distribution can be implemented by choosing a chain length distribution as shown in Fig. 3.11.

However, one must note that not all chain end densities can be enforced and that the approximations of SST such as positive tension etc., need to be obeyed for the solution to be physical and to be in accordance with SST.

3.4 Conclusion

We have extended the mean-field theory model of Milner *et al.* [61, 94], which employs the Strong-Stretching limit, to curved substrates, for both convex and concave geometries for simple polydisperse linear polymers in a good solvent and the melt.

We have focused primarily on spherical geometries in good solvent and investigated the variations in the properties of the brushes composed of experimentally relevant chain length distributions such as the Schulz-Zimm distribution for different polydispersity indices. Among other, we found that in convex geometries, polydispersity has a strong impact on the properties of the chain end distribution as a function of grafting density and geometry, in particular in the range $H\,h \sim 0 - 10$. In contrast, the influence of polydispersity on the properties of concave brushes is much less pronounced in the regime where the theory can be applied.

Furthermore, we have investigated the bending modulus, the Gaussian modulus, and the spontaneous curvature – which characterizes the driving force towards bending – as a function of polydispersity and $\sigma w/a$ for surfaces decorated with such polymer brushes. We found that the moduli are remarkably unaffected by polydispersity. Interestingly, the (small) impact of polydispersity on the bending moduli for brushes in good solvent is opposite to that for molten brushes: Brushes in good solvent stiffen, whereas molten brushes become softer. On the other hand, the analysis of the spontaneous curvature indicates that polydispersity reduces the tendency of brushes to bend for both types of brushes.

Moreover we have successfully accounted for the emergence of End Exclusion Zones in distributions with non-zero minimum chain length. We have shown that End Exclusion Zones can appear in arbitrary positions in the brush, as long as the right chain length distribution, geometry and grafting density are chosen. Finally, we have also developed a method for engineering specific chain end distributions by manipulating the chain length distribution and geometry.

Although we have focused on the good solvent case, the same procedure can be applied to the melt case, as discussed in Section 3.2.2 (Eq. (3.11)) and Appendix 3.7.1. In the limiting case of a uniform distribution with vanishing width, we can compare our numerical results for the EEZ to those of Dimitriyev *et al.* [118]. The agreement is excellent. The comparison can be found in the supporting material.

3.5 Data

The data shown here along with the code that performs the iteration loops described in Appendix 3.7.6 and Appendix 3.7.7 can be found under the link: `https://gitlab.rlp.net/mgiannak/polydispersity-in-curved-substrates-sst`.

3.6 Acknowledgments

The authors are grateful to Le Qiao for valuable discussions and comments. This work was funded by the German Science Foundation (DFG) within Grant number 446008821, and the Agence Nationale de La Recherche, France. Partial funding was also received by the DFG within Grant number 429613790. M.G. is associate member of the integrated graduate school of the collaborative research center TRR 146 "Multiscale modeling of soft matter systems", grant number 233630050.

3.7 Appendix

3.7.1 Free energy

We begin with recapitulating the formal derivation of the SCF theory and the resulting SCF free energy. The starting point is the partition function of the system,

$$\mathcal{Z} \propto \prod_i \int \mathscr{D}\boldsymbol{r}_i \exp\left[-\frac{\mathcal{H}[\{\boldsymbol{r}_i\}]}{k_B T}\right] \tag{3.26}$$

The Hamiltonian $\mathcal{H}$ has been introduced in Eq. (3.3). The sum i runs over all chains in the system, which are taken to be distinguishable because they have different lengths N_i. After some field-theoretic transformations[48], the partition function is expressed as an integral over fluctuating fields ϕ_f and W_f,

$$\mathcal{Z} \propto \int \mathscr{D}\phi_f \int_{i\infty} \mathscr{D}W_f \; \exp\left(-\frac{\mathcal{F}[\phi_f, W_f]}{k_B T}\right) \tag{3.27}$$

with

$$\frac{\mathcal{F}[\phi_f, W_f]}{k_B T} = \mathcal{V}[\phi_f] - \int d\boldsymbol{r}\, W_f(\boldsymbol{r})\phi_f(\boldsymbol{r}) - \sum_i \ln(Q_i[W_f]). \tag{3.28}$$

Here $Q_i[W_f]$ is the single chain partition function of a chain of length N_i in the field $W_f(\boldsymbol{r})$,

$$Q_i[W] \propto \int \mathscr{D}\boldsymbol{r}_i \exp\left(-\mathcal{S}_i[\boldsymbol{r}_i; W_f]\right) \tag{3.29}$$

with $\mathcal{S}_i[\boldsymbol{r}_i; W_f]$ as defined by Eq. (3.5) in the main text. We note that, in Eq. (3.27), the field $W_f(\boldsymbol{r})$ is purely imaginary. The SCF approximation consists in approximating the functional integral in (3.27) by the extremum of the integrand[48]. This results in the free energy

$$F = -k_B T \ln(\mathcal{Z}) \approx \mathcal{F}[\phi, W], \tag{3.30}$$

where $\phi(\boldsymbol{r})$ and $W(\boldsymbol{r})$ are the fields that extremize the functional $\mathcal{F}$ given by Eq. (3.28). At the extremum (saddle point), the field $W(\boldsymbol{r})$ is real, $W(\boldsymbol{r}) = \delta\mathcal{V}/\delta\phi(\boldsymbol{r})$, and $\phi(\boldsymbol{r}) = -\sum_i \delta(\ln Q_i)/\delta W(\boldsymbol{r})$ is effectively the density of noninteracting graft chains i in the field $W(\boldsymbol{r})$. For brushes in solvent, the field $W(\boldsymbol{r})$ can be calculated from $W(\boldsymbol{r}) = \delta\mathcal{V}/\delta\phi(\boldsymbol{r})$.

The same formalism can also be applied to incompressible melts in a straightforward manner. The integral $\int \mathscr{D}\phi_f$ in Eq. (3.27) is then replaced by the constraint $\phi_f(\boldsymbol{r}) \equiv \bar{\phi}$ everywhere, and the field $W(\boldsymbol{r})$ which extremizes $\mathcal{F}$ is a Lagrange field that enforces this constraint. The interaction term $\mathcal{V}[\phi_f] = \mathcal{V}[\bar{\phi}]$ is a constant and can usually be omitted.

Now, turning to the SST approximation, the main new aspect compared to the SCF theory is that we apply a second saddle-point approximation to evaluate the integral in single chain partition function in Eq. (3.29). This allows us to derive an explicit expression for $\ln(Q_i)$:

$$\begin{aligned}
-\ln(Q_i) &\approx \min_{[\boldsymbol{r}_i]} \mathcal{S}[\boldsymbol{r}_i; W] \\
&= \int_0^{N_i} \mathrm{d}n \left(\frac{3}{2a^2} \left(\frac{\mathrm{d}z_i}{\mathrm{d}n}\right)^2 + W(z_i) \right) \\
&= \int_0^{N_i} \mathrm{d}n \, \frac{3}{a^2} \left(\frac{\mathrm{d}z_i}{\mathrm{d}n}\right)^2 + \big(U_{\max} - E(N_i)\big)\, N_i \\
&= \sqrt{\frac{3}{2a^2}} \int_0^{E(N_i)} \mathrm{d}U' \, \frac{\mathrm{d}z}{\mathrm{d}U'} \, \frac{E(N_i) + U_{\max} - 2U'}{\sqrt{E(N_i) - U'}}.
\end{aligned}$$

Here we have used Eqs. (3.6,3.8) in the second step, and (3.9, 3.34) along with the identity $N_i = N\big(E(N_i)\big)$ in the third step.

Based on the above expression for $\ln(Q_i)$, we can now calculate the last term in Eq. (3.30, 3.28). To this end, we sum over chains i grafted onto a patch with substrate area A, taking into account that Q_i only depends on the chain length N_i and that chains have the chain length distribution $P(N)$ and the grafting density σ.

$$\begin{aligned}
-\frac{1}{A} \sum_i \ln(Q_i) &= \sigma \int \mathrm{d}N \, P(N) \, \ln\big(Q(N)\big) \\
&= \int_0^{U_{\max}} \mathrm{d}U \, \frac{\mathrm{d}\sigma_c}{\mathrm{d}U} \sqrt{\frac{3}{2a^2}} \int_0^{U} \mathrm{d}U' \, \frac{\mathrm{d}z}{\mathrm{d}U'} \, \frac{U + U_{\max} - 2U'}{\sqrt{U - U'}} \\
&= \int_0^{U_{\max}} \mathrm{d}U' \, \frac{\mathrm{d}z}{\mathrm{d}U'} \sqrt{\frac{3}{2a^2}} \int_{U'}^{U_{\max}} \mathrm{d}U \, \frac{\mathrm{d}\sigma_c}{\mathrm{d}U} \, \frac{U + U_{\max} - 2U'}{\sqrt{U - U'}} \\
&= \int_0^{U_{\max}} \mathrm{d}U' \, \frac{\mathrm{d}z}{\mathrm{d}U'} \left((U_{\max} - U')\, \lambda(U') - \frac{1}{2}\Lambda(U') \right) \\
&= \int_0^{U_{\max}} \mathrm{d}U' \, \lambda(U') \left(\frac{\mathrm{d}z}{\mathrm{d}U'} \, (U_{\max} - U') + \frac{z(U')}{2} \right)
\end{aligned}$$

In the first step, we have set $U = E(N_i)$ and used Eq. (3.20); in the second step, we have exchanged the integration bounds; in the third step, we have used Eq. (3.35) and introduced the auxiliary quantity

$$\Lambda(U) = -\sqrt{\frac{6}{a^2}} \int_{U'}^{U_{\max}} \mathrm{d}U \, \frac{\mathrm{d}\sigma_c}{\mathrm{d}U} \sqrt{U - U'},$$

noting $\mathrm{d}\Lambda/\mathrm{d}U = \lambda(U)$ with $\Lambda(U_{\max}) = 0$, and in the last step, we have performed an integration by parts.

The second term in Eq. (3.30, 3.28) can be rewritten as

$$\begin{aligned} \int \mathrm{d}\boldsymbol{r} \, \phi(\boldsymbol{r}) \, W(\boldsymbol{r}) &= A \int_0^\infty \mathrm{d}z \, g(z) \, \phi(z) \, W(z) \\ &= A \int_0^{U_{\max}} \mathrm{d}U' \, \frac{\mathrm{d}z}{\mathrm{d}U'} \, \lambda(U') \, (U_{\max} - U'), \end{aligned} \tag{3.31}$$

where we have used Eqs. (3.6) and (3.13) in the last step.

Putting everything together, we get the following final result for the free energy per substrate area in SST approximation:

$$\frac{F}{A \, k_B T} = \mathcal{V}[\phi] + \frac{1}{2} \int_0^{U_{\max}} \mathrm{d}U' \, \lambda(U') \, z(U'), \tag{3.32}$$

which is listed as Eq. (3.18) in the main text. For melts, the first term, $\mathcal{V}[\phi]$ vanishes as discussed earlier. In good solvent, using Eq. (3.4) and $W(\boldsymbol{r}) = w\phi(\boldsymbol{r})$, it takes the form

$$\mathcal{V}[\phi] = \frac{1}{A} \frac{w}{2} \int \mathrm{d}\boldsymbol{r} \, \phi(\boldsymbol{r})^2 = \frac{1}{2A} \int \mathrm{d}\boldsymbol{r} \, \phi(\boldsymbol{r}) \, W(\boldsymbol{r}), \tag{3.33}$$

which can be simplified in the same way as (3.31), leading to Eq. (3.19) in the main text.

3.7.2 Derivation of self-consistent SST equations and additional auxiliary equations

In this section, we derive the Eqs. (3.12), (3.14), and (3.17) in the main text, as well as a few other useful auxiliary equations.

The starting point is Eq. (3.9) in the main text, which gives an expression for the tension in a chain i, $\mathrm{d}z_i/\mathrm{d}n$, as a function of the integration constant $E(N_i)$ and the potential $U(z_i)$ at the position z_i. We will use this expression to derive an relation between $N(U)$ and $z(U)$, and one between $\lambda(U)$ and $\mathrm{d}\sigma_c/\mathrm{d}U$. We recall that $N(U)$ is the length of chains with end monomers situated at distance $z(U)$ from the substrate, $\lambda(U)$ is the projected monomer density at $z(U)$, and $(\mathrm{d}\sigma_c/\mathrm{d}U)\,\mathrm{d}U$ is the number of chains grafted on a patch of unit area with chain ends located in the interval $[z(U), z(U + \mathrm{d}U)]$.

The derivation of the equation for $N(U)$ is straightforward. We set $U = E(N_i)$, $U' = U\big(z_i(n)\big)$, and drop indices i for simplicity. Then we can write

$$\begin{aligned} N(U) &= \int_0^{N(U)} \mathrm{d}n = \int_0^U \mathrm{d}U' \Big/ \Big(\frac{\mathrm{d}U'}{\mathrm{d}z} \cdot \frac{\mathrm{d}z}{\mathrm{d}n}\Big) \\ &= \sqrt{\frac{3}{2a^2}} \int_0^U \mathrm{d}U' \frac{\mathrm{d}z}{\mathrm{d}U'} \frac{1}{\sqrt{U-U'}}. \end{aligned} \tag{3.34}$$

We should note that, strictly speaking, Eq. (3.34) has no physical meaning for values of U inside an EEZ, as the EEZ does not contain any chain ends by definition. However, mathematically, the expression (3.34) is still perfectly defined, as $z(U)$ is defined everywhere. Hence we can use Eq. (3.34) to extrapolate the function $N(U)$ such that it is defined in the whole range of U.

To obtain an equation for $\lambda(U)$ as a function of $\mathrm{d}\sigma_c(U)/\mathrm{d}U$, we use the fact that chains of length N_i with conformation $z_i(n)$ deposit $1/\frac{\mathrm{d}z_i}{\mathrm{d}n}\big|_{z_i=z}$ monomers in the interval $[z, z+\mathrm{d}z]$. We sum over all chains with chain ends at positions $z_i(N_i) > z$, i.e., with characteristic integration constants $E(N_i) = U\big(z_i(N_i)\big) > U(z)$ (see Eq. (3.8)). This gives

$$\begin{aligned} \lambda(U) &= \sum_{i: z_i(N_i) > z(U)} \frac{1}{\mathrm{d}z_i/\mathrm{d}n}\Big|_{z_i(n)=z(U)} \\ &= \sqrt{\frac{3}{2a^2}} \int_U^{U_{\max}} \mathrm{d}U' \, \frac{\mathrm{d}\sigma_c(U')}{\mathrm{d}U'} \, \frac{1}{\sqrt{U'-U}}, \end{aligned} \tag{3.35}$$

where we have now set $U' = E(N_i)$.

Eq. (3.34) can be reversed via an Abel transform (see Appendix 3.7.4, using Eq. (3.47) and $z(0) = 0$), giving an integral equation for $z(U)$ in terms of the function $N(U)$:

$$z(U) = \sqrt{\frac{2}{3}} \, \frac{a}{\pi} \int_0^U \mathrm{d}U' \, N(U') \, \frac{1}{\sqrt{U-U'}}.$$

This equation is listed as Eq. (3.12) in the main text. Similarly, Eq. (3.35) can be reversed, giving (using Eq. (3.50))

$$\frac{\mathrm{d}\sigma_c}{\mathrm{d}U} = \sqrt{\frac{2}{3}} \frac{a}{\pi} \left(\frac{\lambda(U_{\max})}{\sqrt{U_{\max}-U}} - \int_U^{U_{\max}} \mathrm{d}U' \, \frac{\mathrm{d}\lambda}{\mathrm{d}U'} \frac{1}{\sqrt{U'-U}} \right),$$

or, (using Eqs. (3.51) and $\sigma_c(U_{\max}) = \sigma$)

$$\sigma_c(U) = \sigma - \sqrt{\frac{2}{3}} \frac{a}{\pi} \int_U^{U_{\max}} \mathrm{d}U' \, \frac{\lambda(U')}{\sqrt{U'-U}}.$$

These equations are listed as Eq. (3.17) and Eq. (3.14) in the main text.

For future reference, we also introduce an equation that expresses $z(U)$ as a function of $\lambda(U)$, and is obtained directly from (3.13):

$$z(U) = \begin{cases} \frac{H}{K}\left(-1+\sqrt{1-\frac{K}{H^2}\left(1-\frac{\lambda(U)}{\phi(U)}\right)}\right) & \text{for } K \neq 0 \\ \frac{1}{2H}\left(-1+\frac{\lambda(U)}{\phi(U)}\right) & \text{for } K = 0 \end{cases} \tag{3.36}$$

This equation cannot be applied for planar surfaces, but we also do not need it there.

Finally, we note that in numerical implementations, it is convenient to re-express the integrals in Eqs. (3.34) and (3.17) in terms of integrands that involve $z(U')$ and $\lambda(U')$ rather than their derivatives. Furthermore, to improve the numerical accuracy, we re-arrange the expressions Eqs. (3.12), (3.14), (3.17), and (3.34) such that integrands do not diverge in the vicinity of integration boundaries. This can be achieved by rewriting the equations as

$$z(U) = \sqrt{\tfrac{2}{3}}\tfrac{a}{\pi}\left(2N(U)\sqrt{U} - \int_0^U \mathrm{d}U' \, \tfrac{N(U)-N(U')}{\sqrt{U-U'}}\right), \tag{3.37}$$

$$\sigma_c(U) = \sigma - \sqrt{\tfrac{2}{3}}\tfrac{a}{\pi}\left(2\lambda(U)\sqrt{U_{\max}-U} + \int_U^{U_{\max}} \mathrm{d}U' \, \tfrac{\lambda(U')-\lambda(U)}{\sqrt{U'-U}}\right), \tag{3.38}$$

$$\lambda(U) = \sqrt{\tfrac{3}{2a^2}}\left(2\sigma_c'(U)\sqrt{U_{\max}-U} + \int_U^{U_{\max}} \mathrm{d}U' \, \tfrac{\sigma_c'(U')-\sigma_c'(U)}{\sqrt{U'-U}}\right) \tag{3.39}$$

and (using (3.48) and (3.51))

$$\begin{aligned} N(U) \;=\; & \sqrt{\tfrac{3}{2a^2}}\left(\tfrac{z(U)}{\sqrt{U}} + z'(U)\,\sqrt{U}\right. \\ & \left. + \tfrac{1}{2}\int_0^U \mathrm{d}U' \, \tfrac{z(U)-z(U')-z'(U)\,(U-U')}{\sqrt{U-U'}^3}\right), \end{aligned} \tag{3.40}$$

$$\begin{aligned} \frac{\mathrm{d}\sigma_c}{\mathrm{d}U} \;=\; & \sqrt{\tfrac{2}{3}}\,\tfrac{a}{\pi}\left(\tfrac{\lambda(U)}{\sqrt{U_{\max}-U}} - \lambda'(U)\,\sqrt{U_{\max}-U}\right. \\ & \left. - \tfrac{1}{2}\int_U^{U_{\max}} \mathrm{d}U' \, \tfrac{\lambda(U')-\lambda(U)-\lambda'(U)\,(U'-U)}{\sqrt{U'-U}^3}\right). \end{aligned} \tag{3.41}$$

3.7.3 Planar and monodisperse brushes

For planar brushes, we have $g(z) \equiv 1$ in Eq. (3.13) and recover the results of Milner *et al.* [94]. In particular, the integral in Eq. (3.14) can be evaluated explicitly and one obtains

$$\sigma_c(U) = \sigma\,(\,1 - \sqrt{1-U/U_{\max}}^{\,3}\,) \tag{3.42}$$

for brushes in good solvent and

$$\sigma_c(U) = \sigma\,(\,1 - \sqrt{1 - U/U_{\max}}\,) \tag{3.43}$$

for melt brushes. These results are independent of the chain end distribution.

We can also consider specifically the monodisperse case $N(U) \equiv N_o$. For planar and concave brushes, where no EEZ is present, Eq. (3.12) then gives

$$z(U) = \sqrt{\frac{8}{3}}\frac{a}{\pi} N_o \sqrt{U}, \tag{3.44}$$

and one recovers the familiar parabolic profile[61,70] $U(z) = U_{\max}(z/h)^2$ with $h = z(U_{\max})$. This result is independent of curvature. For convex brushes, an EEZ emerges, and chain ends are present ($\mathrm{d}\sigma_c/\mathrm{d}U = 0$) in a regime $U \in [0 : U_{\min}]$. In this regime, $N(U)$ must be determined self-consistently. It increases monotonically and can no longer be expressed in a simple analytical form[118].

For planar monodisperse brushes, we can combine Eqs. (3.44) with Eqs. (3.42) or (3.43) and calculate further properties of planar brushes such as, e.g., the chain end density:

$$\varepsilon(z) = \frac{\mathrm{d}\sigma_c}{\mathrm{d}U}\frac{\mathrm{d}U}{\mathrm{d}z} = \sigma\,\frac{z}{h^2}\begin{cases} 3\sqrt{1-(z/h)^2} & \text{solvent} \\ 1/\sqrt{1-(z/h)^2} & \text{melt} \end{cases} \tag{3.45}$$

3.7.4 Abel integral equations

Most integral equations appearing in the SST formalism have the form of Abel integrals[123]. For the convenience of the reader, we recapitulate the relations used in this work.

An integral equation of the form

$$f(x) = \int_0^x \mathrm{d}s\,\frac{\varphi(s)}{\sqrt{x-s}}$$

can be inverted[123] according to

$$\varphi(x) = \frac{1}{\pi}\left(\frac{f(0)}{\sqrt{x}} + \int_0^x \mathrm{d}\tau\,\frac{f'(\tau)}{\sqrt{x-\tau}}\right). \tag{3.46}$$

Specifically, if $\varphi(s) = \mathrm{d}\Phi(s)/\mathrm{d}s$, we have

$$\Phi(x) = \Phi(0) + \frac{1}{\pi}\int_0^x \mathrm{d}\tau\frac{f(\tau)}{\sqrt{x-\tau}}. \tag{3.47}$$

Eq. (3.47) can be derived from (3.46) by inserting $\Phi(x) = \Phi(0) + \int_0^x \mathrm{d}\tau\, \varphi(\tau)$ in (3.46), rearranging double integrals and then performing a partial integration. In addition, we can then rewrite $f(x)$ in terms of $\Phi(s)$ as

$$f(x) = \frac{\Phi(x) - \Phi(0)}{\sqrt{x}} + \frac{1}{2}\int_0^x \frac{\Phi(x) - \Phi(s)}{\sqrt{x-s}^3}. \tag{3.48}$$

This can be seen by considering the last term on the r.h.s. of the equation and performing a partial integration.

Likewise an integral of the form

$$f(x) = \int_x^1 \mathrm{d}s\, \frac{\varphi(s)}{\sqrt{s-x}},$$

can be inverted according to

$$\varphi(x) = \frac{1}{\pi}\left(\frac{f(1)}{\sqrt{1-x}} - \int_x^1 \mathrm{d}\tau\, \frac{f'(\tau)}{\sqrt{\tau - x}}\right). \tag{3.49}$$

For $\varphi(s) = \mathrm{d}\Phi(s)/\mathrm{d}s$, we have

$$\Phi(x) = \Phi(1) - \frac{1}{\pi}\int_x^1 \mathrm{d}\tau \frac{f(\tau)}{\sqrt{\tau - x}} \tag{3.50}$$

and

$$f(x) = \frac{\Phi(1) - \Phi(x)}{\sqrt{1-x}} + \frac{1}{2}\int_x^1 \frac{\Phi(s) - \Phi(x)}{\sqrt{s-x}^3}. \tag{3.51}$$

3.7.5 Rescaling the SST equations

An inspection of the SST equations (3.12)–(3.16) and the auxiliary equations (3.34) – (3.41) shows that their form is invariant if we rescale all quantities according to

$$U = \widetilde{U}\, U_{\max} \qquad N = N_o\, \widetilde{N} \qquad z = \widetilde{z}\, U_{\max}^{\frac{1}{2}}\, a N_o$$

$$\phi = \widetilde{\phi}\, U_{\max}/w \qquad \text{(Melt brushes: Set } w := U_{\max}/\bar{\phi}_{\text{melt}}\text{)}$$

$$\sigma = \widetilde{\sigma}\, \frac{U_{\max}^{\frac{3}{2}} a}{w} \qquad \frac{\mathrm{d}\sigma_c}{\mathrm{d}U} = \frac{\mathrm{d}\widetilde{\sigma}_c}{\mathrm{d}\widetilde{U}}\, \frac{U_{\max}^{\frac{1}{2}} a}{w} \qquad \lambda = \widetilde{\lambda}\, \frac{U_{\max}}{w}$$

$$H = \frac{\widetilde{H}}{a U_{\max}^{1/2} N_o} \qquad \epsilon(z) = \widetilde{\epsilon}(\widetilde{z})\, \frac{U_{\max}}{w N_o} \qquad F = \widetilde{F}\, \frac{a N_o U_{\max}^{\frac{5}{2}}}{w}$$

$$K = \frac{\widetilde{K}}{a^2 U_{\max} N_o^2}$$

Here N_o is an (arbitrary) reference chain length. Written in these rescaled quantities, the parameters a, w and $U_{\max}$ are replaced by unity in the equations. This means that, when solving the equations, it is sufficient to consider the case $U_{\max} = 1$, $a = 1$, $w = 1$, $N_o = 1$. The solutions for other values of, e.g., $U_{\max}$ and N_o, can be recovered by rescaling the results accordingly. We note that the grafting density, σ, is not an input parameter in the equations. Rather, $U_{\max}$ has to be tuned such that the desired value of σ is obtained.

3.7.6 Numerical Scheme

Here we demonstrate our numerical scheme for the solution of the SST equations given a chain length distribution and geometry $\widetilde{H}$ and $\widetilde{K}$ with the flow chart shown in Fig. 3.12. We use the rescaled equations introduced in Appendix 3.7.5.

The mixing of new and old values of $\widetilde{N}(\widetilde{U})$ is done via the λ mixing method described in Refs. [59, 124] . The value of $\mathcal{E}$ is defined as:

$$\mathcal{E} = \int_0^1 \mathrm{d}\widetilde{U} \left(\widetilde{N}_{new}(\widetilde{U}) - \widetilde{N}_{old}(\widetilde{U}) \right)^2. \tag{3.52}$$

We conclude with a few comments on numerical aspects of the algorithm:

- In practice, it is convenient to use Eqs. (3.37)-(3.41) for evaluating the Abel integrals. Nevertheless, the numerical (discretization) errors of these integrals may cause problems which can be reduced by some tricks.
- An additional check is that in the converged solution, the number of monomers above a unit area should be equal to:

$$\widetilde{\sigma} \int_0^{\widetilde{N}_{max}} \mathrm{d}\widetilde{N}' \, \widetilde{N}' \, \widetilde{P}(\widetilde{N}') = \widetilde{\sigma}\langle \widetilde{N} \rangle = \int_0^{\widetilde{h}} d\widetilde{z} \, \widetilde{\lambda}(\widetilde{U}).$$

3.7.7 Scheme for designing chain end densities

Here we demonstrate our numerical scheme for solving the SST equations given a chain end density and geometry $\widetilde{H}\widetilde{\sigma}^{1/3}$ and $\widetilde{K}\widetilde{\sigma}^{2/3}$ with the flow chart shown in Fig. 3.13.

In this case we define:

$$\mathcal{E} = (\tilde{\sigma}^{-1/3}) \int_0^1 \mathrm{d}\widetilde{U} \left(\widetilde{z}_{new}(\widetilde{U}) - \widetilde{z}_{old}(\widetilde{U}) \right)^2. \tag{3.53}$$

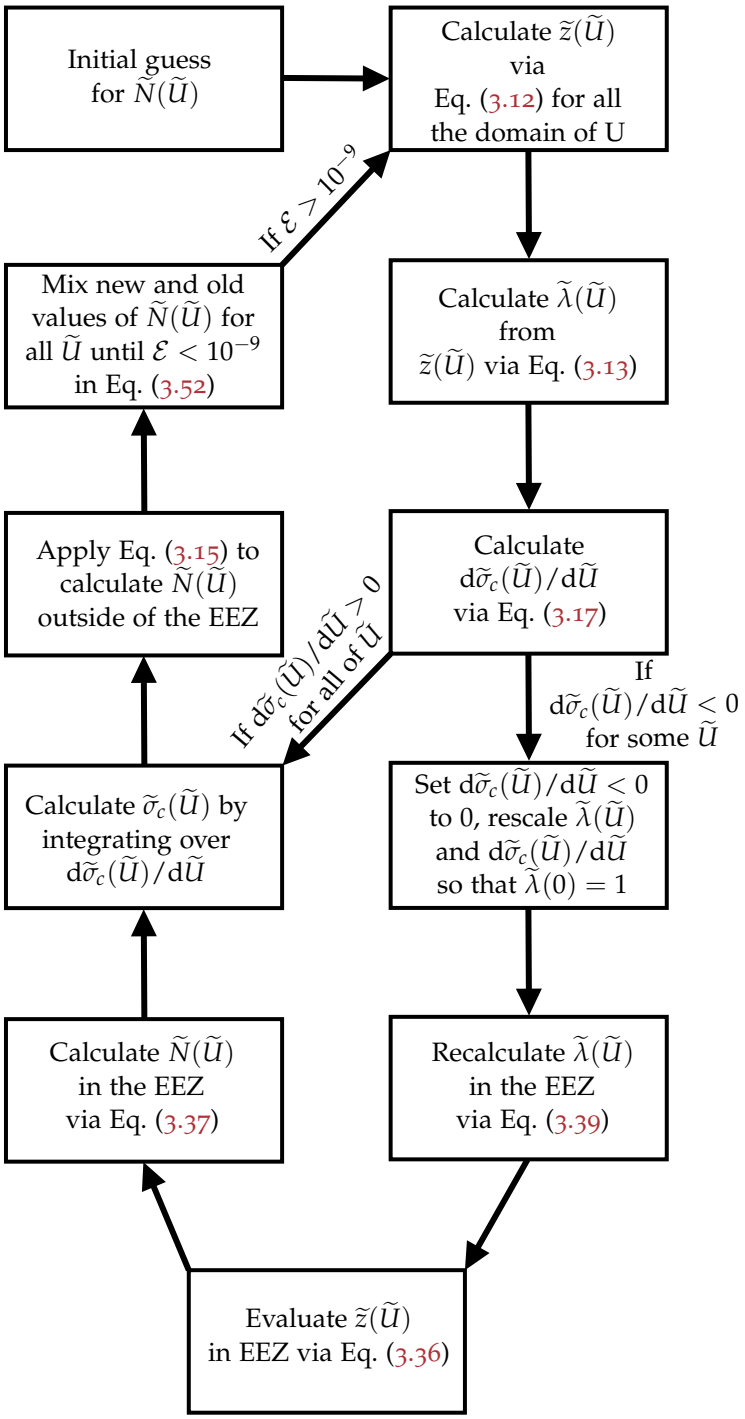

Figure 3.12: Numerical scheme used to solve the self-consistent equations given a chain length distribution.

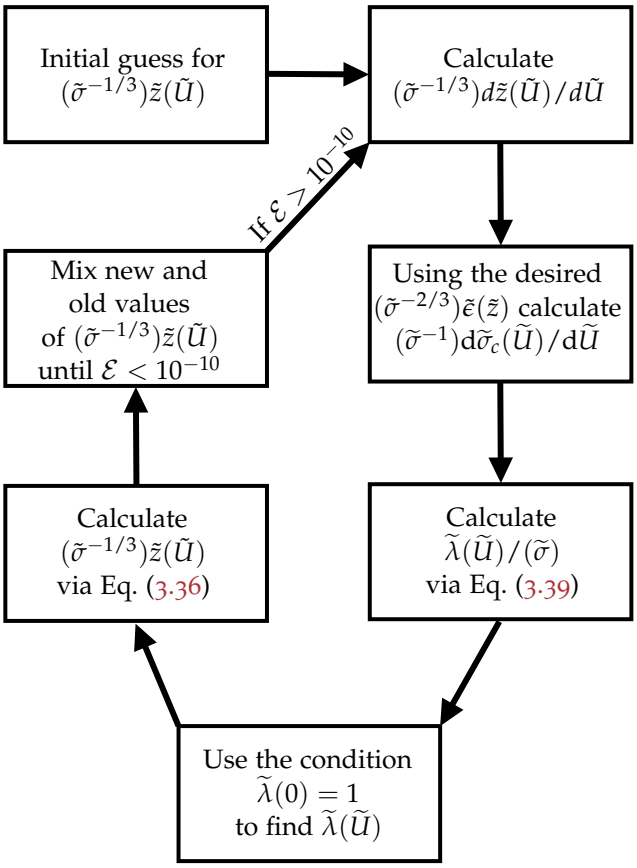

Figure 3.13: Numerical scheme used to solve the self-consistent equations given a projected chain end density.

3.8 Supporting Information

Here, we show a comparison of our results for the EEZ with results from Dimitriyev *et al.* [118] and two examples of shapes of "potentials" $U(z)$ inside the EEZ of brushes.

3.8.1 Test of EEZ results against literature data

To validate our SST approach, we tested it by comparing the results from SST calculations using our approach with published data from [118] where the authors explored the melt case in the monodisperse limit in various geometries. We do this by taking the limit of decreasing width for the uniform distribution to approximate the case of the monodisperse limit. We plot the results for the ratio between the EEZ thickness and the thickness of the brush versus the product of the thickness of the brush and the mean curvature Fig. 3.14. There appears to be good agreement.

3.8.2 Potentials in EEZ

In Fig. 3.15 we plot the potential against the distance for two different chain length distributions, where the EEZ is either adjacent or not adjacent to the substrate. As it can be seen, the potentials still monotonically increase with z as per the assumptions made in the model.

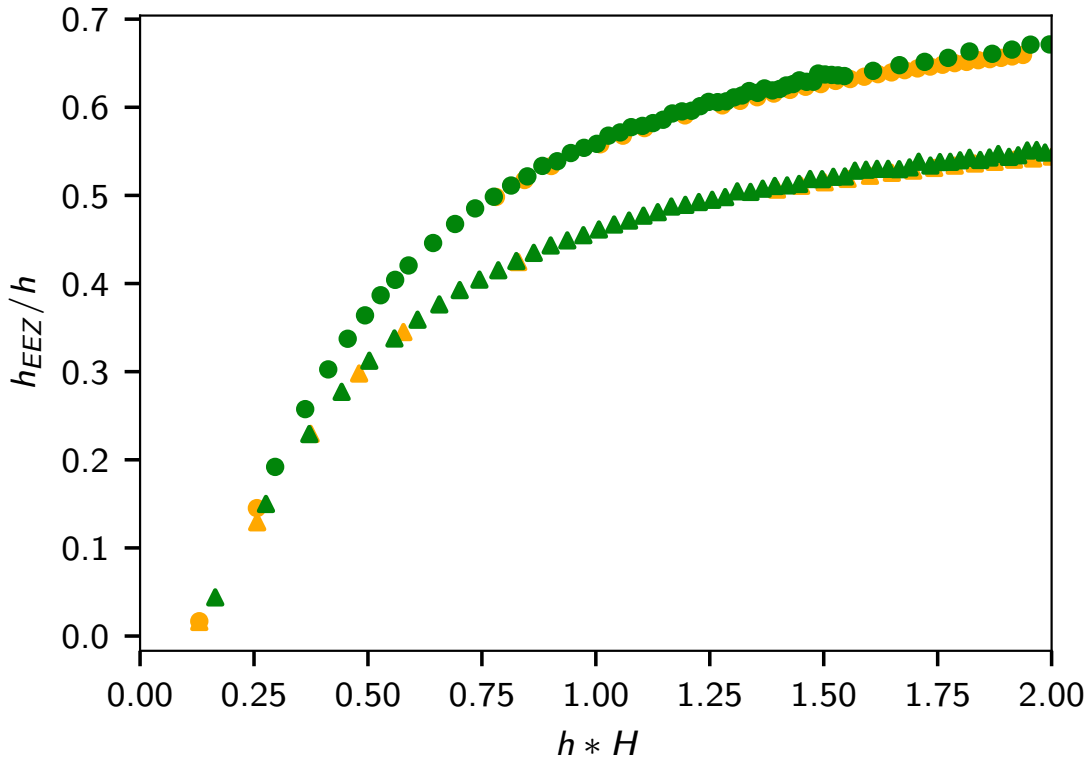

Figure 3.14: $h * H$ against h_{eez}/h of our results (orange) against Dimitriyev *et al.* (green) results for both spherical (●) and cylindrical (▲) geometries. These calculations were performed for collapsed melt brushes (with constant density), and not for brushes in good solvent as in the main text. The monodisperse brush was approximated by a brush with very narrow uniform distribution, i.e. $N_{min} = 0.9999$ and $N_{max} = 1.0001$.

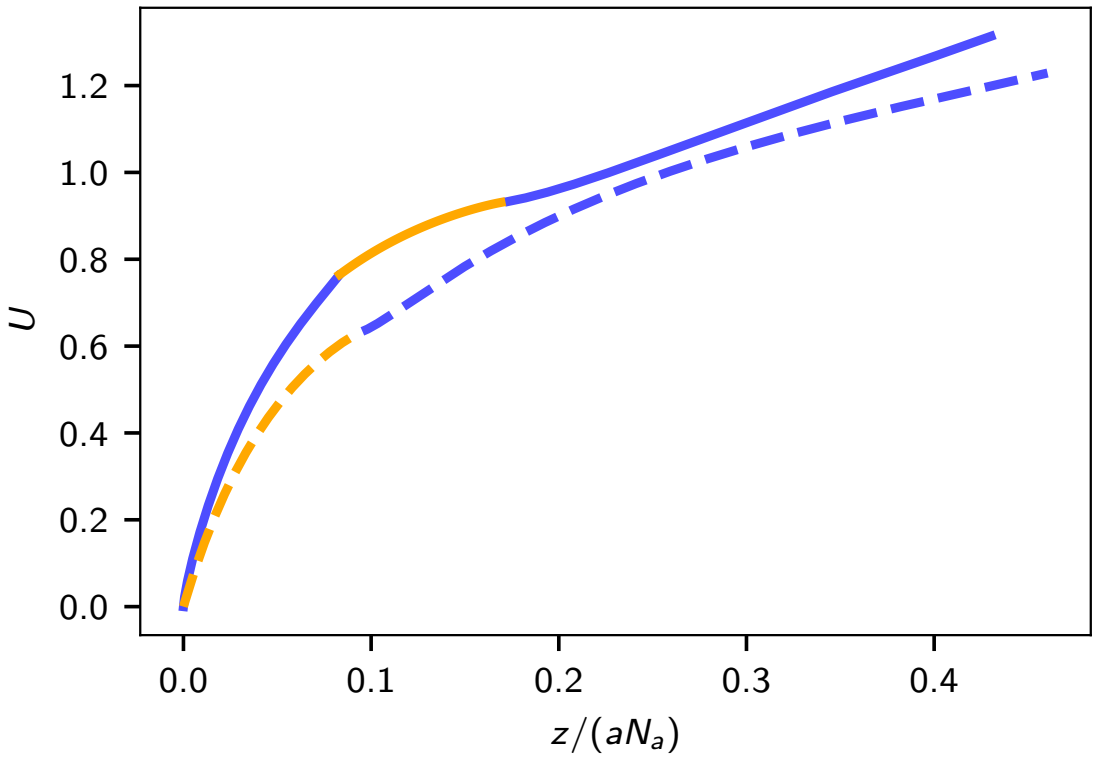

Figure 3.15: Plots of the potentials U against the distance from the substrate for spherically convex geometries with $\sigma w/a = 1$ and $R/(aN_a) = 0.1$ for two different chain length distributions. The 'solid' line represents the 'double step' distribution investigated in the main text, while the 'dashed' line represents the 'single step' distribution with polydispersity index of $N_w/N_a = 1.1$. The 'blue' and 'orange' regions in each plot, represent the potential for the brush outside and inside of the EEZ respectively.

4

AN EFFICIENT AND ACCURATE SCF ALGORITHM FOR BLOCK COPOLYMER FILMS AND BRUSHES USING ADAPTIVE DISCRETIZATIONS

Note: This chapter is a reproduction of the publication:

Qiao Le, Giannakou Marios and Friederike Schmid. An Efficient and Accurate SCF Algorithm for Block Copolymer Films and Brushes Using Adaptive Discretizations. *Polymers* **16** (2024), 1228.

Any additions are marked in violet, while removals are marked like ~~so~~.

Contributions to the publication:

- **Numerics:** The bulk of the SCF code was written by F. Schmid, while the adaptive discretization was implemented by Le Qiao and M. Giannakou implemented the polymer brush code.
- **Analysis and figures:** The analysis and figure production was made by Le Qiao for all figures except the figure on polymer brushes that was done by M. Giannakou.
- **Writing:** Le Qiao wrote most of the manuscript with minor contributions from M. Giannakou and revisions by F. Schmid.

4.1 Introduction

Self-assembled copolymer materials have diverse applications in both industry and daily life, due to the wide and complex spectrum of possible morphological patterns into which the copolymer molecules may assemble spontaneously. Self-consistent field (SCF) theory, which employs a simplified chain representation and a mean-field approximation to predict the spatial distribution of polymer segments, has proven to be a reliable and powerful tool for predicting the equilibrium morphology of many polymeric systems[11,125,126].

The SCF calculation iteratively computes space-dependent polymer density and associated potential fields from chain statistics propagators until the self-consistent condition is satisfied[46]. The chain propagators satisfy nonlinear modified diffusion equations in the variables space and chain contour ("time"), which have to be numerically solved using spectral or real-space methods. Pure spectral methods based on, e.g., Fourier series-based spectral solutions, have the advantage that they don't require a discretization of the chain contour. Matsen and coworkers have demonstrated their capability in accurately constructing morphology phase diagrams for periodic block-copolymer melts[11,127–129]. However, they demand a priori knowledge of morphology, assuming symmetry in the considered phase, limiting their applicability for discovering new phases[130–133]. To address these limitations, the pseudo-spectral method was introduced, which does rely on a discretization of the contour and switches between Fourier and real space representations of the system, utilizing the Fourier representation for the evaluation of gradient terms and the real space representation for the evaluation of nonlinear self-consistent fields[132,134]. In contrast, pure real-space methods discretize the diffusion equation within a simulation box and solve for the solution using finite difference schemes[130,135–138]. This approach is particularly advantageous for complex polymer systems characterized by symmetry breaking or non-periodic boundary conditions but can be computational expensive in three dimensions. A comprehensive exploration of the advantages and disadvantages of these methods can be found in Ceniceros and Frederickson's detailed review[133].

Our primary objective in this paper is to enhance the efficiency and accuracy of real-space methods, which heavily rely on the discretization of space/chain contours. The solution of modified diffusion equations in the SCF context typically employs lower-order finite difference, but unless the discretization is very fine, the accuracy and stability of SCF calculations suffer, especially when dealing with polymer systems containing sharp interfaces[139,140]. For instance, in simulating polymer films, where the substrate/air interface is often represented by a Dirichlet boundary condition and surface interactions with the polymer are introduced artificially through an external potential field, numerical inaccuracies can significantly affect the calculated free energy of the film[141]. Similarly, in the context of polymer brushes[136,142], ensuring proper attachment of the grafting end to the substrate involves fixing an end segment on one

space grid using a Dirac delta function as the initial condition for the modified diffusion equations[126,136,143]. Achieving convergence to an accurate SCF solution necessitates much finer contour discretization compared to free chains, demanding additional computational effort.

The trade-off between spatial discretization and computational efficiency presents a critical challenge, especially for systems requiring higher-dimensional calculations, such as cylinders and spheres in thin copolymer films[141,144,145], or particle-grafted chain polymer brushes with angular or radial-dependent morphology[143,146,147]. To address this challenge, our paper introduces a simple scheme that adaptively increases discretization in the spatial domain where external forces are present and refines the discretization in contour domain at the grafting point. The approach is similar in spirit to other, more sophisticated adaptive methods that have recently been proposed in the literature, such as the use of Oc-Tree data structures[148], polygonal meshes[149], or finite element methods[138,150]. By optimizing the spatial resolution according to the system's composition, our approach achieves very high accuracy while keeping computational resources low compared to uniform finite-difference grid methods. In the following sections, we evaluate and demonstrate the effectiveness of our adaptive scheme with two test cases of polymeric systems – block copolymer (BCP) films and polymer brushes.

4.2 Background: SCF equations for two test cases

We use the SCF theory for inhomogeneous systems of Gaussian polymers[151]. In the following, we just list the most important equations relevant for our test systems, and refer to the literature for details of the derivations[152].

4.2.1 Test case 1: Diblock copolymer film

We consider an incompressible melt of asymmetric AB diblock copolymer molecules with a degree of polymerization N, confined between two flat surfaces. We assume that the majority block A occupies a volume fraction f of each diblock copolymer chain, and both blocks share the same statistical segment length b. In the grand canonical ensemble, the free energy takes the form[141]:

$$\begin{aligned}\frac{F}{k_bT} =& -e^{\mu}Q+\rho_c\int d\mathbf{r}\left[\chi N\phi_A(\mathbf{r})\phi_B(\mathbf{r})+\frac{1}{2}\kappa N\left(\phi_A(\mathbf{r})+\phi_B(\mathbf{r})-1\right)^2\right]\\ &-\rho_c\int d\mathbf{r}\left[\omega_A(\mathbf{r})\phi_A(\mathbf{r})+\omega_B(\mathbf{r})\phi_B(\mathbf{r})\right]\\ &+\rho_c\int d\mathbf{r}H(\mathbf{r})N\left[\Lambda_A\phi_A(\mathbf{r})+\Lambda_B\phi_B(\mathbf{r})\right]\end{aligned} \tag{4.1}$$

where $\mu = \mu_0 + \ln G$ is the chemical potential, $G = \rho_c R_g^3$ is the rescaled dimensionless copolymer density in the bulk, $\rho_c = n/V$ is the average molecular number density with n being the total number of copolymer molecules and V the volume of the film, $R_g = \sqrt{Nb^2/6}$ is the radius of gyration of the noninteracting copolymer chain, serving as the spatial length unit throughout the paper, Q is the partition function of a single copolymer chain in the mean field of the other chains, $\phi_A(\mathbf{r})$ and $\phi_B(\mathbf{r})$ are the volume fractions of A- and B-segments at a given point $\mathbf{r}$, and χ is the Flory-Huggins parameter specifying the incompatibility of the two segments. The incompressibility of the BCP melt is ensured by the inverse of the isothermal compressibility parameter κ. The last term on the right-hand side of Eq. (4.1) describes the interaction energy with the substrate/interface, with $\Lambda_{A,B}H(\mathbf{r})$ being the surface field. We assume symmetric boundary wetting conditions; the surface interaction energies with A and B segments are Λ_A and Λ_B, respectively. The surface field,

$$H(\mathbf{r}) = \begin{cases} (1+\cos(\pi z/\epsilon)) & 0 \leqslant z \leqslant \epsilon \\ 0 & \epsilon \leqslant z \leqslant h-\epsilon \\ (1+\cos(\pi(h-z)/\epsilon)) & h-\epsilon \leqslant z \leqslant h \end{cases} \tag{4.2}$$

is applied within a depth of ϵ from the two surfaces, where h is the distance between the two surfaces. By finding the extremum of the free energy in Eq. (4.1) with respect to $\phi_{A,B}(\mathbf{r})$, we obtain the fields experienced by A and B segments:

$$\frac{\omega_A(\mathbf{r})}{N} = \chi\phi_B(\mathbf{r}) + \kappa\left[\phi_A(\mathbf{r}) + \phi_B(\mathbf{r}) - 1\right] + \Lambda_A H(\mathbf{r}) \tag{4.3}$$

$$\frac{\omega_B(\mathbf{r})}{N} = \chi\phi_A(\mathbf{r}) + \kappa\left[\phi_A(\mathbf{r}) + \phi_B(\mathbf{r}) - 1\right] + \Lambda_B H(\mathbf{r}) \tag{4.4}$$

The partition function for single chain is simply $Q = \int d\mathbf{r}\, q(\mathbf{r},s)q^\dagger(\mathbf{r},1-s)$, with $q(\mathbf{r},1-s)$ and $q^\dagger(\mathbf{r},s)$ being the partial partition functions for the first Ns and last $N(1-s)$ segments. Note that Q does not depend on the specific choice of s. The propagators $q(\mathbf{r},s)$ and $q^\dagger(\mathbf{r},1-s)$ obey the modified diffusion equation

$$\frac{\partial q(\mathbf{r},s)}{\partial s} = \Delta q(\mathbf{r},s) - \omega(\mathbf{r})q(\mathbf{r},s). \tag{4.5}$$

with initial conditions $q(\mathbf{r},0) = 1$ and $q^\dagger(\mathbf{r},1) = 1$. Here Δ represents the Laplacian, $\mathbf{r}$ denotes the spatial coordinate in the unit of R_g and $0 \leq s \leq 1$ represents the chain coordinate of the coarse-grained chain segment in the unit of chain contour length L_c. The field $\omega(\mathbf{r}) \equiv \omega_A(\mathbf{r})$ for $0 \leq s \leq f$ and $\omega(\mathbf{r}) \equiv \omega_B(\mathbf{r})$ for $f < s \leq 1$. The local concentration of A- and B- segments are simply

$$\phi_A(\mathbf{r}) = \frac{1}{\cancel{\rho_c}} e^{\mu} \int_0^f ds q(\mathbf{r},s)q^\dagger(\mathbf{r},1-s) \tag{4.6}$$

$$\phi_B(\mathbf{r}) = \frac{1}{\cancel{\rho_c}} e^{\mu} \int_f^1 ds q(\mathbf{r}, s) q^\dagger(\mathbf{r}, 1-s) \tag{4.7}$$

Starting with an initial guess of the field in Eq. (4.5), one solves the propagator $q(\mathbf{r}, s)$ and $q^\dagger(\mathbf{r}, 1-s)$. Next, one obtains the new local concentrations $\phi_A(\mathbf{r})$ and $\phi_B(\mathbf{r})$ from Eqs. (4.6) and (4.7), respectively. Finally, one uses these concentrations in Eqs. (4.3) and (4.4) to solve for the new fields and mixes the old and new fields according to a prescription of choice[59]. This is repeated until convergence to either a metastable or an equilibrium state.

4.2.2 Test case 2: Homopolymer brush

We consider a monodisperse brush solution in which n linear homopolymer chains with a degree of polymerization N are grafted onto a flat substrate at one end. In the canonical ensemble, the free energy of such a system is given by:

$$F/k_BT = \rho_o \int d\mathbf{r} \left[\frac{1}{2} \nu \rho_o \phi(\mathbf{r})^2 + \Lambda H(\mathbf{r}) \phi(\mathbf{r}) - \phi(\mathbf{r}) \omega(\mathbf{r})/N \right] - n(\ln(Q\cancel{\rho_o}/n) + 1) \tag{4.8}$$

where ν is the excluded-volume parameter and ρ_o is the bulk segment density. Similar to the BCP film system, the interactions between the segments and substrate where the chains are grafted are imposed by an external field $H(r)$ as in Eq. (4.2). The self-consistent equations are determined by the extremum of the free energy, leading to:

$$\omega(\mathbf{r})/N = \nu \rho_o \phi(\mathbf{r}) + \Lambda H(\mathbf{r}) \tag{4.9}$$

$$\phi(\mathbf{r}) = \frac{nN}{Q\cancel{\rho_o}} \int_0^1 ds\, q(\mathbf{r}, s) q^\dagger(\mathbf{r}, s) \tag{4.10}$$

$$Q = \rho_o \int d\mathbf{r}\, q(\mathbf{r}, 1) \tag{4.11}$$

The initial conditions for such a system are given by:

$$q(\mathbf{r}, 0) = 1 \tag{4.12}$$

$$q^\dagger(\mathbf{r}, 0) = \rho_o^{-1/3} \delta(z - g_p) \tag{4.13}$$

where g_p is the grafting point and δ is the Dirac delta function.

4.3 Adaptive discretization

We solve the diffusion equation using the semi-implicit Crank-Nicolson discretization scheme combined with the alternating direction implicit method (ADI)[153]. For simplicity,

we illustrate the method for the one dimensional diffusion equation. Provided the discretization points are arranged on a grid, the ADI extension to three dimensions is straightforward. In one dimension, the diffusion equation reads

$$\frac{\partial q(z,s)}{\partial s} = \frac{\partial^2}{\partial z^2} q(z,s) - \omega(z,s) q(z,s) \tag{4.14}$$

which can be discretized in s and z as

$$\frac{q_i^{m+1} - q_i^m}{\delta s_{m+1}} = (\Delta_z - \omega_i) \frac{q_i^m + q_i^{m+1}}{2}, \tag{4.15}$$

where $q_i^m \equiv q(z_i, s_m)$ with $m = \{1, N\}$ the contour steps in s with contour step size, $\delta s_m = s_m - s_{m-1}$, and $i = \{1, n_z\}$ the spatial steps in z with spatially varying discretization, $\delta z_i = z_i - z_{i-1}$. Taking the second-order approximation for the Laplacian Δ_z[154], we have $\Delta_z f_i / 2 \approx a_i f_{i-1} - b_i f_i + c_i f_{i+1}$, with $a_i = \frac{1}{\delta z_i (\delta z_i + \delta z_{i+1})}$, $b_i = \frac{1}{\delta z_i \delta z_{i+1}}$, and $c_i = \frac{1}{\delta z_{i+1}(\delta z_i + \delta z_{i+1})}$. Rearranging Eq. (4.15), we obtain

$$\begin{aligned} &- a_i \delta s_{m+1} q_{i-1}^{m+1} + (1 + b_i \delta s_{m+1} + \frac{\omega_i \delta s_{m+1}}{2}) q_i^{m+1} - c_i \delta s_{m+1} q_{i+1}^{m+1} \\ &= a_i \delta s_{m+1} q_{i-1}^m + (1 - b_i \delta s_{m+1} - \frac{\omega_i \delta s_{m+1}}{2}) q_i^m + c_i \delta s_{m+1} q_{i+1}^m. \end{aligned} \tag{4.16}$$

We can calculate the propagator q_i^{m+1} at step $m+1$ from the propagator q_i^m at step m. The key lies in choosing proper adaptive discretization tailored to the system, which enables gains in both computational time and accuracy.

In the thin film case, where the loss of accuracy mainly arises from the external potential added to mimic interactions with the substrate or air interface, we employ finer discretization only in the z direction where external force is present. We keep uniform contour discretization where $\delta s / L_c = 1/N$. Our approach involves adaptive discretization with a total of n_z grids, achieved through either a cosine function[138] or a step function. The former has a form of $\delta z_i = \frac{L_z}{2} \left[\cos(\frac{i-1}{n_z}\pi) - \cos(\frac{i}{n_z}\pi) \right]$ for $i = \{1, n_z\}$, providing continuous discretization. The latter uses a finer $\delta z_s = \frac{\epsilon}{\alpha_s n_z}$ near the surface ($z \leq \epsilon$ or $L_z - \epsilon < z \leq L_z$) while a coarser $\delta z_b = \frac{L_z - 2\epsilon}{(1-2\alpha_s) n_z}$ for the rest. The latter providing finer discretization Here, α_s represents the fraction of grids allocated to the surface region ϵ. Throughout this work, we refer to these adaptive schemes as "cos" and "step," respectively.

For polymer brushes, additional adaptive contour discretization turns out to be crucial. We utilize $\delta s_m = \left[\cos(\frac{m-1}{2N}\pi) - \cos(\frac{m}{2N}\pi) \right]$, $m = \{1, N\}$ to discretize the contour. Similar to the approach for thin films, we employ two Dirichlet wall boundaries in the z direction. The separation L_z are chosen to be greater than the brush height to ensure that the brush's free end is maintained. The grafting point of the polymer is located at a distance of $g_p = 0.05$ from the substrate. Initially, we employ a uniform

grid spacing of $\delta z_g = 0.001$ for $z \leq 2g_p$, utilizing $n_g = 100$ grids to ensure fine discretization at the grafting site. Subsequently, we gradually increase the discretization by $\delta z_i = \delta z_g + \frac{L_z - 2g_p}{2}\left[\cos(\frac{i-1}{2(n_z-n_g)}\pi) - \cos(\frac{i}{2(n_z-n_g)}\pi)\right]$, $i = \{1, n_z - n_g\}$.

4.4 Results

4.4.1 Block copolymer film

We first demonstrate the effectiveness of our adaptive discretization scheme in computing the free energy of BCP films, specifically focusing on lamellar-forming BCP films (with $f = 0.5$) as an example. Figures 4.1(a)-(c) illustrate the calculated free energy as a function of film thickness using three different discretization schemes.

In the case of uniform discretization, the energy curves diverge for varying discretizations, denoted by different grid numbers. These discrepancies become more pronounced for larger thicknesses due to the coarser discretization. In contrast, our adaptive scheme consistently generates the same free energy curves regardless of the number of discretization grids used. Although a minor discrepancy arises for larger thicknesses in the step adaptive case, the overall performance is still superior to that of the uniform case.

Fig. 4.1d illustrates the inaccuracies versus discretization, quantified by the shift in energy from the extrapolated energy at spatial discretization $\delta z \to 0$. To facilitate the comparison with the uniform case, the energy shift in the adaptive case is plotted versus the averaged discretization defined by $\delta z_{\text{av}} \equiv L_z/n_z$. In the uniform case, the energy shift can be fitted by a cubic polynomial, which converges to zero with increased discretization. As expected, the accuracy in the energy deteriorates more rapidly with coarser discretization when stronger surface interactions are employed. In contrast, the cos-adaptive scheme consistently produces highly accurate energy values for all tested discretizations, as evident in the data points overlapping on the zero-error baseline. While surface interaction slightly impacts the shift in energy for larger discretizations, it is inconspicuous compared to the uniform case.

Figure 4.1e plots the energy shift versus $\delta s/L_c$ for three different discretization schemes and various δz_{av}. The fact that all the curves collapse regardless of the discretization scheme and δz_{av} indicates that adaptive discretization of space does not require special treatment of δs. The numerical error caused by δs converges to zero when $\delta s/L_c < 10^{-3}$ for all three cases.

Our SCF calculations for lamellar BCP films show a significant improvement in accuracy with adaptive discretization, especially using the cos-adaptive scheme. This allows for coarser discretization, making SCF simulations more efficient and enabling the investigation of multi-layered structures in thicker films.

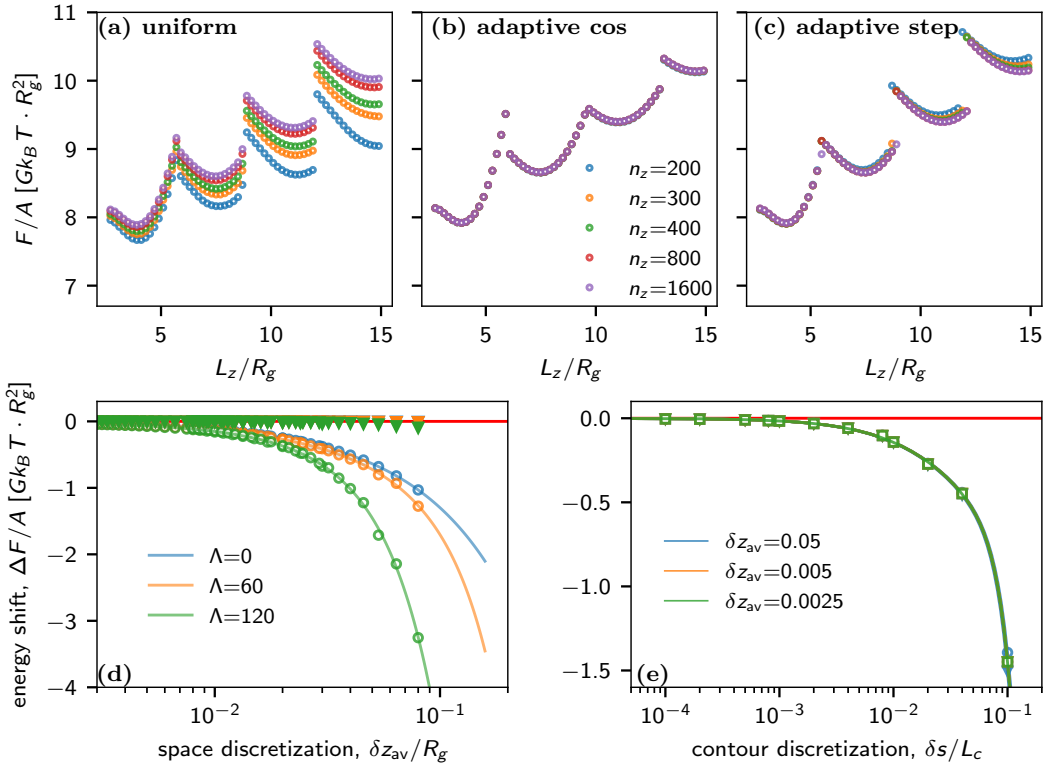

Figure 4.1: (a)-(c) SCF-calculated free energy, F/A, versus the thickness of the film, L_z/R_g, using three different discretization schemes described in the text. The data are generated using $f = 0.5$, $\mu_0 = 2.55$, $\chi N = 20$, $\kappa N = 25$, and $\Lambda_A = \Lambda_B = 60$. (d) Energy shift per area ($\Delta F/A$) as a function of averaged space discretizations δz_{av} for three different strengths of surface interactions $\Lambda_A = \Lambda_B = 0, 60$, and 120, where $\Delta F = F(\Delta z) - F(0)$ with $F(0)$ being the extrapolated value for $N_z = \infty$. Empty circle (○) and solid triangle (▼) symbols represent uniform discretization and adaptive "cos" discretization, respectively. The red horizontal line indicates $\Delta F = 0$. (e) Energy shift per area ($\Delta F/A$) as a function of contour discretizations $\delta s/L_c$ with $\Lambda_A = \Lambda_B = 60$. Empty circle (○), square (□), and triangle (▽) indicate uniform, cos-adaptive, and step-adaptive discretization. Solid lines of different colors in (d) and (e) are polynomial fits of ΔF using $f(x) = ax + bx^2 + cx^3$ for different surface interaction strengths and δz_{av}.

As a further example, we study thin films of sphere forming BCPs. In the bulk, prior SCF studies revealed tiny free energy differences between Hexagonally Close-Packed (HCP) and Face-Centered Cubic (FCC) packings, showing that the HCP phase is the true stable phase[129]. Here, we investigate whether this remains true for thin films. Unlike in the case of thin films with lamellar or cylindrical order, the study of sphere packings in thin films requires three dimensional calculations and large systems, which presents a substantial computational challenge.

Using the cos-adaptive scheme, we are able to compute the free energy of films containing three layers of spheres (Fig. 4.1(a)). The close packings of FCC and HCP correspond to ABC and ABA stackings of three layers as illustrated by the inset drawing in Fig. 4.2(a) and the SCF calculated density plot in Fig. 4.1(b) and (c). The free energy curves demonstrate that the HCP phase remains the stable phase in films, i.e., it has the lower free energy. Furthermore, they show that the HCP film has a smaller equilibrium thickness (free energy minimum at $h^* = 9.57R_g$) than the FCC film ($h^* = 9.60R_g$).

4.4.2 Homopolymer brush

Next, we consider polymer brushes. In this case, inaccuracies in SCF calculations arise not only due to spatial discretization errors, but the SCF results also turn out to suffer from contour discretization errors. Specifically, implementing the delta function to graft the chain onto the substrate demands a much smaller δs compared to free polymer chains. Additionally, as the system approaches the Strong-Stretching limit, which is characterized by significant chain interactions and brush thicknesses much larger than the radius of gyration of free chains, R_g, SCF calculations typically face convergence issues unless a very fine contour discretization is chosen.

Figure 4.3 (a) plots the energy shift as a function of averaged spatial discretization $\delta z_{\text{av}}/R_g$ for both uniform and adaptive spatial discretization and a fixed contour discretization of $\delta s/L_c = 0.0001$. Similar to the previous example of the thin film, the calculations perform badly in the case of uniform discretization as δz increases. This is particularly evident in scenarios with attractive walls where more segments are attracted to regions with external potential (blue curve). Conversely, cos-adaptive δz_{av} consistently yields much more accurate energy calculations, as illustrated by the fact that all filled symbols align with the zero-error baseline.

In Fig. 4.3 (b), we compare the energy shift relative to the average contour discretization δs_{av} for both uniform and cos-adaptive methods, considering various wall interactions, while maintaining a small uniform $\delta z/R_g = 0.002$ throughout the analysis. For the case of uniform δs, the energy shift converges to zero at around $\delta s/L_c = 10^{-5}$, contrasting with 10^{-3} in the free chain melt case. Moreover, the SCF calculation fails to converge beyond $\delta s/L_c \gtrapprox 10^{-3}$ under uniform conditions. However, the adaptive δs scheme is able to accommodate larger discretization values while consistently main-

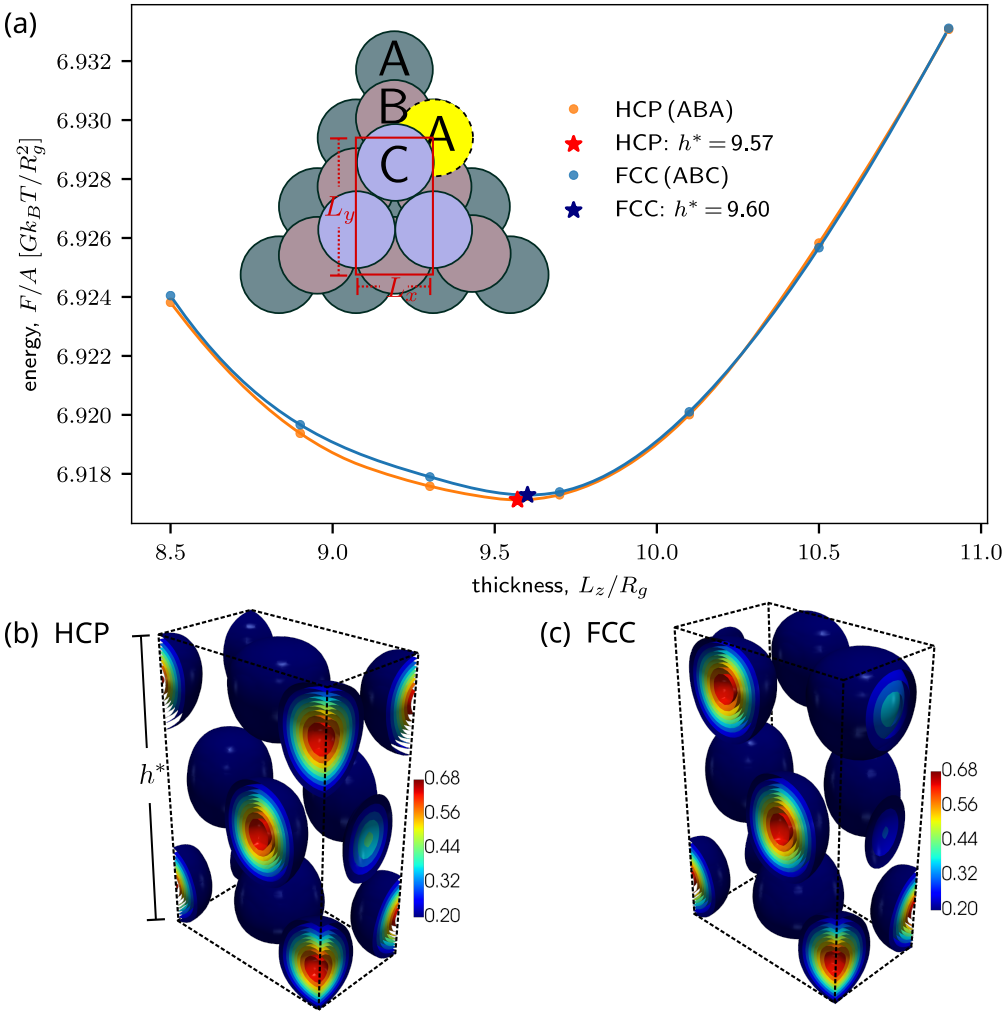

Figure 4.2: Spherical BCP film consisting of three layers. (a) SCF free energy per area, F/A, of the film as a function of film thickness, L_z. The data are generated using $f = 0.76$, $\mu_0 = 2.25$, $\chi N = 20$, $\kappa N = 25$, $\Lambda_A = 60$ and $\Lambda_B = 5$. The optimum thickness, which corresponds to the minimum free energy, is marked by $\star$. The inset drawing shows the grid of the FCC (ABC) and HCP (ABA) packing. The green rectangle shows the selected periodic cell for the SCF calculation. (b)-(c): 3D contour plot of the density of the B-block calculated with the SCF for HCP and FCC packings.

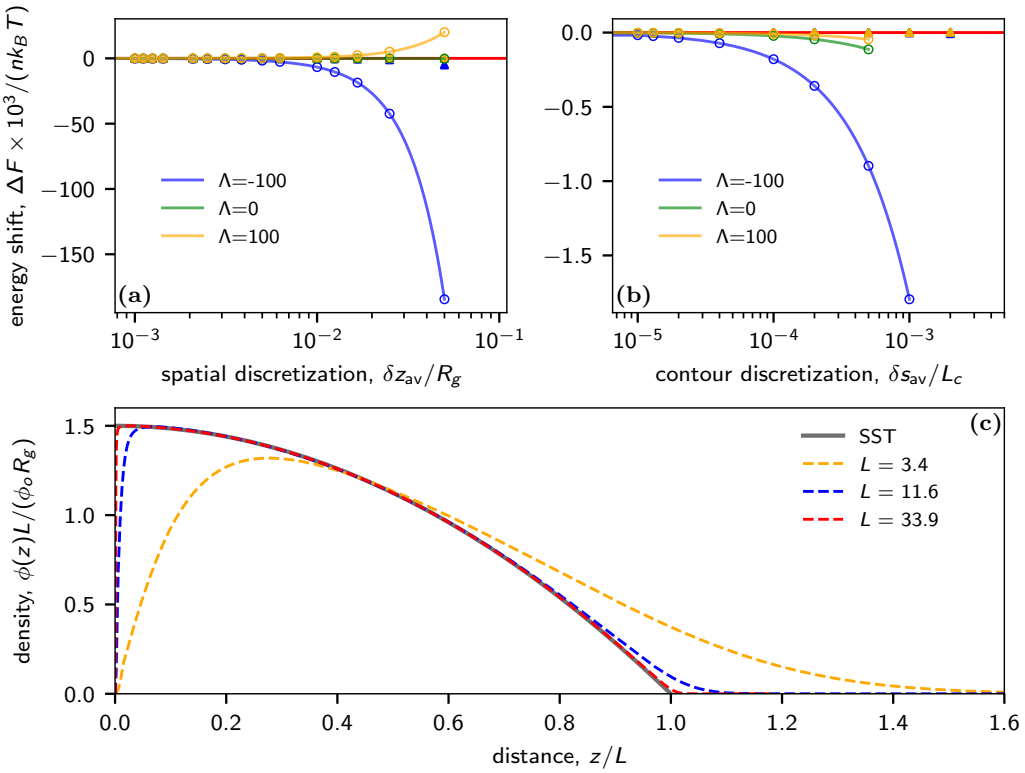

Figure 4.3: (a) SCF-calculated energy shift per polymer as a function of the averaged spatial discretization with a attractive ($\Lambda = -100$), repulsive ($\Lambda = 100$) and neutral ($\Lambda = 0$) interactions with the substrate. Here $\phi_0 = 2$ and $N\nu = 1$. (b) SCF-calculated free energy per polymer as a function of the contour discretization. In (a) and (b), empty circles correspond to uniform discretization in space and time, filled circles (in a) to adaptive discretization in space, empty triangles (in b) to adaptive contour discretization, and the red horizontal line indicates zero error $\Delta F = 0$. The solid curves in (a) and (b) are fits to the function $f(x) = ax + bx^2 + cx^3$. (c) Normalized segment density $\phi(z)L/\phi_0 R_g$ as a function of z/L (see text for definitions) at $\Lambda = 0$. The distance is rescaled by the thickness of the brush estimated by the strong stretching theory (SST).

taining significantly higher accuracy for different types of wall interactions, as shown by the empty triangles.

We further extend our calculations to the strong stretching limit. The Strong Stretching Theory (SST) predicts a parabolic density profile for the polymer[61,70]. The normalized concentration can be written as

$$\phi_{sst}(z) = \frac{3}{2}\phi_o \left(1 - \left(\frac{z}{L}\right)^2\right) \frac{R_g}{L} \tag{4.17}$$

where $\phi_0 = \frac{\sqrt{6}N^{1/2}n}{b\rho_o A}$ is the renormalization factor for the concentration and $\frac{L}{R_g} = \left(\frac{24N\nu}{\pi^2}\phi_0\right)^{1/3}$ is the absolute thickness of the brush.

The SCF-calculated densities are showcased in Fig. 4.3 (c). In the dilute regime, characterized by a small L, the SCF captures both the depletion region near the wall and the tail at the top of the brush. As the graft density escalates, the monomer density profile in the brush approaches the prediction of the strong stretching limit. Here, the depletion width narrows, accompanied by a sharp concentration increase from zero. Despite nearing the strong stretching limit, our SCF calculations using the adaptive scheme continue to deliver accurate results. This is evident from the close alignment between the SST theory and the red dashed curve, particularly notable at $L = 33.9$.

4.5 Conclusion

We have proposed a method to incorporate adaptive discretization schemes in real-space SCF calculations to improve both their accuracy and computational efficiency. By implementing finer discretization near surfaces, where strong polymer-substrate interactions occur, we effectively reduce numerical errors in the calculated free energy. Notably, our study shows that the cos-adaptive scheme consistently achieves superior accuracy, even with spatial discretizations larger than $\delta z_{\text{av}} > 0.1$, outperforming the uniform scheme by requiring discretization at least ten times smaller.

To illustrate the potential of our method, we have studied the morphologies of sphere-forming BCP films, focusing on the question whether the HCP or the FCC stacking is more favorable. Our analysis indicates that HCP stacking is the thermodynamically stable state in thin films, at least in the example studied by us (confinement between two attractive surfaces); however, the free energy differences between HCP and FCC stacked films are very small.

When looking at polymer brushes, we again find that adaptive spatial discretization significantly enhances the accuracy of SCF calculations. In addition, adaptive discretization of the contour length parameter turns out to be essential not only for obtaining accurate results, but for obtaining converged SCF solutions to begin with, if the total number of discretization points is low. Choosing finer values of δs_{av} enables capturing subtle features, such as the depletion region near the grafting point, which are easily

overlooked when using uniform discretization schemes, especially if δz is comparable to the depletion width. Importantly, our adaptive scheme alleviates the computational burden associated with brush simulations by allowing to choose larger values of the averaged discretization parameter δs_{av}, similar to that of ungrafted chains in the bulk, without sacrificing accuracy. This enhancement of efficiency is particularly noteworthy in view of the fact that the costs of SCF calculations are dominated by the costs of repeatedly solving modified diffusion equations in order to obtain the propagators q and $q^{\dagger}$. Furthermore, our adaptive scheme remains robust in the Strong Stretching limit, accommodating scenarios where inter-chain interactions exert substantial influence, resulting in brush heights $L \gg R_g$. While polymer brush SCF calculations in one dimension remain feasible with manageable computational costs even when using uniform discretization schemes, the integration of adaptive contour discretization and spatial discretization extends the computational capabilities, facilitating SCFT calculations in two or three dimensions for intricate morphologies[143,146,147,155,156].

In summary, our study highlights the crucial role of adaptive discretization schemes in advancing SCF calculations, delivering significant enhancements in accuracy and computational efficiency for various polymeric systems. The versatility of our simple approach is demonstrated by two illustrative examples, which showcase its applicability to problems involving interfaces and external potentials. In general the required accuracy of SCF calculations depends on the specific quantity of interest. In the present paper, we have mainly focused on the free energy, which helps to identify the true equilibrium phase from a set of competing candidate structures. In other applications, accurate predictions for density profiles of specific chain segments may be more important.

We have introduced two types of adaptive discretization schemes, adaptive spatial discretization and adaptive contour discretization. Adaptive spatial discretization will be useful in all situations where density or composition profiles vary strongly in selected regions in space. Adaptive contour discretization will be useful in situations where particularly strong variations of the propagator function, $q(\mathbf{r}, s)$, are expected for well-defined values of s – as is the case, e.g., for polymer brushes or for copolymers close to junction points that connect different blocks. In general, it would be desirable to couple spatial discretization and contour discretization. This is because the basic equation of any SCF iteration scheme, Eq. (4.5), has the form of a modified diffusion equation. In such cases, the contour step should not be chosen independent of the spatial discretization[157,158]. In fact, an upper bound for δs should typically scale with δz as $\delta s \sim \delta z^{1+\epsilon}$ with $\epsilon = 2$[158]. Here we have chosen δs sufficiently small, smaller than the upper bound. In future work, we will explore possibilities to couple the spatial and contour length discretization such that the contour discretization adjusts and becomes finer in regions of space where the spatial discretization is finer.

We should also note that the term "adaptive" in the present work refers to situations where a specific inhomogeneous discretization scheme is chosen at the beginning of an SCF calculation and not changed thereafter. In fact, we would strongly recommend

not to proceed otherwise, as changing the discretization in the middle of an SCF iteration loop will likely result in convergence problems. However, in algorithms that involve many successive SCF calculations, such as dynamic density functional (DDF) simulations, our scheme could also be used to set up dynamically adaptive grids that adjust to the current state of the polymer system.

To foster broader adoption and further refinement, we have made our SCF code publicly available (see below). The code has a modular structure. It provides both adaptive real-space methods and uniform discretization pseudospectral methods, and, in the latter case, options to perform dynamic density functional (DDF) simulations following the DDF models used in Refs. [159] and [160, 161]. It can be applied to arbitrary mixtures of linear multiblock-copolymers, and can easily be extended to other polymer architectures as well.

4.6 Data

Code to produce the data used in the manuscript is available at `https://github.com/leqiao/ADSCF.git`.

4.7 Acknowledgments

This research was funded by funded by the Deutsche Forschungsgemeinschaft (DFG, Germany), Grant number 248882694 (LQ) and 446008821 (MG). FS and LQ are members of and acknowledge partial funding from CRC 1552, Grant number 465145163 (project C02). Parts of this research was conducted using the supercomputer MOGON 2, which is a member of the AHRP (Alliance for High Performance Computing in Rhineland Palatinate, www.ahrp.info) and the Gauss Alliance e.V. The authors gratefully acknowledge the computing time granted on the supercomputer MOGON 2 at Johannes Gutenberg University Mainz (hpc.uni-mainz.de).

5

MICELLE FORMING LINEAR-DENDRITIC BLOCK COPOLYMERS: A THEORETICAL COMPARISON BETWEEN RANDOM HYPERBRANCHED AND PRECISE DENDRIMER POLYMER ARCHITECTURES

Note: This chapter is a reproduction of the publication:

Giannakou Marios, Oleg V. Borisov, and Friederike Schmid. Micelle Forming Linear–Dendritic Block Copolymers: A Theoretical Comparison between Random Hyperbranched and Precise Dendrimer Polymer Architectures. *Macromolecules* **58** (2025), 5872–5882.

Any additions are marked in violet, while removals are marked like ~~so~~.

Contributions to the publication:

- **Numerics:** The original code for solving the SCF equations was written by F. Schmid, while M. Giannakou has implemented their solution for polydisperse and tree-like architectures.
- **Analysis and figures:** The analysis and figure production was made by M. Giannakou with input from F. Schmid.
- **Writing:** M. Giannakou wrote the original draft which was then edited by F. Schmid, while O. V. Borisov suggested minor modifications to the final draft.

5.1 Introduction

Block copolymers have seen a long and sustained interest, both in experiments and theory, mainly due to their ability to self-assemble into a variety of nanoassemblies. This ability stems from the fact that the constituting blocks of the polymers are made from different types of often incompatible monomers that would like to demix, however due to the connectivity of the blocks they instead microphase separate[162]. In the melt regime, for example, even the simplest type of block copolymer, the linear diblock polymer, can self-assemble into a variety of periodic structures like lamellar, hexagonal, spherical, gyroid and more[13,162–165], with a periodicity determined largely by the macromolecular weight of the molecules themselves and thereby in the nanoscale range[162,166,167]. Such a capability is highly desired in a range of applications, such as surface pattering[168], thin films[169,170], filtration[171] and many more[172,173]. On the other hand, if a solvent is present that is selective toward one of the types of blocks, but poor toward the others, then the polymers may self-assemble into a variety of states depending on the concentration of the polymers, the molecular weight of the polymer, and other parameters[174]. Some common examples include spherical micelles, elongated micelles, worm-like micelles, or vesicles[13,14,175,176]. Such structures have been intensely investigated and have a wide range of applications, *e.g.*, in solubilization[177], stabilization[178], as nanoreactors[179], for drug encapsulation and delivery[180,181] and many others[182]. In the present article we focus on polymeric micelles, which hold promise as nanocarriers for encapsulating and transporting drugs. Micelles do this by incorporating the often hydrophobic drug[181] into their cores, thus solubilizing and protecting it from the highly complex environment *in vivo*[173]. In addition, as drugs need to circulate in the body for some time to reach their target sites, it is vital that the drug release from the nanocarrier happens over hours and not immediately[173] after administration. After entering the bloodstream, the nanoparticles find themselves in a highly dilute environment, much below the critical micelle concentration (CMC), whereupon they disassemble quickly and thus release their drug payload. Polymeric micelles, on the other hand, have a relatively low critical micelle concentration, which enhances their stability and slows down their disassembly to a large extent[183]. Moreover, rather than passively delivering drugs to a site, a more selective strategy involves actively targeting the sites by releasing the drug payload near or inside the affected cells. In this regard, polymeric micelles offer a variety of possibilities. For example, by introducing stimuli-responsive functional groups or monomers, it is possible to induce the release of a drug at a specific site using triggers such as light, temperature or pH[184]. Lastly, decorating micelles with specific moieties, such as ligands, enables targeting of desired sites that have specific receptors for said ligand[185,186], thereby minimizing the contact with healthy cells. Thus, polymeric micelles that serve as drug delivery vehicles should combine a variety of attributes. Fortunately, the vast array of synthetic protocols[187] has made it possible to construct a variety of exotic polymers. One such class, that combines multiple benefits and has

attracted considerable interest in recent years, is linear dendritic block copolymers (LDBCs). These polymers consist of a linear solvophobic block and a precise branched structure consisting of hydrophilic blocks, resembling a tree[26,188,189]. In solvent, they self-assemble into an even greater variety of structures than linear block copolymers[190,191]. Additionally, LDBCs offer several other advantages over linear block copolymers, including smaller micelle sizes, lower aggregation numbers and a greater number of chain ends available for functionalization[27]. However, synthesizing LDBCs with a precise branch structure – *i.e.*, with controlled macromolecular weight and branch generations – requires a multipot process[33,192]. This complexity results in relatively high production costs compared to simpler copolymers. An alternative approach which has gained popularity in recent years is to use their less precise cousins, the so-called linear hyperbranched block copolymers (LHBCs)[193,194]. In contrast to the case of LDBCs, the branched component of LHBCs is highly random. This randomness arises from their synthetic protocols, which are both blessings and a curse. For example LHBCs can be synthesized in a one-pot process[195], considerably reducing production complexity. However, this simplification often comes at the cost of high macromolecular weight and topological polydispersity[196,197]. As drug delivery vehicles must be monodisperse in size and exhibit similar physiological characteristics between batches, it is important for the polymers to form well-defined structures[198]. High macromolecular weight polydispersity can lead to undesirable assemblies[199]. To address this issue, methods that reduce polydispersity, such as slow-monomer addition[35], have been developed. It should be noted that a certain low degree of macromolecular weight polydispersity may have a positive effect on micelle size uniformity, as has been demonstrated for linear block copolymers[36]. Theoretical studies on micelle formation have mostly focused on monodisperse linear block copolymers[200–205] and LDBCs[27,206–208]. A few simulation studies have investigated micelle self-assembly and morphological transitions in solutions of hyperbranched copolymers with irregular architectures[209–212]; however, the systems were still monodisperse in the sense that all molecules were identical. Only few studies have considered effects of molecular weight polydispersity[36,213–217], and the effects of topological polydispersity remain largely unexplored. Here, we attempt to elucidate some of the properties of micelles composed of polydisperse LHBCs, and compare them with their counterparts made of monodisperse linear diblock copolymers and LDBCs. Schematic pictures of such polymers are shown in Fig. 5.1b-e. In the case of LDBCs, the solvophobic blocks comprising the dendritic part have the same total number of monomers and the number of terminal ends doubles with each generation. We investigate a range of metrics such as the morphologies of the micelles, the terminal end distributions, the stability of micelles, their CMC values, and their encapsulation capacities for a model solvophobic drug molecule. We also investigated the limiting molecular weight polydispersity that can still be tolerated. To this end, we employ molecular dynamics (MD) simulations to model the slow-monomer addition method[35,218,219] and construct a variety of LHBCs with predetermined macromolecular

length (weight) polydispersity. The molecular architectures are then extracted and the self-assembly of the molecules is evaluated in the grand canonical ensemble using the Self-Consistent Field Theory (SCFT) framework[48].

5.2 Model and Methods

5.2.1 Molecular Dynamics Model

We employed MD simulations to mimic the slow-monomer addition protocol[220] and used beads labeled A to F, to represent various components of the LHBC. Beads F and C represent polystyrene and the macroinitiator respectively, while the rest are used to represent the AB_2 monomers and are configured in a star-like fashion as shown in Fig. 5.2: The center bead of the star (type D) is connected to two beads B and one bead A such that the four of them form a Y-shape, and further inert beads E are added to stabilize this structure. Beads A can interact via an attractive potential with beads C and B, simulating the irreversible conjugation of AB_2 monomers with the macroinitiator and with each other.

The detailed interactions between each bead type are outlined below:

$$U_{ij}^{\text{harm.}} = \frac{1}{2} k_h (r_{ij} - r_o)^2 \tag{5.1}$$

for bonded beads F-F, F-C, C-C, A-D, B-D, D-E,

$$U_{ij}^{\text{LJ}} = 4\epsilon \left[\left(\frac{\sigma}{r_{ij}} \right)^{12} - \left(\frac{\sigma}{r_{ij}} \right)^{6} \right] \tag{5.2}$$

for all bead pairs except A-C, A-B,

$$U_{ij}^{\text{bind.}} = -d \cos \left(\frac{r_{ij} \pi}{2 r_c} \right) \Theta(r_c - r_{ij}) \tag{5.3}$$

for bead pairs A-C, A-B,

$$U_{ijk}^{\cos} = \frac{1}{2} k_c (\cos(\theta_{ijk}) - \cos(\theta_o))^2 \tag{5.4}$$

for bonded bead triplets A-D-B, B-D-B,

$$U_{ijkl}^{\text{dihedral}} = \frac{1}{2} k_d (1 - \cos(2\phi_{ijkl}))^2 \tag{5.5}$$

for beads E-E-E-E in the same star unit.

Here r_{ij} denotes the distance between beads i and j, θ_{ijk} is the angle between particles i, j and k, ϕ_{ijkl} is the angle between the two planes formed by beads i, j, k and beads j, k, l respectively, and Θ refers to the Heaviside function ($\Theta(x) = 1$ for $x > 0$, $\Theta(x) = 0$ otherwise). The parameters are $\kappa_h = 100\epsilon$, $\rho_o = \sigma$, $d = 100\epsilon$, $r_c = \sigma/2$, $\kappa_c = 100\epsilon$, $\theta_o = 5\pi/6$ for A-D-B and $\theta_o = 2\pi/3$ for B-D-B.

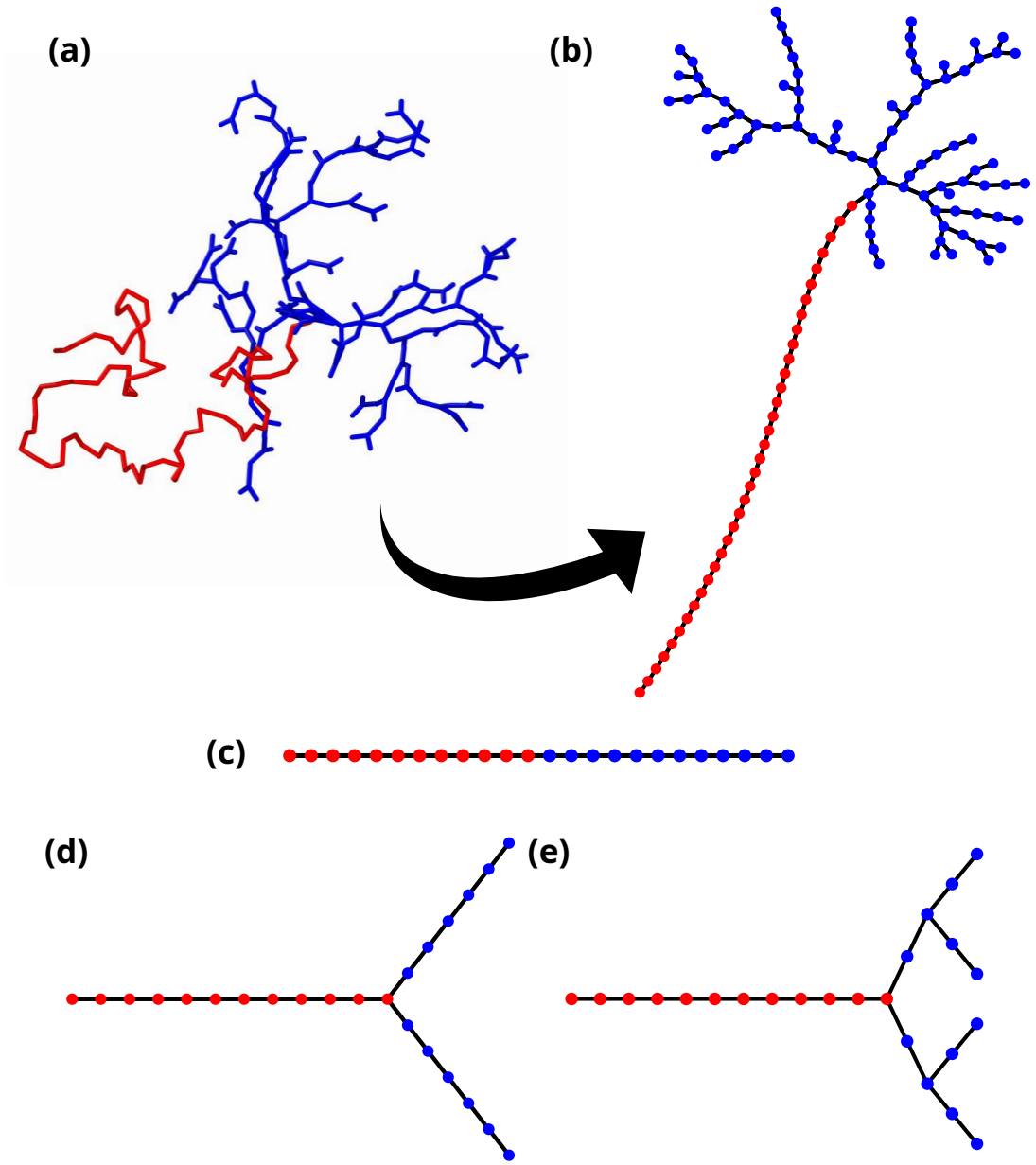

Figure 5.1: Examples of molecular structures. Solvophobic part is shown in red and solvophilic part in blue. (a) Example of an LHBC molecule produced from a molecular dynamics simulation (see Section 5.2.1). (b) Graph representation of the polymer molecule in (a) where each filled circle represents a monomer. Note that the maximum number of generations in this particular example is ten. (c) Representation of a symmetric linear diblock molecule. (d,e) Representation of a LDBC molecule of generation one (d) and generation two (e).

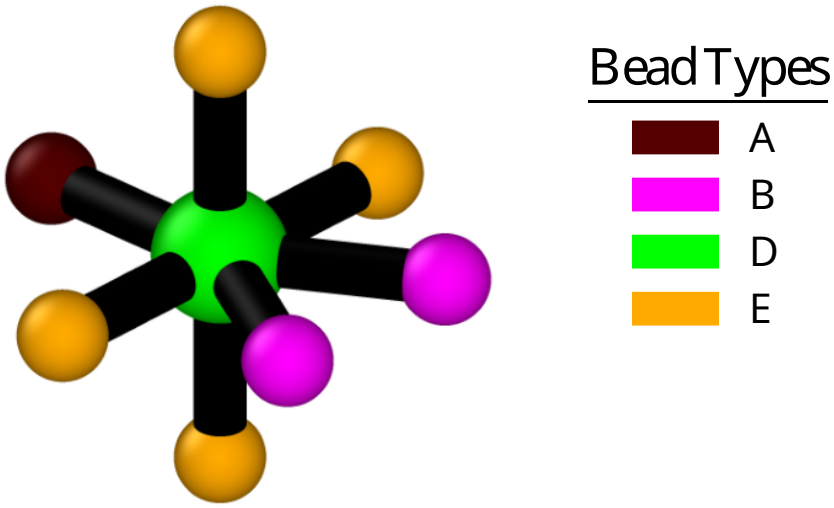

Figure 5.2: Sketch of the AB_2 monomer used in the MD simulations. Each color corresponds to a different type of bead as indicated, and bonds are depicted in black. In the SCFT calculations, this whole monomer is turned into a single solvophilic segment.

We simulated the aforementioned system under constant temperature and volume conditions using Langevin dynamics as implemented in the HOOMD-blue molecular dynamics package[221]. Starting with a linear chain of 84 F-beads followed by 8 C-beads connected in a sequential arrangement, we then introduced a designated number of AB_2 monomers. This number is sampled randomly from a Schulz-Zimm distribution[102] with an average value of $\bar{N}_{AB_2} = 76$ monomers, and varying, but prescribed polydispersity index PDI $= \overline{N^2_{AB_2}}/\bar{N}^2_{AB_2}$. We note that the choice of $\bar{N}_{AB_2} = 76$ is based on the fact that in SCF, F beads act as solvophobic monomers, while C beads and AB_2 monomers act as identical solvophilic monomers, thus the resulting LHBCs are, on average, symmetric in terms of the solvophobic-to-solvophilic monomer ratio. For the case of PDI = 1, the ensemble generated consists of LHBCs that are monodisperse in length yet display a diversity of topologies.

The AB_2 monomers are added sequentially, with the condition that the preceding monomer must first be attached to the growing central molecule before a new monomer can be introduced. This prevents premature connections between free AB_2 monomers. A schematic representation of such a polymer molecule and its graph structure is shown in Fig. 5.1a,b. The graph representation of this molecule, along with others that constitute the polydisperse ensemble of LHBCs, is subsequently recorded and used for further calculations within the SCF framework. To avoid confusion we note that, although more than two types of MD monomers are introduced in the construction

of the LHBC polymers, the MD monomers are then mapped onto only two types of segments, either solvophobic or solvophilic, in the SCFT model.

The SCF calculations are done in batches B1-B4, consisting of 128 different polymers each, which are a result of the "greedy algorithm". This algorithm sorts the 512 polymers, which we refer to as the BA batch, into four equally sized sub-batches (B1-B4). It does this by progressively filling these sub-batches while tracking the total sum of monomers in each batch. It then assigns the next polymer to the sub-batch with the lowest total, ensuring that no sub-batch exceeds the target of 128 polymers. More details about the SCF simulations are provided in Section 5.2.2.

5.2.2 SCFT Model

To model a system of copolymers with solvophobic (H) and solvophilic (P) monomers in solvent (S), capable of exchanging polymer chains with its environment (bath), we employ SCFT calculations in the grand canonical ensemble.

We consider a polymer solution in implicit solvent, modeled according to the Sanchez–Lacombe theory[48,58], and characterize the system in terms of spatially varying monomer volume fractions $\phi_H(\boldsymbol{r})$ and $\phi_P(\boldsymbol{r})$ that depend on the corresponding monomer number densities $\rho_\alpha(\boldsymbol{r})$ and the monomeric volumes $v_\alpha = v_P$ via $\phi_\alpha = \rho_\alpha v_\alpha$. Thus the solvent volume fraction is given by $\phi_S(\boldsymbol{r}) = 1 - \phi_H(\boldsymbol{r}) - \phi_P(\boldsymbol{r})$ and the solvent number density is given by $\rho_S = \phi_S / v_S$, where v_S is the volume of a solvent molecule. The grand canonical free energy is given by[48]:

$$
\begin{aligned}
\beta F_{\mathrm{GC}} = \Bigg(& U_{\text{inter.}} - \frac{1}{v^*} \int \mathrm{d}\boldsymbol{r} \sum_{\alpha}^{H,P} (\rho_\alpha v^*) W_\alpha \\
& - \sum_{i}^{n_T} \exp\left(\beta \mu_i\right) Q_i \Bigg) \\
U_{\text{inter.}} = \frac{1}{v^*} \Bigg(& \int \mathrm{d}\boldsymbol{r} \sum_{\alpha}^{H,P} \chi_{\alpha S}\, \phi_\alpha(\boldsymbol{r}) \phi_S(\boldsymbol{r}) \\
& + \frac{1}{2} \sum_{\alpha,\beta}^{H,P} \chi_{\alpha\beta}\, \phi_\alpha(\boldsymbol{r})\, \phi_\beta(\boldsymbol{r}) \\
& + v^* \left(\rho_S(\boldsymbol{r}) \ln(\phi_S(\boldsymbol{r})) - \rho_S(\boldsymbol{r}) \right) \Bigg),
\end{aligned}
\tag{5.6}
$$

where v^* is a reference volume, $U_{\text{inter.}}$ is the interaction potential which also includes the translational entropy of the solvent molecules, $\chi_{\alpha\beta}$ are the Flory-Huggins parameters between species α and β, W_α are the self-consistent fields, μ_i and Q_i is the chemical potential and the single chain partition functions of chains of type i respectively, n_T is the number of different types of polymers, and V is the volume of the system.

In these grand canonical SCF calculations, we assume the polymers in the micelle to be in chemical equilibrium with a homogeneous solution of chains of type i with global average polymer volume fraction $\bar{\phi}$. The chemical potentials μ_i are then given by:

$$\exp(\beta\mu_i + \ln(\bar{N})) = \frac{w_i \bar{\phi} V}{\bar{Q}_i v_P}, \tag{5.7}$$

where $\bar{Q}_i$ is the single chain partition function of chain type i in the homogeneous state and w_i is the fraction of chains of type i in the bath such that $\sum_i^{n_T} w_i = 1$. Also, $\bar{N} = \sum_i^{n_T} w_i N_i$ is the average chain length and N_i is the length of polymer type i. The derivation of Eq. (5.7) is given in the Appendix 5.6.

In our study, we consider copolymers that are separated into blocks, each consisting exclusively of either solvophobic or solvophilic monomers. We categorize the blocks into three groups based on their connectivity: (1) Stem (SM, one per molecule), (2) Internal (IL), and (3) Terminal (TL). Stem and terminal blocks each have one free end, while internal blocks have none. Blocks are delimited by junctions, which encompass both the internal branch points and free ends. For each molecule type i, the junctions are numbered consecutively, starting from zero, which is assigned to the free end of the stem block. Thus, a given block in a chain of type i can be identified by the pair $[j_1 j_2]_i$ of confining junctions. Moreover, we assign orientations to molecules, defining the forward direction as running from the stem to the terminal blocks. An example illustrating the nomenclature is given in Fig. 5.3.

For each block $[j_1 j_2]_i$, we calculate a forward propagator $q_{[j_1 j_2]_i}(\boldsymbol{r}, s)$ and a backward propagator $q^\dagger_{[j_1 j_2]_i}(\boldsymbol{r}, s)$, where $s = n/\bar{N}$ and n is a monomer count. This is done by solving the modified diffusion equations[222]

$$\begin{aligned}
\frac{\partial q_{[j_1 j_2]_i}(\boldsymbol{r}, s)}{\partial s} &= \left(\bar{N}\frac{b^2}{6}\nabla^2 - \bar{N} W_{[j_1 j_2]_i}(\boldsymbol{r}) \right) q_{[j_1 j_2]_i}(\boldsymbol{r}, s) \\
\frac{\partial q^\dagger_{[j_1 j_2]_i}(\boldsymbol{r}, s)}{\partial s} &= -\left(\bar{N}\frac{b^2}{6}\nabla^2 - \bar{N} W_{[j_1 j_2]_i}(\boldsymbol{r}) \right) q^\dagger_{[j_1 j_2]_i}(\boldsymbol{r}, s),
\end{aligned} \tag{5.8}$$

where we assumed the statistical segment length of the monomers b to be the same throughout the polymer. Here, $W_{[j_1 j_2]_i}$ is either W_H or W_P, depending on the monomer type of block $[j_1 j_2]_i$. Eqs. (5.8) are solved for values of s in the interval $s \in [0, s^{\max}_{[j_1 j_2]_i}]$, where $\bar{N} s^{\max}_{[j_1 j_2]_i}$ is the macromolecular length of block $[j_1 j_2]_i$, with initial conditions given by the following relations[222]:

$$q_{[j_1 j_2]_i}(\boldsymbol{r}, 0) = 1 \quad \text{for} \quad [j_1 j_2]_i = [01]_i \in \text{SM} \tag{5.9}$$

$$\begin{aligned}
q_{[j_1 j_2]_i}(\boldsymbol{r}, 0) &= q_{[j_3 j_1]_i}(\boldsymbol{r}, s^{\max}_{[j_3 j_1]_i})\, q^\dagger_{[j_1 j_4]_i}(\boldsymbol{r}, 0) \\
&\quad \text{for} \quad [j_1 j_2]_i \notin \text{SM} \quad \text{and,} \\
[j_3 j_1]_i &\in \text{SM or IL}, \; [j_1 j_4]_i \in \text{IL or TL}
\end{aligned} \tag{5.10}$$

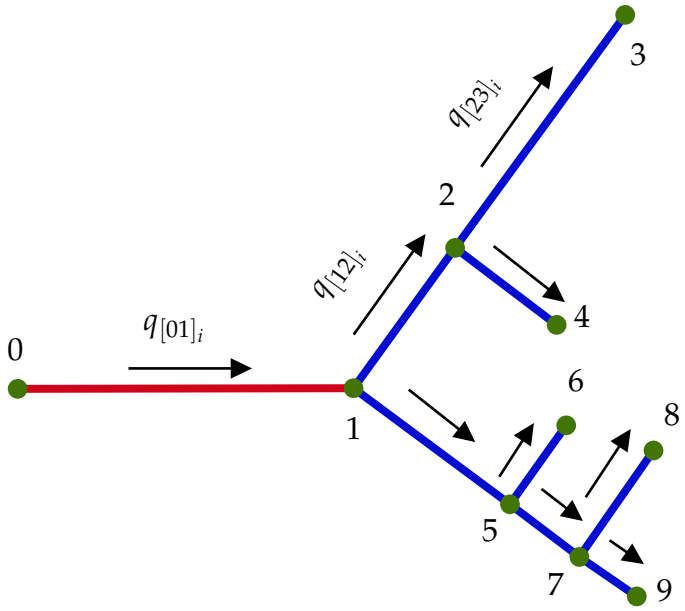

Figure 5.3: Cartoon representation of a hyperbranched polymer indexed to i. Red indicates that block j is solvophobic while blue indicates that the block is solvophilic. Green indicates the junction points numbered here from 0 to 9. For clarity, only some of the forward propagators are shown.

$$q^{\dagger}_{[j_1 j_2]_i}(\boldsymbol{r}, s^{\max}_{[j_1 j_2]_i}) = 1 \quad \text{for} \quad [j_1 j_2]_i \in \text{TL} \tag{5.11}$$

$$q^{\dagger}_{[j_1 j_2]_i}(\boldsymbol{r}, s^{\max}_{[j_1 j_2]_i}) = q^{\dagger}_{[j_2 j_3]_i}(\boldsymbol{r}, 0)\, q^{\dagger}_{[j_2 j_4]_i}(\boldsymbol{r}, 0)$$

$$\text{for} \quad [j_1 j_2]_i \notin \text{TL},\ [j_2 j_3]_i,\ [j_2 j_4]_i \in \text{IL or TL}. \tag{5.12}$$

Eqs. (5.9) and (5.11) are the initial conditions for the free ends of the polymer, while Eqs. (5.10) and (5.12) are the initial conditions for the inner junction points of the polymer. For example, in Fig. 5.3, junction points 1, 2, 5 and 7 are inner junction points while the rest are free ends. Based on these initial conditions, we first calculate the backward propagators of the chain, starting from the terminal groups and proceeding "backward" along the chain, up until the stem's backward propagator is calculated. Then we repeat the procedure for the forward propagator in the reverse order. Once the propagators have been calculated, the volume fractions can be determined *via* the following expression:

$$\phi_\alpha(\boldsymbol{r}) = \sum_i^{n_T} \phi_{\alpha,i}(\boldsymbol{r}) = \sum_i^{n_T} \exp(\beta\mu_i + \ln(\bar{N})) \tag{5.13}$$

$$\times \sum_{[j_1 j_2]_i} \int_0^{s^{\max}_{[j_1 j_2]_i}} \mathrm{d}s\, q_{[j_1 j_2]_i}(\boldsymbol{r}, s) q^{\dagger}_{[j_1 j_2]_i}(\boldsymbol{r}, s) \theta_{\alpha,[j_1 j_2]_i},$$

where $\phi_{\alpha,i}(\boldsymbol{r})$ is the volume fraction contribution from chain i to monomer type α and $\theta_{\alpha,[j_1 j_2]_i}$ is one if the block $[j_1 j_2]_i$ is of type α, and zero otherwise. The single chain partition function of chain of type i can be evaluated from the backward propagators of the corresponding stem blocks,

$$Q_i = \frac{1}{v^*} \int \mathrm{d}\boldsymbol{r}\, q^{\dagger}_{[01]_i}(\boldsymbol{r}, 0). \tag{5.14}$$

Finally, to close the self-consistent loop, the fields $W_\alpha(\boldsymbol{r})$ are calculated from the functional derivatives of $U_{\text{inter.}}$ with respect to the monomeric *number* densities[48], $\rho_\alpha = \phi_\alpha / v_\alpha$, as:

$$W_\alpha(\boldsymbol{r}) = \frac{\delta U_{\text{inter.}}[\phi]}{\delta \rho_\alpha(\boldsymbol{r})}$$

$$= \frac{v_\alpha}{v^*}(\chi_{\alpha S}\phi_S + \sum_\beta^{H,P}(\chi_{\alpha\beta} - \chi_{\beta S})\phi_\beta - \frac{v^*}{v_S}\ln(\phi_S)). \tag{5.15}$$

Given an initial field W_α, we solve Eqs. (5.8), calculate new volume fractions using Eq. (5.13), calculate new fields using Eq. (5.15), mix the new fields with the old ones using lambda mixing[59], and repeat the loop until the following convergence criterion is reached:

$$\text{CF} = \sum_\alpha^{H,P} \int \mathrm{d}\boldsymbol{r}\, (\phi_\alpha^{\text{new}} - \phi_\alpha^{\text{old}})^2 < 10^{-12}. \tag{5.16}$$

All SCF calculations were performed with periodic boundary conditions in a simulation box of volume $V = 15 \times 15 \times 15\,[\bar{R}_g^3]$, using 1024, 128×128 and $64 \times 64 \times 64$ grid points for one, two and three dimensional simulations respectively. The rest of the parameters were chosen as $\chi_{HP}\bar{N} = 30$, $\chi_{HS}\bar{N} = 61$, $\chi_{PS}\bar{N} = 27$, $v_S/(v^*\bar{N}) = 0.02$ and $v^* = v_P$ such that the equilibrium morphology in a system of symmetric diblock copolymers is a spherical micelle. To accelerate the numerical computation of the propagators for highly symmetric architectures like LDBCs, we implemented schemes similar to those in Yong and Kim [223], which avoid redundant calculations of identical propagators.

5.3 Results and Discussion

In this section, we first examine the results related to the size and topological polydispersity of LHBCs generated from MD simulations. We then present results from SCF calculations, comparing micelles formed by polydisperse ensembles of LHBCs with those formed by monodisperse ensembles of linear diblocks or LDBCs of various generations. Key experimentally relevant quantities such as the critical micelle concentrations (CMC), the equilibrium morphologies, the volume fraction profiles, the terminal end distributions, the number of chains n_M and terminal ends c_M per micelle, the micelle size distributions, and the energy penalty associated with asphericity, are discussed. Finally, we investigate the drug encapsulation capacity of these micelles by evaluating the encapsulation of solvophobic homopolymers. For a fair comparison, we limit the study to systems with solvophobic-to-solvophilic monomer ratio maintained at 1 : 1 for all monodisperse LDBC and linear diblock systems, and on average, at 1 : 1 for the polydisperse LHBC systems. We note that, in some of the following plots, we refer to the linear diblock chain as zeroth generation LDBC. Below, lengths are mostly given in units of the average radius of gyration $\bar{R}_g = b\sqrt{\bar{N}/6}$ and the free energy F will be given in units of $k_BT = \beta^{-1}$ and rescaled with the Ginzburg parameter $\bar{C} = \bar{R}_g^3/v^*\bar{N}$.

5.3.1 Generation of representative LHBC polymer sets

As noted in the introduction, slow monomer addition can yield polymers with low macromolecular length polydispersity, which shows particular promise for applications. Therefore, we focus on LHBCs synthesized by using this approach. Specifically, we modeled the slow-monomer addition protocol outlined in Barriau *et al.* [35]. In this process, a linear polystyrene block is initially conjugated to a short, linear hydroxylated polybutadiene block, which serves as a macroinitiator for the subsequent gradual addition of glycidol, ultimately forming the LHBC molecule. Here, glycerol acts as an AB_2-type monomer, thus the branching points in the resulting hyperbranched polyglycerol have a degree of three.

To model the slow monomer addition protocol, we used single-chain coarse-grained MD simulations. In such simulations, a linear block was conjugated to a linear macroinitiator and a predetermined number of AB_2 monomers, that can irreversibly bond with the macroinitiator and other AB_2 monomers, were added sequentially to the growing molecule. This predetermined random number followed a Schulz-Zimm distribution with a specific polydispersity index (PDI) and average number (see Section 5.2.1.)

We investigated different values of PDI, and for each PDI, we simulated the creation of 512 independent polymers. To keep the SCF simulations manageable and enable assessing statistical errors in the SCF results, we divided the complete batch (BA) into four subbatches (B1, B2, B3, B4) of 128 polymers each. Instead of randomly selecting polymers from the BA batch, we used a "greedy number partitioning" algorithm to assign polymers to sub-batches (see Section 5.2.1).

This method ensures that the four sub-batches have similar average chain lengths and was also found to preserve other key characteristics. For instance, the degree of branching[224], which is defined as:

$$DB = 2D/(2D + L), \tag{5.17}$$

where D and L are number of dendritic monomers (branching points) and linear monomers, is also preserved along with the length polydispersity. This is illustrated in both Fig. 5.4 and Table 5.1, which demonstrate that the characteristics of both the topological and chain length polydispersity are overall inherited from the large BA batch in the sub-batches B1-B4. Note that, as explained in Section 5.2.1, the macroinitiator and the AB_2 monomers are considered solvophilic and compose the entire hyperbranched part of the polymer. The results are consistent with previous Monte-Carlo simulations[225].

Target PDI	1.0	1.1	1.2	1.3	1.4	1.5
BA	76.0(1.00)/0.56 ± 0.05	76.1(1.10)/0.56 ± 0.05	74.3(1.18)/0.56 ± 0.05	75.6(1.33)/0.57 ± 0.05	73.4(1.37)/0.57 ± 0.05	74.7(1.56)/0.57 ± 0.06
B1	76.0(1.00)/0.56 ± 0.05	76.1(1.10)/0.56 ± 0.05	74.3(1.18)/0.56 ± 0.05	75.6(1.34)/0.57 ± 0.05	73.5(1.37)/0.57 ± 0.05	74.7(1.56)/0.57 ± 0.06
B2	76.0(1.00)/0.56 ± 0.04	76.2(1.10)/0.56 ± 0.05	74.3(1.18)/0.56 ± 0.05	75.6(1.33)/0.57 ± 0.06	73.4(1.37)/0.56 ± 0.05	74.7(1.56)/0.56 ± 0.05
B3	76.0(1.00)/0.56 ± 0.04	76.2(1.10)/0.56 ± 0.05	74.3(1.18)/0.56 ± 0.05	75.6(1.33)/0.57 ± 0.05	73.4(1.37)/0.57 ± 0.05	74.7(1.55)/0.57 ± 0.06
B4	76.0(1.00)/0.56 ± 0.05	76.0(1.10)/0.56 ± 0.05	74.3(1.18)/0.56 ± 0.05	75.6(1.32)/0.56 ± 0.06	73.4(1.37)/0.56 ± 0.06	74.7(1.55)/0.57 ± 0.06

Table 5.1: Statistical properties of polymers in each representative batch of LHBC molecules (see text), with notation "Average number of AB_2 monomers"("PDI")/"DB ± Error of DB". Note that the calculation of DB only involves the solvophilic part of the polymer, while the calculation of the PDI involves only the AB_2 monomers. Small deviations from the target values arise due to sampling.

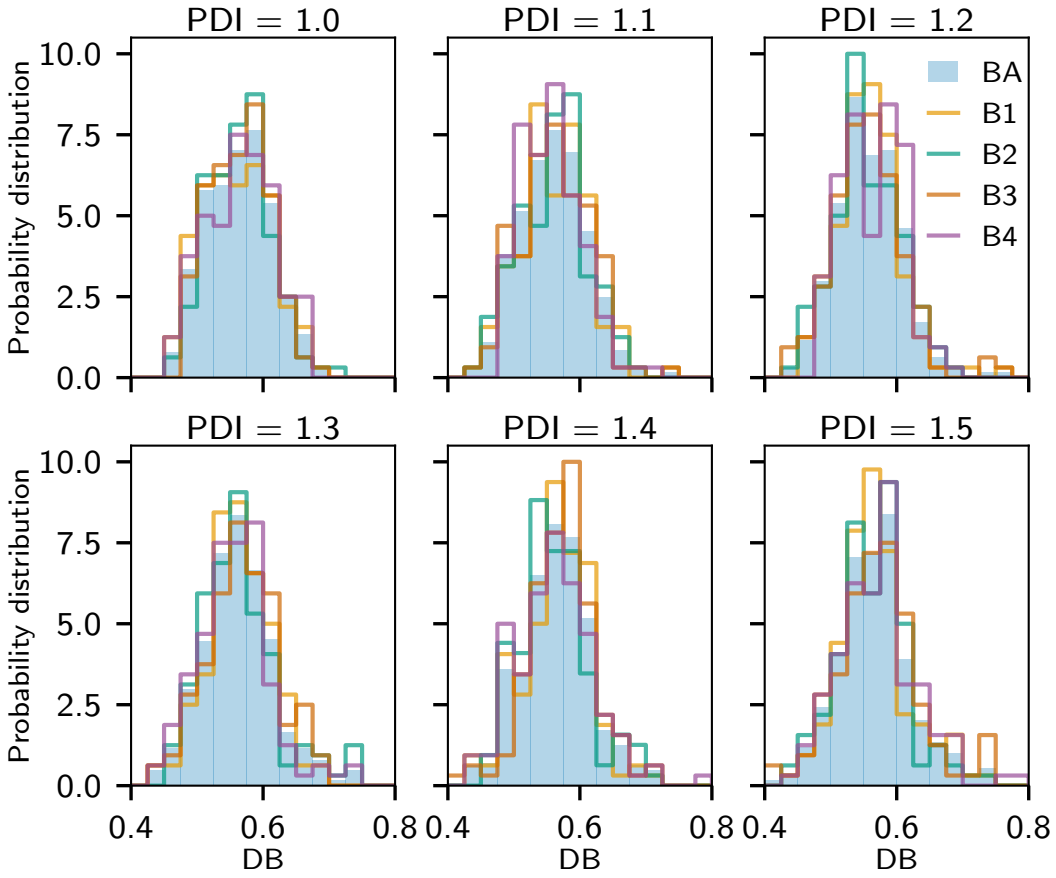

Figure 5.4: Probability distributions of the degree of branching (DB) for the LHBCs with different values of polydispersity index PDI. The whole colored distribution represents the complete batch (BA), while the other four colors represent the sub-batches (B1-B4). Note that the DB values are calculated only for the solvophilic part of the polymer.

5.3.2 Equilibrium micelle structures

To determine the equilibrium morphology and the CMC of the systems, we conducted one-, two-, and three-dimensional SCF calculations in the grand canonical ensemble, which resulted in lamellae, cylindrical, or spherical micelles, respectively. For simplicity, we only consider solvophobic (H), solvophilic (P) and solvent (S) in these calculations and do not distinguish between the macroinitiator and the AB_2 monomers, to which we all refer as P. In particular, we assume that all monomers have the same monomeric volume v_P. We further assume that the polymers in the micelle are in chemical equilibrium with a homogeneous solution (bath) of chains of type i with global average polymer volume fraction $\bar{\phi}$. The chemical potentials μ_i (Eq. (5.7)) of each type, are then given in terms of w_i, which is the fraction of chains of type i in the bath. We set $w_i = 1/n_T$, meaning that chains of all types i are incorporated into the micelle with the same *a priori* probability. The actual fraction of chains i in the micelle may of course differ from w_i.

First, we varied the average polymer volume fraction, $\bar{\phi}$, of the bath and evaluated the free energy difference (ΔF) between the inhomogeneous and homogeneous states for each case. Selected curves for ΔF as a function of $\bar{\phi}$ are shown in Figs. 5.5a and 5.5b. The critical volume fraction, $\bar{\phi}_c$, is defined as the lowest value of $\bar{\phi}$ among the three morphologies for which $\Delta F = 0$. This represents the lowest polymer volume fraction at which micelles begin to form, with the corresponding morphology being the equilibrium micelle morphology. The resulting values of $\bar{\phi}_c$ and the respective morphologies are shown in the insets of Fig. 5.5: as a function of PDI for LHBCs in Fig. 5.5a, and as a function of generations for LDBCs in Fig. 5.5b. In LDBC systems, $\bar{\phi}_c$ increases with increasing generations, consistent with prior findings[27]. In LHBC systems, $\bar{\phi}_c$ decreases with increasing PDI, which aligns with observations from micelles formed by linear block copolymers with a polydisperse solvophilic block[36]. For all polymer systems tested, the equilibrium morphology was spherical micelles, except for LHBCs at PDI = 1.5, which transitioned to cylindrical micelles. In Fig. 5.5c, the differences in the length distribution of the solvophilic part between the micelle and the bath are shown for the different LHBC systems. Greater polydispersity results in a larger proportion of both smaller and larger chains in the bath. Smaller chains, being overall more solvophobic, are preferentially attracted to the micelle, while larger chains are preferred in the bath. Additionally, chains with smaller solvophilic parts lose less configurational entropy upon incorporation into micelles compared to larger chains, which explains the decrease in $\bar{\phi}_c$ with increasing PDI. The eventual transition of the equilibrium morphology from spherical to cylindrical can be attributed to smaller chains having a higher packing parameter[15]. Fig. 5.5d demonstrates that the effects of topology are minimal, as the differences in the degree of branching within the micelle and the bath for the PDI = 1 case are negligible. At PDI = 1, all chains have equal molecular weight, so there is no size-based driving force, unlike in the other cases. Thus, the differences

observed for the other PDI cases can be primarily attributed to indirect effects of molecular weight polydispersity, rather than topological polydispersity. However, this does not rule out a potential impact of topological polydispersity in systems with fewer chains than those tested. Next, we compare the properties of the equilibrated spherical micelles. We define the terminal end distribution $c(r)$, the number of chains n_M, and the number of terminal ends in the micelle, c_M, as:

$$c(\boldsymbol{r}) = \sum_{i}^{n_T} \exp(\beta\mu_i + \ln(\bar{N})) \tag{5.18}$$
$$\times \sum_{[j_1 j_2]_i}^{TL} q_{[j_1 j_2]_i}(\boldsymbol{r}, s^{\max}_{[j_1 j_2]_i})\, q^{\dagger}_{[j_1 j_2]_i}(\boldsymbol{r}, s^{\max}_{[j_1 j_2]_i})$$

$$c_M = \int_{V_c.} \mathrm{d}V\, c(\boldsymbol{r})/v_P \tag{5.19}$$

$$n_M = \int_{V_c.} \mathrm{d}V\, \phi_H(\boldsymbol{r})/(N_H v_P), \tag{5.20}$$

where the sum is performed over the terminal blocks (TL) of chain type i, $\boldsymbol{V_c.}$ is a sphere with a cutoff radius of 6.0 $[\bar{R}_g]$ and N_H is the length of the solvophobic block. The solvophobic volume fraction ϕ_H, the backward propagator q and $q^{\dagger}$, as well as the notation are defined in Section 5.2.2. In Fig. 5.6a, the volume fraction profiles of equilibrium micelles are shown for a selection of polymer systems. These profiles are only marginally influenced by polydispersity, with the LHBC systems exhibiting profiles that lie between those of the linear and the other LDBC-based micelle systems. The results indicate that the impact of polydispersity on the equilibrium volume fraction profiles is relatively minor compared to other factors, such as polymer architecture or the generation of LDBCs. These findings are consistent with a previous study on micelles formed by linear block copolymers[36], which showed that polydispersity in the solvophobic block had a strong effect on the volume fraction profiles, whereas polydispersity in the solvophilic block had little to no effect. We note that the solvent content in the micelle core is relatively high in these calculations, around 25%. This is a consequence of the monomer-solvent interactions ($\chi_{HS} = 0.61$) being relatively small. This value is inspired by an empirical estimate for polystyrene in n-decane based on Hansen's solubility parameters[226]. The χ_{HS} values for hydrophobic components of pharmaceutical micelles in water, such as polylactate, are typically about twice as high, therefore the solvent content in the micelle core will be lower. However, this should not change the general trends.

An interesting effect is observed in the high PDI case (PDI = 1.4). As shown in Fig. 5.6, a sizable amount of solvophilic monomers enters the predominantly solvophobic core, leading to a corresponding decrease in the solvophobic contribution. High PDIs can result in polymers with small solvophilic contributions, which makes them nearly entirely solvophobic. Consequently, the polymers tend to position themselves deeper

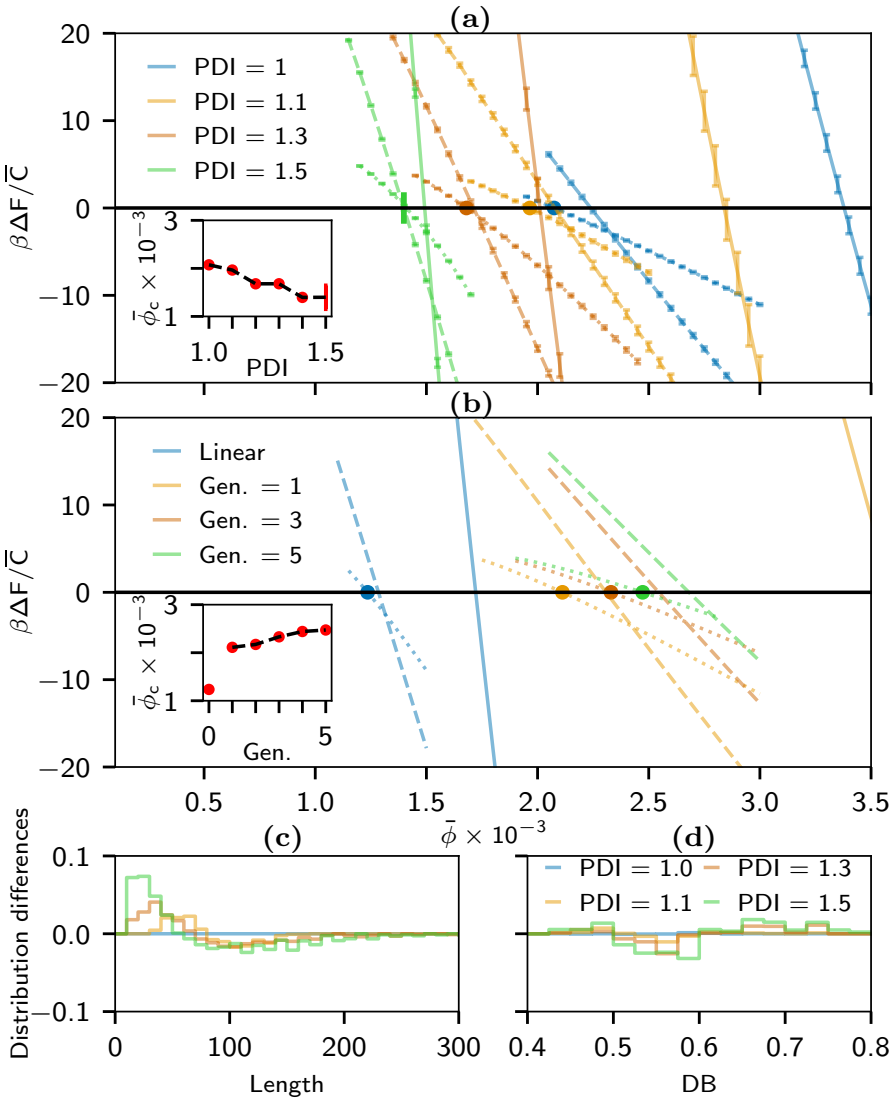

Figure 5.5: (a,b): Rescaled free energy difference ΔF between homogeneous and inhomogeneous states against the average polymer volume fraction in the bath $\bar{\phi}$ for polydisperse LHBCs (a) and monodisperse linear and LDBCs (b). Each color corresponds to a different polymer system, while the style of the line corresponds to lamella (solid line), cylindrical (dashed line) and spherical (dotted line) micelle states. For the LHBCs (a), errors obtained from averaging over batches are also shown. The insets in (a) and (b) show the state with the lowest critical concentration $\bar{\phi}_c$ against PDI and number of generations, respectively. The circular (●) and rectangular (▌) symbols represent spherical micelles and cylindrical micelles respectively as the equilibrium morphology, in both the main and inset plots. (c,d): Differences in the distribution of chain lengths and degree of branching between the bath and micelle were observed for LHBCs. The macromolecular weight and DB are calculated only for the hyperbranched part of the LHBCs.

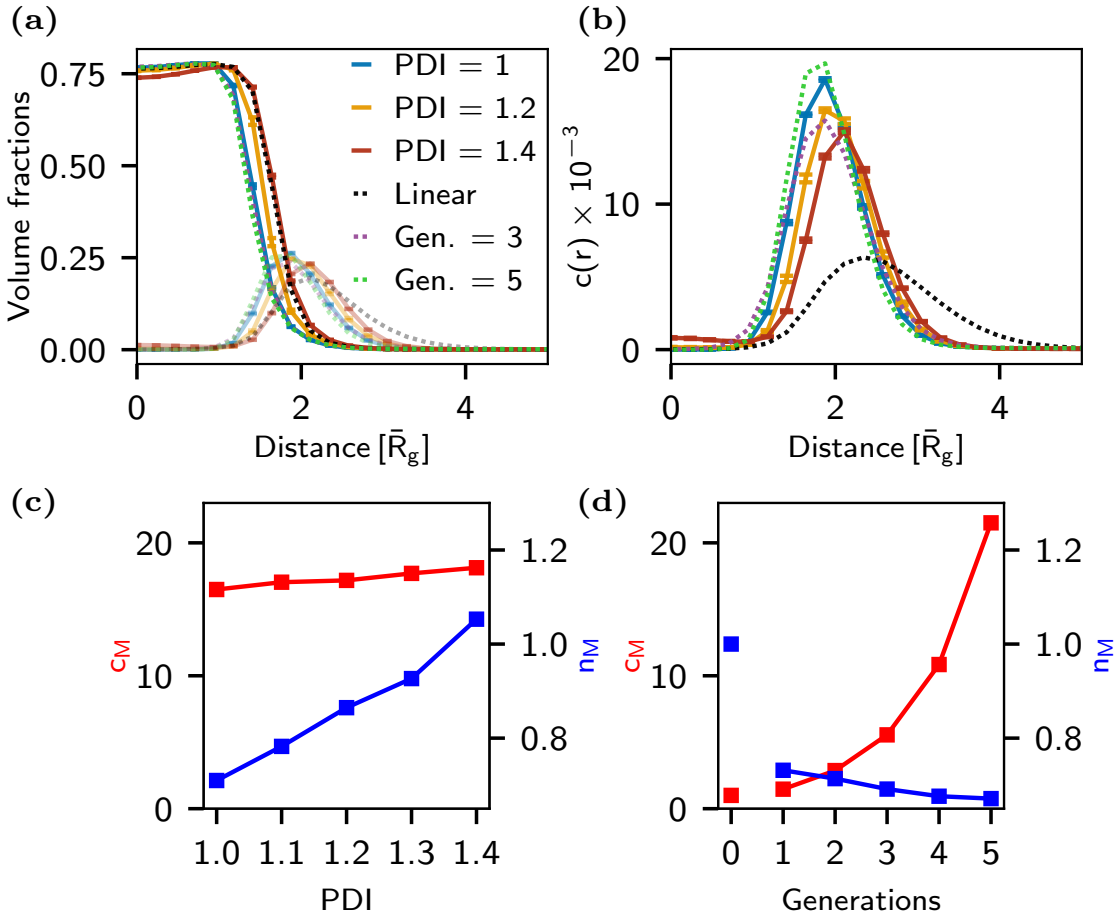

Figure 5.6: (a) Volume fraction profiles for spherical micelles at their CMC vs. the distance from the center. The opaque lines correspond to the solvophobic monomers while the translucent lines correspond to the solvophilic monomers. (b) Normalized average chain end profiles vs. the distance from the center of the micelles. The colors and line style for each polymer system are shown in the legend. For the LHBC systems, errors are also shown. (c,d): Number of solvophilic chain ends in the micelle c_M (red) and number of chains in the micelle n_M (blue) normalized by the corresponding number for monodisperse linear diblock chains, for LHBCs as a function of PDI (c) and LDBCs as a function of generation number (d).

within the micelle core. As a result, polymers with small solvophilic blocks may occasionally flip, with their solvophilic segments pointing inward rather than outward. This flipping behavior explains the reduced solvophobicity and the slight increase of the solvophilic contributions within the core. It highlights the complex nature of micelle formation at high polydispersity, where the distribution of solvophobic and solvophilic monomers becomes less predictable. The phenomenon may also explain the paradoxical observation that the equilibrium micelle size increases with increasing PDI, despite being composed of smaller chains. In other words, the shorter chains, which behave almost entirely as solvophobic molecules, contribute to swelling of the micelle core. When comparing the volume fraction profiles of LHBC and LDBC micelles to those of micelles composed of linear chains, as shown in Fig. 5.6a, one finds that the LHBC micelles at high PDI exhibit the highest resemblance. In contrast, the normalized terminal end distributions in Fig. 5.6b present a different picture. Here, LHBCs show greater similarity to LDBCs than to their linear counterparts, as they feature a much more concentrated corona. Increasing the PDI shifts the peak of the distribution toward larger values, which is consistent with the expected increase in micelle size. Unexpectedly, the number of terminal ends, c_M, for LHBCs appears to remain relatively constant with respect to PDI, showing only a minute increase as PDI increases, as illustrated in Fig. 5.6c (red curve). This results from the interplay of two opposing factors: As can be seen in Fig. 5.6c (blue curve), the number of chains, n_M, increases with increasing PDI in LHBC micelles, consistent with the increase in the micelle size discussed above. On the other hand, the ratio c_M/n_M, which corresponds to the average number of terminal ends per polymer in the micelle, decreases with PDI due to the preference for shorter chains in such micelles. Therefore, despite larger PDIs leading to larger micelles, which would typically result in a higher c_M, the presence of shorter chains with fewer terminal ends keeps c_M relatively unchanged. In LDBC micelles, a similar competition arises. The number of terminal ends per chain increases exponentially with increasing number of generations, but the number of chains n_M decreases (see Fig. 5.6d, blue curve). However, in this case, the first effect dominates by far, such that the number of chain ends in LDBC micelles still increases exponentially as a function of the generation number (Fig. 5.6d, red curve), at least up to the fifth generation.

5.3.3 Micelle size and shape fluctuations

After we discussed the properties of equilibrium micelles, we now turn to the free energy penalties associated with deviations from the preferred micelle size and shape. This analysis gives information on the stability and polydispersity of micelles, and on their resistance to deformations. The small statistical errors observed in Figs. 5.5 and 5.6 for LHBCs indicate that a single sub-batch is sufficient to capture the behavior of the

entire ensemble. Therefore, from this point onward, the results for the LHBC ensembles will be based on the B1 batch for each PDI.

We first examine the energy difference $F_M(R_M)$ between the equilibrium spherical micelle and a micelle of radius R_M in a bath with an average polymer volume fraction $\bar{\phi}_c$. To this end, we introduce a constraint potential in Eq. (5.21),

$$V_{\text{con}}[\phi_A] = \frac{\kappa_{\text{con}}}{2v^*}\Big(\int_{\boldsymbol{V}_{\text{ell.}}} \mathrm{d}\boldsymbol{r}\, \phi_H(\boldsymbol{r}) - \phi_{\text{con}}\Big)^2, \tag{5.21}$$

where the integral is performed over an ellipsoid of volume $\boldsymbol{V}_{\text{ell.}}$ concentered with the micelles. We note that the additional energy term from Eq. (5.21) is not explicitly added to the free energy $F_M(R_M)$, only the field contribution of this potential is included, as was similarly done in Mantha *et al.* [36]. We define the micelle radius (R_M) as the radius at which $\phi_H = 0.5$, and the radius is calculated post hoc following the SCF calculations.

The results, shown in Fig. 5.7, indicate that the most stable micelles, as characterized by the height of the energy barrier, are those composed of linear polymers, followed by the system with PDI = 1.4. Increasing the PDI leads to a moderate increase in the energy barrier, while for LDBCs, increasing the number of generations slightly reduces it. Both behaviors can be attributed to the growing and decreasing number of chains within the micelle for increasing PDI and number of generations respectively.

Furthermore, we can inspect the curvature of $F_M(R_M)$ at the minimum, which is related to the size distribution of micelles *via* $P(R_M) \propto \exp(\beta F(R_M))$. For micelles composed of monodisperse copolymers, the curvature appears to be largely independent of the copolymer architecture. It is very similar for linear copolymers, LDBCs, and LHBCs with PDI = 1. However, if one increases the PDI in the LHBC systems, the curvature decreases, indicating a broadening of the micelle size distribution. We attribute this to the greater number of smaller chains within the micelles. These smaller chains contribute to the swelling of the micelles and help stabilize a broader range of micelle sizes.

In a similar manner, we investigate the penalty associated with deforming the equilibrium micelles, thus making them aspherical. To define this quantity we consider the normalized moment of inertia tensor, which we define as

$$I_{ij} = \frac{\sum_p \phi_H^{(p)}(|r_{(p)}|^2\delta_{ij} - x_i^{(p)}x_j^{(p)})}{\sum_p \phi_H^{(p)}} \text{ for } i,j = 1,\,2,\,3, \tag{5.22}$$

where the sum over p runs over all grid points obeying $\phi_H \geq 0.05$, $x_i^{(p)}$ and $|r_{(p)}|$ are the Cartesian components and the distance from the center of the micelle respectively. The asphericity of a micelle is then defined as:

$$A = \lambda_z^2 - \frac{(\lambda_x^2 + \lambda_y^2)}{2}, \tag{5.23}$$

where $\lambda_{x,y,z}$ are the eigenvalues of the tensor in Eq. (5.22).

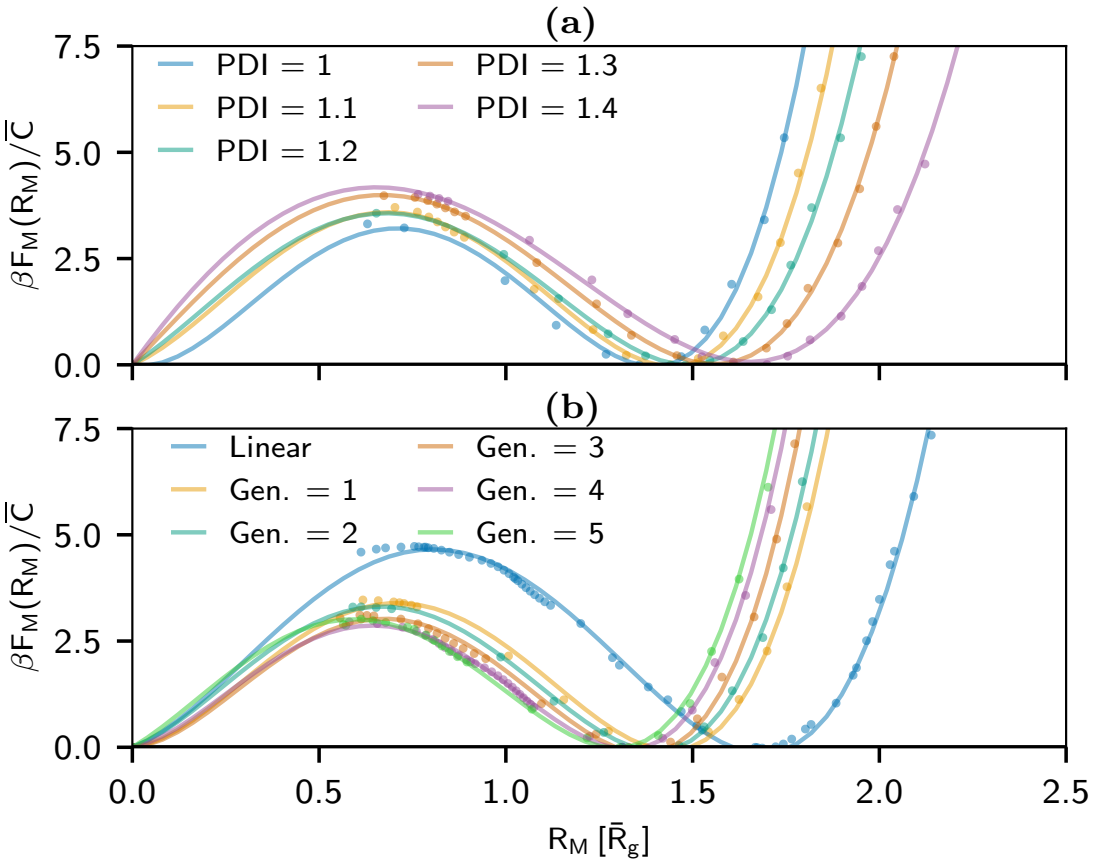

Figure 5.7: Rescaled free energy of the micelle $F_M(R_M)$ vs. the radius of the micelle R_M, for different PDIs (a) or linear and LDBCs (b) at their respective critical volume fractions $\bar{\phi}_c$. The results were obtained by varying ϕ_{con} in the constraint potential of Eq. (5.21), while $\kappa_{\text{con}}\bar{N} = 1$ and $\boldsymbol{V}_{\text{ell.}}$ which is a sphere of radius $R/\bar{R}_g = 5$, were kept constant. A fourth order polynomial was fitted to each system.

To impose different asphericities, we again use the constraint potential defined in Eq. (5.21). However, since this time, we wish to study the response of a given equilibrium micelle to mechanical deformation, we fix the total number of chains in the system, n_b, as well as the chain composition, and perform the SCF calculations in the canonical ensemble. Fig. 5.8 presents the energy penalty for deforming micelles as a function of asphericity in the systems of interest along with two example morphologies depicting the change from a spherical micelle to a cigar like micelle. The figures shows that LDBC micelles and LHBC micelles at PDI = 1 case exhibit similar resistance to deformation from their spherical shape, featuring the highest structural stability compared to other, more deformable systems. This is expected, as the topology of LDBCs aligns naturally with spherical micelles, and PDI = 1 polymers, although slightly more flexible, mimic LDBCs. This minor increase in malleability in LHBC micelles at PDI = 1 can be attributed to the diversity of polymer topologies within the micelle, that can arrange themselves in favorable positions so that for a given asphericity a smaller energy penalty is paid. Conversely, increasing the PDI in LHBC systems enhances the structural flexibility of the micelles, making the PDI = 1.4 system even more flexible than the linear micelle.

As the PDI increases, the diversity in chain topology and size also grows. Consequently, chains of different lengths adopt different spatial conformations within the micelle, as shown in Fig. 5.11a,b. The increased diversity enhances adaptability to stress, since chains can adjust to micelle deformations by repositioning and reorientating. This is illustrated in Fig. 5.11d which demonstrates that in a stretched micelle, the proportion of long chains oriented along the stretched axis, relative to short chains, is higher along the long axis than along the short axis.

5.3.4 Encapsulation of solvophobic drug molecules

To conclude our investigation, we analyzed the encapsulation properties of the micelle systems using a solvophobic homopolymer made of type A monomers, with a length equivalent to the linear solvophobic segment of each system. We fixed this homopolymer's contribution to the total polymer volume fraction at $\bar{\phi}_h = 10^{-5}$, to maintain consistent encapsulation conditions across all micelle configurations. Simulations were then rerun for each system of interest. The resulting data are presented in Fig. 5.9.

The CMC follows trends similar to those observed without encapsulation; however, CMC values across all systems are lower, a phenomenon commonly reported with the addition of solvophobic drugs[227] Encapsulation also affects the equilibrium morphology in LHBCs such that they adopt a cylindrical morphology already at PDI = 1.4.

All LHBC systems exhibit superior encapsulation capacities compared with LDBC systems, and increasing PDI further increases this capacity. We attribute this to the fact that, as the homopolymer is incorporated within the micelle, the micelle swells and its size deviates from the equilibrium values in the absence of the drug, as illustrated in Fig. 5.12a. As we noted before, swelling is penalized more strongly in LDBCs

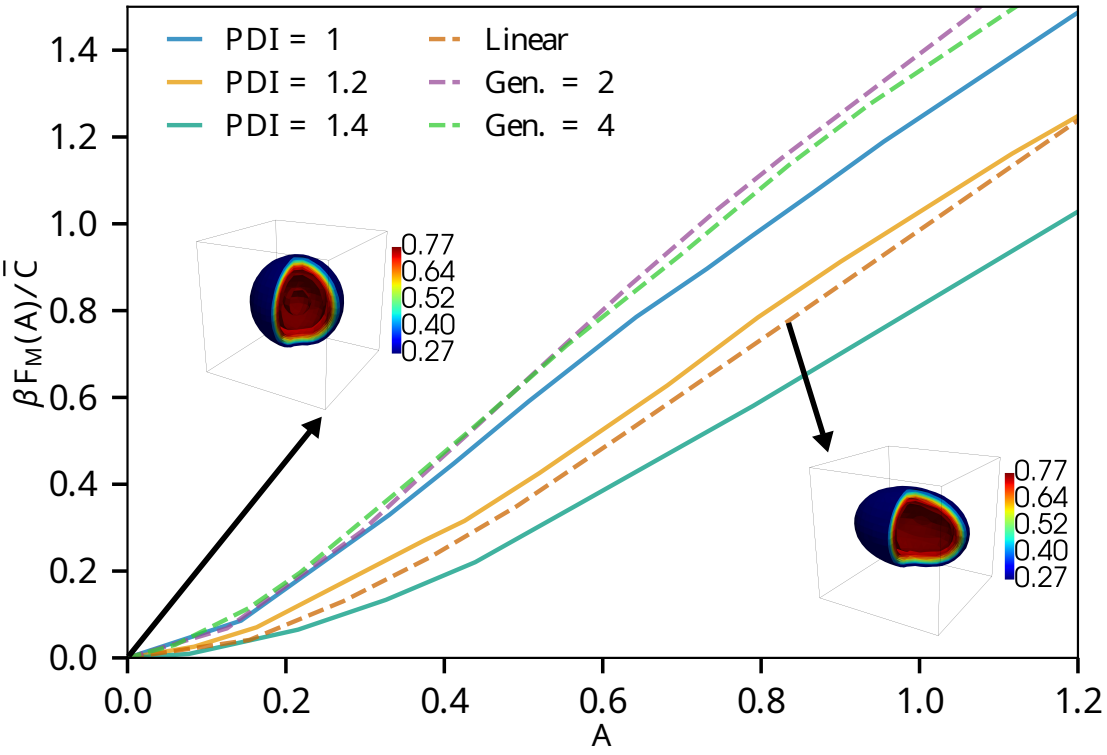

Figure 5.8: Free energy penalty F_M for deforming a micelle from spherical to aspherical vs. asphericity A for LHBC micelles (solid lines) and micelles composed of monodisperse LDBCs and linear copolymers (dashed lines). To enforce different asphericities, the constraint potential of Eq. (5.21) was used, with $V_{\text{ell.}}$ representing a spheroid with increasing size in the x-direction and decreasing size in the y and z directions such that $V_{\text{ell.}}$ matches the volume of the equilibrium micelle core, which was defined as the volume that obeys $\phi_H \geq 0.5$. $\kappa_{\text{con}}\bar{N}$ was set to 1 while ϕ_{con} was determined by the volume contribution of the solvophobic micelle core at $A = 0$. Also shown with corresponding arrows, are contour plots of the resulting morphology for the linear diblock results at $A = 0$ and $A = 0.84$.

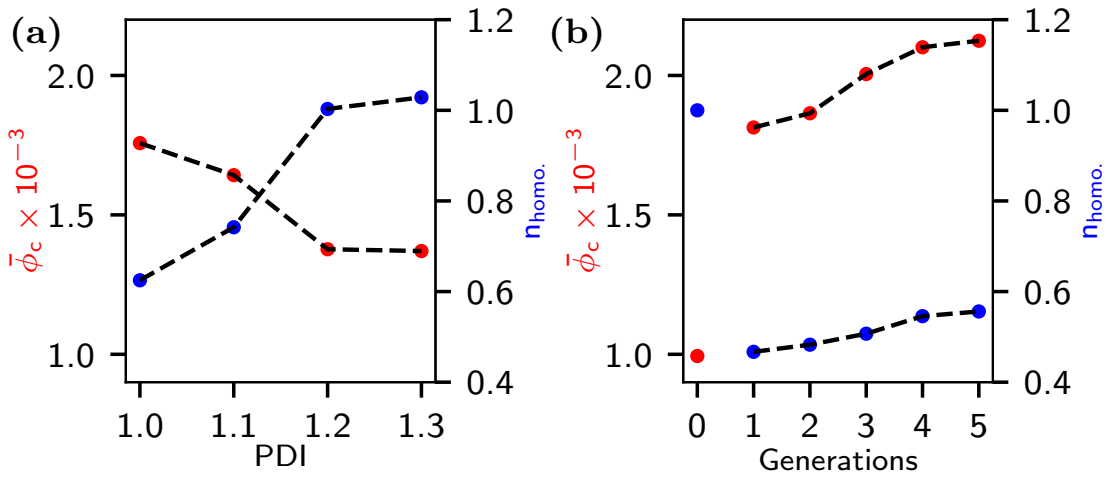

Figure 5.9: Critical volume fraction $\bar{\phi}_c$ (excluding the contribution from the homopolymers $\bar{\phi}_h$) (red) and average number of homopolymer chains in the simulation box $n_{homo.}$, normalized by the corresponding number for monodisperse linear diblock chain (blue) vs. the polydispersity of LHBCs (a) and the number of generations of LDBCs (b). The homopolymer volume fraction in the reservoir solution is kept fixed at $\bar{\phi}_h = 10^{-5}$.

compared with LHBCs (Fig. 5.7). Indeed, Fig. 5.12 shows that the micelle core size of LDBCs does not change upon incorporation of the homopolymer. Therefore, LHBCs can accommodate a higher payload due to their flexibility in size fluctuations.

5.4 Conclusion

We investigated self-assembled micelles composed of polymers with a monodisperse linear solvophobic block and a solvophilic block of equal average molecular weight, which are either polydisperse hyperbranched (LHBC), monodisperse dendritic (LDBC) or monodisperse linear (diblock). To do so, we first constructed a set of polydisperse topologies for the hyperbranched case, mimicking the slow-monomer addition synthesis protocol in MD simulations. Subsequently, we continued our investigation using self-consistent field (SCF) numerical calculations. For this purpose, we developed a methodology that incorporates the random branching characteristics of LHBCs, and we simulated these systems in the grand canonical ensemble to account for the exchange of polymers between micelles and their environment.

We found that increasing the polydispersity in LHBCs improves the stability of micelles and lowers the critical micelle concentration (CMC). This effect is largely driven by smaller chains, that are relatively more solvophobic, and therefore exhibit an increased tendency to be incorporated into micelles. In contrast, the topology of the

polymers appears to have a smaller impact in these systems, resulting in only slight differences in the aforementioned characteristics compared to LDBC systems.

Volume fraction profiles and terminal end distributions were also found to be broadly similar between LHBC and LDBC micelles. However, the number of chain ends in LHBC micelles was found to be surprisingly independent of polydispersity, and comparable to micelles composed of LDBCs with five generations. This independence is attributed to a combination of two factors: an increase in the number of chains within the micelle with increasing polydispersity, and a simultaneous decrease in the average number of terminal ends per chain in the micelle due to the higher content of shorter chains, which naturally have a smaller number of terminal ends.

Our calculations suggest that LHBC micelles are generally more diverse in size and offer less resistance to deformations from their spherical shape compared to that of LDBC micelles. Finally, we probed the capability of the micelles to encapsulate solvophobic drugs by testing them with a solvophobic homopolymer. We found that, due to their increased malleability, LHBCs can accommodate a larger payload than LDBCs, although encapsulation can influence their equilibrium morphologies and may induce a transition from spherical to cylindrical morphologies.

In summary, we have demonstrated that LHBC micelles exhibit behaviors similar to those of LDBC micelles, with findings indicating that the random topology of LHBCs is not the primary determinant of their characteristics. The polydispersity in size plays a more significant role. Additionally, the increased diversity in LHBCs proves advantageous, contributing to the enhanced encapsulation capacity and improved stability. We believe, therefore, that the randomness inherent in LHBCs can be thought of not as a drawback, but as an attribute that can be explored and taken advantage of.

Future research could explore reverse micelles, where the branched blocks form the core, as in this type of systems, the influence of topology is expected to be more pronounced compared to the systems examined here[209,228]. Additionally, exploring the effects of terminal group modifications on these polymers could further refine our understanding of micelle behavior. We have made our code available as part of the SCF package published in Qiao *et al.* [229], which can be used to simulate multiblock copolymers of any tree-like graph topology and is parallelized for polydisperse systems.

5.5 Data

The data and code for the MD simulations and SCF calculations can be found at: `https://gitlab.rlp.net/mgiannak/hyperbranched`.

Acknowledgments

This work was funded by the German Science Foundation (DFG) within Grant number 446008821, and the Agence Nationale de La Recherche, France. Partial funding was also received by the DFG within Grant number 429613790. M.G. is associate member of the integrated graduate school of the collaborative research center TRR 146 "Multiscale modeling of soft matter systems", grant number 233630050.

5.6 Appendix

In homogeneous systems, the fields and propagators do not vary spatially and the propagator equations, Eqs. (5.8), can be solved analytically. This results in:

$$q_{[j_1 j_2]_i}(s) q^{\dagger}_{[j_1 j_2]_i}(s) \equiv \frac{v_P \bar{Q}_i}{V} \quad \text{for all } [j_1 j_2]_i \text{ and } s,$$

and the following expression for the contribution of chain i to the volume fraction of type α:

$$\begin{aligned} \bar{\phi}_{\alpha,i} &= \cancel{v_P} \exp(\beta\mu_i + \ln(\bar{N})) \times \\ &\qquad \sum_{[j_1 j_2]_i} \int \mathrm{d}s\, q_{[j_1 j_2]_i}(s) q^{\dagger}_{[j_1 j_2]_i}(s) \theta_{\alpha,[j_1 j_2]_i} \\ &= v_P \exp(\beta\mu_i + \ln(\bar{N})) \frac{\bar{Q}_i}{V} f_{\alpha,i} \frac{N_i}{\bar{N}}, \end{aligned}$$

where $\theta_{\alpha,[j_1 j_2]_i}$ is one if the block $[j_1 j_2]_i$ has the type α and zero otherwise, the sum $[j_1 j_2]_i$ runs over all blocks in the chain i and $f_{\alpha,i}$ is the fraction of chain type i that is of type α. The average volume contribution of the polymer i of monomer type α can also be written as:

$$\bar{\phi}_{\alpha,i} = \frac{w_i f_{\alpha,i} N_i}{\bar{N}} \bar{\phi}.$$

Equating the two equations above leads to Eq. (5.7). We should note that Eq. (5.7) remains valid even if $\bar{Q}_i$ is not evaluated in SCF approximation, but by more sophisticated means. Taking into account effects of nonideal chain conformations, *e.g.*, due to the fact that solvophobic blocks of isolated chains might collapse[230], would shift the values of $\bar{Q}_i$ and hence μ_i. Here, we neglect such effects for consistency. In full inhomogeneous SCF calculations, the micelles are also surrounded by a homogeneous solution, and we design the study such that this solution is equivalent to the reservoir solution.

5.7 Supporting Information

Here we show some additional results to further illustrate or support arguments made in the main text. Fig. 5.10 shows the distribution differences between micelles of different sizes and the bath. As is evident, smaller chains contribute to an increase in the size of the micelle, although from the PDI = 1 case it is also clear that also chains with certain degrees of branching might be more favored with increasing micelle size. The latter effect is albeit less pronounced. In Fig. 5.11, we plot the volume fraction contributions from two different types of polymers, a short and a long one, in a LHBC system containing an equilibrium spherical micelle (Fig. 5.11a,b) and a stretched micelle (Fig. 5.11c,d), as obtained from the work presented in the main text. To interpret the results, we recall some specifics of our setup: Whereas the sets of chain types in an SCF calculation are constructed such that the molecular weights distributions roughly follow a Schulz-Zimm distribution, all chain types within such a set have equal *a priori* probability. Moreover, the solvophobic blocks of all chains have equal length. Therefore, Figs. 5.11a,c illustrate that micelles preferably recruit chains with short solvophilic parts, consistent with Fig. 5.10 and Fig. 5.5c in the main text. Interestingly, however, the contribution of solvophilic monomers to the total volume fraction is comparable for short and long chain types, the main difference being that the solvophilic monomers of shorter chains tend to be closer to the core than those of longer chains. Additionally, the short chain's solvophilic contribution shown in (b) exhibits two maxima, one in the center and one near the corona, which is not seen at all for the long chain. As explained in the main text, this effect is attributed to the fact that the short chain is almost completely solvophobic, such that solvophilic blocks can be pulled inside the core at low energy cost. The same trends are observed in the aspherical micelle shown in (c) and (d). In the aspherical case, the main maxima of the solvophilic distributions shift to larger distances along the long axis and smaller distances along the short axis for both short and long chains, while their positions relative to each other remain unchanged.

Fig. 5.12 shows the radius of the micelles for spherical micelles with and without encapsulation of homopolymers. The results demonstrate that the radius of the micelle increases with encapsulation for all LHBC systems, whereas for the LDBC systems, the radius of the micelles is unchanged. This is consistent with the picture that LDBC micelles are less prone to changes in their structure and therefore accommodate a reduced payload compared to the other classes of polymers.

In Fig. 5.13, the free energy difference between the inhomogeneous state and the homogeneous state, ΔF, is shown for the different polymer systems with encapsulated homopolymers. Also shown is the the critical volume fraction $\bar{\phi}_c$ and the equilibrium morphology.

Finally, as illustrated in Figs. 5.14a and 5.14b, there exists a positive correlation between the order of addition of the AB_2 monomers, the generation they occupy on the

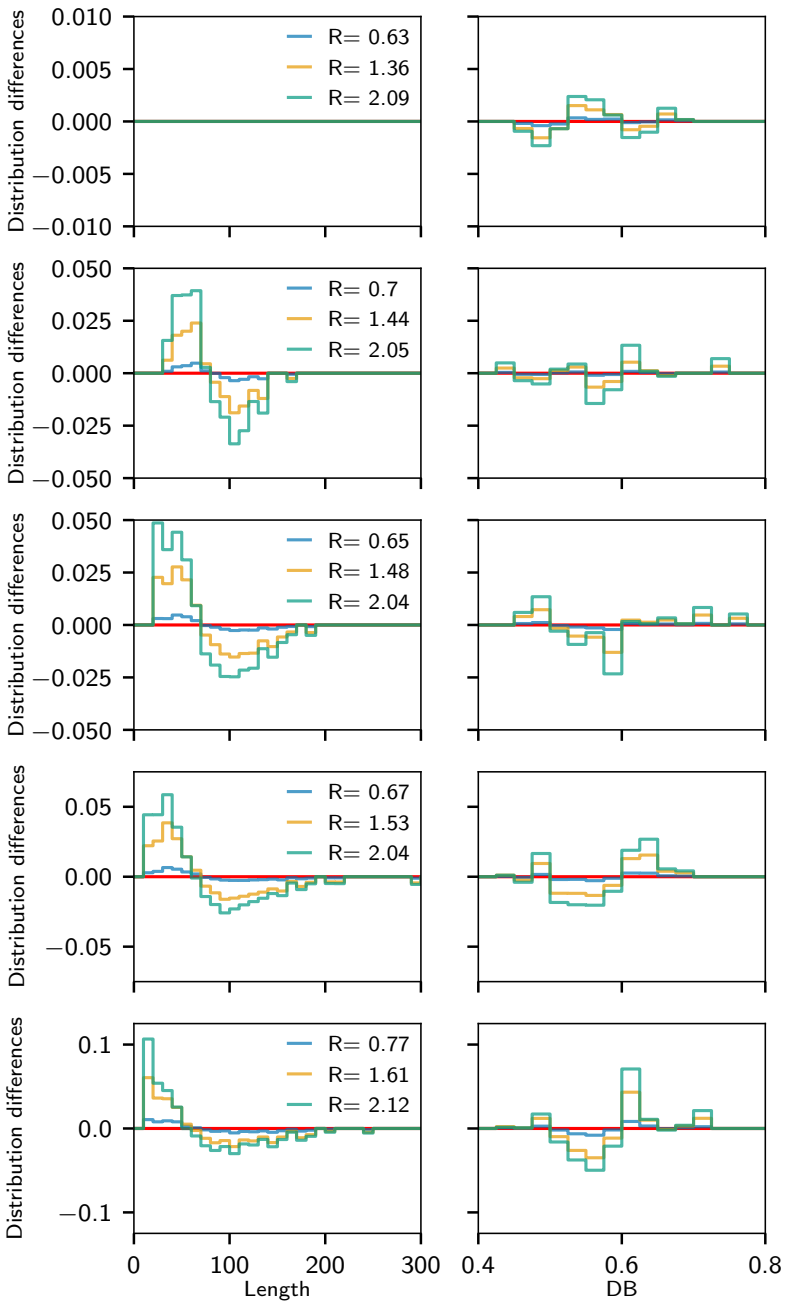

Figure 5.10: Probability distributions differences between the micelle and the bath, in the length (left) and degree of branching (DB) (right) for the hyperbranched part of the LHBCs for different values of PDI. From top to bottom each row corresponds to PDIs of 1, 1.1, 1.2, 1.3 and 1.4. The different colors correspond to the critical micelle (micelle at maximum), the equilibrium micelle (micelle at minimum) and the largest micelle we obtained from Fig. 5.7 in the main text respectively.

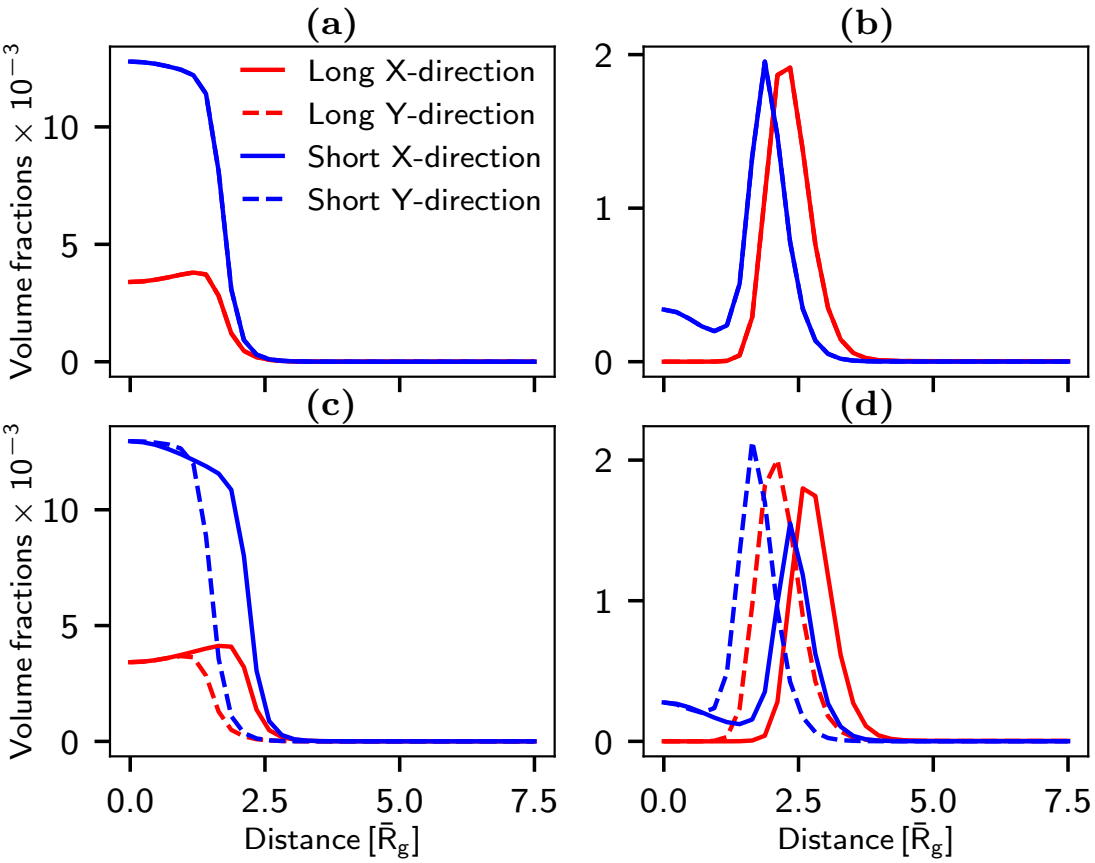

Figure 5.11: (a) Solvophobic and (b) solvophilic volume fraction contribution of a short chain (blue) and a long chain (red) in a spherical micelle. (c) Solvophobic and (d) solvophilic volume fraction contribution of a short chain (blue) and a long chain (red) in a micelle with an asphericity of A=0.8 in the long axis direction X (solid line) and the short axis direction Y (dashed line). The short chain has a solvophilic length of 23 while the long chain has a length of 109, while the solvophobic block is 84 for both as stated in the main text. The results correspond to the system with PDI = 1.4 as shown in Fig. 5.8 in the main text.

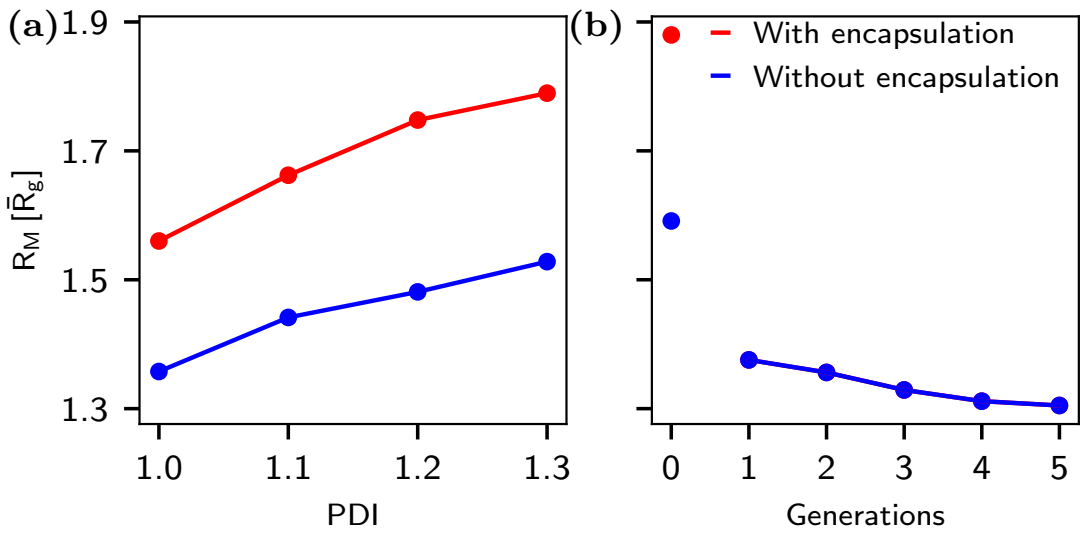

Figure 5.12: Radius R_M of the micelle as a function of the polydispersity for the LHBC systems (a) and as a function of the number of generations for the LDBC systems (b). The red lines correspond to the case where the calculations have been performed with encapsulation of a homopolymer and blue without. All calculations were performed for the equilibrium spherical micelle. Note that the red and blue lines coincide in (b).

growing molecule, and their distance from the micelle center. Although the spread is significant, adding suitably functionalized AB_2 monomers either at the very beginning or the very end of the synthesis process could be viable strategies for positioning functional units inside or at the outer end of the corona, respectively.

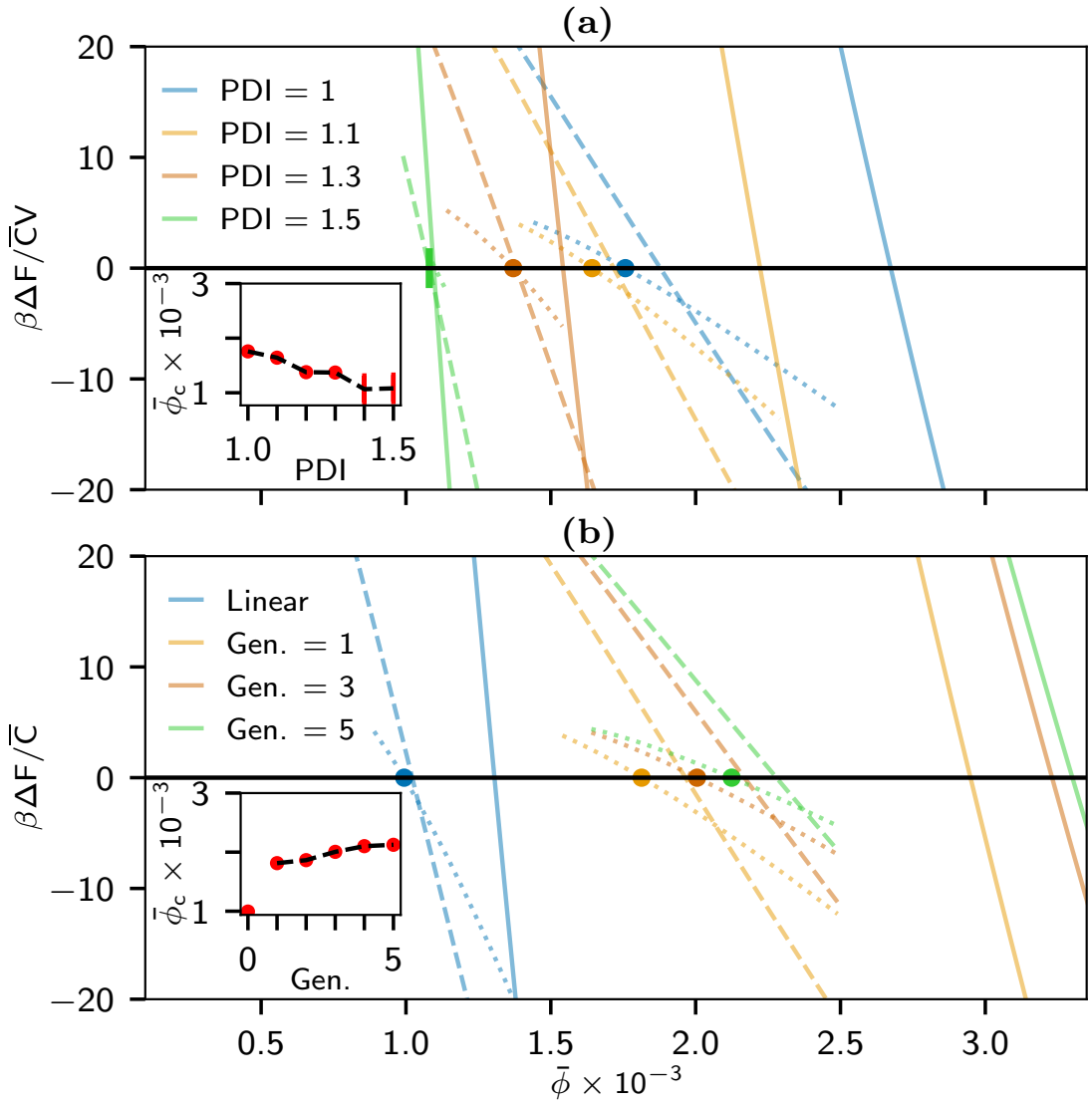

Figure 5.13: Rescaled free energy difference ΔF between homogeneous and inhomogeneous states in the presence of homopolymer model drug ($\bar{\phi}_h = 10^{-5}$ in the bath) against the average copolymer volume fraction $\bar{\phi}$ in the bath for polydisperse LHBCs and monodisperse linear and LDBCs respectively. Each color corresponds to a different polymer system, while the style of the line corresponds to lamella (solid line), cylindrical (dashed line) and spherical (dotted line) micelle states. The inset axes in figures (a) and (b) show the state with the lowest critical concentration $\bar{\phi}_c$ against PDI and number of generations respectively. The circular (●) and rectangular (▌) symbols indicate spherical micelles and cylindrical micelles respectively as the equilibrium morphology. These symbols are also shown in Fig. 5.5 in the main text. Note that $\bar{\phi}_c$ and $\bar{\phi}$ are calculated without $\bar{\phi}_h$.

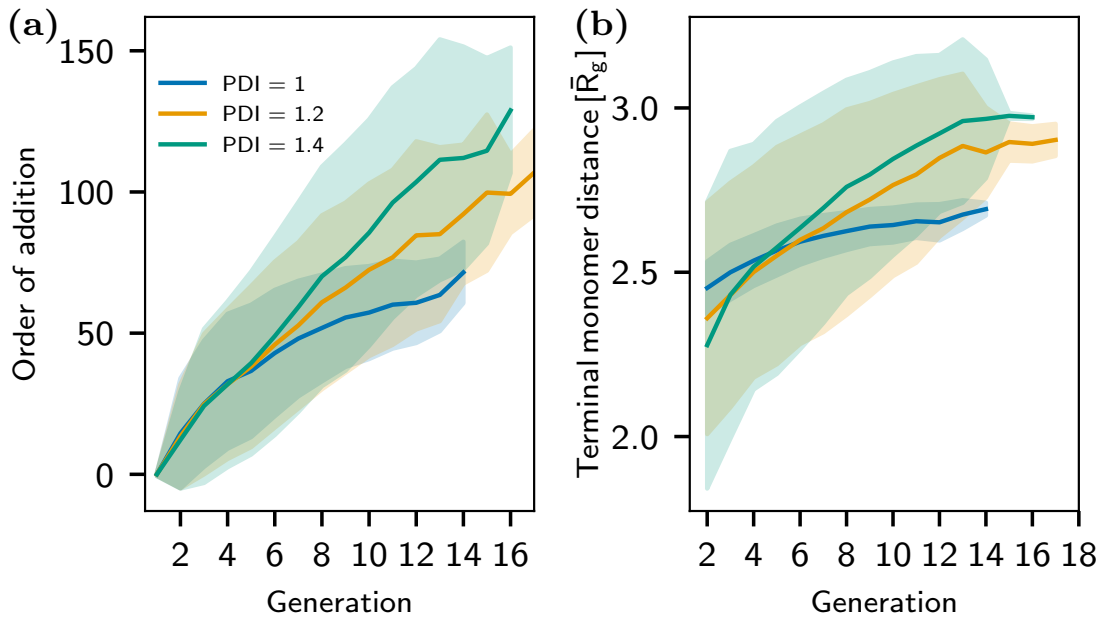

Figure 5.14: (a) Order of addition of monomers vs. their corresponding generation in each polymer molecule. Results from BA batch. (b) Mean distance of terminal monomers from the center of the equilibrium micelle vs. corresponding generation. Results from averaging B1-B4.

6

INFLUENCE OF GRADIENT ON GRADIENT COPOLYMER MICELLE MORPHOLOGIES IN SOLUTION

Note: A publication containing the content of this chapter and additional experimental and theoretical results by other authors is currently in preparation.

Author list: Thi T. D. Dinh, Giannakou Marios, Mikhail Laktionov, Kinza Y. Ghulam, Sebastian Pusse, Ioannis Tzourtzouklis, Nora Fribiczer, Sebastian Seiffer, George Floudas, Markus Gallei, Oleg V. Borisov, Friederike Schmid and Axel Müller.

6.1 Introduction

Over the past decades, driven by the need to explore alternatives to traditional block copolymers, scientists have developed new synthetic protocols that enable the preparation of copolymers with a prescribed monomer distribution along the polymer backbone[231]. These polymers, known as gradient copolymers, differ from similar types such as alternating or random copolymers[232], in that they can undergo microphase separation in solution to form symmetric structures, including spherical micelles, worm-like micelles, vesicles, multimicellar aggregates, and more[40,231,233–236].

Gradient copolymers have been studied extensively due to the unique advantages they offer over traditional block copolymers. For instance, spherical micelles formed by gradient copolymers exhibit morphologies that differ significantly from those predicted for diblock copolymers. In the case of diblock copolymers, micelles typically consist of two well-defined regions: a core composed of solvophobic monomers and a corona dominated by solvophilic monomers. In contrast, gradient copolymers can produce micelles with less distinct core–corona separation, depending on the nature of the gradient. As a result, solvophilic monomers may be found within the core, and solvophobic monomers may extend into the corona[38–40].

The distinct internal environment of gradient copolymer micelles has attracted significant interest for drug delivery applications[237]. These micelles provide a unique core environment for drug encapsulation, offer advantageous drug release profiles[41], and have been shown to enhance transfection efficiency[42]. Additionally, they are often synthesized via a one-pot or one-step process, which simplifies production by circumventing the multi-step synthesis typically required for block copolymers. In such protocols, monomers are added sequentially to a growing polymer chain, with the more reactive monomer incorporated earlier and the less reactive monomer later in the sequence[238]. When all monomers are added at once, the resulting gradient is governed by both the relative reactivities of the monomers and their initial feed ratios[238,239]. However, the gradient profile can also be tuned by controlling the monomer addition rate[238,240] or by using light-mediated polymerization techniques[241].

Another approach to tuning gradient copolymer structure involves using a suitable solvent and/or catalyst to modify monomer reactivity. For example, Steube *et al.* [29], demonstrated that the polymerization of styrene and isoprene monomers in cyclohexane can be controlled via the ratio of tetrahydrofuran [THF] to sec-butyllithium [Li], which governs the kinetics of the polymerization. By selecting an appropriate ratio, the gradient of the final polymer could be effectively tuned. This tunability was then used to show that a melt of polymers composed of a 1:1 styrene–isoprene monomer ratio could adopt a variety of morphologies depending on the gradient. This is shown in Fig. 6.1, which illustrates the possible morphologies, including lamellae, hexagonally packed cylinders, and gyroid structures.

To a certain extent, one can envision these gradient copolymers as equivalent to diblock copolymers with block fraction f, whereby modifying the gradient effectively shifts f from approximately 0 to 1. As a result, increasing the [THF]/[Li] ratio corresponds to moving from left to right across the phase diagram for diblock copolymer melts (shown in Fig. 2.4c).

The purpose of this study is therefore to examine whether changes in the polymer gradient of gradient copolymers in solution can induce morphological transitions analogous to those observed in the melt—i.e., from spherical micelles to worm-like micelles or vesicles.

6.2 Theoretical modeling of gradient copolymers

We model styrene-isoprene gradient copolymers in *n*-decane at the mesoscale using self-consistent field theory (SCFT). Given that the system consists of nanoparticles dispersed in a solvent, and that polymer chains can dynamically exchange with the surrounding medium, we adopt a grand canonical ensemble framework. This approach allows for the exchange of polymer chains between the system and its environment.

To describe interactions both among polymers and between polymers and the solvent, we employ Flory–Huggins theory. The solvent is treated implicitly and modeled using the Sanchez–Lacombe theory[58].

For clarity in notation, we denote solvophobic monomers as A (styrene), solvophilic monomers as B (isoprene), and the solvent as S (*n*-decane). Their corresponding volumes are given by v_A, v_B, and v_S, respectively. We assume a monodisperse ensemble of Gaussian chains, each consisting of N segments, with an ideal radius of gyration denoted by R_g.

The system is then described by the following equations:

$$\beta F_{GC} = \left(U_{inter.} - \frac{1}{v^*} \int d\boldsymbol{r} \sum_{\alpha}^{A,B} (\rho_\alpha(\boldsymbol{r}) v^*) W_\alpha(\boldsymbol{r}) - \exp(\beta\mu) Q \right) \tag{6.1}$$

$$U_{inter.} = \frac{1}{v^*} \int d\boldsymbol{r} \left(\sum_{\alpha}^{A,B} \chi_{\alpha S} \phi_\alpha(\boldsymbol{r}) + \frac{1}{2} \sum_{\alpha,\beta}^{A,B} \chi_{\alpha\beta} \phi_\alpha(\boldsymbol{r}) \phi_\beta(\boldsymbol{r}) + v^* (\rho_S(\boldsymbol{r}) \ln(\phi_S(\boldsymbol{r})) - \rho_S(\boldsymbol{r})) \right) \tag{6.2}$$

$$\phi_\alpha(\boldsymbol{r}) = \rho_\alpha(\boldsymbol{r}) v_\alpha \tag{6.3}$$

$$\phi_S(\boldsymbol{r}) = \rho_S(\boldsymbol{r}) v_S = 1 - \sum_{\alpha}^{A,B} \phi_\alpha(\boldsymbol{r}) \,, \tag{6.4}$$

where F_{GC} is the grand canonical free energy, $U_{inter.}$ is the interaction potential associated with an implicit solvent and the Flory-Huggins interactions, v^* is a reference volume, ρ_α and ϕ_α are the number density and volume fraction of the monomer of

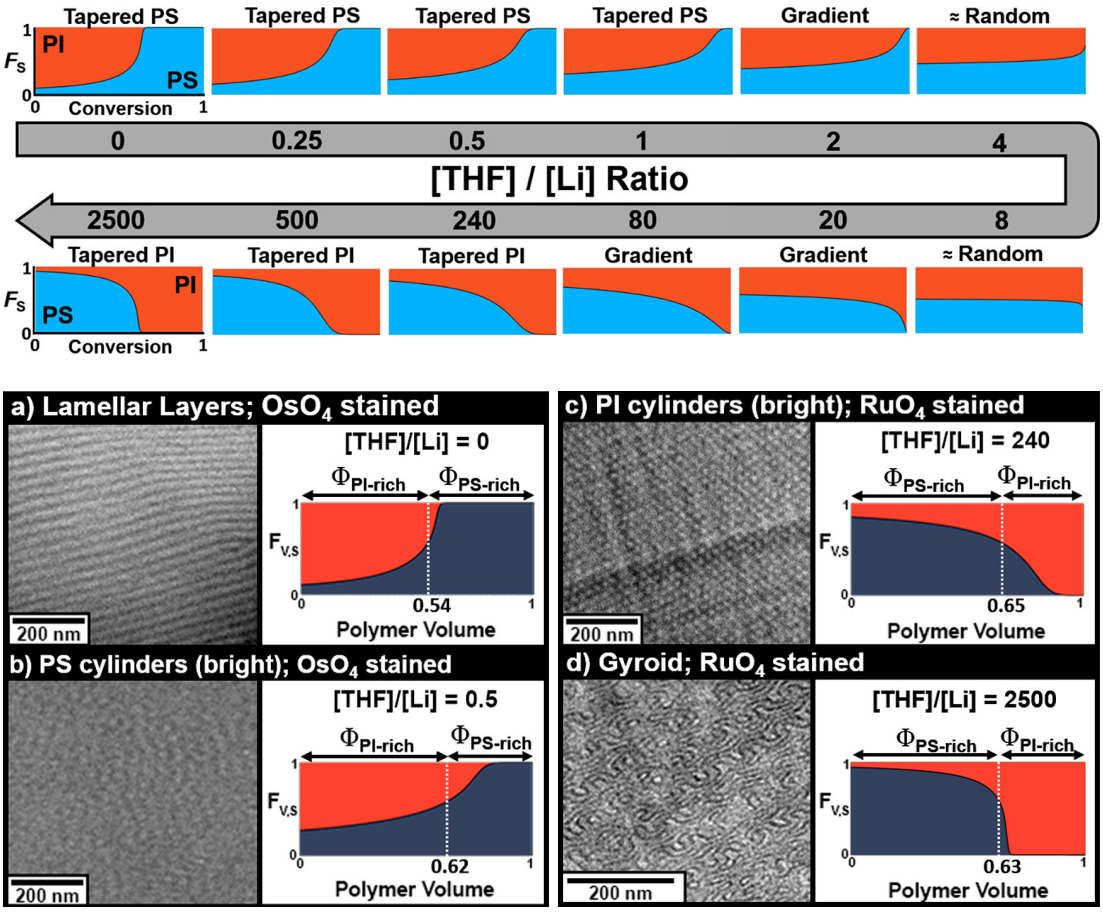

Figure 6.1: Top: Gradient compositions achieved using different [THF]/[Li] ratios, with polystyrene (PS) and polyisoprene (PI) segments shown in blue and red, respectively. Bottom: Transmission electron microscopy images of polymer melts from gradient copolymers synthesized under varying [THF]/[Li] ratios, resulting in the following morphologies: (a) lamellae, (b) hexagonally packed PS-rich cylinders, (c) hexagonally packed PI-rich cylinders, and (d) bicontinuous gyroid. Adapted with permission from Steube *et al.* [29]. Copyright 2025 American Chemical Society.

type α respectively, ρ_S and ϕ_S are the solvent's number density and volume fraction respectively, W_α (given in the Appendix by Eq. (6.8)) is the self-consistent field of monomer type α, μ is the chemical potential, V is the volume of the simulation box and Q is the single chain partition function (given in the Appendix by Eq. (6.15)). The chemical potential μ is determined by assuming that the system is in contact with a homogeneously distributed reservoir of free chains, characterized by an average volume fraction $\bar{\phi}$. In SCFT, this average volume fraction determines the chemical potential via Eq. (6.17), given in the Appendix.

Lastly, we assume that the monomers comprising the polymer chains are described by a hybrid of A and B types, such that the local composition along the chain is governed by gradient functions $g(s)$ and $1 - g(s)$, representing the contributions of A and B monomers, respectively. Here, $s = \mathfrak{n}/N$ is the normalized contour variable, where $\mathfrak{n}$ is the monomer index and N is the total number of statistical segments, which we assumed to be all of equal size b. The gradient function $g(s)$ is normalized such that $\int_0^1 ds\, g(s) = f_A$, with the condition $f_A + f_B = 1$, where f_A and f_B denote the overall fractions of A and B monomers in the copolymer.

6.3 Results & Discussion

6.3.1 Theoretical predictions for experimental gradient copolymers

The Flory-Huggins parameters between the solvent and the polymer can be empirically estimated via the "Flory-Huggins/Hansen Solubility Parameters" (FH/HSP) formula[226]. The FH/HSP equation between solvent "S" and monomer type "α" is given by:

$$\chi_{12} = \frac{\lambda\, v_S \left((\delta_{dS} - \delta_{d\alpha})^2 + 0.25(\delta_{pS} - \delta_{p\alpha})^2 + 0.25(\delta_{hS} - \delta_{h\alpha})^2 \right)}{RT}, \tag{6.5}$$

where δ_d, δ_p and δ_h are the dispersion, polar and hydrogen bonding cohesion parameters respectively and v_S is the molar volume of the solvent. The multiplicative term $\lambda = 0.6$ is empirical, R is the gas constant, T is the temperature and the dispersion parameters are given in Table 6.1.

The dispersion parameters for the lone molecules of styrene and isoprene, as well as for their polymers, polystyrene and polyisoprene are also presented in Table 6.1. At a temperature of 25°C, given the parameters for the lone molecule parameters, the predicted Flory-Huggins parameters are $\chi_{AS} = 0.61$ (poor solvent) and $\chi_{BS} = 0.27$ (good solvent), while using the parameters for the polymers, the parameters are $\chi_{AS} = 2.1$ (poor solvent) and $\chi_{BS} = 0.07$ (good solvent). The Flory–Huggins interaction parameter between polystyrene and polyisoprene can be more accurately estimated using the approach found in Willis *et al.* [242], which yields a value of $\chi_{AB} = 0.13$. Due to the significant discrepancy between the more accurately predicted value of χ_{AB} and the empirically estimated χ_{AS} derived from polystyrene solubility parameters, we

	δ_d (MPa)$^{1/2}$	δ_p (MPa)$^{1/2}$	δ_h (MPa)$^{1/2}$
Styrene	18.6	1.0	4.1
Polystyrene	21.3	5.8	4.3
Isoprene	14.7	1.4	4.1
Polyisoprene	16.57	1.41	−0.82
n-decane	15.7	0.0	0.0

Table 6.1: Hansen solubility parameters table as found in Ref. [226].

choose to estimate the Flory–Huggins parameters using the solubility parameters of the individual molecules, as this approach appears more appropriate for the systems considered. In addition, we assume the statistical segment volumes of styrene and isoprene are the same and equal to the reference volume, i.e. $v_A = v_B = v^*$, and take the reference molar volume to be the average molar volume between styrene (115.6 mL/mol) and isoprene (100.9 mL/mol). Lastly, we choose a macromolecular length of $\mathcal{N} = 232$ based on experiments done by our collaborators [243] and since the molar volume of *n*-decane is $v_S = 196$ mL/mol, then $v_S/(v^*\mathcal{N}) = 0.00776$.

Now consider a scenario in which polymer chains are gradually introduced into a solution from the bulk phase. At low polymer concentrations, the chains tend to disperse to maximize their configurational entropy. As the concentration increases, a critical point is reached where self-assembly begins, resulting in the formation of distinct nanostructures. This process can be modeled within the grand canonical ensemble, where the chemical potential—acting as the driving "force"—is incrementally increased to promote chain incorporation into the nanostructures. We define the critical chemical potential as the value at which the free energy of the inhomogeneous system equals that of the homogeneous state, as determined by SCFT.

Using this framework, SCFT can converge to both equilibrium and metastable states that remain stable relative to the homogeneous phase within specific chemical potential ranges. The true equilibrium state corresponds to the lowest free energy. However, the final state to which the SCFT scheme converges depends, among other factors, on the initial guess, the mixing method, the imposed symmetry constraints, and the discretization of both the polymer chain and spatial domain.

This dependence restricts the exploration to a limited set of nanoparticle configurations. For example, in three-dimensional Cartesian coordinates, we were only able to recover the spherical micelle structure. In contrast, by using two- and one-dimensional Cartesian coordinates, we successfully converged to additional morphologies, including infinite cylindrical micelles (ignoring caps at the end) and lamellae, the latter also corresponding to large vesicle-like formations.

To accurately evaluate the relative energetic stability of these conformations, precise free energy calculations are crucial. Accordingly, we exploited the spherical and cylindrical symmetries of the aforementioned states and performed one-dimensional calculations, which enable finer chain discretization and consequently improve the accuracy of the results. To maintain consistency across all cases, we used a chain discretization of $0.0001N$, a spatial discretization of $0.1R_g$ and the simulation domains extended $15\,R_g$ in the relevant coordinate direction (Cartesian, cylindrical, or spherical).

In Fig. 6.2, we present the difference in free energy between the homogeneous and inhomogeneous states, given by $\beta\Delta F/\overline{C} = \beta(F_{GC}^{hom.} - F_{GC}^{inhom.})/\overline{C}$, where:

$$\overline{C} = R_g^3/(v^*N), \tag{6.6}$$

denotes the Ginzburg parameter. This is shown for various gradient conditions and three different morphologies: spherical micelles, infinite cylindrical micelles, and vesicles. The critical concentration, $\bar{\phi}_c$, is identified as the point at which each curve intersects the zero line. Only gradients that result in a stable inhomogeneous state are shown, although all twelve were tested (all gradients shown in Fig. 6.1).

For the cases [THF]/[Li] = 0, 0.25, 0.5, 240, 500, and 2500, stable nanostructures were obtained across all three morphologies. In contrast, for [THF]/[Li] = 80, only the lamellar structure proved stable. The figure also highlights, for each gradient, the morphology with the lowest $\bar{\phi}_c$, indicating the most stable morphology. The resulting stable morphologies are: [THF]/[Li] = 0 (sphere), 0.25 (cylinder), 0.5 (vesicle), 80 (vesicle), 240 (cylinder), 500 (sphere), and 2500 (sphere). This behavior aligns with previous observations in the bulk phase of gradient copolymers[29], where morphological variation arises from changes in the gradient under otherwise identical conditions.

It is important to note that, except for the case of [THF]/[Li] = 80, the other gradients that exhibit stable morphologies, also exhibit near degeneracy between spherical and infinite cylindrical micelles near the CMC, making it challenging to unambiguously identify the most stable configuration. A limitation of the current model is the neglect of the translational entropy and interactions between the nanoparticles. Additionally, in the case of infinite cylindrical micelles, the energetic contribution from spherical end caps—necessary to make them finite—is not accounted for. This omission effectively results in a rightward shift of the energy curves for the cylindrical and lamellar states, which would then help lift their near degeneracy near the CMC.

Preliminary experimental results on the same system, shared via private communication[243], using dynamic light scattering (DLS) and transmission electron microscopy (TEM), confirm the presence of spherical micelles in several cases (Fig. 6.3). However, vesicles or worm-like micelles have not been confirmed. Small-angle X-ray scattering (SAXS) measurements, on the other hand, suggest the presence of elongated micelles—morphologies (at high concentrations) that cannot be distinguished by DLS and are potentially altered during TEM sample preparation due to the drying procedure required in taking the images.

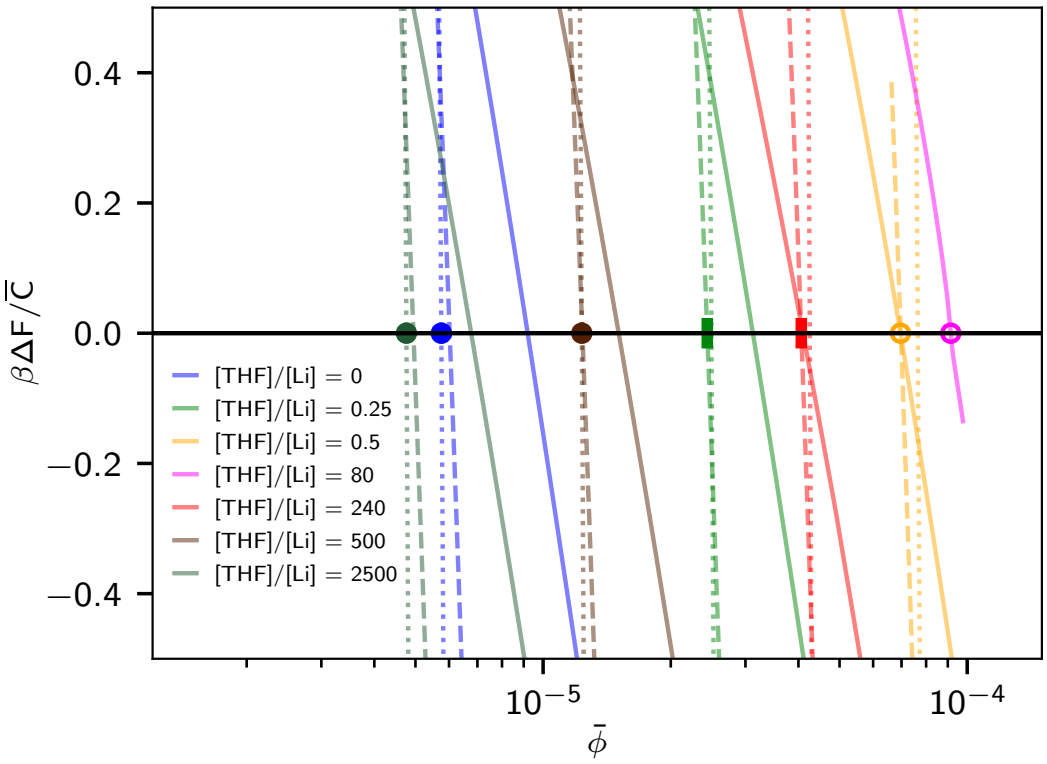

Figure 6.2: Plot of average volume fraction of free polymer chains $\bar{\phi}$ as determined by Eq. (6.17) against the difference in energy of $\beta\Delta F/\overline{C}$ as defined in the main text, where $\overline{C}$ is the Ginzburg parameter (Eq. (6.6)). Each color represents different gradients determined from the [THF]/[Li] ratios as shown in Fig. 6.1. The solid lines represent the lamellae, the dashed lines the cylindrical micelle and the dotted lines the spherical micelles. The circular (●), rectangular (▮) and open circle (○) symbols denote the state with the lowest critical concentration $\bar{\phi}_c$ out of all three states, with each symbol representing the spherical micelles, cylindrical micelles and the lamellae respectively. Note that although all twelve [THF]/[Li] ratios were tested, only the gradients with at least one converged morphology are shown.

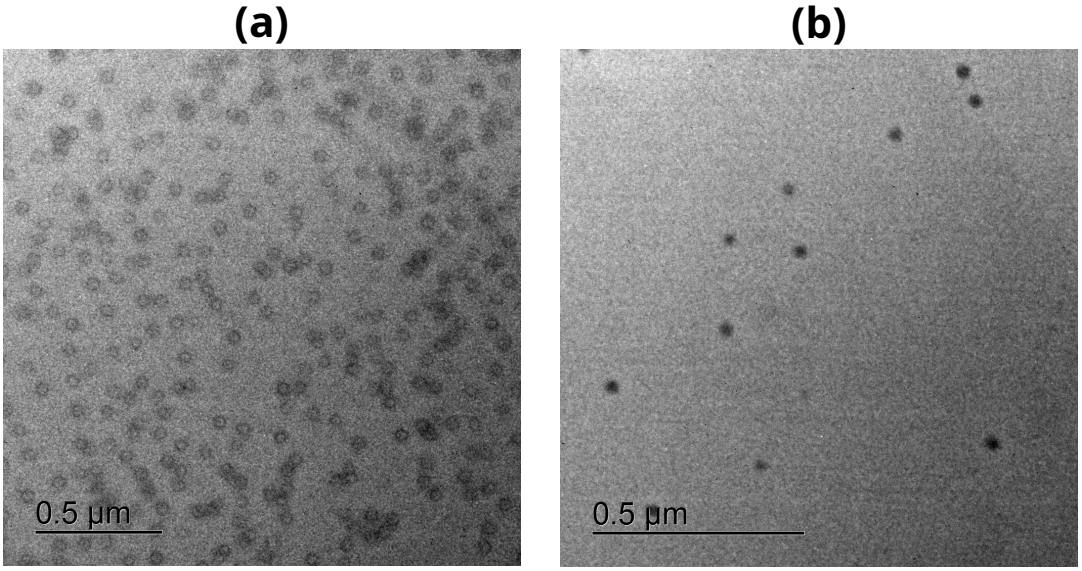

Figure 6.3: Transmission electron microscopy images of micelles composed of gradient copolymers of styrene and isoprene, synthesized at a [THF]/[Li] = 0 ratio (see Fig. 6.1), with a molecular weight of 80,000 g/mol in *n*-decane. (a) The isoprene monomers forming the corona were stained with OsO_4. (b) The styrene monomers forming the core were stained with RuO_4. Preliminary results used with permission of the authors[243].

Before proceeding further, several caveats must be addressed. First, the Flory-Huggins parameters used in the model are derived from Hansen solubility parameters and are therefore empirical estimates that may not accurately reflect true interaction strengths. Second, the experimental observation of elongated micelles, coupled with the near-degeneracy in SCFT free energies between cylindrical and spherical micelles, strongly suggests that intermediate structures like elongated micelles would also be energetically competitive—although we fail to capture these less symmetric states using 3D SCFT calculations. Lastly, while Fig. 6.2 clearly shows that the gradient of the polymer affects the relative free energies of different morphologies, the particular region of parameter space considered here does not strongly emphasize these differences.

For the remainder of this subsection, we focus on spherical micelles. In Fig. 6.4, we present the volume fraction profiles along with the chain-end distributions for the spherical micelles, corresponding to their respective critical micelle concentrations from Fig. 6.2. While the solvophobic- and solvophilic-rich chain-end distributions are similar in all cases, the volume fraction profiles differ significantly. The solvophobic-rich chain ends are consistently concentrated at the micelle center, whereas the solvophilic-rich chain ends are localized near the corona.

As the gradient flattens (from left to right), the proportion of solvophilic volume fraction within the micelle core increases. The most pronounced contrast is observed between the [THF]/[Li] = 0 and 240 cases (note that [THF]/[Li] = 0.5 and 240 are metastable), corresponding to copolymers with sharp and flat gradients, respectively. In the former case, solvophilic monomers near the micelle center are nearly absent, whereas in the latter, they contribute a substantial fraction. This shows that a change in gradient can influence the internal micelle structure, transforming the core from solvophilic-poor to solvophilic-rich—so-called bitterball micelles[244]. This is most likely due to the solvophilic monomers present in the solvophobic rich part of the polymer, which is the case for the [THF]/[Li] = 240, 500 and 2500 ratios.

Additionally, as the gradient flattens, the corona becomes sharper and smaller. This is caused by solvophobic monomers retracting into the core—an effect observed in both experiments[234] and molecular dynamics simulations[40]. Also, as seen in both simulations[40] and in our results, the maximum volume fraction of solvophilic monomers occurs at the core–corona interface. It is important to note that our choice of Flory–Huggins parameters means that the interaction between solvophilic monomers and the solvent is less favorable than that between the solvophobic monomers and the solvent. However, as seen from the volume fraction profiles of the symmetric diblock spherical micelle shown in the Supporting Information (Fig. 6.8), the same maximum occurs away from the interface.

Finally, the micelle radius, R_M, defined as the point where the solvophobic volume fraction equals 0.2, remains roughly constant across all cases. This observation is also supported by preliminary DLS experiments shared via private communication[243].

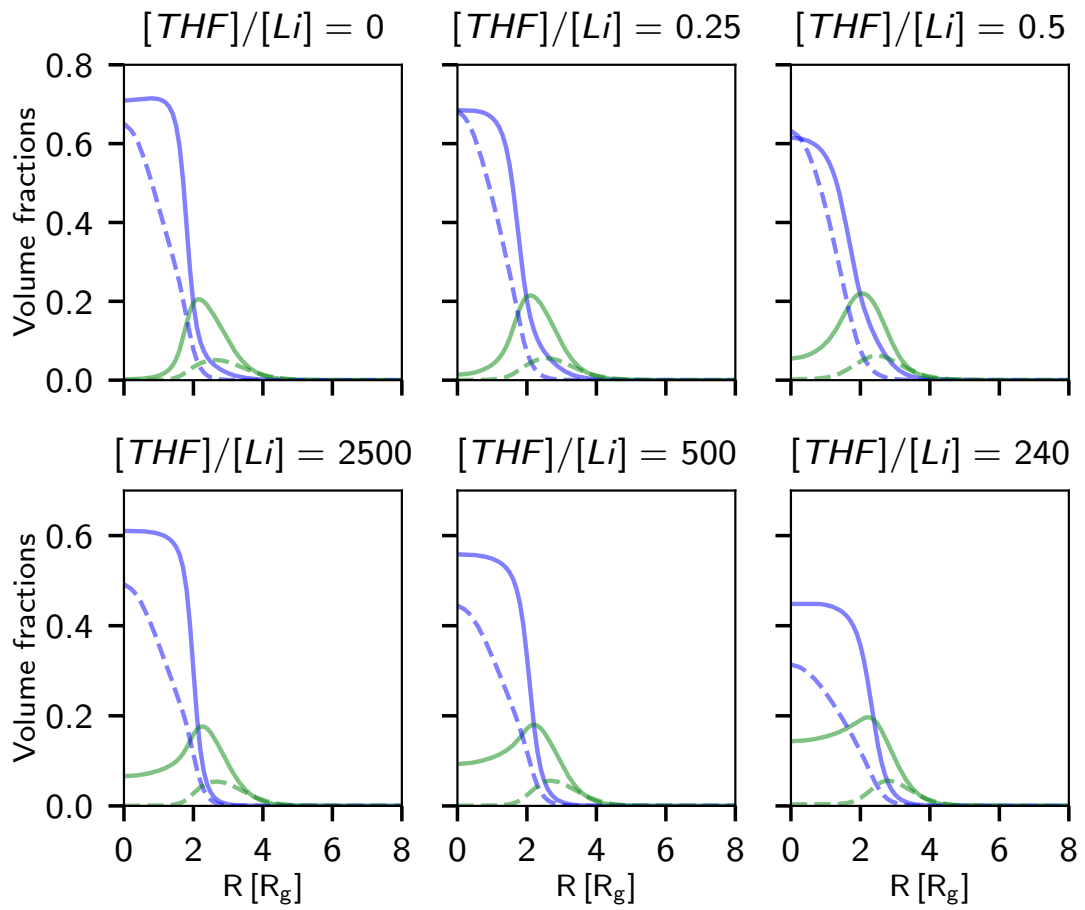

Figure 6.4: Plots of volume fraction profiles (solid lines) and unnormalized chain-end distributions (dashed lines) as a function of radial distance R from the micelle center for various spherical micelles. Blue lines represent the solvophobic volume fraction or the solvophobic-rich chain-end distribution, while green lines represent the corresponding solvophilic components. The first row shows gradient copolymers with only a solvophobic block, while the second row shows those with only a solvophilic block.

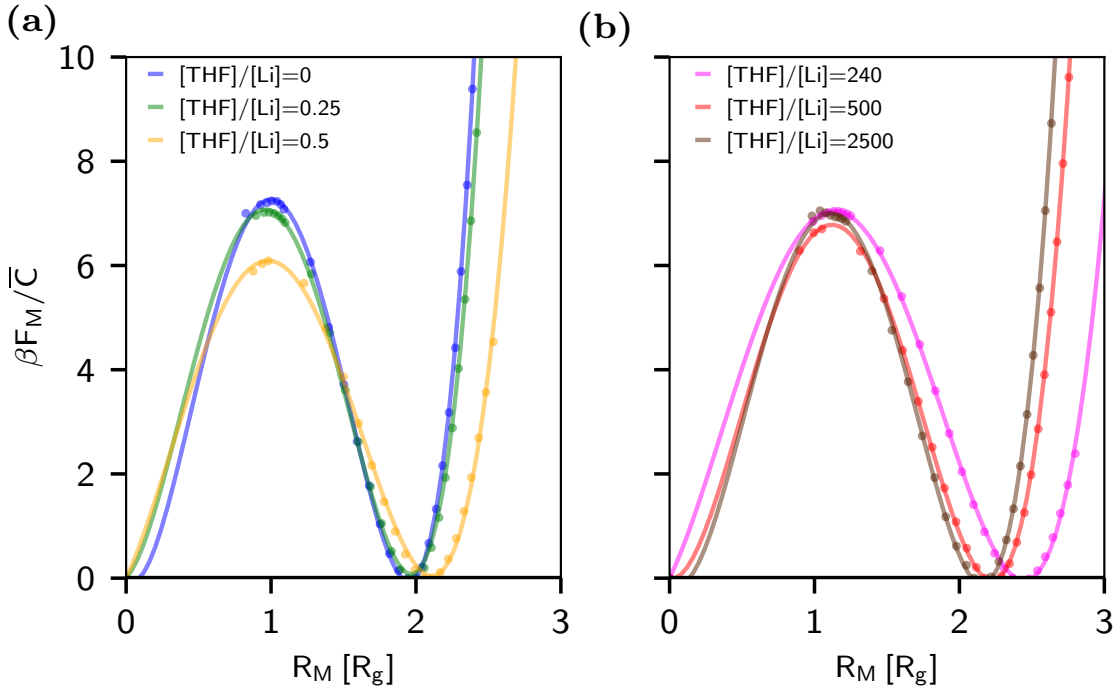

Figure 6.5: Plots of free energy penalty F_M as a function of the micelle radius R_M. The calculations were performed at the critical concentrations. The points correspond to data points and the lines corresponds to a fourth order polynomial fit $f(x) = a_1x^1 + a_2x^2 + a_3x^3 + a_4x^4$ where a_i are all fitting parameters. Figures (a) and (b) show gradient copolymers with a solvophobic block and a solvophilic block, respectively.

Additionally, we investigated the free energy penalty associated with spherical micelles of radius R_M, denoted as $F_M(R_M)$. To this end, we introduce a constraint potential that enables controlled variation of the micelle radius and allows extraction of the corresponding free energy penalty. This constraint potential and its contribution to the field are detailed in the Appendix (Eqs. (6.18)). After convergence, the micelle radius is determined by analyzing the micelle profiles according to our definition of R_M, following a method similar to that of Giannakou *et al.* [245] (Chapter 5). In principle, the micelle size distribution can also be inferred from $F_M(R_M)$, as it is proportional to the Boltzmann factor, i.e., $\propto \exp(-\beta F_M(R_M))$.

The results are presented in Fig. 6.5. Both plots indicate that the micelle radius marginally increases with the flattening of the gradient, although the precise role of the gradient in micelle stability—reflected by the position and size of the maximum in $F_M(R_M)$—remains unclear.

To elucidate the relationship between the gradient and its effect on the properties of the nanoparticles, at a deeper level we explore idealized gradient copolymers in the next section.

6.3.2 Idealized gradient copolymers

We define the idealized gradients by the following functional form:

$$g(s) = \Theta(f_o - s) + \Theta(s - f_o)(\exp\left(-g_o(s - f_o)\right)(1 - c_o) + c_o), \tag{6.7}$$

where Θ is the Heaviside function, f_o signifies the solvophobic block portion of the chain, g_o is what we will refer to as the gradient parameter and c_o is a constant that ensures there are equal parts of solvophobic to solvophilic monomers as in the previous example (see Fig. 6.11 for examples of such gradients).

In Fig. 6.6, we present a phase diagram alongside a density map of the average free chain volume fraction, $\bar{\phi}_c$. To identify the minimum-energy configuration, calculations were performed for three candidate morphologies—spherical, cylindrical, and lamellar—as shown in Fig. 6.2. The resulting morphology of the gradient polymer was determined using the same criteria as before. While the solvophobic block ratio, f_o, exerts the strongest influence on both the values of $\bar{\phi}_c$ and the final morphology, the gradient itself also plays a significant role. In particular, the impact of the gradient is most pronounced within the range $f_o \in [0, 0.25]$ and for flatter gradient parameters, $g_o \in [0, 5]$.

Furthermore, as the gradient flattens or as f_o increases, the critical concentration decreases. Both trends can be attributed to the solvophobic blockiness of the gradient copolymer, which primarily governs its structural behavior. The key observation is that a flatter gradient effectively lengthens the solvophobic block, leading to a shift toward morphologies favored by larger solvophobic blocks. This explains why lower values of g_o produce effects similar to increasing values of f_o.

Lastly, we performed additional calculations on spherical micelles to investigate the micelle size distribution for selected gradients, as shown in Fig. 6.7. The gradient parameter g_o appears to have only a minor effect on the distributions, primarily causing a slight decrease in the equilibrium micelle radius as g_o increases. In contrast, f_o exerts a more significant influence, although its precise role remains somewhat ambiguous. As illustrated in the inset, the micelle's energy barrier to dissolution—i.e., the maximum free energy—increases gradually with increasing values of f_o. However, at $f_o = 0.35$, there is an abrupt rise in the barrier height. This jump may indicate that blockiness near $f_o = 0.35$ is optimal for the formation of stable spherical micelles given our chosen parameters.

6.4 Conclusion

In summary, we have investigated the self-assembly behavior of gradient copolymers composed of a 1 : 1 styrene-isoprene ratio, as described by Steube *et al.* [29], in *n*-decane using SCF calculations. Our results predict a morphological transition from spherical to cylindrical micelles, and eventually to lamellar structures, as the gradient changes

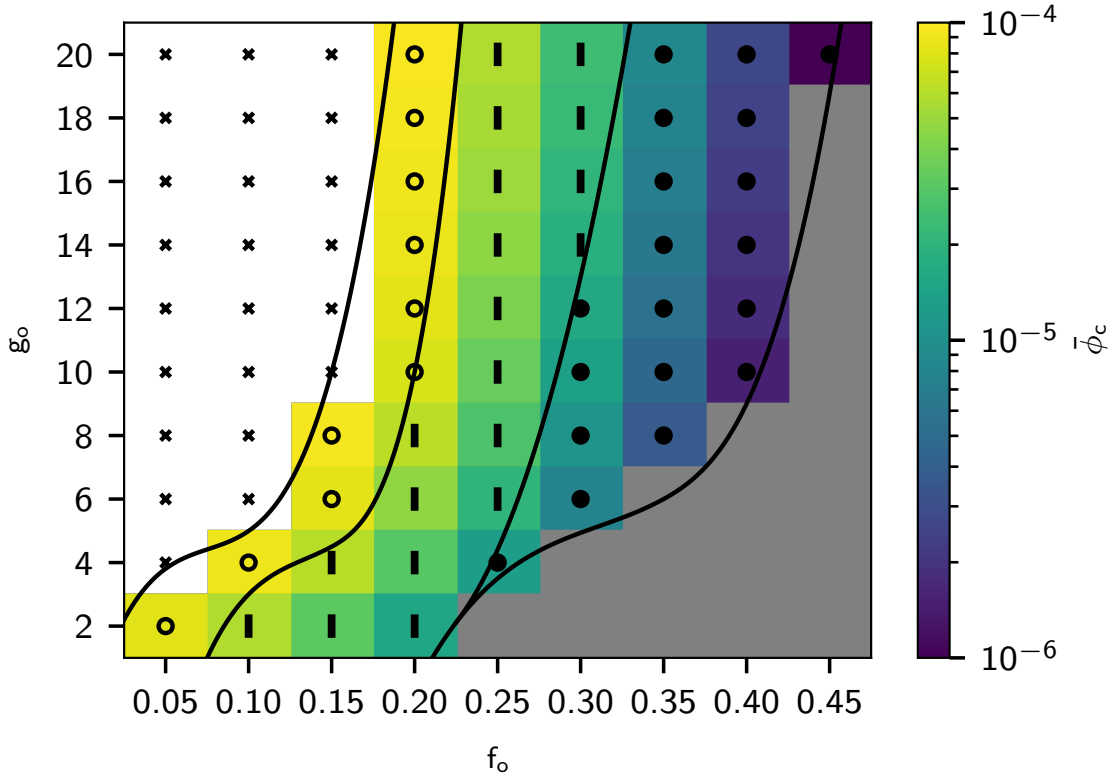

Figure 6.6: Phase diagram and density map of the average free chain volume fraction $\bar{\phi}_c$. Plotted for f_o against g_o, for the idealized gradient polymers defined in Eq. (6.7). The symbols (×), (○), (▌) and (●) signify the disordered, vesicle, cylindrical and spherical states respectively. The grey area signifies the domain of g_o and f_o, which is not possible given the constraint of equal parts of solvophobic to solvophilic monomers. The lines serve as a guide to the eye.

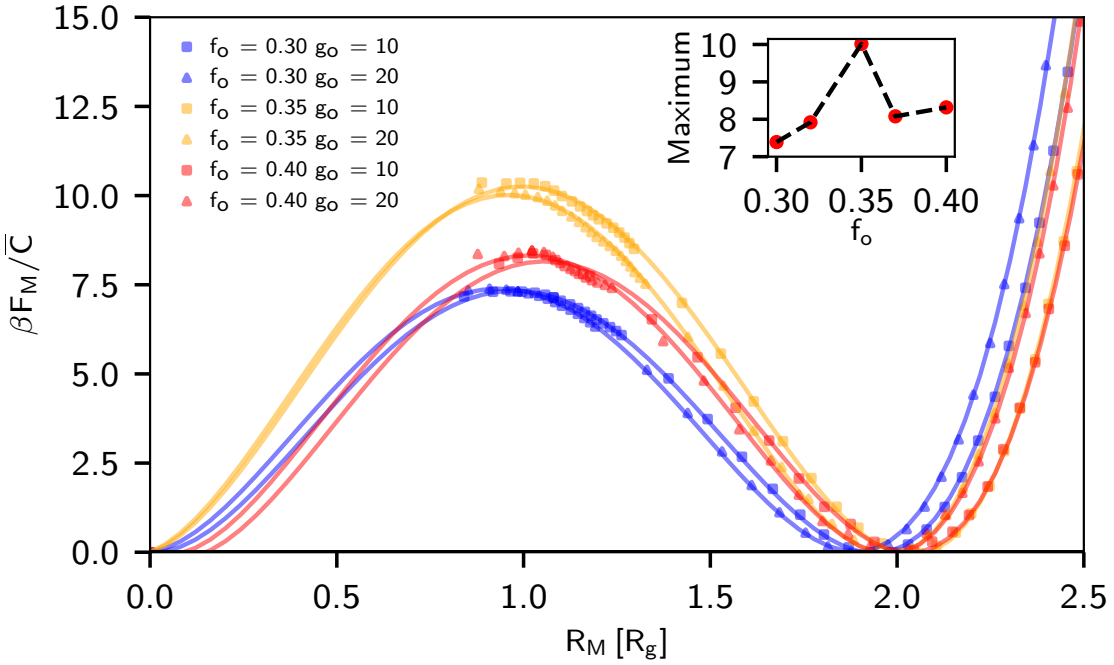

Figure 6.7: Plots of the free energy penalty F_M as a function of the spherical micelle radius R_M for various gradient parameters of idealized gradient copolymers. The parameters used are $f_o = 0.30$ (blue), 0.35 (orange), 0.40 (red), $g_o = 10$ (■) and 20 (▲). The calculations were performed at the critical concentrations. The points correspond to data points and the lines corresponds to a fourth order polynomial fit $f(x) = \sum_{i=1}^{4} a_i x^i$ where a_i are all fitting parameters. The inset shows the maximum values from the main figure's plots for various f_o values at a fixed $g_o = 20$ (including additional points at $f_o = 0.325$ and $f_o = 0.375$ that are omitted from the main figure for clarity). Note that the spherical micelle predicted for the case $f_o = 0.30$ and $g_o = 20$ is only metastable, as illustrated in Fig. 6.6.

from sharp to flat. However, this prediction relies on certain approximations, and the free energy difference between the spherical and cylindrical micelles is relatively small. This suggests that an intermediate morphology—such as elongated micelles, which are challenging to capture in SCF calculations—may be also favorable. Preliminary SAXS experiments, shared via private communication[243], also support this interpretation.

Furthermore, the micelle properties themselves are affected by changes in the gradient. Specifically, we found that the complete absence of either solvophobic or solvophilic monomers from a region of the polymer contour did not affect the position of the maximum in the solvophilic volume fraction profile. This maximum consistently appears at the core–corona interface for our chosen interaction parameters. However, the transition from a solvophilic-poor to a solvophilic-rich core is influenced by solvophilic monomers present within the solvophobic-rich region of the polymer contour.

Additionally, we studied idealized gradient copolymers, also composed of a $1:1$ ratio of solvophobic and solvophilic monomers, with controlled solvophobic block size and gradient sharpness, and constructed a phase diagram based on these parameters. We found that the block size is the dominant factor determining the equilibrium morphology, while flatter gradients also significantly influence morphology by effectively extending the solvophobic block.

Finally, we examined the energy barrier to micelle dissolution and observed that it primarily depends on the solvophobic block size, although the relationship is not strictly monotonic.

Acknowledgments

This work was funded by the German Science Foundation (DFG) within Grant number 446008821, and the Agence Nationale de La Recherche, France. Partial funding was also received by the DFG within Grant number 429613790. M.G. is associate member of the integrated graduate school of the collaborative research center TRR 146 "Multiscale modeling of soft matter systems", grant number 233630050.

6.5 Appendix

In SCFT, it is assumed that polymer chains are long and that the fluctuations of the monomer densities are small, thus the mean field approximation is valid. Therefore it can be assumed that the solution lies upon a saddle-point of the free energy and thus $\delta F_{GC}/\delta\rho_\alpha = 0$, which results in the following expressions for the fields:

$$W_\alpha(\boldsymbol{r}) = \frac{\delta U_{inter}[\phi]}{\delta\phi_\alpha(\boldsymbol{r})}\frac{v_\alpha}{v^*} = \frac{v_\alpha}{v^*}\left(\chi_{\alpha S}\phi_S + \sum_{\beta}^{A,B}(\chi_{\alpha\beta}-\chi_{\beta S})\phi_\beta - \frac{v^*}{v_S}\ln(\phi_S)\right). \tag{6.8}$$

This solution does not necessarily correspond to the global minimum; it may also represent metastable or unstable equilibrium states.

It can also be shown that for a Gaussian chain the forward propagator $q(\boldsymbol{r}, s)$ and backward propagators $q^\dagger(\boldsymbol{r}, s)$, which are the probability distributions of a segment at a point s given an initial condition for each chain end respectively, obey a modified diffusion equation:

$$\frac{dq(\boldsymbol{r}, s)}{ds} = (\frac{b^2}{6}\nabla^2 - \frac{W(\boldsymbol{r}, s)}{N})q(\boldsymbol{r}, s) \tag{6.9}$$

$$\frac{dq^\dagger(\boldsymbol{r}, s)}{ds} = -(\frac{b^2}{6}\nabla^2 - \frac{W(\boldsymbol{r}, s)}{N})q^\dagger(\boldsymbol{r}, s) \tag{6.10}$$

$$W(\boldsymbol{r}, s) = W_A(\boldsymbol{r})g(s) + W_B(\boldsymbol{r})(1 - g(s)), \tag{6.11}$$

where b is the statistical segment length and we have assumed $v_A = v_B$, to simplify the expressions. Since the chain ends are not bound anywhere and they are free to explore the space around them, the initial conditions are given by $q(\boldsymbol{r}, s = 0) = 1$ and $q^\dagger(\boldsymbol{r}, s = 1) = 1$. The propagators are further connected to the volume fractions via the following equations:

$$\phi_A(\boldsymbol{r}) = \frac{v_A}{v^*}\exp(\beta\mu)\int_0^1 ds\, g(s)q(\boldsymbol{r}, s)q^\dagger(\boldsymbol{r}, s) \tag{6.12}$$

$$\phi_B(\boldsymbol{r}) = \frac{v_B}{v^*}\exp(\beta\mu)\int_0^1 ds\, (1 - g(s))q(\boldsymbol{r}, s)q^\dagger(\boldsymbol{r}, s) \tag{6.13}$$

$$\phi_S(\boldsymbol{r}) = 1 - \sum_\alpha^{A,B}\phi_\alpha(\boldsymbol{r}). \tag{6.14}$$

Lastly the single chain partition function is given by:

$$Q = \frac{1}{v^*}\int d\boldsymbol{r}\, q(\boldsymbol{r}, s)q^\dagger(\boldsymbol{r}, s). \tag{6.15}$$

This completes the self-consistent loop, which, given an initial guess for $\phi_\alpha(\boldsymbol{r})$, proceeds by calculating the fields using Eq. (6.8), then solving the modified diffusion equations (Eqs. (6.9)), and finally updating the polymer volume fractions via Eqs. (6.12) along with the new fields. Lastly we define the convergence factor as:

$$CF = \sum_\alpha^{A,B}\int d\boldsymbol{r}\, (\phi_\alpha^{new} - \phi_\alpha^{old})^2, \tag{6.16}$$

and we consider the solution as converged if $CF < 10^{-10}$.

In addition, in a homogeneous fully mixed state, the chemical potential and the average volume fraction of the free polymer chains $\bar{\phi}$ are related by the equation:

$$\exp(\beta\mu) = \bar{\phi}\exp(N(W_A^0 f_A + W_B^0 f_B)), \tag{6.17}$$

where W_α^0 is the homogeneous field that depends on $\bar{\phi}$. Note that there could be two solutions of $\bar{\phi}_c$, for a given chemical potential, in which case we take the lower one.

The differential Eqs. (6.9) were solved in all cases in one dimensional spherical, cylindrical and Cartesian coordinates using the Crank-Nicolson scheme with the Neumann boundary condition $dq(r = 0, s)/dr = 0$ in all cases except the latter, where we used the Pseudo-Spectral method with periodic boundary conditions. As for the mixing scheme, we used Lambda mixing[59] (see Eq. (2.73)).

Lastly we define the constraint potential used to determine the size distribution of the spherical micelles:

$$V_{con}[\phi_A] = \frac{\kappa_{con}}{2v^*}\left(\int d\boldsymbol{r}\phi_A(\boldsymbol{r})\Theta(r - R_{con}) - \phi_{con}\right)^2 \tag{6.18}$$

$$W_A^{con.}(\boldsymbol{r}) = \frac{\delta V_{con}[\phi_A]}{\delta\phi_A(\boldsymbol{r})}\frac{v_A}{v^*} = \kappa_{con}\left(\int d\boldsymbol{r}\phi_A(\boldsymbol{r}) - \phi_{con}\right)\Theta(r - R_{con}), \tag{6.19}$$

where $\kappa_{con}N = 1$ and $R_{con}/R_g = 5$ and ϕ_{con} is varied to yield differently sized micelles.

6.6 Supporting Information

6.6.1 Symmetric diblock

In Fig. 6.8, the volume fractions of a symmetric diblock equilibrium spherical micelle are shown, computed using the parameters provided in the main text. The results indicate that the maximum of the solvophilic volume fraction is shifted away from the core–corona interface, in contrast to the gradient copolymers investigated in the main text.

6.6.2 Constrained micelles

In Fig. 6.5, the energy of micelles is shown as a function of micelle size, which is controlled by the value of ϕ_{con}. As illustrated in Fig. 6.9, varying ϕ_{con} leads not only to changes in micelle radius but also in morphology. Specifically, for all gradient cases shown, the configurations corresponding to $\phi_{con} = -30$, 0, and 60 result in no nanostructure, a spherical micelle, and a semi-vesicle, respectively. Only the spherical micelle data points are included in the derivation of Fig. 6.5.

If we replot Fig. 6.5 with the semi-vesicle points included (taking their radius R_N to be the farthest point found on the $\phi_A = 0.2$ line) we get Fig. 6.10. As shown, the energy of the semi-vesicle is, for certain R_N values, lower than that of the unconstrained spherical micelle in the [THF]/[Li] = 0.5 and 240 cases. Further continuation of the SCF runs using the lowest-energy semi-vesicle as the initial state causes the structure to grow into a vesicle that reaches the boundary of the simulation box, set to $R_{box}/R_g = 15$. However, this does not represent a properly converged state due to boundary constraints.

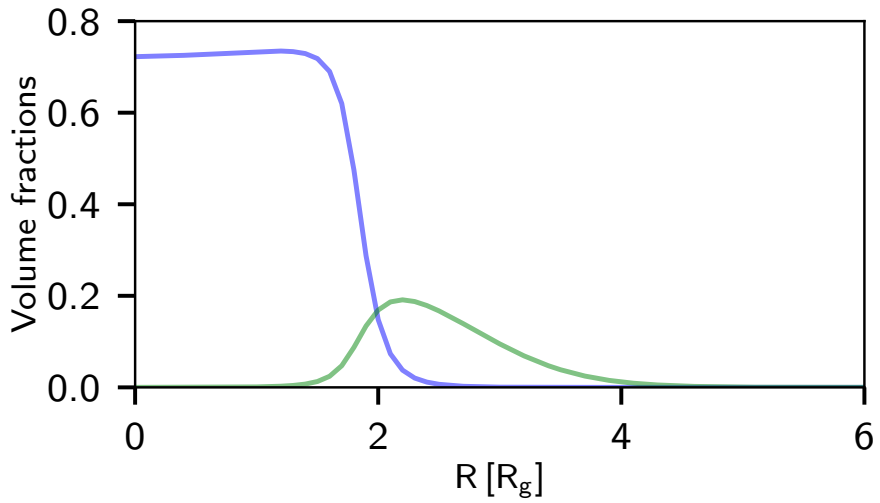

Figure 6.8: Volume fraction profiles of an equilibrium spherical micelle formed by a symmetric diblock copolymer, computed using the parameters provided in the main text. The solvophobic component is shown in blue, and the solvophilic component in green.

In Fig. 6.2, we concluded that the favored morphologies for [THF]/[Li] = 0.25 and 0.5 were infinite cylindrical micelles, while for [THF]/[Li] = 240, it was the vesicle, thus the spherical micelle in these cases is metastable. In the [THF]/[Li] = 0.25 case, the spherical state is almost degenerate to the cylindrical one, while the vesicle state is much less stable than both. However, in the cases [THF]/[Li] = 0.5 and 240, the vesicle state is predicted to be more stable than the spherical state, and these are the two cases where we observe the semi-vesicle states in Fig. 6.10.

6.6.3 Idealized gradients

Examples of various idealized gradients for reference are shown in Fig. 6.11. In Fig. 6.12 the fit of the idealized gradient Eq. (6.7) was performed for six different experimental gradient copolymers, namely the [THF]/[Li] = 0, 0.25, 0.5, 240, 500 and 2500 cases. If we refer to Fig. 6.6 and the fitting parameters f_o and g_o in Fig. 6.12, we can see that the fitting parameters correspond to the spherical, cylindrical and lamellar morphologies which agree with the results of Fig. 6.2.

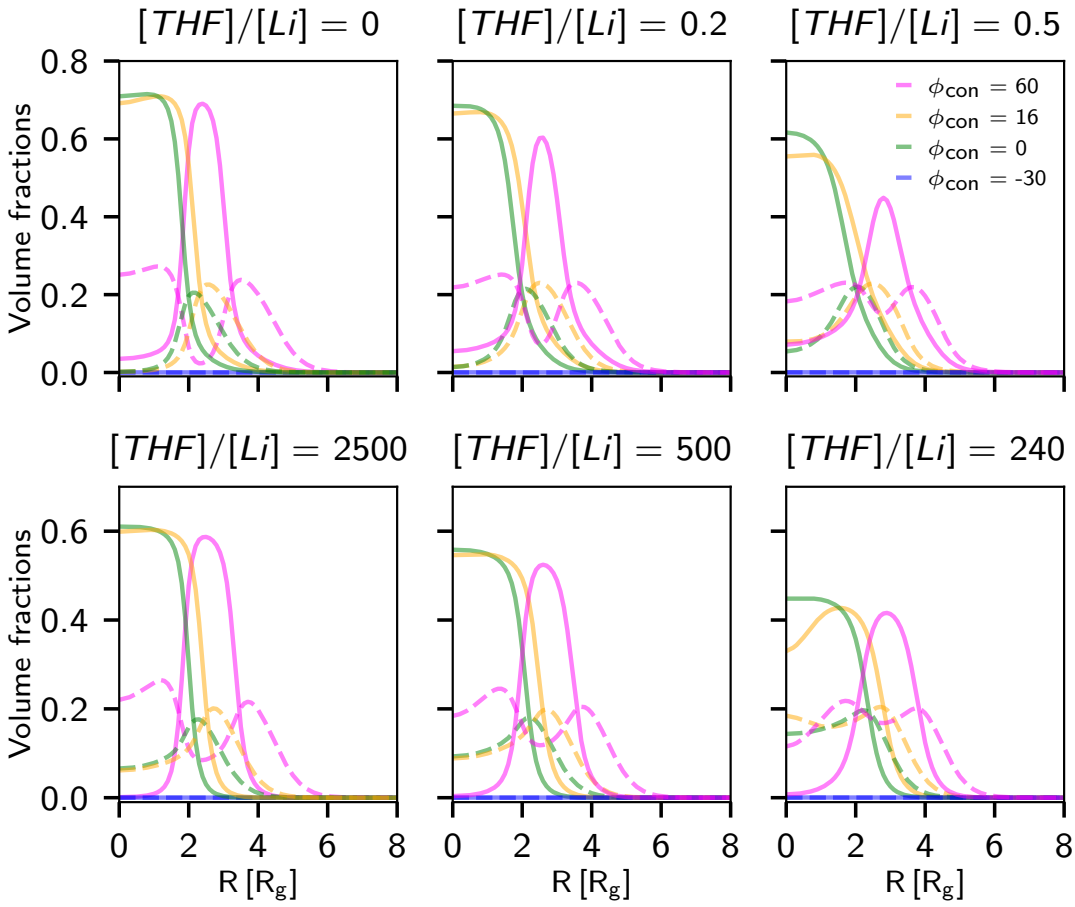

Figure 6.9: Volume fraction profiles for solvophobic (solid lines) and solvophilic (dashed lines) monomers as a function of radial distance R. Colors correspond to different ϕ_{con} values, as labeled in the [THF]/[Li] = 0.5 panel.

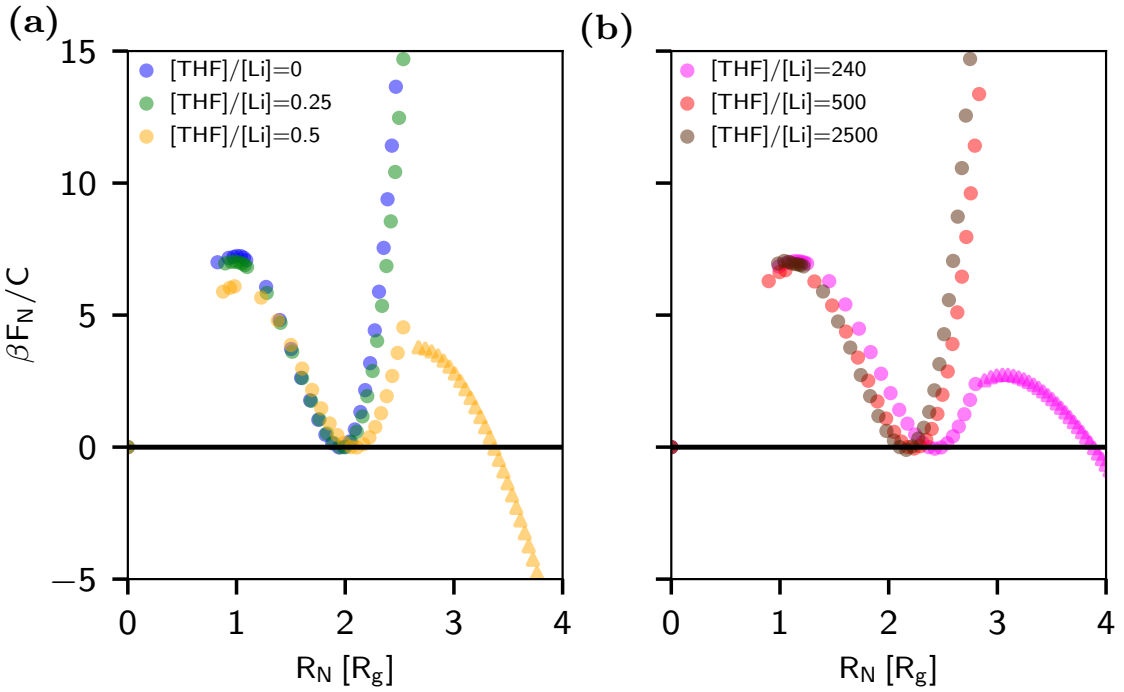

Figure 6.10: Constrained nanoparticle energies as a function of nanoparticle radius R_N. Calculations were performed at the critical concentrations. Circles (●) denote spherical micelles, and triangles (▲) represent semi-vesicles. Colors indicate different copolymer gradients. Note that the spherical micelle morphologies for the cases [THF]/[Li] = 0.25, 0.5 and 240 are metastable, as illustrated in Fig. 6.2.

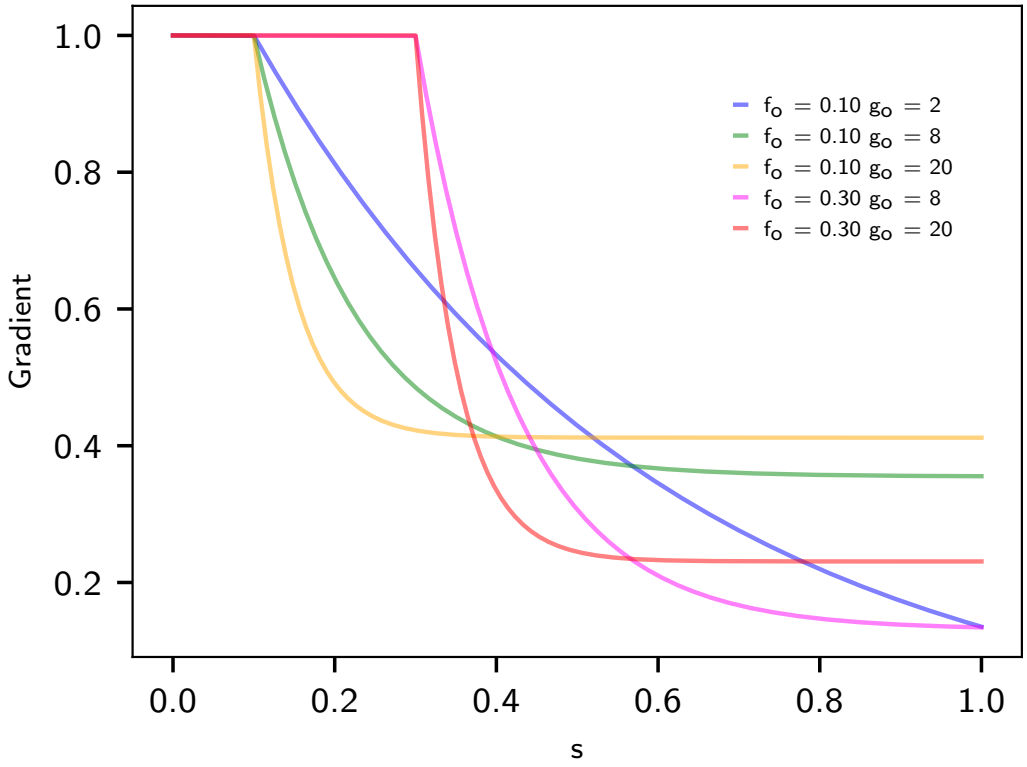

Figure 6.11: Plots of various idealized gradients used in the main text for reference. Only the gradient of the solvophobic part is shown.

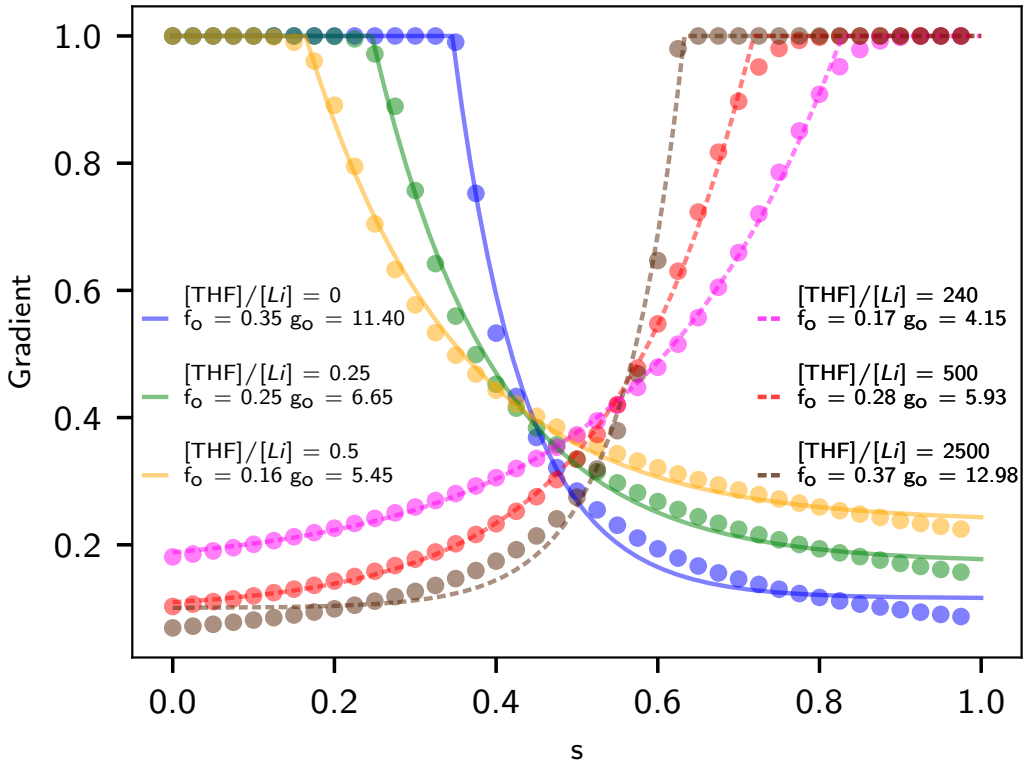

Figure 6.12: Plots of different experimental gradients (data points) along with their fits to the idealized gradient. Note that $g(s)$ in Eq. (6.7) was fitted to the solvophobic part the gradients with the solid lines while $g(1-s)$ was fit to the solvophilic part of the gradients with the dashed lines. The fitting parameters for each case are found in the legend.

Part III

CONCLUSIONS & PERSPECTIVES

In this thesis we have employed mainly self-consistent field theory (SCFT) calculations, along with the strong stretching limit (SSL) and molecular dynamics (MD) simulations to explore a variety of systems, including polydisperse polymer brushes, thin polymer films, amphiphilic linear-hyperbranched block copolymers (LHBCs) and amphiphilic gradient copolymers.

In Chapter 3, a mean-field theory based on the SSL, originally developed by Milner *et al.* [61] was extended to analyze polymer brushes grafted onto curved substrates—specifically focusing on both convex and concave spherical geometries in good solvent and melt conditions. Special attention was given to polydisperse brushes with realistic chain length distributions such as the Schulz-Zimm distribution.

Our analysis revealed that polydispersity significantly modifies the chain end distribution in convex geometries, especially when the brush height-to-radius ratio is small $(0 - 10)$. Interestingly, while bending and Gaussian moduli remain largely unaffected by polydispersity, the spontaneous curvature is consistently reduced, indicating a suppression of natural bending tendencies in both solvent environments. Notably, the good solvent and melt regimes respond oppositely to polydispersity in terms of mechanical stiffness: good solvent brushes stiffen, while melt brushes soften.

We also demonstrated the emergence of End Exclusion Zones (EEZs) as a result of chain length distributions with finite minimum lengths and showed how these zones can be engineered to appear at specific brush locations through careful design of grafting density and geometry. Additionally, our method offers a practical approach to tailoring chain end profiles through distribution and geometric control.

In Chapter 4, we introduced and evaluated adaptive discretization strategies to enhance the accuracy and computational efficiency of SCFT calculations for thin films and polymer brushes. By refining spatial resolution near surfaces, where strong interactions with polymers occur, and introducing adaptive contour discretization along polymer chains, we managed to reduce numerical errors and improve convergence.

Our method proved particularly useful in brush systems and strongly stretched polymer configurations, where accurate resolution near interfaces or grafting points is critical. For example, in polymer brushes, fine contour discretization was necessary to resolve the depletion region occuring near the surface, while adaptive spatial grids reduced the required number of points without compromising accuracy.

In Chapter 5, we examined the formation and properties of micelles composed of block copolymers with varying architectures: polydisperse linear-hyperbranched block copolymers (LHBC), monodisperse linear-dendritic block copolymers (LDBC), and monodisperse linear diblocks. Using MD simulations mimicking slow-monomer addition, we constructed realistic LHBC polymer architectures and subsequent SCFT calculations in the grand canonical ensemble, were used to model how random branching and size distribution affect micelle behavior.

A key finding is that higher polydispersity in LHBCs improves micelle stability and lowers the critical micelle concentration (CMC), mainly because shorter, more solvopho-

bic chains preferentially enter micelles. Surprisingly, while branching architecture plays a secondary role, the number of terminal chain ends within LHBC micelles remains nearly constant across varying polydispersity levels. This balance is attributed to a compensating increase in total chains and a decrease in the number of ends per chain.

Despite similarities in internal density and end distributions between LHBC and LDBC micelles, LHBCs tend to be softer and more size-diverse. These structural features where found to enhance their capacity for encapsulating solvophobic guest molecules, making them promising drug carriers. However, encapsulation can lead to morphological transitions, such as from spherical to cylindrical micelles.

In Chapter 6 we employed SCFT calculations to investigate the self-assembly of gradient copolymers with a 1 : 1 styrene-isoprene composition in *n*-decane, as inspired by the experimental work of our collaborators[243]. Our calculations show a progression from spherical to cylindrical and eventually lamellar morphologies as the copolymer gradient is flattened. However, because the free energy differences between spherical and cylindrical micelles are small, intermediate or mixed morphologies—such as ellipsoidal micelles—may also be energetically competitive, a view supported by SAXS experiments.

We further examined how compositional gradients affect internal micelle structure. Regardless of gradient sharpness, the peak in the solvophilic volume fraction always occurs at the interface between core and corona. Yet, the internal composition of the core shifts depending on the gradient, with flatter gradients allowing solvophilic monomers to penetrate deeper if the gradient occurs in the solvophobic-rich part of the polymer chain.

We also studied idealized gradients with varying block size and gradient steepness and constructed a phase diagram indicating that block size primarily determines the micelle morphology. On the other hand, flatter gradients were found to effectively act as an extension to the block.

Lastly, we studied micelle dissolution and found that the energy barrier is primarily governed by the length of the solvophobic block. Although not strictly monotonic, this trend emphasizes the importance of the solvophobic block's part in determining micelle stability.

Future work could focus on further improving the stability and accuracy of SCFT calculations. One persistent challenge is the presence of sharp field gradients, which remain computationally demanding. Unlike in our example—where the sharpness was expected near the surface—in many systems, the location and nature of these sharp features are unknown a priori. Therefore, it would be highly beneficial to develop a fully adaptive discretization scheme in both real-space and contour variables. Such a method would dynamically refine the grid at each iteration, resolving sharp gradients more effectively and improving the overall stability of the SCFT iteration process.

Our SCFT implementation for parallelized polydisperse, tree-like polymer topologies also opens new opportunities for investigating complex systems that have been tradi-

tionally underexplored due to their structural complexity and the computational cost involved. A particularly interesting case is that of core-forming hyperbranched polymers, whose intrinsic topological polydispersity is expected to significantly influence their self-assembly thermodynamics.

Another promising direction is the study of amphiphilic gradient copolymer self-assembly, which remains only partially understood. The influence of the gradient profile, block composition, and solvent interactions on the final morphology is still not fully resolved. A systematic exploration across different interaction parameters and gradient profiles is needed to clarify the self-assembly thermodynamics of these systems—particularly the free energy differences between spherical and cylindrical micelles as in our test case these two morphologies appeared almost degenerate in a lot of cases.

Finally, more broadly, throughout this thesis we have repeatedly encountered the importance of accessing exotic phase morphologies in solution, a task that is often hampered by the initial conditions of the SCFT numerical scheme. While we have partially addressed this issue—by employing constraint potentials to enforce specific features (e.g., ellipsoidal shapes or spherical cores), or by favoring the more stable canonical ensemble over the grand canonical formulation—a more systematic approach is still needed to reliably converge to complex morphologies.

BIBLIOGRAPHY

[1] R. B. Seymour et al. Pioneers in Polymer Science. Kluwer Academic Publishers, 1989.

[2] T. Graham. X. Liquid diffusion applied to analysis. *Philosophical Transactions of the Royal Society of London* **151** (1861), 183–224.

[3] P. Shrowder. The constitution and synthesis of caoutchouc. *Journal of the Chemical Society, Transactions* **97** (1910), 1085–1090.

[4] R. Mülhaupt. Hermann Staudinger and the Origin of Macromolecular Chemistry. *Angewandte Chemie International Edition* **43** (2004), 1054–1063.

[5] H. Staudinger. Über Polymerisation. *European Journal of Inorganic Chemistry* **53** (1920), 1073–1085.

[6] H. Staudinger et al. Der polymere Formaldehyd, ein Modell der Zellulose. *Zeitschrift für Physikalische Chemie* **126** (1927), 425–448.

[7] W. Kuhn. Gestalt und Eigenschaften fadenförmiger Moleküle in Lösungen (und im elastisch festen Zustande). *Angewandte Chemie* **49** (1936), 858–862.

[8] P. J. Flory. Principles of polymer chemistry. Cornell university press, 1953.

[9] S. F. Edwards. The statistical mechanics of polymers with excluded volume. *Proceedings of the Physical Society* **85** (1965), 613.

[10] A. N. Semenov. Contribution to the theory of microphase layering in block-copolymer melts. *Journal of Experimental and Theoretical Physics* **88** (1985), 1242–1256.

[11] M. W. Matsen and M. Schick. Stable and unstable phases of a diblock copolymer melt. *Physical Review Letters* **72** (1994), 2660–2663.

[12] D. Braun et al. Polymer Synthesis: Theory and Practice: Fundamentals, Methods, Experiments. Springer Berlin Heidelberg, 2013.

[13] Y. Mai and A. Eisenberg. Self-assembly of block copolymers. *Chemical Society Reviews* **41** (2012), 5969–5985.

[14] G. Battaglia and A. J. Ryan. Effect of Amphiphile Size on the Transformation from a Lyotropic Gel to a Vesicular Dispersion. *Macromolecules* **39** (2006), 798–805.

[15] J. N. Israelachvili, D. J. Mitchell, and B. W. Ninham. Theory of self-assembly of hydrocarbon amphiphiles into micelles and bilayers. *Journal of the Chemical Society, Faraday Transactions 2: Molecular and Chemical Physics* **72** (1976), 1525–1568.

[16] U. Tritschler et al. 50th Anniversary Perspective: Functional Nanoparticles from the Solution Self-Assembly of Block Copolymers. *Macromolecules* **50** (2017), 3439–3463.

[17] A. Blanazs, S. P. Armes, and A. J. Ryan. Self-Assembled Block Copolymer Aggregates: From Micelles to Vesicles and their Biological Applications. *Macromolecular Rapid Communications* **30** (2009), 267–277.

[18] C. Lipinski. Poor aqueous solubility—an industry wide problem in drug discovery. *American Pharmaceutical Review* **5** (2002), 82–85.

[19] Z Sezgin, N Yuksel, and T Baykara. Preparation and characterization of polymeric micelles for solubilization of poorly soluble anticancer drugs. *European Journal of Pharmaceutics and Biopharmaceutics* **64** (2006), 261–268.

[20] S. M. Moghimi, A. C. Hunter, and J. C. Murray. Long-Circulating and Target-Specific Nanoparticles: Theory to Practice. *Pharmacological Reviews* **53** (2001), 283–318.

[21] Q. Zhou et al. Stimuli-responsive polymeric micelles for drug delivery and cancer therapy. *International Journal of Nanomedicine* **13** (2018), 2921–2942.

[22] S. R. Croy and G. S. Kwon. Polymeric Micelles for Drug Delivery. *Current Pharmaceutical Design* **12** (2006), 4669–4684.

[23] N. Nasongkla et al. cRGD-Functionalized Polymer Micelles for Targeted Doxorubicin Delivery. *Angewandte Chemie International Edition* **43** (2004), 6323–6327.

[24] A. V. Ambade, E. N. Savariar, and S. Thayumanavan. Dendrimeric Micelles for Controlled Drug Release and Targeted Delivery. *Molecular Pharmaceutics* **2** (2005), 264–272.

[25] E Gillies and J Frechet. Dendrimers and dendritic polymers in drug delivery. *Drug Discovery Today* **10** (2005), 35–43.

[26] F. Wurm and H. Frey. Linear–dendritic block copolymers: The state of the art and exciting perspectives. *Progress in Polymer Science* **36** (2011), 1–52.

[27] I. O. Lebedeva, E. B. Zhulina, and O. V. Borisov. Theory of Linear-Dendritic Block Copolymer Micelles. *ACS Macro Letters* **7** (2018), 42–46.

[28] M. D. Lefebvre, M. Olvera de la Cruz, and K. R. Shull. Phase Segregation in Gradient Copolymer Melts. *Macromolecules* **37** (2004), 1118–1123.

[29] M. Steube et al. Tetrahydrofuran: More than a "Randomizer" in the Living Anionic Copolymerization of Styrene and Isoprene: Kinetics, Microstructures, Morphologies, and Mechanical Properties. *Macromolecules* **53** (2020), 5512–5527.

[30] J. Pyun, T. Kowalewski, and K. Matyjaszewski. Synthesis of Polymer Brushes Using Atom Transfer Radical Polymerization. *Macromolecular Rapid Communications* **24** (2003), 1043–1059.

[31] N. Hadjesfandiari et al. Polymer brush-based approaches for the development of infection-resistant surfaces. *Journal of Materials Chemistry B* **2** (2014), 4968–4978.

[32] Y. Liu et al. Tuning Surface Functions by Hydrophilic/Hydrophobic Polymer Brushes. *ACS Nano* **19** (2025), 11576–11603.

[33] D. A. Tomalia et al. A New Class of Polymers: Starburst-Dendritic Macromolecules. *Polymer Journal* **17** (1985), 117–132.

[34] J. Rühe, and W. Knoll. Functional Polymer Brushes*. *Journal of Macromolecular Science, Part C* **42** (2002), 91–138.

[35] E. Barriau et al. Linear-Hyperbranched Amphiphilic AB Diblock Copolymers Based on Polystyrene and Hyperbranched Polyglycerol. *Macromolecular Rapid Communications* **26** (2005), 862–867.

[36] S. Mantha et al. How ill-defined constituents produce well-defined nanoparticles: Effect of polymer dispersity on the uniformity of copolymeric micelles. *Physical Review Materials* **3** (2019), 026002.

[37] C. B. Gorman, R. J. Petrie, and J. Genzer. Effect of Substrate Geometry on Polymer Molecular Weight and Polydispersity during Surface-Initiated Polymerization. *Macromolecules* **41** (2008), 4856–4865.

[38] V. S. Kravchenko, V. Abetz, and I. I. Potemkin. Self-assembly of gradient copolymers in a selective solvent. New structures and comparison with diblock and statistical copolymers. *Polymer* **235** (2021), 124288.

[39] J. Kuldová et al. Self-association of copolymers with various composition profiles. *Collection of Czechoslovak Chemical Communications* **75** (2010), 493–505.

[40] V. S. Kravchenko and I. I. Potemkin. Micelles of Gradient vs Diblock Copolymers: Difference in the Internal Structure and Properties. *The Journal of Physical Chemistry B* **120** (2016), 12211–12217.

[41] N. Pippa et al. Gradient Block Copolymer Structures as Drug Nanocarriers. *Advanced Science, Engineering and Medicine* **6** (2014), 642–648.

[42] J. L. Lawson et al. The Spatial Distribution of Lipophilic Cations in Gradient Copolymers Regulates Polymer–pDNA Complexation, Polyplex Aggregation, and Intracellular pDNA Delivery. *Biomacromolecules* **25** (2024), 6855–6870.

[43] A. Halperin and S. Alexander. Polymeric micelles: their relaxation kinetics. *Macromolecules* **22** (1989), 2403–2412.

[44] G. Fredrickson. The equilibrium theory of inhomogeneous polymers. Oxford University Press, 2006.

[45] M. Rubinstein and R. H. Colby. Polymer physics. Oxford University Press, 2003.

[46] M. W. Matsen. Soft Matter: Polymer Melts and Mixtures. Wiley Online Library, 2006. Chap. Self-consistent field theory and its applications.

[47] J. M. H. M. Scheutjens and G. J. Fleer. Statistical theory of the adsorption of interacting chain molecules. 1. Partition function, segment density distribution, and adsorption isotherms. *The Journal of Physical Chemistry* **83** (1979), 1619–1635.

[48] F. Schmid. Self-consistent-field theories for complex fluids. *Journal of Physics: Condensed Matter* **10** (1998), 8105.

[49] E. Helfand and Y. Tagami. Theory of the interface between immiscible polymers. *Journal of Polymer Science Part B* **9** (1971), 741–746.

[50] E. Helfand. Theory of inhomogeneous polymers: Fundamentals of the Gaussian random-walk model. *The Journal of Chemical Physics* **62** (1975), 999–1005.

[51] F. S. Bates et al. Fluctuations, conformational asymmetry and block copolymer phase behaviour. *Faraday Discussions* **98** (1994), 7–18.

[52] G. H. Fredrickson and E. Helfand. Fluctuation effects in the theory of microphase separation in block copolymers. *The Journal of Chemical Physics* **87** (1987), 697–705.

[53] V Ganesan and G. H Fredrickson. Field-theoretic polymer simulations. *Europhysics Letters* **55** (2001), 814–820.

[54] P. Stasiak and M. W. Matsen. Monte Carlo Field-Theoretic Simulations for Melts of Symmetric Diblock Copolymer. *Macromolecules* **46** (2013), 8037–8045.

[55] J. He and Q. Wang. Frank–Kasper Phases of Diblock Copolymer Melts: Self-Consistent Field Results of Two Commonly Used Models. *Polymers* **16** (2024), 372.

[56] M. W. Matsen, T. M. Beardsley, and J. D. Willis. Fluctuation stabilization of the Fddd network phase in diblock, triblock, and starblock copolymer melts. *Physical Review Materials* **7** (2023), 105605.

[57] M. W. Matsen. Effect of Architecture on the Phase Behavior of AB-Type Block Copolymer Melts. *Macromolecules* **45** (2012), 2161–2165.

[58] I. C. Sanchez and R. H. Lacombe. Statistical Thermodynamics of Polymer Solutions. *Macromolecules* **11** (1978), 1145–1156.

[59] M. Müller and F. Schmid. Advanced Computer Simulation Approaches for Soft Matter Sciences II. Springer, 2005. Chap. Incorporating Fluctuations and Dynamics in Self-Consistent Field Theories for Polymer Blends.

[60] D. G. Anderson. Iterative Procedures for Nonlinear Integral Equations. *Journal of the ACM* **12** (1965), 547–560.

[61] S. T. Milner, T. A. Witten, and M. E. Cates. Theory of the Grafted Polymer Brush. *Macromolecules* **21** (1988), 2610–2619.

[62] F. Schmid. A self-consistent-field approach to surfaces of compressible polymer blends. *The Journal of Chemical Physics* **104** (1996), 9191–9201.

[63] P. Jain, G. L. Baker, and M. L. Bruening. Applications of polymer brushes in protein analysis and purification. *Annual Review of Analytical Chemistry* **2** (2009), 387–408.

[64] H. Jiang and F.-J. Xu. Biomolecule-functionalized polymer brushes. *Chemical Society Reviews* **42** (2013), 3394–3426.

[65] J. J. Keating IV, J. Imbrogno, and G. Belfort. Polymer brushes for membrane separations: a review. *ACS applied materials and interfaces* **8** (2016), 28383–28399.

[66] L. Madhura et al. Membrane technology for water purification. *Environmental Chemistry Letters* **16** (2018), 343–365.

[67] O. Azzaroni. Polymer brushes here, there, and everywhere: Recent advances in their practical applications and emerging opportunities in multiple research fields. *Journal of Polymer Science Part A* **50** (2012), 3225–3258.

[68] K. Glinel et al. Antibacterial and antifouling polymer brushes incorporating antimicrobial peptide. *Bioconjugate chemistry* **20** (2009), 71–77.

[69] M. Kobayashi et al. Wettability and antifouling behavior on the surfaces of superhydrophilic polymer brushes. *Langmuir* **28** (2012), 7212–7222.

[70] E. B. Zhulina, O. V. Borisov, and V. A. Priamitsyn. Theory of steric stabilization of colloid dispersions by grafted polymers. *Journal of colloid and interface science* **137** (1990), 495–511.

[71] M. Motornov et al. Stimuli-responsive colloidal systems from mixed brush-coated nanoparticles. *Advanced functional materials* **17** (2007), 2307–2314.

[72] S. Qi et al. Tuning Transition Properties of Stimuli-Responsive Brushes by Polydispersity. *Advanced Functional Materials* **28** (2018), 1800745.

[73] S. Qi et al. Stimuli-responsive brushes with active minority components: Monte Carlo study and analytical theory. *Macromolecules* **48** (2015), 3775–3787.

[74] S. Qi et al. Using copolymers to design tunable stimuli-reponsive brushes. *Macromolecules* **53** (2020), 5326–5336.

[75] P. De Gennes. Scaling theory of polymer adsorption. *Journal de physique* **37** (1976), 1445–1452.

[76] S Alexander. Adsorption of chain molecules with a polar head a scaling description. *Journal De Physique* **38** (1977), 983–987.

[77] T. Cosgrove et al. Configuration of terminally attached chains at the solid/solvent interface: Self-consistent field theory and a Monte Carlo model. *Macromolecules* **20** (1987), 1692–1696.

[78] K. Binder and A. Milchev. Polymer brushes on flat and curved surfaces: How computer simulations can help to test theories and to interpret experiments. *Journal of Polymer Science Part B* **50** (2012), 1515–1555.

[79] T. Suo and M. D. Whitmore. Self-consistent field theory of tethered polymers: One dimensional, three dimensional, strong stretching theories and the effects of excluded-volume-only interactions. *The Journal of Chemical Physics* **141** (2014), 204903.

[80] S. Yang et al. Regulating block copolymer phases via selective homopolymers. *The Journal of Chemical Physics* **142** (2015), 124903.

[81] I. O. Lebedeva et al. Dendron and Hyperbranched Polymer Brushes in Good and Poor Solvents. *Langmuir* **33** (2017), 1315–1325.

[82] A. S. Andreu Artola and E. Rodolfo Soule. Theory of polymer brushes grafted to finite surfaces. *Journal of Polymer Science Part B* **56** (2018), 663–672.

[83] I. V. Mikhailov, E. B. Zhulina, and O. V. Borisov. Brushes and lamellar mesophases of comb-shaped (co)polymers: a self-consistent field theory. *PCCP* **22** (2020), 23385–23398.

[84] G. Pickett. Lamellae at a preferential wall. *The Journal of Chemical Physics* **104** (1996), 1657–1671.

[85] M. Matsen and J. Gardiner. Anomalous domain spacing difference between AB diblock and homologous A_2B_2 starblock copolymers. *The Journal of Chemical Physics* **113** (2000), 1673–1676.

[86] M. Matsen. Testing strong-segregation theory against self-consistent field theory for block copolymer melts. *The Journal of Chemical Physics* **114** (2001), 10528–10530.

[87] M. Heckmann and B. Drossel. Strong stretching theory for diblock copolymers in thin films. *The Journal of Chemical Physics* **129** (2008), 214903.

[88] M. W. Matsen. Strong-segregation limit of the self-consistent field theory for diblock copolymer melts. *The European Physical Journal E* **33** (2010), 297–306.

[89] N. B. Tito, S. T. Milner, and J. E. G. Lipson. Self-Assembly of Lamellar Microphases in Linear Gradient Copolymer Melts. *Macromolecules* **43** (2010), 10612–10620.

[90] I. Mikhailov V et al. Theory of Microphase Segregation in ABA Triblock Comb-Shaped Copolymers: Lamellar Mesophase. *Macromolecules* **54** (2021), 4747–4759.

[91] E. B. Zhulina, I. V. Mikhailov, and O. V. Borisov. Theory of Mesophases of Triblock Comb-Shaped Copolymers: Effects of Dead Zones and Bridging. *Macromolecules* **55** (2022), 6040–6055.

[92] D. A. Filatov and E. N. Govorun. Microphase separation in the melts of diblock copolymers with amphiphilic blocks. *Soft matter* **17** (2021), 90–101.

[93] M. S. Dimitriyev, A. Reddy, and G. M. Grason. Medial Packing, Frustration, and Competing Network Phases in Strongly Segregated Block Copolymers. *Macromolecules* **56** (2023), 7184–7202.

[94] S. T. Milner, T. A. Witten, and M. E. Cates. Effects of polydispersity in the end-grafted polymer brush. *Macromolecules* **22** (1989), 853–861.

[95] W. M. de Vos and F. A. Leermakers. Modeling the structure of a polydisperse polymer brush. *Polymer* **50** (2009), 305–316.

[96] S. Qi et al. Polydisperse polymer brushces: Internal structure, critical behavior, and interaction with flow. *Macromolecules* **49** (2016), 9665–9683.

[97] M. Kim et al. From self-assembled monolayers to coatings: Advances in the synthesis and nanobio applications of polymer brushes. *Polymers* **7** (2015), 1346–1378.

[98] B. Zdyrko and I. Luzinov. Polymer brushes by the "grafting to" method. *Macromolecular rapid communications* **32** (2011), 859–869.

[99] W. J. Brittain and S. Minko. A structural definition of polymer brushes. *Journal of Polymer Science Part A* **45** (2007), 3505–3512.

[100] A. P. Martinez et al. Distribution of chains in polymer brushes produced by a "grafting from" mechanism. *Macromolecules* **49** (2016), 547–553.

[101] R. Mohammadi Sejoubsari et al. "Grafting-through": growing polymer brushes by supplying monomers through the surface. *Macromolecules* **49** (2016), 2477–2483.

[102] B. H. Zimm. Apparatus and methods for measurement and interpretation of the angular variation of light scattering; preliminary results on polystyrene solutions. *The Journal of Chemical Physics* **16** (1948), 1099–1116.

[103] R. R. Patil et al. On-demand degrafting and the study of molecular weight and grafting density of poly (methyl methacrylate) brushes on flat silica substrates. *Langmuir* **31** (2015), 2372–2381.

[104] P. Akcora et al. Anisotropic self-assembly of spherical polymer-grafted nanoparticles. *Nature materials* **8** (2009), 354–359.

[105] C. Chevigny et al. Polymer-grafted-nanoparticles nanocomposites: dispersion, grafted chain conformation, and rheological behavior. *Macromolecules* **44** (2011), 122–133.

[106] J. Midya et al. Structure of polymer-grafted nanoparticle melts. *ACS nano* **14** (2020), 15505–15516.

[107] C. R. Bilchak et al. Understanding Gas Transport in Polymer-Grafted Nanoparticle Assemblies. *Macromolecules* **55** (2022), 3011–3019.

[108] S. P. Adiga and D. W. Brenner. Stimuli-responsive polymer brushes for flow control through nanopores. *Journal of functional biomaterials* **3** (2012), 239–256.

[109] M. Tagliazucchi and I. Szleifer. Stimuli-responsive polymers grafted to nanopores and other nano-curved surfaces: structure, chemical equilibrium and transport. *Soft Matter* **8** (2012), 7292–7305.

[110] R. D. Coalson et al. A polymer-brush-based nanovalve controlled by nanoparticle additives: design principles. *The Journal of Physical Chemistry B* **119** (2015), 11858–11866.

[111] K. J. van der Weg, G. C. Ritsema van Eck, and S. de Beer. Polymer Brush Friction in Cylindrical Geometries. *Lubricants* **7** (2019), 84.

[112] R. Ball et al. Polymers grafted to a convex surface. *Macromolecules* **24** (1991), 693–703.

[113] C. Wijmans and E. B. Zhulina. Polymer brushes at curved surfaces. *Macromolecules* **26** (1993), 7214–7224.

[114] N Dan and M Tirrell. Polymers tethered to curves interfaces: a self-consistent-field analysis. *Macromolecules* **25** (1992), 2890–2895.

[115] M. Manghi et al. Inwardly curved polymer brushes: concave is not like convex. *The European Physical Journal E* **5** (2001), 519–530.

[116] V. A. Belyi. Exclusion zone of convex brushes in the strong-stretching limit. *The Journal of Chemical Physics* **121** (2004), 6547–6554.

[117] Z. Lei et al. Curvature elasticity of a grafted polyelectrolyte brush. *Physical Review E* **91** (2015), 062602.

[118] M. S. Dimitriyev and G. M. Grason. End-exclusion zones in strongly stretched, molten polymer brushes of arbitrary shape. *The Journal of Chemical Physics* **155** (2021), 224901.

[119] S. T. Milner and T. A. Witten. Bending moduli of polymeric surfactant interfaces. *Journal de Physique* **49** (1988), 1951–1962.

[120] P. M. Dodd and A. Jayaraman. Monte carlo simulations of polydisperse polymers grafted on spherical surfaces. *Journal of Polymer Science Part B* **50** (2012), 694–705.

[121] L. Hartmann and H. Börner. Precision Polymers: Monodisperse, Monomer-Sequence-Defined Segments to Target Future Demands of Polymers in Medicine. *Advanced Materials* **21** (2009), 3425–3431.

[122] W. Helfrich. Elastic properties of lipid bilayers: theory and possible experiments. *Zeitschrift für Naturforschung C* **28** (1973), 693–703.

[123] N. H. Abel. Oeuvres complètes de Niels Henrik Abel: Nouvelle édition. Cambridge University Press, 2012.

[124] F. Schmid and M. Müller. Quantitative comparison of self-consistent field theories for polymers near interfaces with Monte-Carlo Simulations. *Macromolecules* **28** (1995), 8639–8645.

[125] D. L. Vigil et al. Self-Consistent Field Theory Predicts Universal Phase Behavior for Linear, Comb, and Bottlebrush Diblock Copolymers. *Macromolecules* **55** (2022), 4237–4244.

[126] M. Müller. Phase Diagram of a Mixed Polymer Brush. *Physical Review E* **65** (2002), 030802.

[127] M. W. Matsen and F. S. Bates. Unifying Weak-and Strong-segregation Block Copolymer Theories. *Macromolecules* **29** (1996), 1091–1098.

[128] M. W. Matsen and M. D. Whitmore. Accurate Diblock Copolymer Phase Boundaries at Strong Segregations. *The Journal of Chemical Physics* **105** (1996), 9698–9701.

[129] M. W. Matsen. Fast and Accurate SCFT Calculations for Periodic Block-Copolymer Morphologies Using the Spectral Method with Anderson Mixing. *The European Physical Journal E* **30** (2009), 361.

[130] G. H. Fredrickson, V. Ganesan, and F. Drolet. Field-Theoretic Computer Simulation Methods for Polymers and Complex Fluids. *Macromolecules* **35** (2002), 16–39.

[131] F. Drolet and G. H. Fredrickson. Combinatorial Screening of Complex Block Copolymer Assembly with Self-Consistent Field Theory. *Physical Review Letters* **83** (1999), 4317–4320.

[132] K. Ø. Rasmussen and G. Kalosakas. Improved Numerical Algorithm for Exploring Block Copolymer Mesophases. *Journal of Polymer Science Part B* **40** (2002), 1777–1783.

[133] H. D. Ceniceros and G. H. Fredrickson. Numerical Solution of Polymer Self-Consistent Field Theory. *Multiscale Modelling and Simulation* **2** (2004), 452–474.

[134] G. Tzeremes et al. Efficient Computation of the Structural Phase Behavior of Block Copolymers. *Physical Review E* **65** (2002), 041806.

[135] J. G. E. M. Fraaije et al. The Dynamic Mean-Field Density Functional Method and Its Application to the Mesoscopic Dynamics of Quenched Block Copolymer Melts. *The Journal of Chemical Physics* **106** (1997), 4260–4269.

[136] R. R. Netz and M. Schick. Polymer Brushes: From Self-Consistent Field Theory to Classical Theory. *Macromolecules* **31** (1998), 5105–5122.

[137] K. Ch. Daoulas and M. Müller. Exploring Thermodynamic Stability of the Stalk Fusion-Intermediate with Three-Dimensional Self-Consistent Field Theory Calculations. *Soft Matter* **9** (2013), 4097–4102.

[138] C. J. Revelas et al. RuSseL: A Self-Consistent Field Theory Code for Inhomogeneous Polymer Interphases. *Computation* **9** (2021), 57.

[139] E. W. Cochran, C. J. Garcia-Cervera, and G. H. Fredrickson. Stability of the Gyroid Phase in Diblock Copolymers at Strong Segregation. *Macromolecules* **39** (2006), 2449–2451.

[140] D. L. Vigil et al. Linear Scaling Self-Consistent Field Theory with Spectral Contour Accuracy. *ACS Macro Letters* **8** (2019), 1402–1406.

[141] G. T. Vu et al. Curvature as a Guiding Field for Patterns in Thin Block Copolymer Films. *Physical review letters* **121** (2018), 087801.

[142] S. T. Milner. Polymer Brushes. *Science* **251** (1991), 905–914.

[143] B. Vorselaars et al. Self-Consistent Field Theory for Diblock Copolymers Grafted to a Sphere. *Soft Matter* **7** (2011), 5128.

[144] W. Li et al. Phase Diagram of Diblock Copolymers Confined in Thin Films. *The Journal of Physical Chemistry B* **117** (2013), 5280–5288.

[145] Y. B. Yang et al. Diblock and Triblock Copolymer Thin Films on a Substrate with Controlled Selectivity. *The European Physical Journal E* **35** (2012), 86.

[146] J.-R. Roan and T. Kawakatsu. Self-Consistent-Field Theory for Interacting Polymeric Assemblies. I. Formulation, Implementation, and Benchmark Tests. *The Journal of Chemical Physics* **116** (2002), 7283–7294.

[147] T. L. Chantawansri et al. Self-Consistent Field Theory Simulations of Block Copolymer Assembly on a Sphere. *Physical Review E* **75** (2007), 031802.

[148] G. Ouaknin et al. Self-Consistent Field Theory Simulations of Polymers on Arbitrary Domains. *Journal of Computational Physics* **327** (2016), 168–185.

[149] H. Wei et al. An Adaptive Virtual Element Method for the Polymeric Self-Consistent Field Theory. *Computers and Mathematics with Applications* **141** (2023), 242–254.

[150] C. J. Revelas et al. Addressing Nanocomposite Systems via 3D-SCFT: Assessment of Smearing Approximation and Irregular Grafting Distributions. *Macromolecules* **56** (2023), 1731–1746.

[151] E Helfand. Theory of Inhomogeneous Polymers – Fundamentals of Gaussian Random-Walk Model. *The Journal of Chemical Physics* **62** (1975), 999–1005.

[152] M. Matsen. The Standard Gaussian Model for Block Copolymer Melts. *Journal of Physics: Condensed Matter* **14** (2002), R21–R47.

[153] J. Douglas and H. H. Rachford. On the Numerical Solution of Heat Conduction Problems in Two and Three Space Variables. *Transactions of the American mathematical Society* **82** (1956), 421–439.

[154] T. H. Chong. A Variable Mesh Finite Difference Method for Solving a Class of Parabolic Differential Equations in One Space Variable. *SIAM Journal on Numerical Analysis* **15** (1978), 835–857.

[155] R. Wang et al. Driving Polymer Brushes from Synthesis to Functioning. *Angewandte Chemie International Edition* **62** (2023), e202219312.

[156] X. Zhou et al. 3D-patterned Polymer Brush Surfaces. *Nanoscale* **3** (2011), 4929–4939.

[157] H. William et al. Numerical Recipes: The Art of Scientific Computing, 3rd edition. Cambridge University Press, 2007.

[158] L. Rezzolla and O. Zanotti. Relativistic Hydrodynamics. Oxford University Press, 2013.

[159] S. Qi and F. Schmid. Dynamic Density Functional Theories for Inhomogeneous Polymer Systems Compared to Brownian Dynamics Simulations. *Macromolecules* **50** (2017), 9831–9845.

[160] S. Mantha, S. Qi, and F. Schmid. Bottom-up Construction of Dynamic Density Functional Theories for Inhomogeneous Polymer Systems from Microscropic Simulations. *Macromolecules* **53** (2020), 3409–3423.

[161] F. Schmid and B. Li. Dynamic Self-Consistent Field Approach for Studying Kinetic Processes in Multiblock Copolymer Melts. *Polymers* **12** (2020), 2205.

[162] I. W. Hamley. The Physics of Block Copolymers. Oxford University Press, 1998.

[163] M. W. Matsen and M. Schick. Microphases of a Diblock Copolymer with Conformational Asymmetry. *Macromolecules* **27** (1994), 4014–4015.

[164] A. K. Khandpur et al. Polyisoprene-Polystyrene Diblock Copolymer Phase Diagram near the Order-Disorder Transition. *Macromolecules* **28** (1995), 8796–8806.

[165] M. W. Bates et al. Stability of the A15 phase in diblock copolymer melts. *Proceedings of the National Academy of Sciences* **116** (2019), 13194–13199.

[166] D. J. Meier. Theory of block copolymers. I. Domain formation in A-B block copolymers. *Journal of Polymer Science Part C* **26** (1969), 81–98.

[167] T. Ohta and K. Kawasaki. Equilibrium Morphology of Block Copolymer Melts. *Macromolecules* **19** (1986), 2621–2632.

[168] M. Park et al. Block copolymer lithography: Periodic arrays of ∼1011 holes in 1 square centimeter. *Science* **276** (1997), 1401–1404.

[169] T. Thurn-Albrecht et al. Overcoming interfacial interactions with electric fields. *Macromolecules* **33** (2000), 3250–3253.

[170] G. Krausch and R. Magerle. Nanostructured thin films via self-assembly of block copolymers. *Advanced Materials* **14** (2002), 1579–1583.

[171] H. Ahn et al. Nanoporous block copolymer membranes for ultrafiltration: A simple approach to size tunability. *ACS Nano* **8** (2014), 11745–11752.

[172] M. Lazzari and M. Arturo López-Quintela. Block Copolymers as a Tool for Nanomaterial Fabrication. *Advanced Materials* **15** (2003), 1583–1594.

[173] J. K. Kim et al. Functional nanomaterials based on block copolymer self-assembly. *Progress in Polymer Science* **35** (2010), 1325–1349.

[174] T. P. Lodge, B. Pudil, and K. J. Hanley. The full phase behavior for block copolymers in solvents of varying selectivity. *Macromolecules* **35** (2002), 4707–4717.

[175] K. J. Hanley, T. P. Lodge, and C. I. Huang. Phase behavior of a block copolymer in solvents of varying selectivity. *Macromolecules* **33** (2000), 5918–5931.

[176] S. A. Barnhill et al. Phase diagrams of polynorbornene amphiphilic block copolymers in solution. *Macromolecules* **48** (2015), 1152–1161.

[177] F. Gadelle, W. J. Koros, and R. S. Schechter. Solubilization of aromatic solutes in block copolymers. *Macromolecules* **28** (1995), 4883–4892.

[178] T. Sakai and P. Alexandridis. Single-step synthesis and stabilization of metal nanoparticles in aqueous pluronic block copolymer solutions at ambient temperature. *Langmuir* **20** (2004), 8426–8430.

[179] R. J. Peters, I. Louzao, and J. C. Van Hest. From polymeric nanoreactors to artificial organelles. *Chemical Science* **3** (2012), 335–342.

[180] K. Kataoka, A. Harada, and Y. Nagasaki. Block copolymer micelles for drug delivery: Design, characterization and biological significance. *Advanced Drug Delivery Reviews* **64** (2012), 37–48.

[181] A. Bose et al. Nanomicelles: Types, properties and applications in drug delivery. *IET Nanobiotechnology* **15** (2021), 19–27.

[182] I. W. Hamley. Block copolymers in solution: fundamentals and applications. John Wiley and Sons, 2005.

[183] S. C. Owen, D. P. Chan, and M. S. Shoichet. Polymeric micelle stability. *Nano Today* **7** (2012), 53–65.

[184] E. G. Kelley et al. Stimuli-responsive copolymer solution and surface assemblies for biomedical applications. *Chemical Society Reviews* **42** (2013), 7057–7071.

[185] T. M. Allen. Ligand-targeted therapeutics in anticancer therapy. *Nature Reviews Cancer* **2** (2002), 750–763.

[186] A. L. Ruiz, A. Ramirez, and K. McEnnis. Single and Multiple Stimuli-Responsive Polymer Particles for Controlled Drug Delivery. *Pharmaceutics* **14** (2022), 421.

[187] N. Hadjichristidis, M. Pitsikalis, and H. Iatrou. Synthesis of Block Copolymers. *Advances in Polymer Science* **189** (2005), 1–124.

[188] I. Gitsov. Hybrid linear dendritic macromolecules: From synthesis to applications. *Journal of Polymer Science Part A* **46** (2008), 5295–5314.

[189] X. Fan et al. Linear-dendritic block copolymer for drug and gene delivery. *Materials Science and Engineering C* **62** (2016), 943–959.

[190] G. Whitton and E. R. Gillies. Functional aqueous assemblies of linear-dendron hybrids. *Journal of Polymer Science Part A* **53** (2015), 148–172.

[191] X. Liu and I. Gitsov. Nonionic Amphiphilic Linear Dendritic Block Copolymers. Solvent-Induced Self-Assembly and Morphology Tuning. *Macromolecules* **52** (2019), 5563–5573.

[192] S. M. Grayson and J. M. Fréchet. Divergent synthesis of dendronized poly(p-hydroxystyrene). *Macromolecules* **34** (2001), 6542–6544.

[193] L. Nuhn et al. Combining ring-opening multibranching and RAFT polymerization: Multifunctional linear-hyperbranched block copolymers via hyperbranched macro-chain-transfer agents. *Macromolecules* **46** (2013), 2892–2904.

[194] Y. Oikawa et al. One-pot synthesis of linear-hyperbranched amphiphilic block copolymers based on polyglycerol derivatives and their micelles. *Biomacromolecules* **14** (2013), 2171–2178.

[195] T. Cuneo and H. Gao. Recent advances on synthesis and biomaterials applications of hyperbranched polymers. *Wiley Interdisciplinary Reviews: Nanomedicine and Nanobiotechnology* **12** (2020).

[196] K. E. Uhrich et al. One-Pot Synthesis of Hyperbranched Polyethers. *Macromolecules* **25** (1992), 4583–4587.

[197] Y. H. Kim and O. W. Webster. Water soluble hyperbranched polyphenylene:" a unimolecular micelle?" *Journal of the American Chemical Society* **112** (1990), 4592–4593.

[198] T. L. Andresen and J. B. Larsen. Compositional inhomogeneity of drug delivery liposomes quantified at the single liposome level. *Acta Biomaterialia* **118** (2020), 207–214.

[199] A. L. Schmitt, M. H. Repollet-Pedrosa, and M. K. Mahanthappa. Polydispersity-driven block copolymer amphiphile self-assembly into prolate-spheroid micelles. *ACS Macro Letters* **1** (2012), 300–304.

[200] P. DE GENNES. Macromolecules and Liquid Crystals: Reflections on Certain Lines of Research. *Liquid Crystals* (1978), 1–18.

[201] J. Noolandi and K. M. Hong. Theory of Block Copolymer Micelles in Solution. *Macromolecules* **16** (1983), 1443–1448.

[202] L. Leibler, H. Orland, and J. C. Wheeler. Theory of critical micelle concentration for solutions of block copolymers. *The Journal of Chemical Physics* **79** (1983), 3550–3557.

[203] F. A. M. Leermakers, C. M. Wijmans, and G. J. Fleer. On the Structure of Polymeric Micelles: Self-Consistent-Field Theory and Universal Properties for Volume Fraction Profiles. *Macromolecules* **28** (1995), 3434–3443.

[204] P. H. Nelson, G. C. Rutledge, and T. A. Hatton. On the size and shape of self-assembled micelles. *The Journal of Chemical Physics* **107** (1997), 10777–10781.

[205] E. B. Zhulina and O. V. Borisov. Theory of Block Polymer Micelles: Recent Advances and Current Challenges. *Macromolecules* **45** (2012), 4429–4440.

[206] Y. Wang et al. Dissipative particle dynamics simulation study on the mechanisms of self-assembly of large multimolecular micelles from amphiphilic dendritic multiarm copolymers. *Soft Matter* **9** (2013), 3293–3304.

[207] I. O. Lebedeva, E. B. Zhulina, and O. V. Borisov. Self-Assembly of Linear-Dendritic and Double Dendritic Block Copolymers: From Dendromicelles to Dendrimersomes. *Macromolecules* **52** (2019), 3655–3667.

[208] M. E. Brito et al. Implicit-Solvent Coarse-Grained Simulations of Linear–Dendritic Block Copolymer Micelles. *International Journal of Molecular Sciences* **24** (2023), 2763.

[209] H. Tan et al. Dissipative particle dynamics simulation study on self-assembly of amphiphilic hyperbranched multiarm copolymers with different degrees of branching. *Soft Matter* **11** (2015), 8460–8470.

[210] H. Tan et al. A dissipative particle dynamics simulation study on phase diagrams for the self-assembly of amphiphilic hyperbranched multiarm copolymers in various solvents. *Soft Matter* **13** (2017), 6178–6188.

[211] H. Tan et al. Shape Transformations of Vesicles Self-Assembled from Amphiphilic Hyperbranched Multiarm Copolymers via Simulation. *Langmuir* **35** (2019), 6929–6938.

[212] T. Hao et al. Multilayer onion-like vesicles self-assembled from amphiphilic hyperbranched multiarm copolymers via simulation. *Journal of Polymer Science* **58** (2020), 704–715.

[213] Z. Gao and A. Eisenberg. A Model of Micellization for Block Copolymers in Solutions. *Macromolecules* **26** (1993), 7353–7360.

[214] P. Linse. Micellization of Poly(ethylene oxide)–Poly(propylene oxide) Block Copolymers in Aqueous Solution: Effect of Polymer Polydispersity. *Macromolecules* **27** (1994), 6404–6417.

[215] N. A. Lynd, A. J. Meuler, and M. A. Hillmyer. Polydispersity and Block Copolymer Self-assembly. *Progress in Polymer Science* **33** (2008), 875 –893.

[216] K. E. B. Doncom et al. Dispersity effects in polymer self-assemblies: a matter of hierarchical control. *Chemical Society Reviews* **46** (14 2017), 4119–4134.

[217] M. Giannakou, O. V. Borisov, and F. Schmid. Strong stretching theory of polydisperse curved polymer brushes. *The Journal of Chemical Physics* **161** (2024).

[218] A Sunder et al. Controlled synthesis of hyperbranched polyglycerols by ring-opening multibranching polymerization. *Macromolecules* **32** (1999), 4240–4246.

[219] C. Schuell et al. Polydispersity and Molecular Weight Distribution of Hyperbranched Graft Copolymers via "Hypergrafting" of AB_m Monomers from Polydisperse Macroinitiator Cores: Theory Meets Synthesis. *Macromolecules* **46** (2013), 5823–5830.

[220] H. Rabbel, H. Frey, and F. Schmid. Statistical properties of linear-hyperbranched graft copolymers prepared via "hypergrafting" of ABm monomers from linear B-functional core chains: A molecular dynamics simulation. *The Journal of Chemical Physics* **143** (2015), 243125.

[221] J. A. Anderson, J. Glaser, and S. C. Glotzer. HOOMD-blue: A Python package for high-performance molecular dynamics and hard particle Monte Carlo simulations. *Computational Materials Science* **173** (2020), 109363.

[222] G. M. Grason and R. D. Kamien. Self-consistent field theory of multiply branched block copolymer melts. *Physical Review E* **71** (5 2005), 051801.

[223] D. Yong and J. U. Kim. Dynamic Programming for Chain Propagator Computation of Branched Block Copolymers in Polymer Field Theory Simulations. *Journal of Chemical Theory and Computation* **21** (2025), 3676–3690.

[224] H Frey and D Hölter. Degree of branching in hyperbranched polymers. 3 Copolymerization of AB_m-monomers with AB and AB_n-monomers. *Acta polymerica* **50** (1999), 67–76.

[225] R. Hanselmann et al. Hyperbranched Polymers Prepared via the Core-Dilution/Slow Addition Technique: Computer Simulation of Molecular Weight Distribution and Degree of Branching. *Macromolecules* **31** (1998), 3790–3801.

[226] C. M. Hansen. Hansen solubility parameters: a user's handbook. CRC press, 2007.

[227] X. Zhang, J. K. Jackson, and H. M. Burt. Development of amphiphilic diblock copolymers as micellar carriers of taxol. *International Journal of Pharmaceutics* **132** (1996), 195–206.

[228] X. Zhu, Y. Zhou, and D. Yan. Influence of Branching Architecture on Polymer Properties. *Journal of Polymer Science Part B* **49** (2011), 1277–1286.

[229] L. Qiao, M. Giannakou, and F. Schmid. An Efficient and Accurate SCF Algorithm for Block Copolymer Films and Brushes Using Adaptive Discretizations. *Polymers* **16** (2024).

[230] R. Wang and Z.-G. Wang. Theory of Polymers in Poor Solvent: Phase Equilibrium and Nucleation Behavior. *Macromolecules* **45** (2012), 6266–6271.

[231] V. S. Kravchenko, R. A. Gumerov, and I. I. Potemkin. Recent Advances in Diblock and Gradient Copolymers Self-Assembly in Solutions and at the Interfaces. *Reviews and Advances in Chemistry* **14** (2024), 320–338.

[232] A. V. Dobrynin and I. Y. Erukhimovich. Fluctuation Theory of Random Copolymers. *Journal de Physique I* **5** (1995), 365–377.

[233] J. Zhang et al. Effect of Hydrophilic Monomer Distribution on Self-Assembly of a pH-Responsive Copolymer: Spheres, Worms and Vesicles from a Single Copolymer Composition. *Angewandte Chemie International Edition* **60** (2021), 4925–4930.

[234] S. Okabe et al. Micellization Study on Block and Gradient Copolymer Aqueous Solutions by DLS and SANS. *Macromolecules* **39** (2006), 1592–1597.

[235] C. Zheng, H. Huang, and T. He. Micellization of St/MMA Gradient Copolymers: A General Picture of Structural Transitions in Gradient Copolymer Micelles. *Macromolecular Rapid Communications* **34** (2013), 1654–1661.

[236] H. Angerman, G. ten Brinke, and I. Erukhimovich. Microphase Separation in Correlated Random Copolymers. *Macromolecules* **29** (1996), 3255–3262.

[237] Y. Milonaki et al. Amphiphilic gradient copolymers of 2-methyl- and 2-phenyl-2-oxazoline: self-organization in aqueous media and drug encapsulation. *Journal of Polymer Science Part A* **50** (2012), 1226–1237.

[238] C. M. Dettmer et al. Synthesis and Functionalization of ROMP-Based Gradient Copolymers of 5-Substituted Norbornenes. *Macromolecules* **37** (2004), 5504–5512.

[239] K. Matyjaszewski et al. Gradient copolymers by atom transfer radical copolymerization. *Journal of Physical Organic Chemistry* **13** (2000), 775–786.

[240] S. Ishizaka, S. Nakagawa, and N. Yoshie. Computer-Aided Design of Copolymers with Controlled Comonomer Distributions. *Macromolecules* **56** (2023), 7312–7319.

[241] Y. Zhou et al. Facile synthesis of gradient copolymers enabled by droplet-flow photo-controlled reversible deactivation radical polymerization. *Science China Chemistry* **64** (2021), 844–851.

[242] J. D. Willis, T. M. Beardsley, and M. W. Matsen. Simple and accurate calibration of the flory-Huggins interaction parameter. *Macromolecules* **53** (2020), 9973–9982.

[243] T. T. D. Dinh, K. Y. Ghulam, S. Pusse, I. Tzourtzouklis, N. Fribiczer, S. Seiffert, M. Gallei, G. Floudas and A. Müller. Private communication. 2025.

[244] S. K. Filippov et al. Block and Gradient Copoly(2-oxazoline) Micelles: Strikingly Different on the Inside. *The Journal of Physical Chemistry Letters* **8** (2017), 3800–3804.

[245] M. Giannakou, O. Borisov, and F. Schmid. Micelle Forming Linear–Dendritic Block Copolymers: A Theoretical Comparison between Random Hyperbranched and Precise Dendrimer Polymer Architectures. *Macromolecules* **58** (2025), 5872–5882.

Marios Giannakou

mgiannak@uni-mainz.de | Komet 1, 03-530, Staudingerweg 9, 55128 Mainz, Germany

EDUCATION

Johannes Gutenberg University of Mainz — Mainz, Germany
Doctor of Philosophy, Physics — Sep. 2021 - present
Thesis: Theory and computer modelling of self-organization of linear-dendritic macromolecules into colloidal nano-structures: impacts of topological and molecular mass polydispersity.

Princeton University — Princeton, USA
Secondment at the Webb Lab — Jan. 2025 - Mar. 2025
Project: Multi-particle collision dynamics (MPCD) simulations of bottlebrush polymers and their data-driven exploration via variational autoencoders (VAEs)

The University of Edinburgh — Edinburgh, United Kingdom
MPhys Theoretical Physics (Hons) (4.0 GPA) — Sep. 2016 - May 2021
Dissertation: Molecular dynamics (MD) simulations of DNA unknotting.

RESEARCH EXPERIENCE

Johannes Gutenberg University of Mainz — Mainz, Germany
Supervisor: Prof. Friederike Schmid — Sep. 2021 - present

- Investigated polydispersity and curvature effects on linear polymer brushes using self-consistent field (SCF) theory in the strong-stretching limit, allowing for the analytic treatment of such structures. Showed that zones devoid of polymer ends can be found in almost any position by carefully selecting the polydispersity and curvature of the brush.
- Developed in collaboration with others, an SCF code to more accurately calculate free energies of various polymer systems using adaptive discretization.
- Investigated the properties of micelles formed from linear-hyperbranched block copolymers (LHBCs) by mapping polymer structures obtained from molecular dynamics (MD) simulations onto representations compatible with SCF theory. Subsequently, we performed numerical SCF calculations in the grand canonical ensemble and demonstrated that micelles formed from moderately polydisperse polymers exhibit superior encapsulation capacity, enhanced stability, and a higher number of chain ends compared to those formed from monodisperse diblock or linear-dendritic block copolymers.
- Explored micelle forming gradient copolymers using SCF and discovered that the gradient can influence equilibrium morphology. Sharper gradients favor the formation of spherical micelles, while flatter gradients promote cylindrical and lamellar structures, despite the overall chemical composition remaining unchanged.

Princeton University Princeton, USA
Supervisor: Prof. Michael A. Webb Jan. 2025 - Mar. 2025

- In this project, we performed multiparticle collision dynamics (MPCD) simulations of bottlebrush polymers across a range of concentrations and developed a variational autoencoder (VAE) to learn and analyze the latent space representing their architecture and three-dimensional morphologies. We then explored this latent space by generating representative polymer topologies and examining their shear viscosity behavior. In future work, we aim to identify the limits of achievable shear viscosities in these systems via Bayesian optimization.

The University of Edinburgh Edinburgh, United Kingdom
Supervisor: Dr. Davide Michieletto Sep. 2020 - May 2021

- In this master dissertation, we explored the unknotting behavior of composite knots in DNA, initiated by enzymes, using coarse-grained MD simulations. To explain the results, we proposed a 1D simplified model to test our hypothesis for the accelerated unknotting observed.

Supervisor: Dr. Bartlomiej Waclaw Jun. 2018 - Aug. 2018

- During this summer internship, we investigated the phenomenon of resonant amplification of a predator-prey model's population oscillations. For this, we employed both computer simulations and analytical calculations to assess the origins and effect of such a phenomenon on the populations.

SELECTED HONORS AND AWARDS

Theoretical Physics Integrated Masters Class Medal	2021
Dewar & Ritchie Prize	2021
John Laing Scholarship	2020
Theoretical Physics Senior Honours Class Medal	2020
Physics and Astronomy Career Development Scholarship	2019
Edinburgh Award	2018
Pre-Honours Certificate of Merit	2017 and 2018

WORK EXPERIENCE

Johannes Gutenberg University of Mainz Mainz, Germany
Physics Tutor Sep. 2021 - present

The University of Edinburgh Edinburgh, United Kingdom
Volunteer Tutor in a physics peer mentoring scheme Sep. 2017 - May 2019

Tutorful Edinburgh, United Kingdom
Online tutor for undergraduate studies, A-Levels and Scottish Highers Aug. 2020 - May 2021

PUBLICATIONS

1. **Giannakou, M.**; Borisov, O. V.; Schmid, F., Strong Stretching Theory of Polydisperse Curved Polymer Brushes. *J. Chem. Phys.* 2024, 161 (1), 014903.
2. Qiao, L.; **Giannakou, M.**; Schmid, F., An Efficient and Accurate SCF Algorithm for Block Copolymer Films and Brushes Using Adaptive Discretizations. *Polymers* 2024, 16 (9), 1228.
3. **Giannakou, M.**; Bartlomiej, W., Resonant Noise Amplification in a Predator-Prey Model with Quasi-Discrete Generations. *Scientific Reports*, 2024, 14 (1), 16783.
4. **Giannakou, M.**; Borisov, O. V.; Schmid, F., Micelle Forming Linear–Dendritic Block Copolymers: A Theoretical Comparison between Random Hyperbranched and Precise Dendrimer Polymer Architectures. *Macromolecules*, 2025, 58 (11), 5872–5882.

5. Dinh, T. D. T.; **Giannakou, M.**, Laktionov, M.; Ghulam, K. Y.; Pusse, S.; Tzourtzouklis, I.; Fribiczer, N.; Seiffert, S.; Floudas, G.; Gallei, M.; Borisov, O. V., Schmid, F.; Müller, A., Influence of Gradient on Gradient Copolymer Micelle Morphologies in Solution (In preparation)
6. **Giannakou, M.**; Jiang, S.; Webb, M. A. Multi-Particle Collision Dynamics Simulations of Bottlebrush Polymers and their Data-Driven Exploration via Variational Autoencoders (In preparation)

SELECTED TALKS

1. **Giannakou, M**., Strong Stretching Theory of Polydisperse Curved Polymer Brushes, DPG spring meeting, 2023, Regensburg, Germany

REFERENCES

Prof. Friederike Schmid (Phd supervisor)
Johannes Gutenberg University of Mainz
9 Staudingerweg, Komet 1, Mainz, 55128, Germany
+49(6131)39-20365
friederike.schmid@uni-mainz.de

Dr. Bartlomiej Waclaw (Career development scholarship supervisor)
Institute of Physical Chemistry (ICHF), Polish Academy of Sciences
Warsaw, 01-224, Poland
+48223432174
bwaclaw@ichf.edu.pl